X-rays from Central Starburst Galaxies

An Analysis of ROSAT Observations

Dissertation

zur Erlangung des Doktorgrades

der Mathematisch-Naturwissenschaftlichen Fakultät

der Christian-Albrechts-Universität

zu Kiel

vorgelegt von

Daniel Tschöke

Kiel

2001

Referent: ..... Prof. Dr. Gerhard Hensler

Korreferent: ..... Prof. Dr. Volkmar Helbig

Tag der mündlichen Prüfung: ..... 13. Februar 2001

Zum Druck genehmigt: ..... Kiel, 17. Februar 2001

Space... is big. Really big.
You won't believe how vastly hugely
mindboggingly big it is.

Douglas Adams
'The Hitch Hiker's Guide to the Galaxy'

But pardon, gentles all,
The flat unraised spirits that hath dar'd
On this unworthy scaffold to bring forth
So great an object ...

O, pardon! since a crooked figure may
Attest in little place a million;
And let us, ciphers to this great accompt,
On your imaginary forces work.

William Shakespeare
'King Henry V'

Contents

List of Figures

List of Tables

Abbreviations

ACIS	Advanced CCD Imaging Spectrometer
AGB	asymptotic giant branch
AGN	active galactic nucleus
ASCA	Advanced Satellite for Cosmology and Astrophysics
BCDG	blue compact dwarf galaxy
BH	black hole
BMBF	Bundesministerium für Bildung, Wissenschaft, Forschung und Technologie
BMFT	Bundesministerium für Forschung und Technologie
BS	Bremsstrahlung
CCD	charge coupled device
CoI	co-investigator
dE	dwarf elliptical
DG	dwarf galaxy
dIrr	dwarf irregular
ECF	energy conversion factor
EPIC	European Photon Imaging Camera
ESA	European Space Agency
EUV	extreme ultraviolet
EXSAS	Extended Scientific Analysis System
FBG	faint blue galaxy
FIR	far-infrared
FOC	Faint Object Camera
FOV	field of view
FWHM	full width at half maximum
GMC	giant molecular cloud
GSOC	German Space Operation Center
HEAO	High Energy Astrophysics Observatory
HMS	high-mass star
HMXB	high-mass X-ray binary
HRC	High Resolution Camera
HRI	High Resolution Imager
HST	Hubble Space Telescope
ICM	intracluster medium
IDL	Interactive Data Language
IEQ	ionization equilibrium
IGM	intergalactic medium
ILR	inner Lindblad resonance
IMF	initial mass function
IPAC	Infrared Processing and Analysis System

IR	infrared
IRAF	Image Reduction and Analysis Facility
IRAS	Infrared Astronomy Satellite
ISM	interstellar medium
ISO	Infrared Space Observatory
LINER	low-ionization nuclear emission-line region
LMC	Large Magellanic Cloud
LMXB	low-mass X-ray binary
MCP	microchannel plate
MWG	Milky Way Galaxy
MPE	Max-Planck-Institut für extraterrestrische Physik
NASA	National Aeronautics and Space Administration
NED	NASA/IPAC Extragalactic Database
NS	neutron star
OBI	observation interval
PI	principal investigator
PO	power law
POSS	Palomar Observatory Sky Survey
PSF	point spread function
PSPC	Position Sensitive Proportional Counter
QSO	quasi-stellar object
RASS	ROSAT all-sky survey
RGS	Reflection Grating Spectrometer
ROR	ROSAT observation request
ROSAT	Röntgensatellit
RS	Raymond-Smith
SAAD	South Atlantic Anomaly Detector
SAO	Smithsonian Astrophysical Observatory
SB	starburst
SBDG	starburst dwarf galaxy
SED	spectral energy distribution
SERC	Science and Engineering Research Council
SFH	star formation history
SFR	star formation rate
SMC	Small Magellanic Cloud
SN	supernova
SNR	supernova remnant
SSC	super star cluster
Sy	Seyfert galaxy
ULIRG	ultraluminous infrared galaxy
UV	ultraviolet
WFC	Wide Field Camera
WFPC	Wide Field Planetary Camera
XEUS	X-ray Evolving Universe Spectroscopy Mission
XMA	X-ray mirror assembly
XMM	X-ray Multi Mirror Mission
XRT	X-ray telescope

Abstract

Starbursts represent an important phase in galaxy evolution. Mass and energy input from starburst regions into the interstellar medium (ISM) by stellar winds and supernovae have a strong impact on the chemical composition of the ISM in galaxies. Large-scale outflows from starburst galaxies are important for the evolution of the intergalactic medium in galaxy clusters. From theory different triggering mechanisms of starbursts have been discussed, like e.g. a bar potential in giant spirals or gravitational interaction between galaxies. Central activity in giant gas-rich spirals has been observed in the form of a nuclear or circumnuclear starburst as well as an active galactic nucleus (AGN). The consistent requirement for both phenomena, i.e. huge amounts of gas concentrated in the galactic center, rises the question of a possible connection.

This work presents the observed X-ray properties of a small sample of four starburst galaxies differing in distance, morphology, and external influence. The study serves to investigate the complexity of starburst activity, the influence of different external factors, and the detectable consequences for the starburst host systems in the X-ray regime. The observations have been carried out by the German X-ray satellite ROSAT.

NGC 4410 consists of two close gravitationally interacting galaxies. The western spiral component NGC 4410 a reveals an X-ray bright center with a total 0.1–2.4 keV luminosity of 4×10^{41} erg s^{-1}. It is the brightest X-ray sources in the galaxy sample indicating the influence of interaction on central activity, as observed in the majority of luminous IRAS galaxies. For the eastern companion only an upper limit of its X-ray luminosity can be specified.

More details about the spatial distribution of X-ray sources in galactic disks of starburst spirals are investigated in the face-on Virgo galaxy NGC 4303. This galaxy belongs to the class of barred spirals. The X-ray observations are discussed in connection with gas dynamics caused by the bar potential as trigger mechanism of the observed central starburst in NGC 4303. The dominant X-ray source is the nucleus, additional sources are at the tips of the bar and within the spiral arms, consistent with hydrodynamical simulations of the gas component in barred galaxies.

A common phenomenon of spirals with central starbursts is observed in NGC 4569 and NGC 2903. Hydrodynamical simulations predict the existence of kpc-scale gaseous outflows from the center into the halo of these systems. These galactic superwinds have been observed in several edge-on starburst galaxies. In this work I present the first observations of hot X-ray gas several kpc above the galactic disk in spirals with intermediate inclination, i.e. NGC 2903 and NGC 4569. The properties of the X-ray halo gas in these two systems are discussed in comparison with reported X-ray halos of edge-on galaxies. NGC 2903 has a barred morphology and is classified as 'hot-spot' galaxy, i.e. the nucleus consists of several optically bright emission spots. In X-rays NGC 2903 reveals a one-sided gaseous outflow from the center, extending more than 5 kpc into the galactic halo.

In contrast to this isolated galaxy, NGC 4569 experiences strong interaction with the

Virgo ICM. Its H I and Hα structure clearly indicate the influence of the ICM. Most strikingly, the one-sided western X-ray outflow coincides with a giant Hα feature up to 10 kpc above the disk. Such an extended feature has not been observed in any other starburst galaxy of comparable morphology so far. The nature of the very compact core of NGC 4569 is not yet fully understood, whether dominated by an ultraluminous compact super star cluster or an AGN.

The analysis of the ROSAT data, the resulting complexity of central starbursts, and the restricted possibilities of achieving detailed information from the ROSAT data about the nature of these phenomena make clear the requirements to follow-up X-ray missions. Better spatial and spectral resolutions of new instrumentation onboard the recently started satellites *Chandra* and *Newton*-XMM provide a more detailed investigation of starbursts in X-rays. This is necessary to encounter existing contradictory interpretations of observations in the literature and to check the observed properties of starbursts with theoretical predictions from improved X-ray emission models, including e.g. effects from non-ionization equilibrium conditions of the observed hot plasma.

Zusammenfassung

Kurzzeitige hohe Sternbildungsaktivitäten in Galaxien (Starbursts) stellen eine wichtige Phase in der Entwicklung dieser Systeme dar. Materie und Energie, die durch stellare Winde und Supernovae aus Sternentstehungsregionen in das interstellare Medium abgegeben werden, haben einen starken Einfluss auf die chemische Zusammensetzung der interstellaren Materie in Galaxien. Großskalige Gasausflüsse von Galaxien sind für die Entwicklung der Materie in Galaxienhaufen von großer Bedeutung. Aus theoretischen Betrachtungen heraus wurden unterschiedliche Auslösemechanismen, wie beispielsweise ein Balkenpotenital in großen Spiralgalaxien oder gravitative Wechselwirkung zwischen Galaxien, für erhöhte Sternentstehung diskutiert. Aktivität in Zentren von großen gasreichen Spiralgalaxien wurden einerseits in Gestalt eines zentralen oder das Zentrum ringförming umgebenden Starburst, andererseits in Form eines aktiven galaktischen Kerns beobachtet. Die Übereinstimmung der Voraussetzung für diese beiden Phänomene, nämlich die Ansammlung großer Mengen von Gas im galaktischen Zentrum, führt zu der Frage einer möglichen kausalen Verbindung.

In dieser Arbeit werden die Röntgenbeobachtungen einer kleinen Gruppen von vier Starburstgalaxien, die sich in ihrer Entfernung, Morphologie, und außeren Einflüssen voneinander unterscheiden, vorgestellt. Die Untersuchung soll die Komplexität von Regionen mit erhöhter Sternentstehungsaktivität, den Einfluss unterschiedlicher äußerer Faktoren und die beobachtbaren Auswirkungen auf die einen Starburst beherbergenden Galaxien im Röntgenbereich verdeutlichen. Die Beobachtungen wurden mit dem deutschen Röntgensatelliten ROSAT durchgeführt.

NGC 4410 besteht aus zwei dicht beieinanderstehenden, gravitativ wechselwirkenden Galaxien. Die westliche Komponente NGC 4410 a zeigt ein im Röntgenbereich zwischen 0.1 und 2.4 keV hell leuchtendes Zentrum mit einer Gesamtleuchtkraft von 4×10^{41} erg s^{-1}. Sie stellt die leuchtkräftigste Röntgenquelle in der Gruppe der präsentierten Objekte dar. Dies verdeutlicht bereits den Einfluss von Wechselwirkungen auf die zentrale Aktivität, wie er in einem Großteil der leuchtkräftigen IRAS-Galaxien beobachtet wird. Für den östlichen Wechselwirkungspartner kann lediglich eine obere Grenze für die Röntgenleuchtkraft angegeben werden.

Genauere Erkenntnis über die räumliche Verteilung von Röntgenquellen in galaktischen Scheiben von Spiralgalaxien mit einem Starburst kann aus NGC 4303 im Virgo-Haufen gewonnen werden, deren Scheibe nahezu frontal beobachtbar ist. Diese Galaxie gehört zu der Gruppe der Balkenspiralen. Die Röntgenbeobachtungen werden im Zusammenhang mit der Dynamik des Gases in dieser Galaxie, die durch das Balkenpotential als auslösendem Mechanismus der erhöhten Sternentstehung im Zentrum verursacht wird, diskutiert. Die dominierende Röntgenquelle stellt das galaktische Zentrum dar, zusätzliche Quellen befinden sich an den Enden des Balkens, sowie in den Spiralarmen. Dies ist in Übereinstimmung mit hydrodynamischen Simulationen der Gaskomponente in Balkengalaxien.

Ein gängiges Phänomen in Spiralgalaxien mit zentralen Starbursts wird in NGC 2903 und NGC 4569 beobachtet. Hydrodynamische Simulationen solcher Systeme sagen die Existenz großskaliger Gasausflüsse (im kpc-Bereich) aus dem galaktischen Zentrum in Richtung des Halos voraus. Diese galaktischen Superwinde wurden in einer Reihe von in Seitenansicht beobachtbaren Galaxien nachgewiesen. In dieser Arbeit werden die ersten Beobachtungen von Spiralgalaxien mit mittlerer Scheibenneigung vorgestellt in denen heißes Röntgengas mehrere kpc oberhalb der Scheibe beobachtet werden kann, NGC 2903 und NGC 4569. Die Eigenschaften des Röntgenhalogases in diesen beiden Systemen werden im Vergleich mit berichteten Röntgenhalos von Galaxien in Seitenansicht diskutiert. NGC 2903 weist eine Balkenmorphologie auf und wird als 'hot-spot'-Galaxie klassifiziert. Das bedeutet, dass der Kern aus einer Anzahl kleiner optisch leuchtkräftiger Gebiete besteht. Im Röntgenbereich ist in NGC 2903 ein einseitiger Gasausfluss erkennbar, der vom Zentrum mehr als fünf kpc in den galaktischen Halo reicht.

Im Gegensatz zu der isolierten Galaxie NGC 2903 erfährt NGC 4569 eine starke Wechselwirkung mit der Materie innerhalb des Virgo-Haufens. Die Erscheinung der Galaxie in HI- und Hα-Beobachtungen lässt deutlich den Einfluss des Haufengases erkennen. Äußerst auffällig ist, dass der einseitige westliche Ausfluss im Röntgenbereich räumlich mit einer riesigen Hα-Struktur übereinstimmt, die sich bis zu einer Ausdehnung von zehn kpc aus der Scheibe heraus erstreckt. Eine solch ausgedehnte Struktur wurde bisher in keiner anderen Starburst-Galaxie mit vergleichbarer Morphologie beobachtet. Die Natur des sehr kompakten Kerns von NGC 4569 ist noch nicht vollkommen verstanden. Er besteht möglicherweise aus einem extrem leuchtkräftigen kompakten Sternhaufen oder einem aktiven galaktischen Kern.

Die Analyse der ROSAT-Daten, die sich hieraus ergebende Kenntnis der Komplexität zentraler Starbursts und die Einschränkungen, detailierte Information aus den ROSAT-Daten über die Natur dieser Phänomene zu erhalten verdeutlichen die Anforderungen an zukünftige Röntgensatellitenmissionen. Verbesserte räumliche und spektrale Auflösung neuer Messinstrumente an Bord der kürzlich gestarteten Satelliten *Chandra* und *Newton*-XMM ermöglichen eine genauere Untersuchung von Starbursts im Röntgenbereich. Dies ist nötig, um bestehende widersprüchliche Deutungen von Beobachtungen in der Literatur aufzuklären und um die beobachteten Eigenschaften von Starbursts mit theoretischen Vorhersagen aus verbesserten Emissionsmodellen, die unter anderem Einflüsse eines Nicht-Ionisationsgleichgewichts in heißen Plasmen berücksichtigen, zu vergleichen.

Chapter 1

Introduction

Galaxies form very complex systems consisting of different morphological (bulge, disk, halo) and mass components (gas, dust, stars). The interaction between stars, hot (up to several ten million Kelvin) and warm (several thousand Kelvin) interstellar gas, and cold cloudy medium is a continuous process of mass and energy exchange. It is directly connected to morphology and dynamics of the galaxies, and determines their chemical evolution.

Formation of new stars from the cloudy medium, stellar evolution depending on their masses, return of mass by stellar winds, planetary nebulae, and supernovae, evaporation, and condensation build a permanent cycle, which characterizes the observational appearance of galaxies. By understanding these processes, it is possible to get a coherent picture of the past, present, and future of galaxies.

1.1 Starburst galaxies

Starburst galaxies are systems in a brief episode of their evolution where the formation of stars from interstellar gas increases drastically. Starbursts (SBs) in giant spirals occur in the most central regions of galaxies (10^2 to 10^3 pc; 1 pc = 3.086×10^{18} cm) with large amounts of gas and dust, and dominate the overall luminosity of these systems. The conversion of gas into stars in these evolutionary phases would consume the total amount of gas in a timescale much shorter than the lifetime of galaxies. So SBs can only be short transient phenomena. They last for only 10^8 yr or shorter (e.g. Heckman 1998). The main energy source in SBs are luminous ($L \geq$ few 1000 $L_\odot$; $L_\odot = 3.85\times10^{33}$ erg s^{-1}) high-mass O- and B-type stars (HMS; the lower mass limit for HMS depends on the mass loss during the asymptotic-giant-branch or AGB phase of the star; it lies at about $M_{\rm low} = 8\ M_\odot$; $M_\odot = 1.989\times10^{33}$ g). Because of their short evolution of several 10^6 to several 10^7 yr, OB stars are good tracers of the actual star formation rate (SFR). They produce fast stellar winds, propagating supersonically into the ambient ISM and forming expanding bubbles (Castor et al. 1975; Weaver et al. 1977). As Leitherer (1994) showed, the wind speed and the subsequent mass loss of the individual stars are dependent on the stellar metallicity Z:

$$v_{\rm Wind} \propto L^{-0.3}\ M^{0.6}\ T_{\rm eff}^{0.6}\ Z^{0.1} \tag{1.1}$$

$$\dot{M}_{\rm Wind} \propto L^{2.5}\ M^{-1.1}\ T_{\rm eff}^{1.3}\ Z^{0.8}. \tag{1.2}$$

After 20 Myr or less, depending on the stellar mass, the OB stars end up in type II supernova (SN II) explosions, forming expanding bubbles filled with hot gas that emits X-rays.

Due to the strong grouping and the short evolution timescale, stellar winds and expanding SNR shells accumulate to superbubbles. Leitherer (1994) discussed the contribution of energy input $\dot{E}_{\rm Wind}$ and mass injection $\dot{M}_{\rm Wind}$ from stellar winds and SNRs. Up to the time of the first SN II(depending on the upper-mass cutoff of the initial mass function, IMF, of the central stellar cluster) the only energy input is contributed by stellar winds. Then SNRs provide a significant energy fraction. From the equations for $v_{\rm Wind}$ and $\dot{M}_{\rm Wind}$ we can derive $\dot{E}_{\rm Wind} \propto Z$. Model calculations by Leitherer (1994) with a continuous SFR of 1 $\mathrm{M}_\odot$ yr^{-1} have shown that only for $Z > \mathrm{Z}_\odot$ stellar winds are still important after the first SNe IIhave exploded at $t \approx$ several 10^6 yr. For lower metallicities, SNe IItotally dominate the energy input.

First SB galaxies were selected optically, showing bright blue nuclei with strong narrow emission lines (Weedman et al. 1981). The IRAS survey revealed a new class of ultraluminous infrared galaxies (ULIRGs; Soifer et al. 1987; Sanders & Mirabel 1996) with far-infrared (FIR) luminosities of up to a few 10^{12} $\mathrm{L}_\odot$. HMS have temperatures above 25 000 K, their emission thus peaks in the ultraviolet (UV). The UV photons are absorbed effectively by the surrounding dust, whose absorption cross-section is a strong inverse function of the wavelength in the UV. Therefore SBs are believed to be the dominant sources in galaxies with FIR luminosities $L_{\rm FIR} >$ few 10^{10} $\mathrm{L}_\odot$. It turned out that the most luminous ULIRGs are strongly interacting or merging galaxies. For example, one of the most prominent and closest ULIRGs is Arp 220 at a distance of 77 Mpc with a FIR luminosity of $1.3{\times}10^{12}$ $\mathrm{L}_\odot$ (Lutz et al. 1996). Assuming that its FIR emission is dominated by a SB (Sturm et al. 1996), this would imply a SFR of more than 200 $\mathrm{M}_\odot$ yr^{-1} (Kennicutt 1998). A matter of debate is still how much of the produced FIR emission originates from massive star formation or from an active galactic nucleus (AGN). The relation between SBs and AGNs will be discussed shortly in Sect. 1.4.

The importance of SBs can be realized when we consider that SBs are the dominant type of galaxies in the FIR galaxy luminosity function with $L_{\rm FIR} >$ few 10^{10} $\mathrm{L}_\odot$ (Heckman 1998). They contribute by about 10% to the total bolometric emissivity of the local universe. Heckman also concluded that in the four galaxies with the most luminous circumnuclear SBs within a distance of less than 10 Mpc (i.e. M 82, NGC 253, M 83, NGC 4945) 25% of all HMS in this region of the near universe are formed. So SBs are important energy sources and contribute significantly to the structure of galaxies.

SBs provide excellent laboratories for studying the formation and evolution of HMS and their impact on the surrounding interstellar medium (ISM). Energy and mass transfer into the ISM by stellar winds and supernovae observed in these systems are of great interest for the inpact on theoretical stellar models (Leitherer 1994). One important goal is to answer the question how strong these winds and outflows of processed matter contribute to the chemical enrichment not only of the local ISM but also of the intracluster medium (ICM) in clusters of galaxies.

The detection of field galaxies at $z > 3$ with enhanced star-formation activity (Steidel et al. 1996) leeds to the question whether nearby SBs are similar to galaxy formation processes in the early universe. This makes the study of SBs also very important in a cosmological sense.

1.2 Star formation and galaxy morphology

Often the expression 'central SB' refers to the central active region of spiral galaxies. In fact, from the two main morphology groups in the Hubble sequence, spirals and ellipticals (for a more detailed classification of galaxy morphologies see e.g. Binggeli (1994)), only

the first one shows typical features of SBs. On the other hand, several giant ellipticals contain supermassive BHs at their center and show strong non-thermal nuclear activity. A prominent example is the central giant elliptical galaxy in the Virgo cluster, M87, with an estimated central mass of 3×10^9 $M_\odot$ (Kormendy & Richstone 1995; Junor et al. 1999). One big difference to spirals is that most ellipticals contain no or only a little amount of cool gas (e.g. Phillips et al. 1986; Wiklind et al. 1995) and reveal no recent star formation. However, observations with the *Einstein* satellitediscovered a hot ISM component in Virgo cluster ellipticals (Forman et al. 1979). Because of the high X-ray luminosities of this gas (up to 10^{42} erg s^{-1} at 0.5–4.5 keV; Fabbiano 1989, and references therein), this emission is believed to originate from a sequence of outflow and inflow of interstellar gas rather than from galactic superwinds, as observed in SBs (Ciotti et al. 1991). The formation of elliptical galaxies is still in question. In hierarchical scenarios, where ellipticals are believed to form from mergers, the influence of star formation and starbursts may be very important to produce the observed structural and dynamical properties (e.g. Hultman & Pharasyn 1999). But the understanding of galaxy formation has not progressed sufficiently to rule out dissipationless formation processes (see e.g. de Zeeuw & Franx 1991 and references therein).

A further type of galaxies, forming the low-mass end of morphological classification, is the group of dwarf galaxies (DGs), presumably dominating all other galaxies by number in the universe (Binggeli & Cameron 1991; Ferguson & Binggeli 1994), with total masses between 10^6 and 10^{10} $M_\odot$ and diameters of $\leq$10 kpc. The group contains a variety of morphologies, arising the question of formation and evolution of such galaxies. In contrast to giant spirals and ellipticals, the formation of DGs can be observed up to the present as products of galaxy interactions, i.e. formed in tidal arms and stripped off or by self-gravitationally collapsing clouds in gas bridges (Mirabel et al. 1992; Duc & Mirabel 1994; Miller et al. 1997; Duc & Mirabel 1998). For an overview on the different morphologies of DGs see e.g. Binggeli (1994).

One major subgroup of DGs are the dwarf ellipticals (dEs), containing only a very old stellar population and representing the small analogy of giant ellipticals. dEs are typical cluster galaxies, dominating their central regions (e.g. Virgo: Binggeli et al. 1985; Coma: Thompson & Gregory 1993; Fornax: Bothun et al. 1991). Comparable to giant ellipticals they do not show evidence of recent star formation. In contrast to dEs, dwarf irregulars (dIrrs) contain large amounts of gas, comparable to or even exceeding the gas amount of giant spirals. Their appearance is much more multiplex than the one of dEs. Several subgroups have been defined, concerning their appearance and characteristics: HII DGs, containing large H II regions like 30 Dor in the Large Magellanic Cloud; blue compact DGs (BCDGs); X-ray DGs; Wolf-Rayet DGs. In BCDGs one or several violently star-forming regions are observed, forming massive super star clusters (SSCs), embedded in an old elliptical stellar population. They are also called starburst dwarf galaxies (SBDGs) (Driver et al. 1995; Papaderos et al. 1996; Guzman et al. 1998). HII DGs are characterized by strong narrow emission line features, which originate from recent star formation, also indicated by their blue color and mass-to-light ratio (Koo et al. 1995). Also SBDGs in form of faint DGs with blue colors (therefore called faint blue galaxies FBGs) and similar features as local SBDGs have been observed at intermediate redshifts $z \leq 0.7$ (Colless et al. 1990; Lilly et al. 1991; Guzman et al. 1998).

A significant property of dIrrs and SBDGs is the overall lower metallicity (up to 1/40 Z$\odot$) in comparison to giant spirals (Skillman et al. 1989). If we consider the impact of gas flow and galactic winds in SB galaxies and the much lower gravitational potential well in DGs, the chemical and dynamical evolution of SBDGs is of special interest to

understand the observed chemical properties in DGs. Different stellar components often hint to a complex star formation history (SFH) in these systems, often with several active phases of star formation followed by more quiescent epochs. Of special interest are DGs with the lowest observed metallicities, like I Zw 18 (Kunth et al. 1995) and SBS 0335-52 (Izotov et al. 1990), because they might reflect the early epoch of the ISM. In this context mixing processes, galactic winds from SBs and different SFHs are discussed to explain the observations (Matteucci & Tosi 1985; Garnett 1990; Pilyugin 1992; Marconi et al. 1994; Bradamante et al. 1998).

1.3 Triggering mechanisms of central starbursts

Observations reveal a clear relation between the SB phenomenon and galaxy interaction. Approximately 70% of interacting galaxies show enhanced star formation (Bushouse 1986). Most of the interacting systems, which are strong infrared emitters, also contain nuclear SBs (Joseph et al. 1984; Lonsdale et al. 1984; Telesco 1988). The number of interacting galaxies and mergers in the FIR galaxy luminosity function increases drastically from 10% at $L_{\rm FIR} = 10^{10}$ L$_\odot$ to 95% at $L_{\rm FIR} = 10^{12}$ L$_\odot$ (Sanders & Mirabel 1996). It should be noted, however, that the fraction of AGN features in these systems also increases with luminosity.

Also results from numerical simulations connect SBs with interaction processes (Mihos & Hernquist 1994a,b). Chemodynamical models calculated in our working group at Kiel University lead to the result that enhanced star formation on short timescales, strong enough to suffice observations can only be achieved by means of external disturbances or an early rapid cooling and collapse phase of the system. Energy input from massive stars into the ISM, evaporation and condensation cause a self-regulating effect which keeps a galaxy in a quiet equilibrium (Köppen et al. 1995; Köppen et al. 1995).

The main problem in triggering a central SB is the mechanism to accumulate a large amount of gas in the central 1 kpc of the galaxy on a timescale short enough with respect to the feedback time of star formation (few 10^7 yr). Therefore this mechanism has to be effective in transferring angular momentum from the gaseous component. Numerical simulations are used to investigate how strongly merging processes or encounters of galaxies induce enhanced star formation (e.g. Jog 1995 and references therein; Mihos & Hernquist 1996).

Generally, an $m=2$ non-axialsymmetrical bar potential is the most effective way for angular momentum transfer, a radial gas flow toward the center, and gas accumulation in the central 1 kpc of a galaxy (Noguchi 1988; Heller & Shlosman 1994; Piner et al. 1995). The location of the principal resonances, particularly the inner Lindblad resonances (ILRs), arising from the interplay between the bar and the stellar orbits, are of importance. Depending on the disk rotation curve and the rotation velocity of the bar, a galaxy can have zero, one, or two ILRs (for a more detailed description on this subject see, e.g., Binney & Tremaine 1987). These resonances produce density waves of ring-like structure at the location of the ILR. The density waves cause an enhancement of cloud collisions and coalescence of giant molecular clouds (Combes & Gerin 1985) leading to enhanced star formation (Roberts & Stewart 1987).

The possibility of a connection between bar strength, FIR luminosity, and activity (SB and/or AGN) has been investigated in several galaxy samples. Huang et al. (1996) find that stellar bars have a strong enhancing effect on the SFR for galaxies with a ratio of FIR to optical B-band luminosity $L_{\rm FIR}/L_{\rm B} > 1/3$. According to the authors the importance of bars is only given for morphological types earlier than Sbc. In contrast, Martinet & Friedli

(1997) and Chapelon et al. (1999) found a strong correlation between strong, long bars and star formation activity for late-type (> SBbc) morphologies in their samples of 32 and 121 barred galaxies, respectively. Although the sample of Martinet & Friedli (1997) only consists of late-type galaxies, Chapelon et al. (1999) have not found any correlation between bar strength and activity or bar length and activity for early-type systems. The influence of bars has also been discussed concerning radial abundance gradients in spiral galaxies (e.g. Vila-Costas & Edmunds 1992). Martinet & Friedli (1997) found that young strong bars are connected to high SFRs. While young bars show very steep and spatially distinct gradients, indicating strong star formation at the central region, the strength of the bar is an indicator for the speed of flattening of the initial gradient.

1.4 The starburst–AGN connection

A major discussion issue is a possible connection between central SBs and AGNs. In both cases one critical point is the fueling with a sufficient amount of gas to maintain the central activity. Since this requires similar triggering processes, like galaxy interaction and bars, the question arises whether both phenomena are of the same physical nature.

The acronym AGN samples a number of various objects (Woltjer 1990). A common feature of these objects is a very compact massive central source, emitting a non-thermal continuum, in contrast to SBs whose emission mechanism is based on stars and supernovae. AGNs show strong variability on short timescales indicating the very high compactness of the central source. From large emission line widths we know that very deep potential wells cause high gas velocities at the center. The large rate of continuum energy output highly exceeds that of known stellar sources. So the common model for the central source is a massive black hole (BH) accreting gas from a surrounding disk, powered by the gravitational energy. The group of AGNs is empirically divided into three subgroups, characterized by their total central luminosity (Netzer 1990): a) Quasars (QSOs) with $L \approx 10^{45}$–10^{47} erg s^{-1}; b) Seyfert 1 (Sy 1) and Seyfert 2 (Sy 2) with $L \approx 10^{43}$–10^{45} erg s^{-1}; c) LINERs (low-ionization nuclear emission-line regions) with $L \approx 10^{41}$–10^{43} erg s^{-1}.

Although the powering sources in SBs differ from those in AGNs, several authors discussed the question whether the connection SB–AGN represents an evolutionary track (Weedman 1983; Shapiro & Teukolsky 1985; Norman & Scoville 1988). In these models a central stellar cluster evolves, collapses into a BH, and thereby creates an AGN. A symbiotic model describing the coexistence of a nuclear SB and a massive BH at the center of active galaxies has been discussed by Perry (1992) and Williams et al. (1999). In this model the AGN is powered by accretion of the nuclear ISM produced by the stellar mass-loss from the central stellar cluster. Other authors consider AGNs as manifestations of different evolution phases of a central stellar cluster and the extreme examples of nuclear SBs (Terlevich 1990; Terlevich et al. 1994; Cid Fernandes 1997).

Terlevich (1990) pointed out the similarities of a 40 Myr old SB to a typical AGN. According to the author, the sum of spectral features from a young stellar population, supernovae, and supernova remnants produces the energy distribution as observed in active nuclear regions. Many observations of AGNs do not contradict the scenario of a connection between SBs and LINERs or Seyfert 2 nuclei being an evolution track from central giant HII regions over a Seyfert phase with strong narrow forbidden lines, to a typical appearance of a LINER (Terlevich & Melnick 1985). In this model the strong high-excitation lines are produced by photoionization of the HII regions by very hot Wolf-Rayet stars of a special spectral type, called warmers. Nevertheless, this would not explain every type of AGNs, like Blazars and BL Lacs, showing strong collimated emission in the radio regime.

Sanders et al. (1988) studied a sample of 10 ULIRGs observed with IRAS and found a smooth progression from SB-dominated to AGN-dominated systems with increasing luminosity. In fact there is a number of galaxies which can be resolved into a central compact non-thermal nucleus surrounded by a circumnuclear star-forming ring, typically a few hundred pc in diameter, e.g. NGC 1097, NGC 7469, and NGC 1068 (Keel 1985; Pérez-Olea & Colina 1996; Davies et al. 1998).

1.5 Galactic superwinds

In this section I want to introduce the phenomenon of galactic superwinds since the X-ray data hint to the existence of such large-scaled outflows within two galaxies in our sample, i.e. NGC 4569 and NGC 2903. These two objects reveal a one-sided extraplanar diffuse X-ray component, comparable to X-ray halos observed in a number of edge-on galaxies (e.g. Dahlem 1997). The X-ray properties of these halos will be introduced in Sect.2.3.2. Here I will give a short general overview on the formation and evolution of superbubbles and galactic superwinds.

The term 'superwinds' denotes kiloparsec-scale gaseous outflows from galactic disks into the halo. They are driven by stellar winds from massive stars and cumulatively exploding SNe II. The hot gas from these stellar winds and supernovae merges to build a superbubble around the star-forming region expanding into the ambient ISM (Castor et al. 1975; Mac Low & McCray 1988). To create and drive a superwind two basic conditions have to be fulfilled: a) The energy injection rate from the SB must be sufficient to create a region filled with hot gas having a cooling timescale much higher than the expansion timescale. b) The outflow must be powerful enough to break out of the ambient ISM of the galactic disk. Otherwise it would remain embedded as hot bubble in the disk. These conditions are given for typical SBs as Heckman et al. (1990) and Norman & Ikeuchi (1989) have concluded.

The evolution of such expanding superbubbles can be subdivided into several phases, the very short free expansion phase and Sedov phase of the stellar winds and supernova ejecta, the snowplow phase, and the blow-out phase. In the free expansion phase the ejecta expand until the swept up mass of the ISM comparable to their own. In the Sedov adiabatic expansion phase the bubble is driven by thermal pressure. The swept material forms a shell behind the shock front. After a few 10^4 yr the bubble enters the radiative or snowplow phase where the swept-up material cools radiatively. In the blow-out phase the diameter of the superbubble exceeds several times the scaleheight of the disk, breaks out from the disk and expands almost freely into the halo or beyond. Starting from a SB embedded in a molecular disk, the bubble will expand most rapidly along the steepest pressure gradient, i.e. perpendicular to the disk (e.g. Schiano 1985; Mac Low & McCray 1988; Tomisaka & Ikeuchi 1988; Suchkov et al. 1994). In the snowplow phase the expansion time of the bubble exceeds the radiative cooling time of the ambient material. The expanding bubble sweeps up and shock-heats the surrounding ISM. This scenario contains five physically different zones: 1) The SB itself as the innermost region where energy and momentum from the stellar winds of the massive stars and from the supernovae are injected into the bubble. This region is filled with hot ($T \approx 10^8$ K) gas expanding slowly with subsonic speed. The gas has been shock-heated by high-speed collisions of the ejected material from stellar winds and supernovae. 2) The expanding gas passes through the sonic radius into a supersonic-outflow zone. The pressure in this region is dominated by ram pressure depending on the momentum ejected from the SB into the outflow. The gas in this zone undergoes a free expansion and reaches velocities up to several 1000 km s^{-1}. 3) The gas

passes an internal wind shock. The shocked material is reheated to $\sim 10^8$ K and is a strong source of thermal X-ray emission. 4) It is surrounded by a thin shell of swept-up, shocked ambient ISM causing the shocked wind gas in zone 3. It cools radiatively and emits strong optical lines. The expansion of this shell reaches velocities of a few hundred km s^{-1}. 5) The outermost zone is the undisturbed ambient medium.

The bubble reaches the blow-out phase when it has a diameter of a few times the scaleheight of the disk. The swept-up thin shell fragments via Rayleigh-Taylor instabilities and the hot wind material breaks out of the disk of the galaxy. The wind expands into the halo at velocities of several thousand km s^{-1} and builds bow shocks in front of density inhomogeneities immersed in and shock-heated by the outflow. These clouds are possible sources of optical and UV emission lines and soft X-ray emission, depending on the speed of the wind. The wind material may then condensate in the halo and fall back to the disk or escape the gravitation potential of the galaxy and propagate out into the intergalactic medium (IGM). A fraction of the swept-up material from the ISM may also be accelerated to velocities high enough to escape the galaxy.

Superwinds are an important process in many galactic and intergalactic environments. The dynamics of the metal-enriched material in the superwind represents an effective way of mixing material from star-forming regions and the ISM on galactic scales. Since the wind material consists of metal-enriched gas from the stellar winds and supernovae it has been assumed to be the source of a hot ICM (de Young 1978). Enhanced interactions of galaxies in clusters trigger SBs which chemically enrich and heat up the ICM (White 1990; Heckman et al. 1990). Superwinds may also play an important role in formation and evolution of diverse galaxy types (Ostriker & Cowie 1981; Dekel & Silk 1986; Mathews 1989; Berman & Suchkov 1991). The contribution from galactic winds to the cosmic X-ray background has been discussed, e.g., by Bookbinder et al. (1980), Breitschwerdt & Schmutzler (1999), and Moran et al. (1999). Finally, some complex QSO absorption lines may be explained by metal-rich gaseous halos around Magellanic-type dwarf irregulars originating from galactic outflows (York et al. 1986).

In this work I will focus on the X-ray properties of four different galaxies where each SB is triggered by a different dynamical process: NGC 4410, NGC 4303, NGC 4569, and NGC 2903. The main selection criterion for these systems was the existence of indicators for a nuclear SB, although the central source also may be dominated by an AGN. The objects differ in some way from each other, whether in orientation, morphology, or environment.

NGC 4410 is a distant strongly interacting system of two merging galaxies within a group of 11 members. Smith (2000) has observed the entire group in the radio regime and discusses the influence of galaxy–galaxy and galaxy–ICM interaction in the NGC 4410 group. The work on this object was focussed on the two merging galaxies NGC 4410a and NGC 4410b. NGC 4303 is a nearby face-on barred late-type galaxy where one can nicely study different X-ray sources distinguishable within the galactic disk. I will discuss the influence of the bar on the central starburst and the appearance in X-rays of this object. The Virgo cluster member NGC 4569 is of interest due to its interaction with the ICM. This system and the isolated 'hot-spot' galaxy NGC 2903 are observed at intermediate inclination ($i \approx 60°$). So the central source is still not totally covered by the disk component. The most interesting fact about the X-ray observations of these two galaxies are the

one-sided diffuse X-ray halos. Additionally, a very interesting giant Hα outflow coincides with the extraplanar X-ray gas in NGC 4569 and will be discussed separately.

Of course with such a small and inhomogeneous sample of objects the aim of this work is not to find any statistical conclusions. Rather the influence of different factors on the X-ray properties of the single objects, like interaction or barred morphology, was of interest for studying these galaxies. Because of the inhomogeneity, the study of each object is unique and illustrates the complexity of the astrophysical phenomenon with the collective notation 'starburst'. Also the analysis of the ROSAT data reveals the limit of interpretation from the X-ray observations alone, providing the requirements for follow-up X-ray missions like XMM-*Newton* or *Chandra*.

The work is structured as follows: In the Chapter 2 I shall summarize astrophysical sources and emission mechanisms in the X-ray energy range within SB galaxies. Chapter 3 contains general information about the X-ray satellite ROSAT and the reduction and analysis techniques used for the applied data. The central part of this thesis are Chapters 4 to 8, containing the analysis of the individual objects of the galaxy sample. Chapters 4 and 5 have been published in the European journal *ASTRONOMY AND ASTROPHYSICS*. Chapters 6 to 8 have been submitted to the same journal. Each of those chapters is presented in the form as they are published or have been submitted, respectively. The attainments from the analyzed X-ray data are summarized in chapter 9. It furthermore deals with the approach of open questions and the requirement and possibilities of sequencing X-ray missions.

Chapter 2

X-ray sources and emission models

What do we observe from SBs in X-rays? In general, X-ray emitting sources can roughly be divided into two subgroups: discrete point-like objects and extended diffuse sources. Since it is often a question of resolution, it is not always trivial to determine if a source belongs to the first or the second category. An intensively discussed example is the soft X-ray background (e.g. McCammon & Sanders 1990; Fabian 1992), a composition of different components from the Local Bubble (Snowden 1998), the Galactic Halo (Pietz et al. 1998), and distant extragalactic sources (Burrows & Mendenhall 1991; Barber et al. 1996). It is often also at the edge of or beyond the capability of available instruments to resolve single point sources in distant galaxies, and to distinguish them from extended gaseous emission. A concrete example is one subject of this work, i.e. X-rays from active galactic nuclei, which could be caused by a compact AGN or by circumnuclear star-forming regions. In the following, I specify the most important X-ray sources in galaxies and discuss their characteristic spectral energy distributions (SEDs), not only the intrinsic shapes but also the ones we are actually observing, when the photons have passed the Galactic and intergalactic medium.

2.1 Absorption of X-ray emission

ROSAT is sensitive in the soft X-ray regime of 0.1–2.4 keV (see Sect. 3.1). In this spectral range the emission is strongly exposed to photoelectric absorption in the ISM on its way from the source towards the observer. At energies above 2 keV the influence of the ISM is quite low, but for lower energies absorption quickly becomes important. To illustrate this, the mean free path for X-rays in the Galactic plane as a function of photon energy is plotted in Fig. 2.1. Observing in the X-ray regime toward the Galactic center gives a maximum distance of less than 10 kpc for sources at energies of about 2 keV, rapidly decreasing to lower energies. Particularly in the soft X-ray range of ROSAT, absorption plays an important role, and receiving information on the intrinsic emission from distant sources requires to consider this process.

The factor by which the flux is reduced depends on two parameters: the hydrogen column density $N_{\rm HI}$, i.e. the number of neutral hydrogen atoms per $\rm cm^{-2}$ in the line of sight, and the photoelectric absorption cross section σ of the ISM. Besides absorption in the ISM of our own Galaxy, additional components can arise from the IGM and intrinsic absorption within the observed galaxy itself, depending on the location of the X-ray source within the galaxy. This case is of special interest for observations of X-ray emission outside the disk of galaxies, as from extraplanar superbubbles and galactic superwinds (Sect. 1.5).

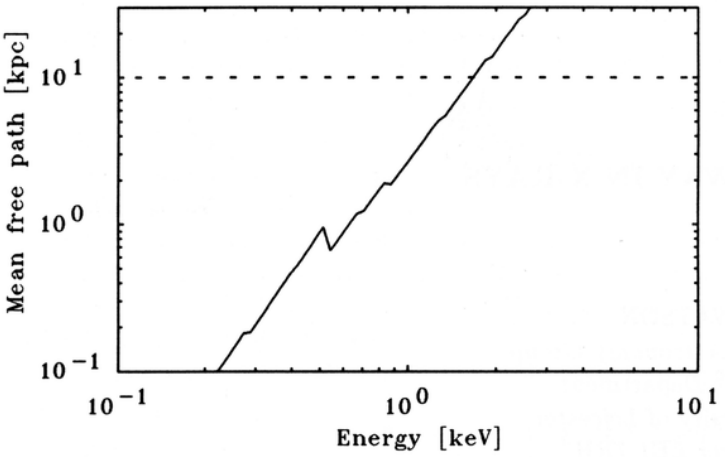

Figure 2.1: Mean free path of X-ray photons through the Galactic plane. The dashed line represents the distance to the Galactic center. Adapted from Watson (1990).

There the orientation of disk and extraplanar component relative to the observer is of importance. In the cases of NGC 4569 and NGC 2903, this will be discussed in more detail.

Since we are observing from a position within the Galactic disk, the amount of $N_{\rm HI}$ strongly depends on the Galactic longitude and latitude of the observed object. The HI all-sky survey by Dickey & Lockman (1990) serves as orientation for particular sky coordinates of interest. This survey is based on a series of several radio observations with $\geq 10'$ angular resolution. So it provides a first estimate to determine the absorption in observed X-ray fluxes, since, as already mentioned, an additional fraction may be caused by intrinsic absorption. On the other hand, small scale fluctuations below the resolution of the survey and, therefore, possibly lower or higher Galactic column densities cannot be excluded. So the flux from extragalactic X-ray sources with low line-of-sight absorption may actually be exposed to a smaller column density than given by the values from Dickey & Lockman (1990).

In the X-ray regime between 100 eV and several keV the cross section σ for photoelectric absorption in the ISM contains contributions from the hydrogen and helium Lyman continuum as well as K absorption edges and some L absorption edges of several heavier elements (Fig. 2.2). The net cross section used in this work is based on Bałucińska-Church & McCammon (1992). Their calculations are based on the results from Henke et al. (1982), and contain 17 relevant elements in the energy range of 0.03–10 keV: H, He, C, N, O, Ne, Na, Mg, Al, Si, S, Cl, Ar, Ca, Cr, Fe, and Ni.

The contribution from absorption to the observed SED is a multiplicative component with an exponential shape:

$$Abs(E) = exp(-N_{\rm HI}\,\sigma(E)), \tag{2.1}$$

where $Abs(E)$ is the factor by which the intrinsic X-ray emission is reduced, $N_{\rm HI}$ is the neutral hydrogen column density, and $\sigma(E)$ is the energy dependent photoelectric absorption cross section.

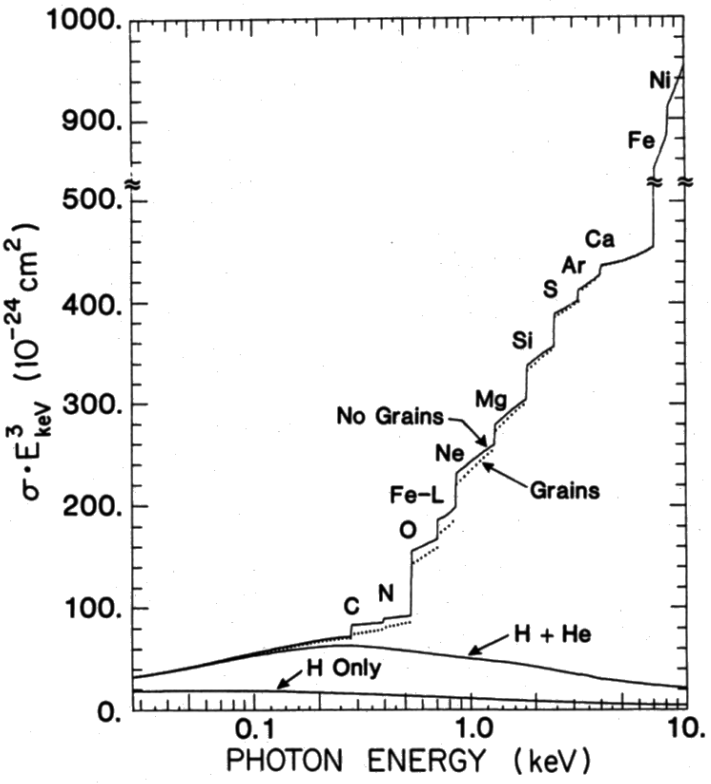

Figure 2.2: Photoelectric absorption cross section as a function of photon energy, scaled by $(E/1\ \mathrm{keV})^3$. The K absorption edges of the single elements are specified in the graph. Contributions by hydrogen and hydrogen+helium are drawn separately. Adapted from Morrison & McCammon (1983).

Besides the multiplicative absorption component, each model of an observed X-ray spectrum contains one or several additive components, describing the intrinsic unabsorbed SED of the astrophysical object. Depending on the nature of the X-ray source, the resulting SED reflects the underlying emission mechanism, like a non-thermal power law, thermal Bremsstrahlung (free-free emission), or emission-line spectra (Raymond-Smith model: Raymond & Smith 1977; MEKAL: Mewe et al. 1986). In general, each emission model f has the following structure:

$$f(E) = \sum_{i=1}^{m} Abs_i(E) \, (\sum_{j=1}^{n} Em_{ij}(E)), \tag{2.2}$$

with the multiplicative absorption components $Abs(E)$, the additive emission components $Em(E)$, m the number of different absorption components, and m the number of emission components diminished by the absorption $Abs_i(E)$. Note that for a model containing more than one emission model, each one can be assigned to a different absorption component. This is useful for complex objects with different intrinsic absorption. However, this differentiation requires a sufficiently bright spectrum, which is usually not the case for the presented data. In the following sections, relevant extragalactic X-ray objects and their typical spectral emission models will be introduced.

2.2 Discrete X-ray sources

In general, basic information about the nature of discrete X-ray sources are obtained from nearby systems within the Local Group, mainly the Milky Way Galaxy (MWG) and the Magellanic Clouds. Main stellar X-ray sources are low-mass X-ray binaries (LMXBs), high-mass X-ray binaries (HMXBs), and supernova remnants (SNRs). The latter objects belong to the category of extended sources and will be discussed in Sect. 2.3.1. Another class of compact X-ray sources are the massive cores of active galaxies.

2.2.1 Low-mass X-ray binaries

LMXBs are binary systems with a low-mass late-type star ($M < 1$ M$_\odot$) and a neutron star (NS) or a BH. Through mass transfer from the late-type star to the compact component via Roche lobe overflow an accretion disk around the NS/BH is created because of conservation of angular momentum. At some stage this material looses angular momentum by friction and falls onto the NS/BH, forming a hot spot on the surface. If a strong magnetic field is present around the neutron star, the mass is diverted to the poles. Rotation of the compact component then leads to the phenomenon of an X-ray pulsar. The energy emitted in the X-rays comes from the gravitational energy of the material falling onto the neutron star/ black hole. The overall shape of the SED of these systems is characterized by a relatively hard ($E > 2$ keV) power law, indicating the non-thermal nature of the emission by the accretion mechanism:

$$I(E) \propto E^{-\Gamma}. \tag{2.3}$$

The exponent Γ is called the spectral index. Typical values for Γ in the SED of LMXBs lie in the range of unity (Nagase 1989). Their X-ray luminosity spans a wide range of $L_{\rm X} \sim 10^{35}$–10^{38} erg s^{-1}. LMXBs are old Population II systems and, therefore, do not contribute significantly to the X-ray flux in SB regions. The number of LMXBs in the MWG is ∼70 objects with about 10 located in the Galactic bulge and also in globular clusters (Watson 1990).

2.2.2 High-mass X-ray binaries

A second, for SBs much more important class of X-ray emitting binary systems are the HMXBs. These objects consist of a massive, early-type star ($M > 5$ M$_\odot$) and, as in LMXBs, a compact companion (either a NS or a BH). These systems are also powered by mass transfer from the first to the latter component. There are two subcategories for the donor star: an OB supergiant, where the mass transfer occurs via Roche lobe overflow or stellar wind capture, or a Be main sequence star. In the latter case the mass accretion is considered to be fed only by the stellar wind. As for LMXBs, the SED of HMXBs has a power-law shape with a spectral index Γ of about unity at energies above 2 keV (Nagase 1989). The X-ray luminosity of the OB binaries lies in the range of $L_{\rm X} \sim 10^{36}$–10^{38} erg s^{-1} (Watson 1990). Most Be binaries have luminosities about 2 or 3 orders of magnitude lower. But they are often highly variable with emission peak close to the level of OB binaries. HMXBs are Population I systems and are therefore important contributors to the observed X-ray emission in highly star-forming regions.

About 100 HMXBs have been detected in the MWG and the Magellanic Clouds. Twelve of these systems are observed in the Large Magellanic Cloud (LMC) and 20 binaries in the Small Magellanic Cloud (SMC) (Coe 2000). Haberl & Sasaki (2000) recently

reported that the number of HMXBs in the SMC is possibly as high as 45. This very high number, compared to the MWG, strongly suggests SB activity in this dwarf galaxy (Popov et al. 1998).

2.2.3 Active Galactic Nuclei

As for HMXBs and LMXBs, the SED of AGNs can be described by a power law, since the energy is also gained by gravitation from accretion of mass onto a central compact source, in this case a massive BH with a total mass in the range of 10^6 to $10^{9.5}$ M$\odot$ (Kormendy & Richstone 1995). It seems from observations that the SED of Seyferts and Quasars is characterized by two different spectral indices. The hard spectrum above about 2 keV can be described by a power law with $\Gamma \sim$1.6–1.9, while the soft range below 2 keV reveals a steeper shape with $\Gamma \sim$2–4 (Turner et al. 1993; Mulchaey et al. 1993; Reeves & Turner 2000).

However, several Seyferts seem to have more complex spectra, i.e. they show a soft excess. The origin of this additional component at energies below about 0.6 keV can have different causes, e.g. a blend of emission lines from the circumnuclear gas, reprocessing of the continuum radiation by material near the nucleus (Netzer 1993), partial covering of the core, where holes in the circumnuclear material cause penetrating X-ray emission to be photoelectrically absorbed by only a very little fraction, or scattering of nuclear radiation by electrons into the line of sight (Mulchaey et al. 1993). The latter assumption arises from comparison of Sy 1 and Sy 2 X-ray spectra, showing similar features. Following a unified model for AGNs (Woltjer 1990), differences in AGN types arise from different line of sights toward the core. While in Sy 1s the observer looks more face-on onto the central accretion disk and core, in the case of Sy 2s the center is covered by that disk. From this geometry also internal absorption features arise in the soft regime (Netzer 1993). In the case of a composite AGN+SB source in our objects, only a simple power-law model was fitted for the non-thermal component, since their PSPC spectra are too faint to be suitable for very complex models.

2.3 Diffuse X-ray emission

2.3.1 Supernova remnants

Observations by ROSAT or the Japanese-American X-ray satellite ASCA (Advanced Satellite for Cosmology and Astrophysics) have spatially resolved X-ray emitting shells around single SNRs in the MWG (e.g. Slane et al. 1999; Borkowski et al. 2000b). Thermal X-ray emission in the range of 100 eV to several keV is produced by the ambient ISM around the SNR and the SN ejecta material, heated up by the blast wave shock from the SN explosion and reverse shocks from interaction of the ejecta material with the surrounding shell (Borkowski et al. 1996; Borkowski et al. 2000a; Decourchelle et al. 2000). Although such a thermal component dominates many X-ray spectra of SNRs, acceleration of electrons by shocks in SNRs is expected to be high enough to produce additional non-thermal synchrotron radiation at higher energies above a few keV (Reynolds 1998). In fact, there are several cases where a high-energetic tail is observed in the X-ray spectrum, consistent with synchrotron emission from shock acceleration (Allen et al. 1997; Borkowski et al. 2000b).

2.3.2 Superbubbles

The strong stellar winds in the OB associations and cumulatively exploding SNe IIare the origin and driving force of superbubbles. Hard X-ray emission will be produced by the hot interior gas of several 10^7 to 10^8 K, heated up by internal shocks (Heckman et al. 1993). The swept-up ambient material is also shock-heated and forms a thin shell, emitting in the soft X-ray regime, like in the case of single SNR shells. Suchkov et al. (1994) calculated hydrodynamical models of superbubbles and galactic superwinds, and found an analytical expression for the produced X-ray luminosity in the 0.1–2.2 keV energy range:

$$L_{\rm X} \propto \dot{E}^{3/5}\ n_{\rm h}^{7/5}\ t^{9/5}, \tag{2.4}$$

where $\dot{E}$ is the energy injection rate from the SB, $n_{\rm h}$ is the halo density, and t is the expansion time of the superbubble. The authors find that this soft component is dominated by the thin swept-up shell around the superbubble. The bulk of hard X-ray radiation above 2 keV is from the galactic superwind material, in agreement with Heckman et al. (1993).

Large kpc-scale outflows from disks of SB galaxies have been observed in several edge-on galaxies, where a distinction from X-ray sources within disk and galactic nucleus is possible. Examples for such X-ray halos are M82 (Lehnert et al. 1999; Weaver et al. 2000), NGC 253 (Dahlem et al. 1998; Pietsch et al. 2000; Weaver et al. 2000), NGC 3628 (Dahlem et al. 1996), NGC 4565 (Vogler et al. 1996). For a review on observed X-ray halos see Dahlem (1997). However, there are significant discrepancies between theory and observations according to the X-ray emission that should be observed from stellar wind bubbles and superbubbles (Mac Low 2000). In general, the X-ray luminosities predicted by simple radial-symmetric models are of the order of one magnitude lower than the observed ones (Chu & Mac Low 1990; Martin & Kennicutt 1995). Several solutions for this disagreement have been proposed. Chu & Mac Low (1990) have considered off-center supernova explosions, Franco et al. (1993) included the interaction of fragmented ejecta with the outer shell, and Martin & Kennicutt (1995) concluded that the evaporation of clouds passed by the shock front and embedded into the hot plume may be a dominant mechanism to increase the X-ray emission. This also reduces the temperature of the hot bubble plasma.

Further controversial properties are metallicities of the X-ray emitting material. Several authors have analyzed observations by applying sub-solar iron abundances and about solar abundances for the α-process elements (Persic et al. 1998; Ptak et al. 1999). In contrast, Dahlem et al. (2000) and Weaver et al. (2000) claim that there is a strong ambiguity in the spectral fits. In the case of the two best studied SB galaxies, M82 and NGC 253, instead of subsolar metallicities, the spectra can be explained by multi-temperature models. The hitherto available spectral X-ray observations leave a lot of different possible interpretations, which will hopefully be much more improved with new observational possibilities in the next months and years. First results from XMM-*Newton* observations of NGC 253 seem to support the picture of a highly complex multi-temperature X-ray halo structure (Pietsch et al. 2000).

2.3.3 Emission models for a hot thermal plasma

The luminosity of a hot plasma, like in stellar winds, SNR shells, and superbubbles, is determined by the emissivity Λ of the gas. This quantity expresses the power emitted by a plasma volume element with temperature T and density n. The luminosity is then given by

$$L = \int n^2 \, \Lambda(T) \, \mathrm{d}V. \tag{2.5}$$

Calculations of the emissivity in X-rays for a hot optically thin plasma have been performed by Raymond & Smith (1977) or Mewe et al. (1986) (see also Kaastra et al. 1996; Dere et al. 1997). These models take into account several contributions, like a continuum component and emission lines from a series of important elements, i.e. He, C, N, O, Ne, Mg, Si, S, Ar, Ca, Fe, and Ni. The continuum emission is a composition of a recombination spectrum, a bremsstrahlung spectrum, and a two-photon spectrum by collisional excitation. In contrast to line emission, the ion is excited to a metastable level and recombines in a two-step continuum emitting process. A Maxwellian electron velocity distribution is assumed. The contribution to the line emission spectrum is from collisional recombination and dielectronic recombination, where a free electron collisionally excites an ion and is simultaneously captured.

For all these processes collisional equilibrium is assumed. This is not necessarily the case for superbubble plasmas with their low densities. The existence or non-existence of ionization equilibrium in superbubbles has strong impact on the interpretation of the observed X-ray spectra, since direct measurement of spectral lines lies beyond the resolution capacity of instruments like the ones onboard ROSAT. Even for the two nearest and best studied SB galaxies, M82 and NGC 253, the interpretation of observations remain equivocal, in terms of ionization equilibrium as well as metallicities, as mentioned above (see Ptak et al. 1997; Tsuru et al. 1997 in contrast to Weaver et al. 2000). This uncertainty continues in interpretation of fainter spectra from more distant galaxies. One only observes integrated blends of emission lines. The fit to these SEDs leaves the possibility of a relatively strong contribution from the continuum with several less strong lines, or a continuum at much lower level with a much larger portion from line emission. This would be the case for non-ionization equilibrium, where high excitation levels are in a quasi-frozen state, because of less recombination processes. As a result, the derived total luminosity for this plasma would be overestimated. Additionally, the completeness of atomic rates from experiment and theory, which the plasma codes are based on, is not given. There are still differences in different codes (Smith & Brickhouse 2000). This again requires high-resolution X-ray spectroscopy, as feasible with XMM-*Newton*.

Chapter 3

X-ray observations and data reduction

The main part of this work is based on ROSAT X-ray observations proposed by Norbert Junkes (principal investigator, PI) and Gerhard Hensler (co-investigator, CoI) from the Institute of Theoretical Physics and Astrophysics, University of Kiel. To get as much information from the sources in the X-ray regime as possible high resolution imaging with the HRI detector (see 3.1.3) as well as spectral information with the PSPC detector (see 3.1.2) has been taken into account. To obtain PSPC observational data of NGC 4303 I used the ROSAT Data Archive at the Max-Planck-Institut für extraterrestrische Physik (MPE) in Garching, Germany. Additional optical data of NGC 4410, NGC 4569, and NGC 2903 are included in the work. Since these data were contributed by external collaborations and the reduction was carried out elsewhere, I shall only report on the reduction techniques of the ROSAT X-ray data performed by myself.

3.1 The X-ray satellite ROSAT

Since the earth's atmosphere is totally opaque for external X-ray radiation, observations in this energy regime cannot be performed by classical ground-based observatories. Therefore the beginning of observational X-ray astrophysics required to bring an X-ray detector several hundred kilometers above the ground outside the protecting atmosphere. It started in 1949 with the detection of X-ray emission from our sun by a photon counter on board of a sounding rocket. The first extrasolar X-ray detection (the binary system Sco X-1) was then obtained in the early sixties (Giacconi et al. 1962). Also balloon experiments carrying detectors to altitudes of about 40 km were used, with the advantage of a larger exposure time of several hours compared to only several minutes for the rocket experiments. On the other hand, the relatively low altitude of several tens of kilometers reached with the balloons made observations only possible in the hard X-ray regime of more than 20 keV. The first X-ray survey has been performed by the *UHURU* satellite, launched in 1970, with a final number of 339 sources (Forman et al. 1978), mainly X-ray binary systems, supernova remnants, Seyfert galaxies, and galaxy clusters. Further important missions in the following decades were, e.g., the *HEAO* project, *Ginga*, the *Einstein* satellite, and the *ROSAT* satellite. For a review on X-ray missions until 1990, see Bradt et al. (1992).

ROSAT (an acronym for the German expression Röntgensatellit) is a joint German, US and British space mission. the project was proposed by the MPE in 1975 and subsequently approved by the Bundesministerium für Forschung und Technologie (BMFT),

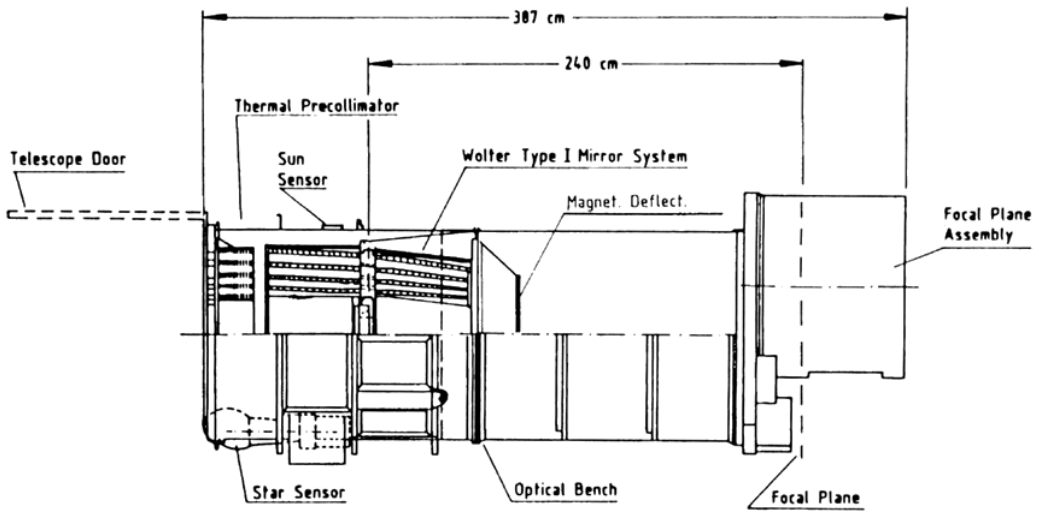

Figure 3.1: Schematic cross-sectional view of the XRT. The focal plane turret on the right houses one HRI and two PSPC detectors with filter wheels. Adapted from Briel et al. (1997).

now Bundesministerium für Bildung, Wissenschaft, Forschung und Technologie (BMBF). The satellite was realized in a collaboration between the MPE, the American National Aeronautics and Space Administration (NASA), and the British Science and Engineering Research Council (SERC). While NASA provided the launch of the satellite, the MPE was responsible for the scientific management and the *Positional Sensitive Proportional Counter* (PSPC), one of three instrument types on bord of ROSAT. The *High Resolution Imager* (HRI) was developed by the Smithsonian Astrophysical Observatory (SAO), and Leicester University was contributing the *Wide Field XUV Camera* (WFC).

The satellite was launched on a Delta-II rocket on June 1, 1990. Ground-based control of the spacecraft was performed by the German Space Operation Center (GSOC) at Weilheim, Germany. The mission ended on February 12, 1999. The scientific goal of the mission was two-fold: at first, the ROSAT all-sky survey (RASS) in the X-ray and EUV range, and, secondly, the detailed study of selected X-ray and EUV sources. The X-ray telescope operated in the energy range of 0.1–2.4 keV (HRI and PSPC), while the WFC observed in the range between 0.04 and 0.2 keV. From the WFC survey, it became clear in May, 1991, that the count rates were systematically (about 20%) lower than expected. Since no data from the WFC is included in this work I shall concentrate on the X-ray telescope and detectors. For more detailed information on ROSAT see Briel et al. (1997).

3.1.1 The X-ray telescope

The X-ray telescope (XRT) consists of the X-ray mirror assembly (XMA), a magnetic deflector, two South Atlantic Anomaly Detectors (SAADs), and the scientific detectors, one HRI and two PSPCs, mounted on a turret in the focal plane (Fig. 3.1). The XMA is a grazing incidence Wolter type I configuration with four parabolic and hyperbolic nested mirror shell pairs. It has an aperture of 84 cm and a focal length of 240 cm. The mirror shells are made out of a glass ceramic with a very small thermal expansion coefficient, called Zerodur, and coated with a thin gold layer in order to increase X-ray reflectivity.

The magnetic deflector serves to reduce any flux from soft electrons in the focal plane. The two SAADs are charged particle detectors, N-type silicon semi-conductors, which monitor the particle background. While orbiting the earth, the satellite crossed regions of intense particle background: the belt regions and the South Atlantic Anomaly. In that case, the high voltage of the operating detector was turned down to a minimum.

3.1.2 The Position Sensitive Proportional Counter (PSPC)

Originally, two PSPC detectors, PSPC-B and PSPC-C, were operating on board of ROSAT. During the RASS, on January 25, 1991, PSPC-C was destroyed, because of an onboard computer error which caused a scan across the sun. Afterwards all observations were performed by PSPC-B (additional detectors PSPC-A and PSPC-D were used for the ground calibration). All PSPC data in this work are obtained by PSPC-B.

The PSPC is a set of two multiwire proportional counters. Two anode grids are made of gold-plated tungsten wires, 10 μm in diameter, with a spacing between the wires of 1.5 mm and 2 mm, respectively. Two cathode grids consist of platinum iridium wires with a diameter of 50 μm and a spacing of 0.5 mm. The counters contain a gas mixture of 65% argon, 20% xenon, and 15% methane. The PSPC entrance window is a 1 μm foil of polypropylene coated with carbon and lexan, making it opaque at energies just above 0.28 keV. The transmission below that energy is about 50%. The protecting foil is supported by a wire grid structure, as shown in Fig. 3.6. An X-ray photon penetrating the detector gas produces an electron by photo-electric absorption. Ionization of other gas atoms causes secondary electrons.

The total field of view (FOV) is 2°. Four different filters can be placed in front of the detector for diverse options, 'standard' observations, monitoring, or calibration purposes. With the cathode wire alignment, an on-axis angular resolution of $\sim 25''$ can be achieved. The energy resolution, depending on the photon energy, is $\Delta E/E = 0.43(E/0.93)^{-0.5}$ full width at half maximum (FWHM). The quantum efficiency (the fraction of photons converted into counts) of the ROSAT PSPC as a function of energy is shown in Fig. 3.2. The curve includes the window transmission, the average transmission of the window support structure, and the absorption of the detector gas.

3.1.3 The High Resolution Imager (HRI)

The second type of detector onboard ROSAT is the HRI, a two-dimensional position sensitive microchannel plate (MCP) detector. This instrument is basically identical to the *Einstein* Observatory HRI. One significant difference is the material of the photocathode, cesium iodide instead of magnesium fluoride, to increase the quantum efficiency by a factor of three (Fig. 3.3). The detector has no intrinsic energy resolution. Since the cesium iodide coated MCPs are sensitive to UV radiation, a 1.05 μm thick aluminium-coated plastic window has been placed in front of the MCPs. This also protects the photocathodes from positive ions near the satellite. The energy detection range is limited by this UV/Ion filter at low energies and by the decreasing mirror reflectivity at high energies.

The FOV of the detector is $38'$. Spatial and timing resolution of the HRI are $\sim 1\farcs7$ (FWHM) and 61 μs, respectively. Main characteristics for the XMA, PSPC, and HRI are summarized in Table 3.1.

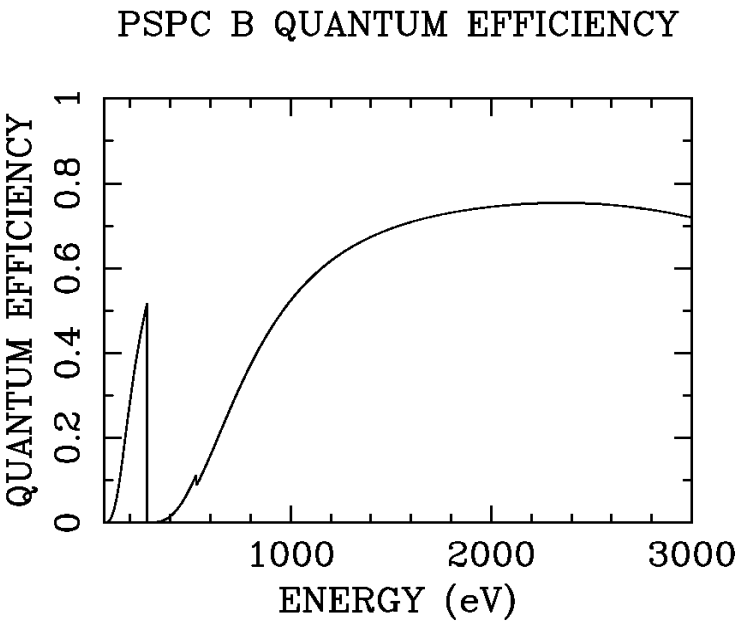

Figure 3.2: Quantum efficiency of the PSPC as a function of energy. Window transmission, transmission of the support structure, and gas absorption efficiency are included. Adapted from Briel et al. (1997).

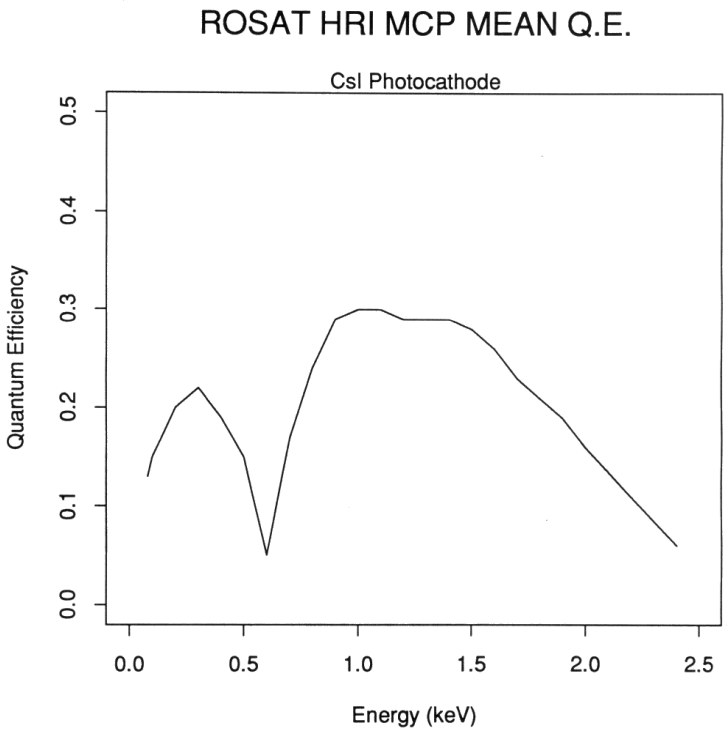

Figure 3.3: Quantum efficiency of the HRI MCPs as a function of energy. Adapted from ROSAT AO-2 (1991).

Table 3.1: Main characteristics of the ROSAT components XMA, PSPC, and HRI.

Component	Attribute	Quantity
XMA	Mirror	Wolter I; 2×4 mirror shells; gold-coated Zerodur
	Focal length	240 cm
	Aperture	84 cm
	Geometric area	1141 cm^2
	High energy cutoff	∼2 keV
	Angular resolution	$\leq 5''$ half energy width
PSPC	FOV	2°
	Detector gas	65% Ar, 20% Xe, 15% CH_4
	Energy resolution	0.43 at 1 keV
	Spatial resolution	$\sim 25''$ at 1 keV
HRI	FOV	$38'$
	Spatial resolution	$1\farcs7$ (FWHM)
	Temporal resolution	61 μs

3.2 Basic reduction of the X-ray data

The ROSAT observations used in this work are listed in Table 3.2. The reduction of the ROSAT data has been performed by means of several software packages. The most basic part, i.e., creation of images and spectra, has been done with already existing data processing codes, written by Ralph Dickow (Dickow 1995), partly upgraded and changed for special purposes. These codes are written in IDL (Interactive Data Language, Research Systems, Inc.). Further analysis of the X-ray spectra was performed by using the interactive X-ray spectral-fitting program XSPEC v10 (Arnaud 1996). I also used the Extended Scientific Analysis System (EXSAS) for interactively analyzing X-ray data in general (Zimmermann et al. 1997).

Several corrections of the raw data have to be performed before a quantitative analysis is possible, i.e.:

- energy dependence of mirror reflectivity and detector sensitivity
- off-axis angle dependence of the point-spread function
- vignetting effects
- shadowing by support structure
- wobble movement of the satellite
- background contamination

These corrections are described in the following. The bf energy dependence is described by the effective area of the combined mirror+detector, which is the integrated collective area size if each incoming photon would be detected. This quantity depends on the **off-axis angle** of incoming photons within the FOV. The effective area is determined by the quantum efficiency of the detector and the mirror collective area. The effective areas for

Table 3.2: List of ROSAT observational data.

Observation ID (ROR)	Object	Detector	Central coordinates RA (J2000)	Dec (J2000)	Date of observation	Exposure time (sec)	Principal investigator	Co-Investigator
600587p	NGC 4410	PSPC	$12^h26^m28^s.8$	$+09°01'12''$	Jun 28–30, 1993	23368	N. Junkes[b]	G. Hensler[b]
600694h	NGC 4410	HRI	$12^h26^m28^s.8$	$+09°01'12''$	Jun 27–Jul 1, 1995	36726	N. Junkes	G. Hensler
701095p[a]	NGC 4303	PSPC	$12^h22^m21^s.6$	$+04°13'11''$	Dec 24–26, 1992	8135	R. Staubert	
600854h	NGC 4303	HRI	$12^h21^m55^s.2$	$+04°28'11''$	Jul 2–8, 1996	16055	N. Junkes	G. Hensler
600854h-1	NGC 4303	HRI	$12^h21^m55^s.2$	$+04°28'11''$	Jun 9–23, 1997	27538	N. Junkes	G. Hensler
600854h-2	NGC 4303	HRI	$12^h21^m55^s.2$	$+04°28'11''$	Jan 6–7, 1998	5600	N. Junkes	G. Hensler
600437p-1	NGC 4569	PSPC	$12^h36^m48^s.0$	$+13°10'12''$	Dec 19–21, 1992	17976	N. Junkes	G. Hensler
600603h	NGC 4569	HRI	$12^h36^m48^s.0$	$+13°09'36''$	Jul 10-11, 1994	2109	N. Junkes	G. Hensler
600603h-1	NGC 4569	HRI	$12^h36^m48^s.0$	$+13°09'36''$	Jun 18–21, 1995	21858	N. Junkes	G. Hensler
600093p	NGC 2903	PSPC	$09^h32^m09^s.6$	$+21°30'00''$	May 6–7, 1991	9184	H. Zinnecker	N. Junkes
600602h	NGC 2903	HRI	$09^h32^m09^s.6$	$+21°30'00''$	Apr 27–29, 1994	13619	N. Junkes	G. Hensler
600602h-1	NGC 2903	HRI	$09^h32^m09^s.6$	$+21°30'00''$	Nov 7, 1994	8284	N. Junkes	G. Hensler

[a] Data taken from the ROSAT Data Archive

[b] University Kiel, Germany

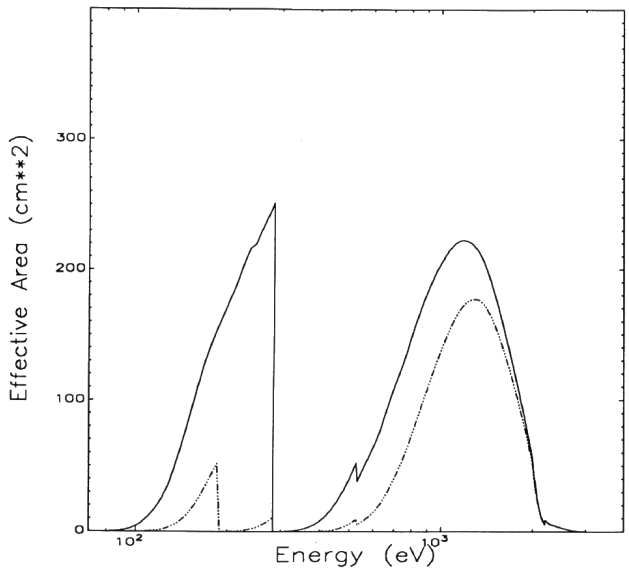

Figure 3.4: XMA/PSPC on-axis effective area with (dotted line) and without (solid line) boron filter. The optional boron filter divides the carbon window below 0.28 keV into two subbands. Adapted from ROSAT AO-2 (1991).

the combinations XMA/PSPC and XMA/HRI are shown in Figs. 3.4 and 3.5. The feature at 0.28 keV is due to the carbon absorption edge of the carbon coated entrance window. The minimum around 0.6 keV in Fig. 3.5 is caused by the Cs and I absorption edges from the MCPs. The drop at high energies comes from the decreasing reflectivity of the mirror.

Vignetting is a radius-dependent effect and occurs from shadowing at the entrance window boundaries increasing toward the edge of the FOV. Another shadowing effect is caused by the PSPC entrance **window support structure** (see Fig. 3.6). To expose the detector areas covered by this structure at least partly the satellite performs a permanent one-dimensional **wobbling** motion perpendicular to the optical axis. This prevents contamination of the images from the small-scale wire grids. However, the large-scale support structure cannot totally be corrected by this method, although it will be taken into account in the exposure maps (see text below). So off-axis sources located in these image areas have to be handled with caution.

For the PSPC observations the vignetting effect, the shadowing by the support structure, and the wobble motion are corrected by a calibration image, called exposure map. Such an exposure map has been generated for each single PSPC observation. In Fig. 3.7 on can nicely discern the radial intensity gradient to take the vignetting into account. The wobble direction is indicated by the blurred support structure. HRI images are corrected by a standard vignetting correction image from calibration measurements.

Contamination by **background** events, i.e., detected photons not originating from the astrophysical object of interest, can have five different reasons:

- Particle background
- Scattered solar X-ray background by the earth's residual atmosphere

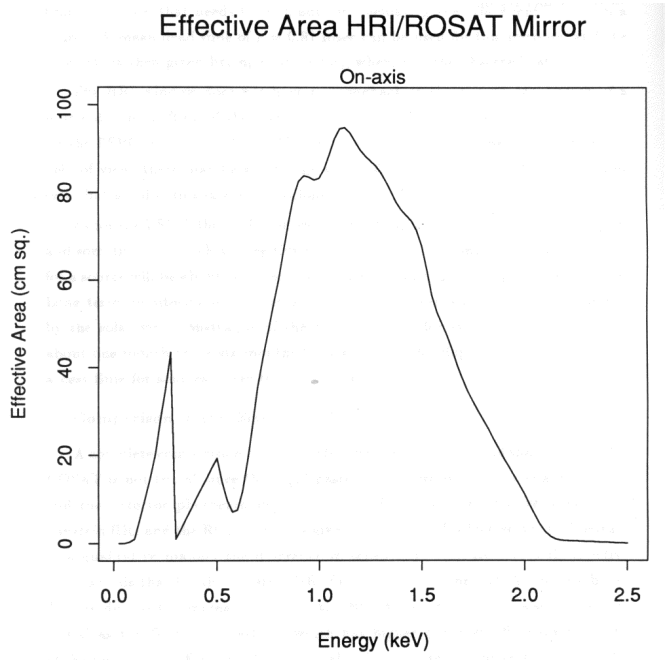

Figure 3.5: XMA/HRI on-axis effective area. Adapted from ROSAT AO-2 (1991).

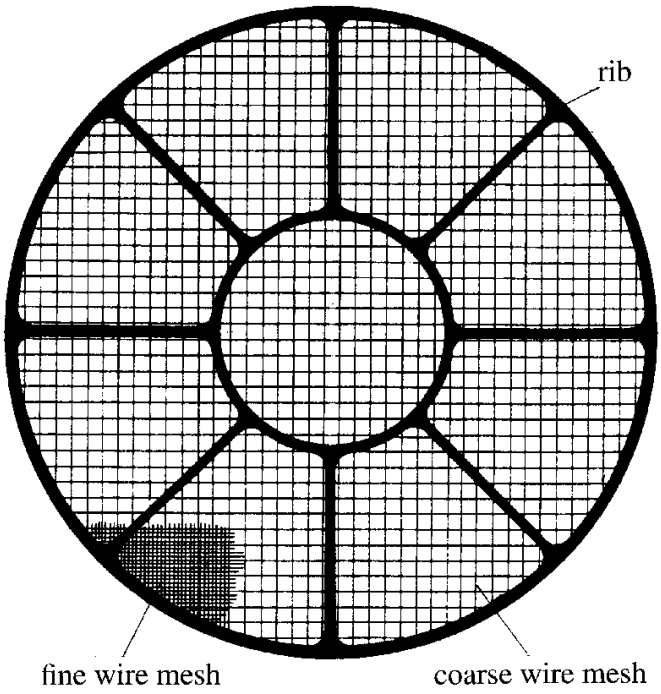

Figure 3.6: ROSAT PSPC window support structure. Adapted from ROSAT AO-2 (1991).

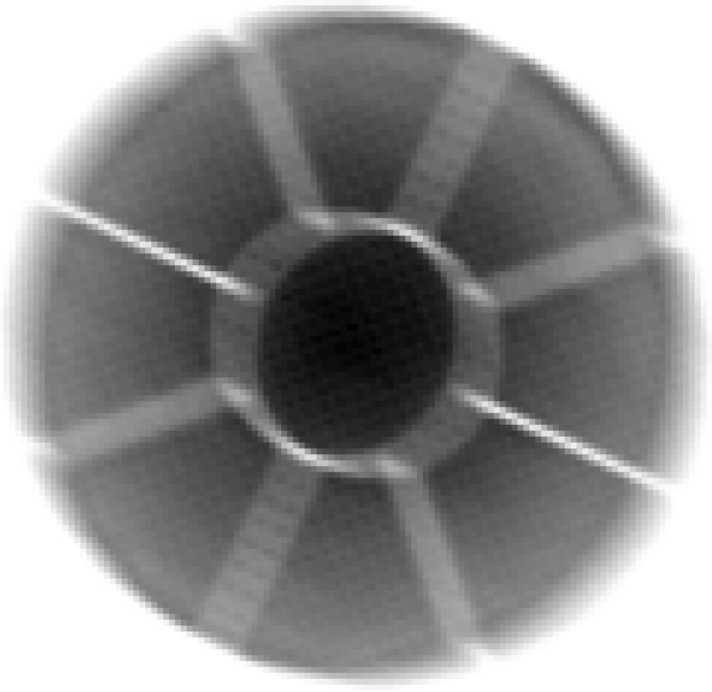

Figure 3.7: Exposure map for the PSPC observation of NGC 4569. The support structure is clearly visible. The blurring in one direction is caused by the wobble motion of the satellite. The radial brightness difference indicates the vignetting effect correction.

- Auroral induced X-ray background
- Cosmic X-ray background
- Long term enhancements of unknown origin

In the HRI an additional component has been detected, an internally produced continuum background. It is supposed to originate mainly from residual radioactivity in the MCPs and surrounding structure. The internal background from the PSPC has turned out to be negligible. To correct for the background contamination, source-free areas in each image were selected and subtracted from the object area. The procedure will be described in more detail in the next section.

3.3 Imaging

X-ray images were created with the IDL code ROSAT_IMAGE (Dickow 1995), which allows to specify pixel binning and resolution. The binning factor determines how many detector pixels are binned to one pixel in the resulting image. At first, a photon list of all events in the defined time and energy range is created. This list contains information about position, arrival time, and energy channel (PSPC) of each detected event. Additionally, two files are

created containing general information about the observation, e.g. total exposure time, object name, sky coordinates, detector information.

From this photon list, a 512×512 pixel image is created. Depending on binning and resolution the image is convolved with a Gaussian filter. Next step is the correction for vignetting and shadowing effects in the image. PSPC images are corrected by dividing through the corresponding exposure map. HRI images are divided by a normalized standard calibration exposure map which has been multiplied by the exposure time. The pixel values of the corrected image are in units of counts per seconds. From the image binning information, the final image is then normalized to pixel value units of cts s^{-1} $pixel^{-1}$. In this context the quantity pixel is independent of the image binning and has a size of 15×15 $arcsec^2$.

3.4 Spectroscopy

The analysis of the energy distribution from PSPC observations is subdivided into two parts: the creation of a background-corrected spectrum with selected energy binning and its interpretation by fitting emission models to the observation. The first part is carried out with the IDL code ROSAT_SPEC (Dickow 1995), while for the model fits the interactive software package XSPEC has been used.

For retrieving the spectral distribution an image was created, as described in Sect. 3.3. From this image the source area and a number of background fields, containing no additional sources, were selected. Typically, three background fields near the source were chosen and concatenated. This was done either interactively or by using the information of area position and size from an input file. For the source field a polygon for extended asymmetric sources or a circular region could be chosen. The background fields were either an area of circular shape beside the source or a ring around the source field (only for the case of a circular source area). From these background areas mean count rates, sigmas, and background-to-source area ratios were determined. The background contamination level was subtracted from the source field, and the remaining source counts were divided in energy bins. The size of the energy bins was chosen either to be the same for each bin or variable yielding the same signal-to-noise ratio. This means the binning boundaries had to be chosen in a way that the number of source counts had to exceed the number of background photons by that ratio. The spectrum was then converted to a format for further processing with XSPEC.

The basic concept performed with XSPEC is as follows: The obtained spectral distribution does not directly correspond to the intrinsic distribution from the astrophysical source. Beside of absorption of X-ray photons on their way from the source to the detector, the spectrum also contains sensitivity characteristics from the observing detector. These characteristics have partly been mentioned above, i.e., the energy and off-axis angle dependent effective area (Sect. 3.2). Additionally, incoming X-ray photons at a defined energy have a considerable probability to be detected in neighbouring energy channels. This is specified by the energy resolution of the detector. Since the inversion of this process is equivocal, one has not the possibility to infer directly the undisturbed energy distribution from the observation. Therefore, the fit of any theoretical emission model to the observation is done iteratively. The model is folded by the detector response matrix, containing the response probability of each energy channel for a photon with a defined energy. Afterwards the folded model is fitted to the observed data.

Chapter 4

ROSAT X-ray observations of the interacting pair of galaxies NGC 4410: evidence for a central starburst

Published in
Astronomy and Astrophysics
Vol. 343, p. 373 (1999)

Astron. Astrophys. 343, 373–384 (1999)

ASTRONOMY AND ASTROPHYSICS

ROSAT X-ray observations of the interacting pair of galaxies NGC 4410: evidence for a central starburst

D. Tschöke[1], **G. Hensler**[1], **and N. Junkes**[2]

[1] Institut für Theoretische Physik und Astrophysik, Universität Kiel, D-24098 Kiel, Germany (tschoeke@astrophysik.uni-kiel.de)
[2] Max-Planck-Institut für Radioastronomie, Auf dem Hügel 69, D-53121 Bonn, Germany

Received 21 July 1998 / Accepted 6 November 1998

Abstract. We present X-ray observations of the interacting pair of galaxies NGC 4410a/b with the ROSAT HRI and PSPC. The ROSAT HRI images reveal a point-like source corresponding to NGC 4410a and an X-ray halo, extending 10″ from the nucleus toward the southeast. The halo emission accounts for ∼1/3 ($L_{\rm X}$ = 1.3×10^{41} erg s^{-1} in the 0.1–2.4 keV ROSAT band) of the total X-ray emission detected from NGC 4410a. The spectrum of the total X-ray emission from NGC 4410a can be fitted at best with a two-component emission model, combining a Raymond-Smith spectrum with T = 10^7 K and a power-law spectrum (Γ = 2.2). The fraction of the thermal component to the total flux within this model is 35%, supporting the results of the HRI observation. The total unresolved X-ray luminosity detected with the PSPC amounts to 4×10^{41} erg s^{-1} in the ROSAT PSPC band (for D = 97 Mpc).

A preferable explanation might be the interaction between the two galaxies causing a circumnuclear starburst around the active nucleus in the peculiar late type Sab galaxy NGC 4410a. As a cumulative effect of exploding stars a superbubble forms a bipolar outflow from the galactic disk with an expansion time of ∼8 Myr. The central source injects mechanical energy at a constant rate of a few times 10^{42} erg s^{-1} into the superbubble.

A HST WFPC2 image decovers that NGC 4410a is seen almost face-on so that only the approaching outflow is visible. The HRI contours reveal an elongation of this outflow indicative for a faint X-ray ridge below the detection limit ($L_{\rm X} \leq 1.4\times10^{39}$ erg s^{-1}) toward the neighbouring galaxy NGC 4410b caused by its tidal interaction. NGC 4410b houses only a faint X-ray source ($L_{\rm X} \leq 3.8\times10^{39}$ erg s^{-1}).

Key words: X-rays: galaxies – galaxies: starbust – galaxies: interactions – galaxies: individual: NGC 4410 – galaxies: active

1. Introduction

The pair of interacting galaxies NGC 4410a/b belongs to a group of 11 members (Hummel et al. 1986, hereafter HKG86) which are located behind the Virgo cluster. It consists of a peculiar Sab (NGC 4410a) (Thuan & Sauvage 1992) and an E galaxy (NGC 4410b) (HKG86) located in east-west direction and separated by 18.″7 (8.8 kpc at a distance of 97 Mpc) (Mazzarella & Boroson 1993, hereafter MB93). NGC 4410a is located at RA = $12^{\rm h}\,26^{\rm m}\,27\overset{\rm s}{.}9$, Dec = +09° 01′ 18″ (J2000). Spectral analysis of the nuclei of both components led to the classification as two LINERs (Mazzarella et al. 1991; Bicay et al. 1995; Thuan & Sauvage 1992). In the eastern component NGC 4410b a supernova type I has been detected in 1965 (SN 1965 A) from which Turatto et al. (1989) derived a distance of 139 Mpc. The system has a radial velocity of about 7300 km s^{-1} (Mazzarella et al. 1991; Batuski et al. 1992; Thuan & Sauvage 1992; MB93). With a Hubble constant of 75 km s^{-1} Mpc^{-1} this leads to a distance of 97 Mpc. In this paper we apply the latter value to all distance-dependent parameters, like e.g. luminosities etc. A distance of 97 Mpc for NGC 4410 results in an absolute length scale of 470 pc arcsec^{-1}.

HKG86 found a spatial coincidence of the western optical component NGC 4410a with a radio point source of luminosity $L_{\rm R}$ ≈10^{39} erg s^{-1} embedded in a strong, extended radio source around NGC 4410a with a total radio luminosity $L_{\rm R}$ ≈7×10^{40} erg s^{-1}.

The phenomenon of interaction between galaxies is closely related to the occurrence of starbursts (SBs): A large fraction of interacting galaxies (∼70%) exhibits typical characteristica of SBs (Bushouse 1986) and vice versa. It is also striking that the majority of infrared-bright galaxies shows evidence for recent interactions as indicated by the presence of close neighbours, or by their disturbed morphology and tidal tails (Joseph et al. 1984; Lonsdale et al. 1984; Telesco 1988). The fraction of mergers increases drastically in the infrared luminosity range L_{IR} from $10^{10}L_{\odot}$(12%) to $10^{12}L_{\odot}$(95%) (Sanders & Mirabel 1996). Although a large IR luminosity is not necessarily a tracer for enhanced star formation, it is one of the typical features for SB galaxies.

Norman & Scoville (1988) demonstrated that gas inflow from the galactic disk toward the central region, as required for building a central SB, will be triggered by a non-axialsymmetric gravitational potential like in interacting galaxies. They argued that perturbed orbits of gas clouds caused by an encounter lead to enhanced cloud collisions within the galactic central region and trigger the formation of massive stars. An alternative model for triggering a central SB was given by Jog & Das (1992) and

Send offprint requests to: D. Tschöke

Jog & Solomon (1992). The infall of giant molecular clouds (GMCs) into an intercloud medium with a higher mean pressure in the central region drives a radiative shock into the GMCs and ignites the SB.

The inflow of gas from the galactic disk is not only required for a central SB but also for fuelling an AGN. It is still under debate whether SBs are progenitors of AGN (Norman & Scoville 1988) or whether both are different physical processes. Weedman (1983) proposed that if a large number of massive stars form fast in a small central volume, the compact stellar remnants from these could act as accretors. Also the stellar dynamical merging of a dense cluster of massive stellar remnants would plausibly form a black hole nucleus (Rees 1984).

The nuclei of several nearby galaxies, like NGC 1068, NGC 1097, and NGC 7469, can be resolved into a central AGN and a circumnuclear SB ring (Keel 1985; Pérez-Olea & Colina 1996, hereafter PC96). Some host galaxies of quasars also exhibit evidence for SBs, such as 3C 48 (Stockton 1990).

Assuming an evolution from starbursts to AGNs during the interaction of galaxies one would expect more AGNs with the age of the merger process. Recent observations of ultraluminous IR galaxies with the infrared satellite ISO however do not show any obvious tendency of an increasing fraction of AGNs within interacting galaxies with advanced merging process (Lutz et al. 1998; Genzel et al. 1998). Half of the observed galaxies reveal both an AGN and starburst activity. It seems more likely that more local and shorter term conditions like time-dependent compression of the circumnuclear interstellar gas, the accretion rate onto the central black hole, and the associate radiation efficiency determine AGN or starburst dominated luminosities.

In this paper we present the spectral and imaging X-ray properties of NGC 4410 observed by the ROSAT Position Sensitive Proportional Counter (PSPC) and High Resolution Imager (HRI), respectively. We are able to resolve the two optical components in the ROSAT HRI image. The paper is structured as follows: In the next section we are considering the X-ray observations in general, detecting and trying to identify the emergent X-ray sources in the field and discussing the data reduction. In Sect. 3 we concentrate on NGC 4410 presenting the HRI results at first before we study the spectral flux distribution of the PSPC data with particular concern of comparison with a sequence of X-ray radiation models. The results are then discussed in Sect. 4 making use of a HST WFPC2 image of NGC 4410a for a geometrical consideration of its inclination.

2. Observations and data reduction

The data presented in this paper were taken with the HRI and the PSPC detectors on board of the X-ray satellite ROSAT. This X-ray telescope is operating in the energy range of 0.1 to 2.4 keV. The spatial resolutions of the HRI is $1\farcs7$. The point spread function (PSF) of this detector at the optical axis in combination with the telescope is $3''$. The PSPC has a PSF of $25''$. The two detectors have a field of view of $38'$ and 2°, respectively. For details concerning ROSAT and its instruments see the ROSAT User's Handbook (Briel et al. 1996).

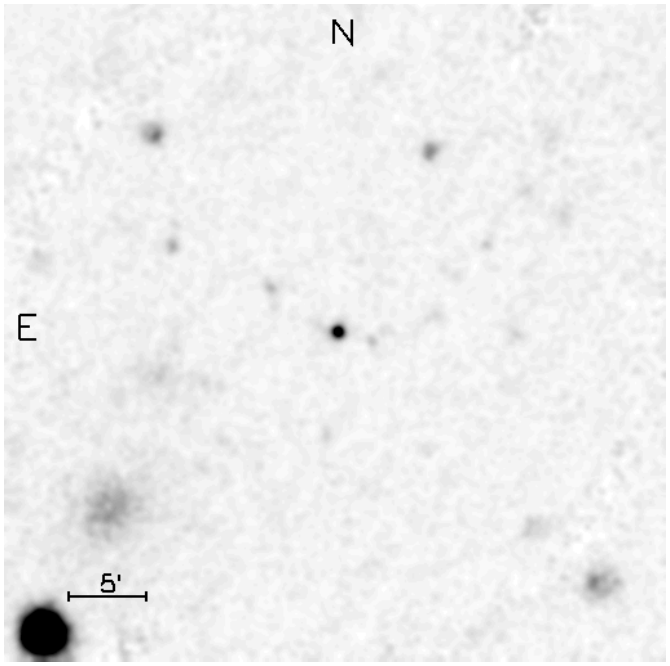

Fig. 1. Central $42'$ of the PSPC field of view centered around NGC 4410 (bright central source) with an exposure time of 23.4 ksec. The image is smoothed with a Gaussian filter ($20''$ FWHM). The scale of the image is slightly different from the one in Fig. 2. North is up, east is to the left.

NGC 4410 was observed on June 28–30, 1993 with the ROSAT PSPC detector for a total effective exposure time of 23.4 ksec. The total number of background-subtracted counts from the central source associated with NGC 4410 is 870 ± 31. Fig. 1 shows the central $42'$ of the PSPC field of view. For the spectral analysis of the source we used the software package IDL. The source photons were extracted from a circular area of $92''$ around the central source and corrected for telescope vignetting and detector dead-time. The spectrum of the source was binned according to a signal-to-noise ratio of 8. For the background correction we selected three uncontaminated circular areas close to NGC 4410 with radii of $86''$, $101''$ and $141''$. The background contributes an X-ray flux of $(1.36\pm0.27)\times10^{-2}$ cts arcsec^{-2} in the ROSAT bandpass. In order to fit a model spectrum to the PSPC data we used the X-ray spectral-fitting software package XSPEC (Arnaud 1996).

Our ROSAT HRI observations have been taken between June 27 and July 1, 1995 with a total effective exposure time of 36.7 ksec which led to 152 ± 24 counts for the central source associated with NGC 4410. The background X-ray flux amounts to $(1.6\pm1.1)\times10^{-2}$ cts arcsec^{-2}.

2.1. Source detection

Ten X-ray sources above a limit of 5σ are found within the field of view of the HRI detector using a standard source-detection algorithm in the EXSAS X-ray analysis software package (Zimmermann et al. 1997) (Fig. 2). In Table 1 the detected sources

Table 1. ROSAT HRI detections in the NGC 4410 frame with a maximum likelihood threshold of 5σ.

No.	RA (2000)	Dec (2000)	countrate (HRI)† [10^{-3} cts s^{-1}]	angular distance from NGC 4410a‡ [arcmin]	identification
1	$12^h\ 27^m\ 16\overset{s}{.}5$	$+9°\,14'\,11\overset{''}{.}8$	3.90±0.50	17.70	QSO 1224+095
2	$12^h\ 26^m\ 03\overset{s}{.}8$	$+9°\,12'\,59\overset{''}{.}4$	2.38±0.33	13.27	
3	$12^h\ 25^m\ 49\overset{s}{.}4$	$+9°\,06'\,56\overset{''}{.}8$	1.17±0.25	11.30	
4	$12^h\ 27^m\ 11\overset{s}{.}5$	$+9°\,06'\,53\overset{''}{.}3$	1.97±0.31	12.20	unidentified optical point source
5	$12^h\ 26^m\ 45\overset{s}{.}7$	$+9°\,04'\,05\overset{''}{.}9$	0.57±0.15	5.21	
6	$12^h\ 26^m\ 02\overset{s}{.}4$	$+9°\,02'\,16\overset{''}{.}4$	0.90±0.18	6.58	
7	$12^h\ 26^m\ 16\overset{s}{.}0$	$+9°\,01'\,18\overset{''}{.}4$	0.54±0.14	3.09	
8	$12^h\ 26^m\ 28\overset{s}{.}2$	$+9°\,01'\,13\overset{''}{.}0$	4.13±0.36	0.00	NGC 4410a
9	$12^h\ 26^m\ 19\overset{s}{.}1$	$+9°\,00'\,36\overset{''}{.}9$	1.32±0.20	2.39	
10	$12^h\ 27^m\ 26\overset{s}{.}0$	$+8°\,50'\,06\overset{''}{.}7$	5.30±0.78	18.20	Abell 1541

† background subtracted ‡ NGC 4410a coordinates see no. 8

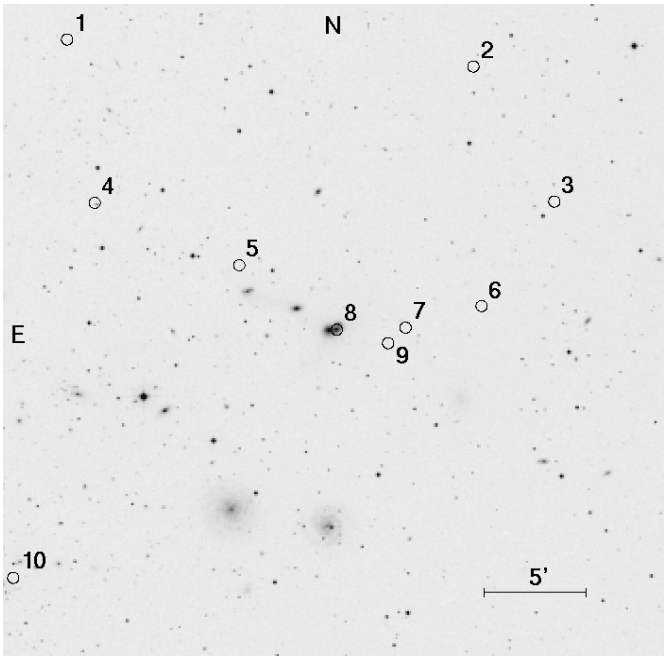

Fig. 2. ROSAT HRI X-ray sources around NGC 4410 (source no. 8) detected by the maximum likelihood method and with a threshold of 5σ ($\sigma = 3.0\times10^{-7}$ cts s^{-1} arcsec^{-2}), plotted over an optical image taken from the Digitized Palomar Observatory Sky Survey. The size of the field corresponds to the HRI field of view. (Note the different scale compared to Fig. 1.) North is up, east is to the left.

are listed with position, background subtracted count rates and optical identifications.

From these detected X-ray sources in the HRI image, four coincidences with optical objects can be found (see Table 1 and Fig. 2). The X-ray source no. 8 can be clearly identified with NGC 4410a, while an extended X-ray source (no. 10, 44″ FWHM) belongs to the galaxy cluster Abell 1541. In addition, the source no. 1 coincides with the QSO 1224+095 and no. 4 is still unidentified in the optical. In order to investigate further identifications of X-ray sources with optical objects we decrease the detection limit to 3σ. This leads to 32 sources in the HRI image with 10 counterparts in the optical. Three of them are identified as the Abell galaxy cluster 1541 (extended), the QSO 1224+095 (1″ offset) and the K7-star G60-2 (8″ offset). The offsets between optical and X-ray sources do not indicate any systematical shift or rotation, requiring a position correction of the superposition of the two images at this point.

3. Results

3.1. X-ray imaging

Using the coordinates of the ROSAT HRI pointing the overlay of X-ray and optical image reveals a shift between the optical (NGC 4410a) and X-ray maximum of 4″. Strikingly, an additional X-ray source, that is visible at the 3σ contour level at a distance of ∼18″ from the central X-ray maximum to the east, has the same displacement from the maximum of the eastern optical component NGC 4410b. It contains about 1% of the count rate of the central source in the HRI image. From the detection limit of $3\sigma = 9.0\times10^{-7}$ cts s^{-1} arcsec^{-2} in the HRI image and the energy conversion factor (ECF) of 6.7×10^9 cts cm^2 erg^{-1} for the HRI and a power-law spectrum with $\Gamma = 2.4$ from the ROSAT User's Handbook (Briel et al. 1996) we get an upper limit of 3.8×10^{39} erg s^{-1} for the X-ray luminosity of NGC 4410b.

Furthermore, radio observations of NGC 4410 present a similar emission feature as the X-ray contours. The maximum radio contours correspond spatially to the optical maximum of NGC 4410a and the lower emission levels are elongated toward the southeast (HKG86). To check whether the eastern X-ray maximum has to coincide with the optical structure of NGC 4410, we compare its X-ray luminosity with the blue luminosity L_B of NGC 4410b. With m_B= 15.28 (MB93) we derive a blue luminosity $L_B = 1.2\times10^{10}\ L_\odot$ for NGC 4410b. Brown & Bregman (1998) analysed a sample of 34 early-type galaxies observed with ROSAT PSPC and HRI and studied the X-ray-to-optical distribution. The estimated X-ray luminosity of $\sim 10^{39}$ erg s^{-1} for NGC 4410b fits well into the observed distribution of the sample. This obtrudes to superpose the X-ray maxima of both components NGC 4410a and b to the optical image of the pair. This fine tuning requirement is not detectable

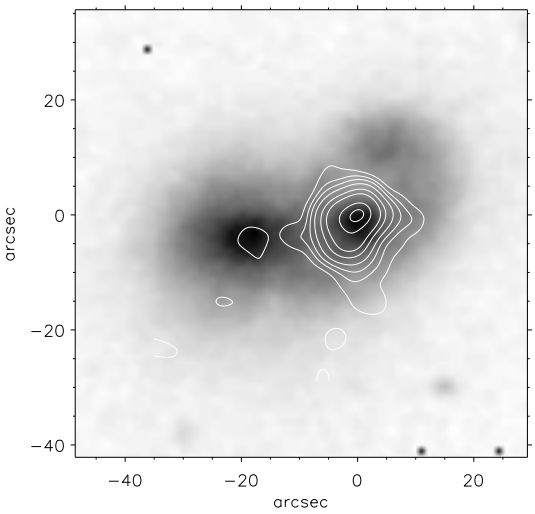

Fig. 3. Overlay of the HRI X-ray contours onto the optical image of NGC 4410 taken from the Digitized Palomar sky survey. The X-ray image was smoothed with a Gaussian filter FWHM of 3″. The contour levels are at 3, 5, 7, 10, 15, 20, 30 and 35σ above the mean background with $\sigma = 3.0\times10^{-7}$ cts s^{-1} arcsec^{-2}. The relative position of optical image and X-ray contours was corrected as explained in Sect. 3.1. North is up, east is to the left.

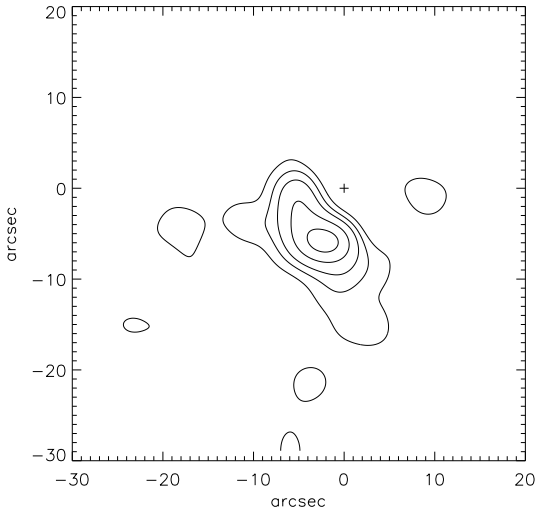

Fig. 4. Residual X-ray flux after subtracting a point-like source with Gaussian distribution (FWHM 3.5″) at the position of the maximum of the X-ray flux from the original total flux image (see Fig. 5). The cross marks the position of the maximum and coincides with the nucleus of NGC 4410a. The contours are 3, 5, 7, 10 and 13σ above the mean background with $\sigma = 3.0\times10^{-7}$ cts s^{-1} arcsec^{-2}. North is up, east is to the left.

and therefore not necessary on the scale of the full HRI image (Fig. 2) as pointed out in Sect. 2.1.

Fig. 3 shows the position corrected contour plot of the central 2′ of the HRI image with the X-ray source overlaid onto an optical image of NGC 4410 of the Digitized Palomar sky survey plates. The HRI image was smoothed with a Gaussian filter FWHM of 3″.

The contours of the HRI image indicate a radial extension from the maximum of NGC 4410a toward the southeast by 3″ to 10″. Since this elongation is close to the resolution limit it has to be checked whether it is real or artificial. Morse (1994) found out that in some ROSAT HRI observations the contours of point-like X-ray sources are elongated over a scale of ∼5″ to 10″ because of errors in the attitude correction as the satellite was wobbled during the observation. On the other hand, it is striking that the extended radio emission of NGC 4410a (HKG86) agrees in its direction with the X-ray contours. Moreover, the elongation of the X-ray contours is not symmetrical with respect to the elongation axis, as one would expect if it is caused by the wobbling satellite, similar to the point-like sources in the paper by Morse (1994). Another possible error namely that the elongation is caused by an incorrect superposition of the different used observation intervals (OBIs) was also checked by us but didn't explain the effect.

We fit a Gaussian distribution with FWHM 3.″5 (spatial resolution of HRI = 1.″7, image smoothed with Gaussian filter FWHM 3″ corresponding to the HRI PSF) to the point-like source and subtract it from the original image. The result is plotted in the Figs. 4 and 5. The residual reveals a ∼10″×5″ emission feature 7″ to the southeast of the X-ray maximum visible up to 13σ above the background. As expected, the wings of the Gaussian distribution in the Figs. 5b–f fit very well to the X-ray source except in the direction of deformation of the X-ray contours.

As a working hypothesis which will be supported by the finding of a thermal emission (see Sect. 3.2) we assume that the extended X-ray contours represent a superbubble originating from type II SNe in the starburst region, and expanding into the halo. Since its elongation is too small to resemble the edge-on view of an outflow we further assume that the residual emission in Fig. 5 represents the front part of a bipolar outflow from the central region of the galactic disk. To verify this assumption, we estimate the ratio of the integrated flux from the residual image with the total flux of the original image. For that we integrate the flux within a radius of 13″ from the maximum in both the residual image and the original one. We derive a ratio of 0.34±0.05 (52±8 counts). The error is estimated by varying the integration radius around the source by 2″ and from the mean fluctuation of the background flux. This result is supported by the spectral analysis of PSPC data where a flux of $L_{\rm X}$ = 1.3×10^{41} erg s^{-1} for the thermal emission component is derived as part of the combined thermal and power-law spectrum (see Sect. 3.2). However, since the fraction of the superbubble within the point-like source is neglected, this estimate is only a lower limit.

An X-ray ridge toward the optical position of NGC4410b is discernible at the 3σ level, which corresponds to an upper count level of 3.0×10^{-7} cts s^{-1} arcsec^{-2}. Using the HRI ECF of 1.8×10^{12} cts cm^2 erg^{-1} for a 1 keV Raymond-Smith plasma with log $N_{\rm H}$ = 20.0 from the ROSAT User's Handbook (Briel et al. 1996) one gets an upper limit for the X-ray luminosity of 1.4×10^{39} erg s^{-1}. Two regions of enhanced X-ray emission

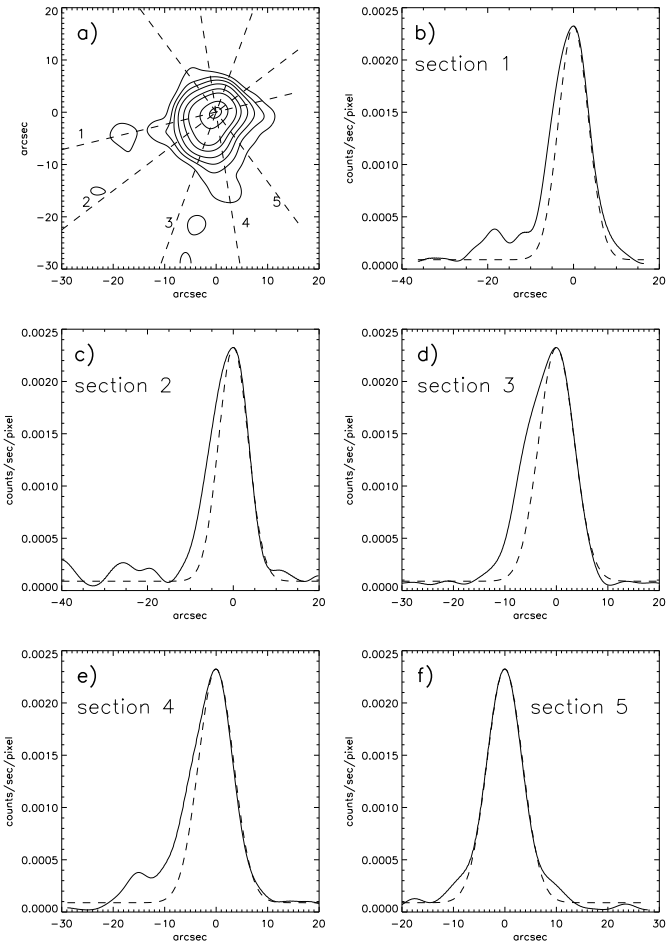

Fig. 5. a Positions of the five sections (dashed lines) through the HRI image of NGC 4410. The contours are the same as in Fig. 3. North is up, east to the left. The following five plots show the corresponding sections through the X-ray maximum of the HRI image. The dashed lines in all five section plots represent the fitted Gaussian distribution with a FWHM 3.″5 to the point-like source of NGC 4410a. **b** Sect. 1, east-to-west. The local maximum 18″ east of the X-ray peak spatially corresponds to NGC 4410b. **c** Sect. 2, southeast-to-northwest. **d** Sect. 3, southeast-to-northwest. **e** Sect. 4, southwest-to-northeast. **f** Sect. 5, southwest-to-northeast. In each plot the Gaussian distributed compact source (dashed lines) fits well to the HRI contours except in the direction of deformation of the X-ray contours.

are visible 15″ and 22″ south of the maximum X-ray source that were not contained in our source list with a 3σ confidence level. Depending on the spectral model and therefore on the ECF the upper limit for the X-ray flux of these sources is 2.25×10^{-16}/ECF erg s^{-1} cm^{-2}.

3.2. Spectral analysis

In addition to the spatial information of emission components we got from the HRI data, we now want to decompose these components by using the spectral information obtained from the PSPC data. With the PSF of 25″ of the PSPC we get no satisfactory spatial resolution.

The 870 background corrected counts of the central source detected with the PSPC in the energy range of 0.1–2.4 keV were binned in order to achieve a constant signal-to-noise ratio of 8. To fit the observed PSPC X-ray spectrum we apply different models of absorbed emission spectra including a thermal Bremsstrahlung spectrum (BS), the spectrum of an optically thin thermal plasma in collisional equilibrium (RS) as calculated by Raymond & Smith (1977) and a power-law spectrum (PO) with a photon energy distribution $\propto E^{-\Gamma}$, as well as several combinations of those. The absorption of the spectra depends on the hydrogen column density $N_{\rm H}$ between the source and the observer. As a first-order estimate and as a lower limit of $N_{\rm H}$ we use the Galactic foreground value in the direction of NGC 4410. This value for $N_{\rm H}$ amounts to 1.73×10^{20} cm^{-2} (Dickey & Lockman 1990).

The model fits for the X-ray emission to the observation are shown in Table 2. Usually the RS model is applied under the assumption of solar abundances (Anders & Grevesse 1989). Reasonably, this is not an ideal approach because expanding SN ejecta should contain the nucleosynthesis products of their massive stellar progenitors. For this reason we use two different sets of chemical abundances. Beside the classical model with solar abundances we fit one with enhanced abundances of SNe according to the yields by Woosley & Weaver (1985), but integrated over all massive stars between 10 and 100 $M_\odot$ and with a Salpeter initial mass function (IMF).

The main uncertainty to fit the data comes in by the value of the hydrogen column density $N_{\rm H}$. In each model, except the combinations of RS+PO and the single component models BS and PO, the free parameter $N_{\rm H}$ turns out to become much too low for the best fit. For the single thermal model RS it is not possible to fit both, the soft and the hard part of the spectrum reasonably without an unrealistically low value of $N_{\rm H}$.

This is also true for the combined two temperature plasma model RS+RS(ww). The best fit results in an unrealistically low $N_{\rm H}$ value of 0.35×10^{20} cm^{-2}. For the same model with solar abundances RS+RS(sol), the best fit yields $N_{\rm H}$ = 0.45×10^{20} cm^{-2}. In addition, the plasma temperature of more than 3×10^7 K for the second component is abnormally high for halo gas. This temperature may only be reached for gas in the central regions of starburst galaxies, for example NGC 253 (Ptak et al. 1997) and M82 (Mathews & Doane 1994). In the case of fixing the column density to the Galactic value, the resulting plasma temperatures of 1.7×10^6 K and 8.8×10^6 K for RS+RS(sol) and 0.9×10^6 K and 9.3×10^6 K for RS+RS(ww) are much more reasonable. But both fits to the observed spectra are much worse (see Table 2).

In the case of fitting the observation with a single PO the column density of 3.4×10^{20} cm^{-2} becomes plausible because of an expected additional absorption within NGC 4410. The photon index of 2.39 ± 0.09 is in agreement with the results from Turner et al. (1993) and Mulchaey et al. (1993), who found a mean value for Seyfert 1 and Seyfert 2 galaxies of Γ = 2.4. Comparing all these single-component models the model PO and BS provide the best fits to the observation. The fits are plotted in Fig. 6.

Table 2. Spectral fits to the PSPC data of NGC 4410 and the derived model parameters. For the determination of the X-ray luminosity a distance of 97 Mpc is assumed.

model	$N_{\rm H}$	T	Γ	norm	red. χ^2	d.o.f.	$F_{\rm X}$	$L_{\rm X}$
(1)	(2)	(3)	(4)	(5)	(6)	(7)	(8)	(9)
BS	$2.06^{+0.30}_{-0.27}$	$11.0^{+1.6}_{-1.4}$	–	8.0	1.6	10	3.62	4.08
RS (sol)	$1.4^{+1.2}_{-1.0}$	$12.7^{+0.5}_{-0.6}$	–	162	4.7	10	2.96	3.33
RS (sol)	1.73 †	$13.0^{+0.5}_{-0.3}$	–	180	10.7	11	2.66	2.99
RS (ww)	$(0.06^{+2000}_{-0.06})\times10^{-5}$	$11.7^{+0.6}_{-0.8}$	–	17	7.0	10	3.28	3.69
RS (ww)	1.73 †	11.4±0.3	–	17	12.7	11	2.81	3.16
RS+RS (sol)	$0.45^{+0.24}_{-0.21}$	$4.4^{+1.6}_{-0.8}$	–	35	1.0	8	3.33	3.75
		32^{+68}_{-13}	–	224				
RS+RS (sol)	1.73 †	$1.7^{+0.2}_{-1.0}$	–	100	6.6	9	2.73	3.07
		$8.8^{+3.4}_{-0.5}$	–	65				
RS+RS (ww)	$0.35^{+0.58}_{-0.24}$	$2.3^{+0.1}_{-0.2}$	–	2.4	0.9	8	3.65	4.10
		$12.0^{+0.8}_{-1.0}$	–	15				
RS+RS (ww)	1.73 †	$0.9^{+0.8}_{-0.9}$	–	2.6	3.1	9	2.78	3.13
		$9.3^{+2.0}_{-0.1}$	–	11				
RS+PO (sol)	$1.16^{+0.51}_{-0.33}$	$7.2^{+2.3}_{-2.6}$	1.85±0.14	76	0.8	8	3.46 (0.88)	3.90 (0.99)
RS+PO (sol)	1.73 †	$7.7^{+1.6}_{-2.2}$	$2.08^{+0.10}_{-0.11}$	25 (RS); 8.0 (PO)	0.7	9	3.44 (0.78)	3.87 (0.87)
RS+PO (ww)	$1.41^{+0.52}_{-0.25}$	$9.1^{+1.4}_{-2.6}$	$2.03^{+0.21}_{-0.19}$	64 (RS); 4.8 (PO)	0.7	8	3.41 (1.15)	3.84 (1.30)
RS+PO (ww)	1.73 †	$9.3^{+0.9}_{-1.0}$	2.17±0.10	5.4 (RS); 6.5 (PO)	0.6	9	3.47 (1.20)	3.91 (1.35)
RS+PO (ww) #	1.73 †	$1.0^{+0.3}_{-1.0}$		2.6 (RS)	1.3	8	3.20 (0.38)	3.60 (0.43)
	$30.6^{+5.8}_{-4.4}$		$4.24^{+0.27}_{-0.28}$	275 (PO)				
PO	$3.42^{+0.30}_{-0.35}$	–	2.39±0.9	12	2.3	10	3.83	4.31

† fixed to Galactic foreground value

separate absorption for each component

Col.(1) Emission models abbreviated as: BS = thermal Bremsstrahlung, RS = Raymond-Smith, PO = power-law. The specification in brackets indicates the used element abundances for the hot thermal plasma, solar (sol) or abundances of a supernova calculated by Woosley and Weaver (ww) and integrated over all stars between 10 and 100 $M_\odot$ for a Salpeter IMF.

Col. (2) column density in units of 10^{20} cm^{-2}.

Col. (3) plasma temperature in units of 10^6 K.

Col. (4) photon index.

Col. (5) scaling factor: for BS in units of $(10^{-19}/(4\pi D^2))\int n_{\rm e} n_{\rm I} {\rm d}V$, $n_{\rm e}, n_{\rm H}$ = electron and ion densities (cm^{-3}); for RS in units of $(10^{-20}/(4\pi D^2))\int n_{\rm e} n_{\rm H} {\rm d}V$, $n_{\rm e}, n_{\rm H}$ = electron and H densities (cm^{-3}); for PO in units of 10^{-5} photons keV^{-1} cm^{-2} s^{-1} at 1 keV.

Col. (6) reduced χ^2.

Col. (7) degrees of freedom.

Col. (8) X-ray flux in units of 10^{-13} erg cm^{-2} s^{-1}, corrected for the fitted absorption. Values in brackets give the contribution of the thermal component.

Col. (9) X-ray luminosity in units of 10^{41} erg s^{-1}. Values in brackets give the contribution of the thermal component.

The best fit by far for the whole observed spectrum can be reached by applying a two-component model which combines a thermal and a power-law spectrum (RS+PO) with a photon index of 2.17±0.10 and a plasma temperature of (9.3±1.0)×10^6 K (see Fig. 9). Nevertheless, the fit becomes worse for applying a higher value for $N_{\rm H}$ than the Galactic one. The combined PO+RS fit yields the best result with an absorption corrected luminosity of (3.91±0.55)×10^{41} erg s^{-1} for the assumed distance of 97 Mpc.

Under the assumption, that the nonthermal emission originates from a central active nucleus heavily obscured by dust and gas, and that hot plasma has expanded into the outer parts of NGC 4410a, we fit the RS+PO model with different column density values for each component. One would expect a column density $N_{\rm H,RS} \approx N_{\rm H,Gal}$ for the less obscured plasma outflow and a much higher $N_{\rm H,PO}$ for the AGN because of the intrinsic absorption within the NGC 4410 nucleus. While we apply $N_{\rm H,RS} = N_{\rm H,Gal} = 1.73\times10^{20}$ cm^{-2} for the RS component, $N_{\rm H,PO}$ for the PO component is set to 3.1×10^{21} cm^{-2}. This yields the best fit for a lower plasma temperature of 1.0×10^6 K and a very steep power-law for the central AGN with Γ = 4.24 (see Fig. 11). In the very soft range (0.1–0.3 keV) the spectrum is determined by the intrisically unobscured RS component. Raising the absorption for the PO component prohibits its con-

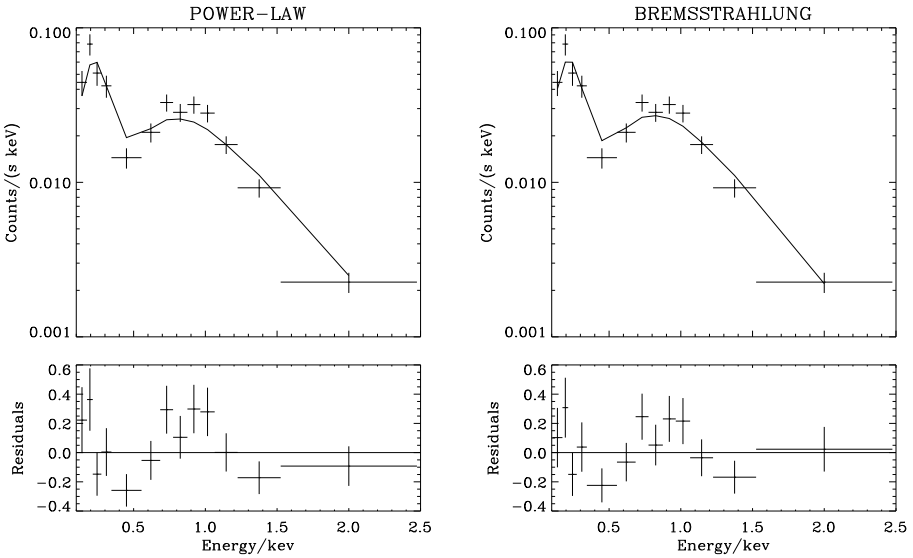

Fig. 6. Best single-component model fits to the observed (0.1–2.4) keV X-ray spectrum of NGC 4410, PO (*left*) and BS (*right*). The channel counts are binned to a signal-to-noise ratio of 8. The parameter values for these models are shown in Table 2. The lower graphs show the residuals of the fits.

tribution to the soft spectral range, which means that the total X-ray flux there has to originate from the hot ionized gas. As a consequence the temperature of the plasma is almost one order of magnitude lower than in the RS+PO model with only one common absorption. The hard spectrum >0.5 keV originates completely from the nonthermal component. Nevertheless the photon index is unplausibly steep.

4. Discussion

4.1. The X-ray halo

The HRI image strongly suggests a twofold spatial correlation between the X-ray and the radio emission: we have a compact central emission peak apparently coinciding with NGC 4410a and a diffuse halo slightly elongated about 10″ toward the south-east. Subtraction of the central point-like source from the total X-ray emission enables us to unveil a clear extension in this direction. Because of the asymmetrical elongation and the spatial correlation in the X-ray and radio flux we are convinced not to be mistaken by an artifact. Furthermore, the flux ratio of 0.34±0.05 from this feature compared to the total flux corresponds to the best fitting model for the observed spectrum, a two-component model, combining a thermal Raymond-Smith spectrum and a power-law spectrum. As a hypothesis we assume that the thermal emission originates from an expanding X-ray halo gas with a plasma temperature of a few 10^6 K whose expulsion is driven by a central engine (SB + AGN).

The SE elongation of the emission contours could be caused by two effects:

(1) If the pec Sab galaxy NGC 4410a is seen at moderate inclination, a circumnuclear superbubble or a bipolar outflow is visible in soft X-ray which expands vertically to both sides out of the galactic disk only the part in front of the HI disk. X-ray emission in the ROSAT band originating from gas outflowing into the reverse halo hemisphere is absorbed by cold gas in the

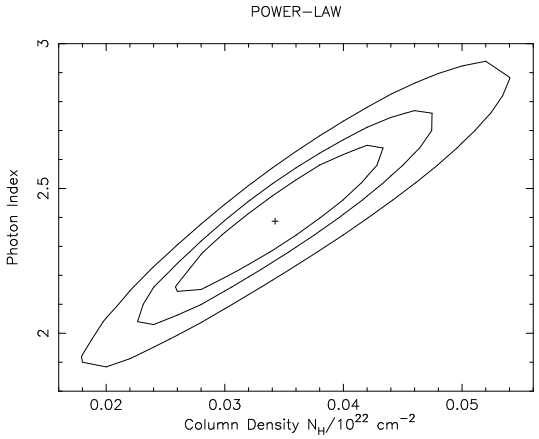

Fig. 7. χ^2 contours of the fit parameters column density $N_{\rm H}$ and photon index Γ of the PO model (Fig. 6). The levels represent 99%, 90% and 68% confidence.

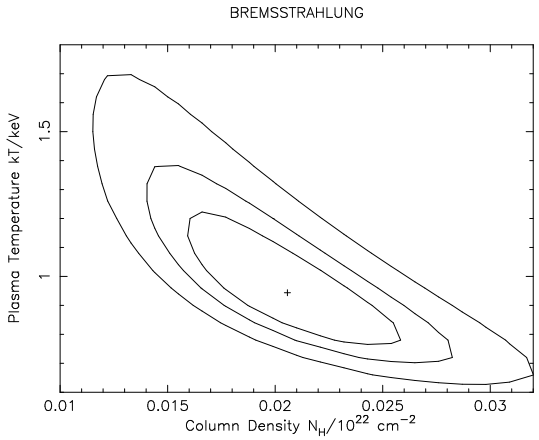

Fig. 8. χ^2 contours of the fit parameters column density $N_{\rm H}$ and plasma temperature kT of the BS model (Fig. 6). The levels represent 99%, 90% and 68% confidence.

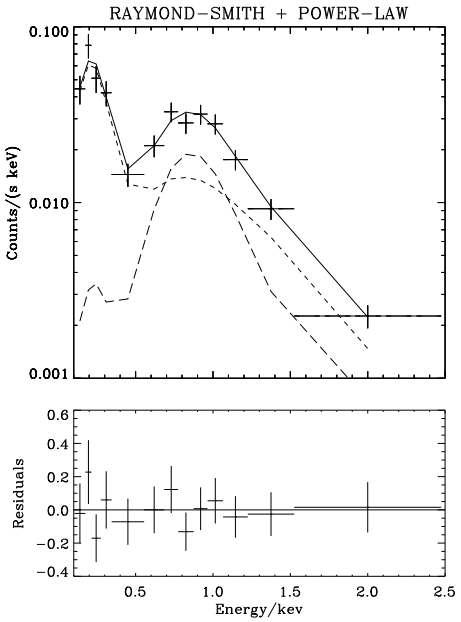

Fig. 9. Observed X-ray spectrum of NGC 4410 and best fit (solid line) with a combined RS and PO model(RS+PO(ww)). The parameter values for this model are shown in Table 2. The long-dashed line shows the spectrum of the thermal component. The short-dashed line shows the contribution of the power-law. The contribution of the RS component to the total flux is 35%. The residuals of this fit are plotted in the lower box.

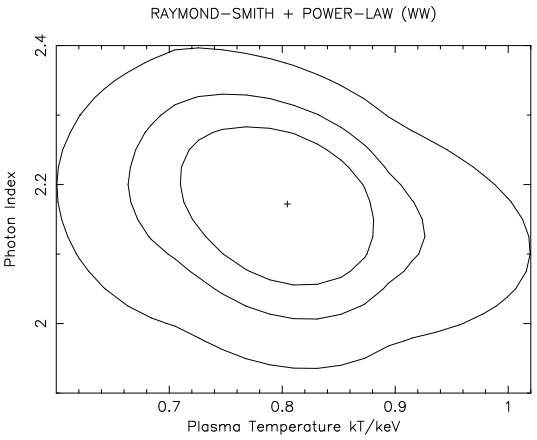

Fig. 10. χ^2 contours of the fit parameters plasma temperature kT and photon index Γ of the two-component RS+PO(ww) model (Fig. 9). The levels represent 99%, 90% and 68% confidence.

disk of NGC 4410. This fact also accounts for the low N_H that is required from the best model fit and is lacking of any additional contribution to the Galactic foreground value.

(2) The X-ray halo gas is exposed to the tidal force of the companion galaxy NGC 4410b.

In order to decide which of the two effects causes the deformation of the X-ray halo, information about the inclination angle of NGC 4410a is necessary. Fig. 12 shows the *Hubble Space Telescope* (HST) WFPC2 image of the central part of NGC 4410a in the V (5843 Å) broad band filter taken from the

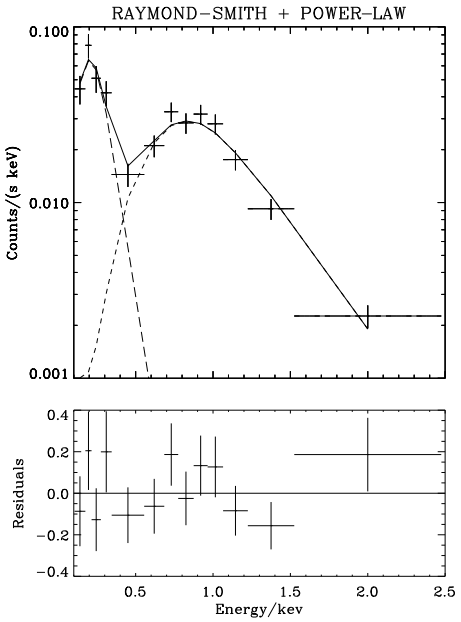

Fig. 11. Fit of the RS+PO(ww) model with individual column densities for each component and residuals of the fit. The different lines represent the same components as in Fig. 9. As expected the soft part of the spectrum is dominated by the unabsorbed thermal emission from the hot plasma. The hard spectrum >0.5 keV originates from the power-law component. Yet the spectrum can only be fitted with much too steep photon index of more than 4.

Hubble Space Telescope archive. One can discern the nucleus, a bright emission region at the lower left, and a line of additional smaller bright knots at the left. At the right-hand side of the nucleus a long tidal arm probably caused by the interaction is clearly visible. Since the morphology in this image leads to a very low inclination, we prefer the second explanation of an interaction-induced deformation of the X-ray halo. However, the HST image suggests an additional possibility, namely, that the bright emission region at the lower left is a starburst region, and that the extended part of the X-ray contours originates from this region.

The X-ray contours reveal a faint ridge toward NGC 4410b ($L_X \leq 1.4\times10^{39}$ erg s^{-1}) which has only a very faint corresponding X-ray counterpart centrally of NGC 4410b ($L_X \leq 3.8\times10^{39}$ erg s^{-1}) as indication of any activity in or around the nucleus of NGC 4410b. The non-detection of a similar radio emission admits at best a radioquiet AGN.

4.2. Physical conditions of the X-ray emission

As one can see in Table 2 the derived values for the X-ray luminosity are all of the same order of 3–4$\times10^{41}$ erg s^{-1} and independent of the applied model. From this point of view it is not possible to distinguish between the different models. The two most acceptable models with reasonable values for N_H are the two-component combination RS+PO and the single-component PO model, respectively.

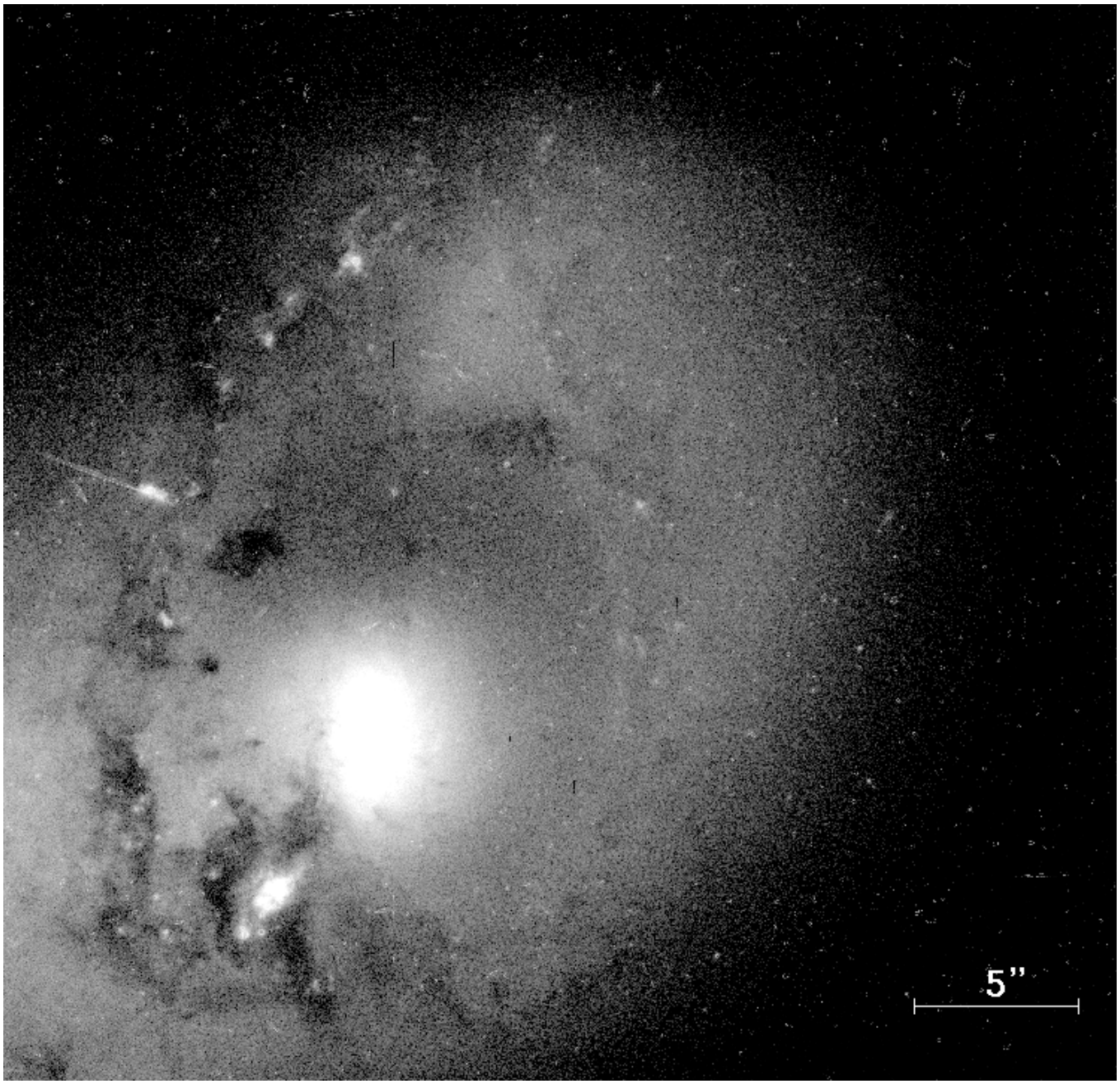

Fig. 12. Broad band image in the V (5843 Å) filter of the nucleus of NGC 4410a with a logarithmic grayscale taken from the Hubble Space Telescope archive. As a consequence of the interaction, a chain of knots and dust, a bright emission region near the nucleus and a long tidal arm are visible. The image has a size of $34'' \times 34''$. North is up, east is to the left.

Although the photon index of $\Gamma = 2.39 \pm 0.09$ of the single PO model is in good agreement with observed values for low luminousity AGNs (Turner et al. 1993; Mulchaey 1993), it is obvious that the observed X-ray spectrum of NGC 4410 cannot be fitted properly by a single PO model but requires an additional component as can be seen in Table 2 and by comparing Fig. 6 with Fig. 9. The RS+PO model for the X-ray source leads to a luminosity of the thermal component $L_{\rm X} = (1.35 \pm 0.19) \times 10^{41}$ erg s^{-1} (35% of the total X-ray luminosity). Nevertheless, the X-ray luminosity can vary by a factor of 4 because of the uncertainty of the distance to the source. To compare the derived properties of NGC 4410 with theoretical calculations, we apply the following model: We assume a central SB to drive an expanding superbubble. The central source injects mechanical energy since a time $t_{\rm exp}$ at a constant rate $L_{\rm mech}$ by sequential supernova explosions into the bubble. The supersonic expansion leads to a shock front and is heating the ambient gas. Assuming a homogeneous density of this ambient

gas would lead to a spherically expanding bubble, as calculated by MacLow & McCray (1988).

This model, however, does not correspond to the realistic conditions of a SB in a disk galaxy. Because of the vertically decreasing gas density the superbubble forms a "chimney" and blows out of the galactic disk into the halo by a bipolar outflow (Norman & Ikeuchi 1989). The dynamics, X-ray emission and disk-halo interaction of these outflows are modeled under different conditions of ambient disk gas density, halo gas density, energetic input into the superbubble, and expansion time of the superbubble in a number of papers (Tomisaka & Ikeuchi 1986; Tomisaka & Ikeuchi 1988; MacLow et al. 1989; Suchkov et al. 1994, hereafter S94; Michaelis et al. 1996). S94 found that the soft X-ray emission of the suberbubble in the range of (0.1–2.2) keV primarily originates from the shock-heated halo and disk gas with temperatures of 10^6 – 10^7 K, rather than from the supernova material itself. Depending on the density of the disk and halo gas, the scale-height of the disk, and the energy deposition rate from the SB, the morphology of the bipolar outflow varies in structural parameters: opening angle within the disk, radius of the chimney, vertical extension of the superbubble, and ratio of the two last properties. Independent of these different conditions, the models always achieve a bipolar morphology. S94 derived an analytic expression for the shell X-ray luminosity in the (0.1–2.2) keV band:

$$L_{\rm X} = 9.7 \times 10^{40}\ (L_{42})^{3/5} (n_{0.01})^{7/5} (t_7)^{9/5} {\rm erg\ s^{-1}}, \qquad (1)$$

where L_{42} is the mechanical input energy in units of 10^{42} erg s^{-1}, $n_{0.01}$ is the particle density of the halo gas in units of 0.01 cm^{-3}, and t_7 is the expansion time of the superbubble in units of 10^7 yr.

From the HRI observation we can estimate a maximum expansion of the outflowing gas into the halo of 10″, scaling to 4.7 kpc at a distance of 97 Mpc. The models of Tomisaka & Ikeuchi (1986), Tomisaka & Ikeuchi (1988), MacLow et al. (1989) and S94 reveal chimney radii within the galactic disk between 200 pc and 600 pc. The much more extended X-ray emission observed in NGC 4410a can therefore only originate from the outflow into the less dense galactic halo where it can expand in each direction. This involves that the SB has to be old enough in order to account for the escape of the expanding superbubble from the disk into the halo. That means a lower limit of $t_{\rm exp} > 4$ Myr for the expansion time (Tomisaka & Ikeuchi 1988).

We estimate the mechanical energy input by the starburst into the superbubble from the emitted Hα radiation using the shock model by Binette et al. (1985). They calculated the radiative cooling mechanism of shock-heated gas, emitting optical line radiation, and found that $L_{\rm H\alpha} \approx 10^{-2} L_{\rm mech}$. With $L_{\rm H\alpha}$ = 6.6×10^{40} erg s^{-1} for NGC 4410 (MB93) this leads to $L_{\rm mech} \approx$ 6×10^{42} erg s^{-1}. Applying 10^{51} erg for the energy release per SNII and taking into account that roughly only 20% is converted into mechanical luminosity we derive a SNII rate of $\sim$1.0 yr^{-1}.

Under the simplified consideration of a spherically expanding gas one can estimate its density. With the scaling factor of the RS model and setting the electron density equal to the hydrogen density we get the following expression for the electron density of the hot gas:

$$n_e^2 = \frac{3 D^2 N_{RS}}{f r^3} \times 10^{14} cm^{-5}, \qquad (2)$$

where N_{RS} is the scaling factor, D is the distance to the source, r is the radius of the superbubble and f is a filling factor taking into account that the hot gas is not distributed homogeneously but broken up into separate bubbles. With the parameters of D = 97 Mpc, r = 4 kpc, N_{RS} = 5×10^{-6} cm^5 and an assumed filling factor of 0.1 one obtains an electron density of 0.03 cm^{-3}. Changing the filling factor to f = 0.9 leads to n_e = 0.01 cm^{-3}.

An expansion time of 10^7 yr with a halo gas density of 0.01 cm^{-3} leads to an X-ray luminosity of the shell of 2.8×10^{41} erg s^{-1}. A lower SNII rate of 0.5 yr^{-1} and a slightly smaller expansion time of 8×10^6 yr reduce the obtained X-ray luminosity to 1.2×10^{41} erg s^{-1} in the ROSAT band. The derived plasma temperature of 10^7 K lies at the upper bound of the range with log T = 6.0–6.9 found by S94 for the (0.1–2.2) keV band.

For a Salpeter IMF, a SNII activity between 10 and 100 M$_\odot$ and a SN rate of 0.5 yr^{-1} the star formation rate results to $\sim$95 M$_\odot$ yr^{-1}. Depending on the fraction of the mechanical energy release of a SNII this value can increase up to a factor of 5.

4.3. Comparison with other galaxies of similar properties

Each galaxy and, in particular, mergers, galaxy pairs or SB galaxies are unique systems. In order to get an insight on whether NGC 4410 and its derived structures are somehow typical for close encounters, we compare the derived X-ray luminosity in the ROSAT band with other disturbed and isolated SB galaxies. The peculiar galaxy NGC 2782 e.g. is thought to be a merger of two disk galaxies of unequal mass and has $L_{\rm X}$ = 4×10^{41} erg s^{-1} (Schulz et al. 1998). Another galaxy with disturbed morphology and comparable X-ray luminosity ($L_{\rm X}$ = 1.4×10^{41} erg s^{-1}) is NGC 1808. In contrast the PSPC data of this object do not show any X-ray outflow out of the central source into the halo. But one has to mention that NGC 1808 has a SFR of only 10 M$_\odot$ yr^{-1} (Junkes et al. 1995). Relatively isolated systems without any companion, like e.g. NGC 253 (Fabbiano et al. 1992), NGC 2903 and NGC 4569 (Junkes et al. in preparation), contain X-ray luminosities of a few 10^{40} erg s^{-1}, emphasizing the importance of interaction for star-forming activity.

PC96 found a significant difference in the $L_{\rm X}/L_{\rm H\alpha}$ ratio between pure AGN, pure SBs and galaxies with circumnuclear star-forming rings with an active nucleus. The pure active nuclei show log($L_{\rm X}/L_{\rm H\alpha}$) between 0.00 and +1.68, while the pure SBs in the sample lie between -1.46 and -0.36. The three galaxies with combined X-ray emission from AGN and SB have values of -0.26 (NGC 1097), +0.16 (NGC 1068) and +0.63 (NGC 7469), indicating a continuous decrease from AGN to SB. From this tendency one would expect a log($L_{\rm X}/L_{\rm H\alpha}$)<0 for the RS+PO model for NGC 4410. Our results, however yields +0.77 thereby, approximately the same as for a single PO model with log($L_{\rm X}/L_{\rm H\alpha}$) = +0.81.

The fraction of $L_{\rm H\alpha}$ from the SB relative to the total Hα luminosity amounts to 98%, 80% and 40% for NGC 1097, NGC 1068 and NGC 7469, respectively. Comparing only the contributions from the SB to the Hα and X-ray luminosity, PC96 found $\log(L_{\rm X}/L_{\rm H\alpha})$ = -0.99, -0.70 and -0.36 for NGC 1097, NGC 1068 and NGC 7469, respectively. If we consider the fraction of Hα luminosity from the SB in these galaxies, and assume that 90% of the total Hα luminosity originates from the SB within NGC 4410a, $L_{\rm H\alpha}$ would result in 5.9×10^{40} erg s^{-1} and $\log(L_{\rm X}/L_{\rm H\alpha})$ = +0.36, which is quite high compared to the sample analysed by PC96.

5. Conclusions

We observed the interacting pair of galaxies NGC 4410 with the ROSAT HRI and PSPC. Spectral investigations of NGC 4410 suggest that the integral X-ray emission ($L_{\rm X}$ = 3.9×10^{41} erg s^{-1}) can be decomposed into a thermal component (described by a RS spectrum) and a component from the AGN (described by a power-law spectrum). The HRI image reveals an extended X-ray halo related to NGC 4410a with an extension of 10″ from the nucleus of NGC 4410a to the south-east. Combining spatial and spectral informations reveals an X-ray luminosity of the halo gas of $L_{\rm X} = 1.3\times10^{41}$ erg s^{-1} (1/3 of the total X-ray emission). The companion galaxy NGC 4410b houses only a very faint central point-like source below the 3σ level, corresponding to an upper limit of 3.8×10^{39} erg s^{-1} for the X-ray luminosity.

As a reasonable model we can assume that the tidal interaction in the pair of galaxies NGC 4410 has two effects on the one partner, the face-on pec Sab galaxy NGC 4410a:

(1) A central monster is either formed due to this interaction or has already existed before and is now fed by infalling gas during the merging event, producing AGN signatures. Evidence for an existing AGN comes from the ROSAT X-ray spectrum supported by the spatially correlated radio emission.

(2) The merging process has ignited a nuclear SB ejecting an X-ray gas into the halo. Due to the tidal forces of NGC 4410b, the X-ray halo of NGC 4410a is deformed toward its neighbouring galaxy, either directly by gravitational forces or indirectly, originating from a decentred starburst region as a consequence of the merging process.

This system of merging galaxies represents a highly interesting object because it is a close interacting pair where the effects of tidal forces on nuclear activity and SB can be studied in detail with large telescopes. The HST WFPC2 image of NGC 4410a suggests a possible relation between the deformed X-ray halo and a bright emission region near the nucleus. With ROSAT imaging it is not possible to distinguish between the nucleus and the bright emission region resolved by HST. Further spectroscopic observations of this region and additional infrared imaging could help answering the question of the exact origin of the X-ray emission.

Acknowledgements. The authors are grateful to an unknown referee for his substantial and constructive report. The ROSAT project is supported by the German Bundesministerium für Bildung, Wissenschaft, Forschung und Technologie (BMBF) and the Max-Planck-Society. The optical image shown is based on photographic data of the National Geographic Society - Palomar Observatory Sky Survey (NGS-POSS) obtained using the Oschin Telescope on Palomar Mountain. The NGS-POSS was funded by a grant from the National Geographic Society to the California Institute of Technology. The plates were processed into the present compressed digital form with their permission. The Digitized Sky Survey was produced at the Space Telescope Science Institute (STScI) under US Government grant NAG W-2166. This research has made use of the NASA/IPAC Extragalactic Database (NED) which is operated by the Jet Propulsion Laboratory, Caltech, under contract with the NASA. Observations made with the NASA/ESA Hubble Space Telescope were used, obtained from data archive at STScI. STScI is operated by the Association of Universities for Research in Astronomy, Inc. (AURA) under the NASA contract NAS 5-26555.

References

Anders E., Grevesse N. 1989, Geochimica et Cosmochimica Acta 53, 197
Arnaud K.A. 1996, Astronomical Data Analysis Software and Systems V, ASP Conf. Ser. vol. 101, eds. Jacoby G. and Barnes J., p. 17
Batuski D.J., Hanisch R.J., Burns J.O. 1992, AJ 103, 1077
Bicay M.D., Kojoian R.J., Seal J., et al. 1995, ApJS 98, 369
Binette L., Dopita M.A., Tuohy I.R. 1985, ApJ 297, 476
Briel U., Aschenbach B., Hasinger G., et al. 1996, ROSAT User's Handbook (MPE, Garching)
Brown B.A., Bregman J.N. 1998, ApJ 495, L75
Bushouse H.A. 1986 AJ 91, 255
Dickey J.M., Lockman F.J. 1990, ARAA 28, 215
Fabbiano G., Kim D.-W., Trinchieri G. 1992, ApJS 80, 531
Genzel R., Lutz D., Sturm E., et al. 1998, ApJ 498, 579
Hummel E., Kotanyi C.G., van Gorkom J.H. 1986, A&A 155, 161 (HKG86)
Jog C.J., Das M. 1992, ApJ 400, 476
Jog C.J., Solomon P.M. 1992, ApJ 387, 152
Joseph R.D., Meikle W.P.S., Robertson N.A., Wright G.S. 1984, MNRAS 209, 111
Junkes N., Zinnecker H., Hensler G., et al. 1995, A&A 294, 8
Keel W.C. 1985, in "Astrophysics of Active Galaxies and Quasi-Stellar Objects", ed. Miller J.S., University Science Books, Mill Valley, p.1
Lonsdale C.J., Persson S.E., Matthews K. 1984, ApJ 287,95
Lutz. D., Spoon H.W.W., Rigopoulou D., et al. 1998, ApJ 505 L103
MacLow M.-M., McCray R. 1988, ApJ 324, 776
MacLow M.-M., McCray R., Norman M.L. 1989, ApJ 337, 141
Mathew W.G., Doane J. 1994, in "Panchromatic View of Galaxies – Their Evolutionary Puzzle", eds. Hensler G., Theis C., Gallagher J.S., Éditions Frontières, p. 221
Mazzarella J.M., Boroson T.A. 1993, ApJS 85, 27 (MB93)
Mazzarella J.M., Bothun G.D., Boroson T.A. 1991 AJ 101, 2034
Michaelis O., Hensler G., Samland M. 1996, in IAP Proc. "The Interplay between Massive Star Formation, the ISM and Galaxy Evolution", eds. Kunth D. et al.,Editions Frontiers, Gif-sur-Yvettes, p. 525
Morse J.A. 1994, PASP 106, 675
Mulchaey J.S., Colbert E., Wilson A.S., et al. 1993, ApJ 414, 144
Norman C.A., Ikeuchi S. 1989, ApJ 345, 372
Norman C.A., Scoville N.Z. 1988, ApJ 332, 124
Pérez-Olea D.E., Colina L. 1996, ApJ 468, 191 (PC96)

Ptak A., Serlemitsos P., Yaqoob T., Mushotzky R. 1997, AJ 113, 1286
Raymond J.C., Smith B.W. 1977, AJS 35, 419
Rees M.J. 1984, ARAA 22, 471
Sanders D.B., Mirabel I.F. 1996, ARAA 34, 749
Schulz H., Komossa S., Berghöfer T.W., Boer B. 1998, A&A 330, 823
Stockton A. 1990, in "Dynamics and Interaction s of Galaxies", ed. Wielen R., Springer Verlag, Berlin, p.440
Suchkov A.A., Balsara D.S., Heckman T.M., Leitherer C. 1994, ApJ 430, 511 (S94)
Telesco C.M. 1988, ARAA 26, 343
Thuan T.X., Sauvage M. 1992 A&AS 92, 749
Tomisaka K., Ikeuchi S. 1986, PASJ 38, 697
Tomisaka K., Ikeuchi S. 1988, ApJ 330, 695
Turatto M., Capellaro E., Petrosian A.R. 1989, A&A 217, 79
Turner T.J., George I.M., Mushotzky R.F. 1993, ApJ 412, 72
Weedman D.W. 1983, ApJ 266, 479
Woosley S.E., Weaver T.A. 1985, in "Radiation Hydrodynamics in Stars and Compact Objects", Proc. of the IAU Colloquium No. 89, eds. Mihalas D., Winkler K.H., p.91
Zimmermann H.U., Becker W., Belloni T., et al. 1997, EXSAS User's Guide, Edition 5, MPE Report, Garching

Chapter 5

X-rays from the barred galaxy NGC 4303

Published in
Astronomy and Astrophysics
Vol. 360, p. 447 (2000)

Astron. Astrophys. 360, 447–456 (2000)

ASTRONOMY AND ASTROPHYSICS

X-rays from the barred galaxy NGC 4303

D. Tschöke[1], **G. Hensler**[1], **and N. Junkes**[2]

[1] Institut für Theoretische Physik und Astrophysik, Universität Kiel, 24098 Kiel, Germany (tschoeke@astrophysik.uni-kiel.de)
[2] Max-Planck-Institut für Radioastronomie, Auf dem Hügel 69, 53121 Bonn, Germany

Received 20 March 2000 / Accepted 21 June 2000

Abstract. The late-type galaxy NGC 4303 (M61) is one of the most intensively studied barred galaxies in the Virgo Cluster. Its prominent enhanced star formation throughout large areas of the disk can be nicely studied due to its low inclination of about 27°.

We present observations of NGC 4303 with the ROSAT PSPC and HRI in the soft X-ray (0.1–2.4 keV). The bulk of the X-ray emission is located at the nuclear region. It contributes more than 80% to the total observed soft X-ray flux. The extension of the central X-ray source and the $L_{\rm X}/L_{\rm H\alpha}$ ratio point to a low luminous AGN (LINER) with a circumnuclear star-forming region. Several separate disk sources can be distinguished with the HRI, coinciding spatially with some of the most luminous H II regions outside the nucleus of NGC 4303. The total star formation rate amounts to 1–2 $M_\odot\,{\rm yr}^{-1}$. The X-ray structure follows the distribution of star formation with enhancement at the bar-typical patterns.

The best spectral fit consists of a power-law component (AGN and HMXBs) and a thermal plasma component of hot gas from supernova remnants and superbubbles. The total 0.1–2.4 keV luminosity of NGC 4303 amounts to 5×10^{40} erg s^{-1}, consistent with comparable galaxies, like e.g. NGC 4569.

Key words: galaxies: individual: NGC 4303 – galaxies: starburst – galaxies: active – X-rays: galaxies

1. Introduction

Barred galaxies constitute a major fraction of all disc galaxies classified in the optical, more than 50% including strong bars and intermediate morphologies (Sellwood & Wilkinson 1993). This fraction increases when also near-infrared images are used for classification, thus underlining the importance for the general understanding of the evolution of galaxies. The non-axisymmetric potential has a strong impact on the gas dynamics and the star formation in barred systems. Observations reveal a correlation between the radial abundance gradient and the strength of the bar (Martin & Roy 1994; Friedli et al. 1994; Martinet & Friedli 1997). This is interpreted as the result of two effects caused by the bar: a stronger radial gas flow and hence a stronger radial mixing of metals and the efficiency of star formation. The radial mass transfer concentrates gas near the galactic center and at the ends of the bar at corotation. Enhanced star formation is the consequence of gas accumulation. The rotating bar potential also heats up the outer disk parts which leads to larger stellar velocity dispersions and a radial diffusion of stars. (Sellwood & Wilkinson 1993).

Galactic bars have also been considered to support the central infall of gas to feed a central "monster"(e.g. Beck et al. 1999). Several authors have claimed that active galactic nuclei (AGN) are more likely in barred galaxies than in non-barred ones (e.g. Simkin et al. 1980; Arsenault 1989). Hummel et al. (1990) note that the fraction of central radio sources in barred spirals is by a factor of 5 higher than in non-barred spirals. Other authors doubt that there is a significantly higher number of bars in galaxies harboring an AGN (e.g. Balick & Heckman 1982; Ho et al. 1997). It appears that the concentration of gas on a scale of $\sim$1 kpc at the galactic center required to enhance the central star formation can easily be achieved by a bar potential. It seems much more difficult, however, to accumulate enough gas on a scale of a few pc to tens of pc in order to produce an AGN. Other effects depending on the environment of the galaxies (interaction: Elmegreen et al. 1990; H I contents: Cayatte et al. 1990) play an important role in mass distribution, gas flow, and therefore in the formation and evolution of bars and the star formation history in these systems.

One of the most famous, closest and most widely studied barred galaxies is NGC 4303 (M61), member of the Virgo Cluster, which is observed at an inclination of 27° (Guhathakurta et al. 1988). Optical spectra of this galaxy indicate that it consists of a nuclear starburst and a LINER or Seyfert 2 nucleus (Filippenko & Sargent 1986; Kennicutt et al. 1989; Colina et al. 1997; Colina & Arribas 1999, hereafter CA99). Indications for a high star formation rate (SFR) in NGC 4303 are given by the numerous H II regions (Hodge & Kennicutt 1983; Martin & Roy 1992, hereafter MR92) and three observed supernovae (van Dyk 1992). It also shows strong radio emission distributed over the entire disk (Condon 1983). Colina et al. (1997) and CA99 discussed the question of a starburst–AGN connection in this barred galaxy, using optical spectroscopy and HST UV images. The data range from a nuclear spiral structure of massive star-forming regions with an outer radius of 225 pc down to the unresolved core of a size $\leq$ 8 pc. From the UV data it is not clear if the core is a massive stellar cluster or a pure AGN.

Send offprint requests to: D. Tschöke

VLA observations (Cayatte et al. 1990) show that NGC 4303 is not highly H I deficient, which can be explained by only slight environmental influences in the outermost region of the Virgo Cluster. The projected distance to M87 is 8.°2 (Warmels 1988). No significant difference of the abundance gradient in the disk of NGC 4303 compared to non-barred spiral galaxies has been observed (MR92). Martinet & Friedli (1997) discussed the abundance gradient slope in terms of bar age. According to them, a steep gradient in the bar and a flat one in the outer disk are typical for a young bar while a single flat gradient in bar and disk characterizes an old bar. MR92 did not determine the gradient at large radii because of a small number of H II regions. Martinet & Friedli (1997) also claimed that bars in late-type spirals with enhanced star formation like NGC 4303 are expected to be young.

Probable interaction companions are the nearby galaxies NGC 4303 A (Condon 1983) and NGC 4292 (Cayatte et al. 1990), at distances of 7.′5 northwest and 10′ northeast, respectively.

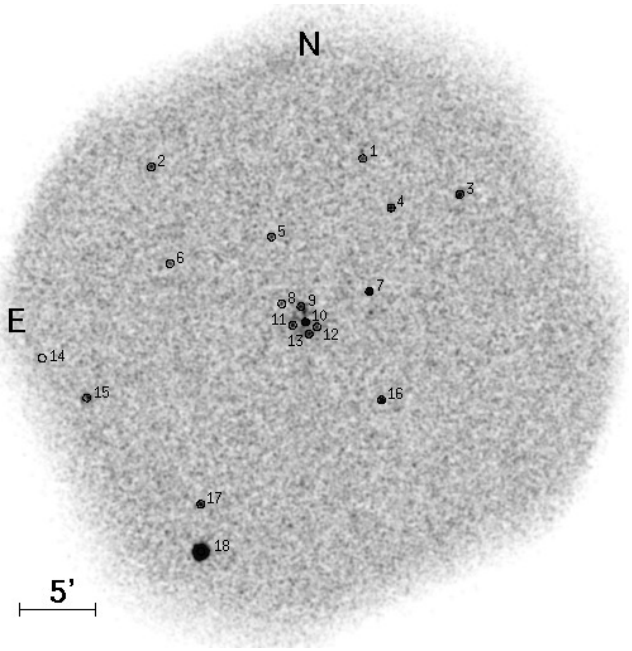

Fig. 1. Total field of view of the combined ROSAT HRI observation of NGC 4303. The detected 5σ sources are labeled with numbers. The sources in the center (nos. 9–13) correspond to NGC 4303.

Table 1. Some basic parameters of NGC 4303.

	NGC 4303	Reference[a]
alternative name	M61	
	IRAS 12194+0444	
type	SAB(rs)bc	1
RA (2000)	$12^{\rm h}21^{\rm m}54.^{\rm s}9$	2
Dec (2000)	$+04^\circ 28' 25''$	2
distance	16.1 Mpc	3
D_{25} diameter	5.′9	4
axis ratio	0.97	4
inclination	27°	5
log $L_{\rm B}$	10.53[b]	4
log $M_{\rm H}$	9.71[b]	4

[a] *References:* 1) de Vaucouleurs et al. (1991)
2) NASA/IPAC Extragalactic Database
3) Ferrarese et al. (1996)
4) Tully (1988)
5) Guharthakurta et al. (1988)
[b] Corrected for a distance of 16.1 Mpc.

2. Observations and data reduction

In this paper we present data from the High Resolution Imager (HRI) and the Position Sensitive Proportional Counter (PSPC) on board of the X-ray satellite ROSAT. This X-ray telescope was operating in the energy range of 0.1–2.4 keV. For details concerning ROSAT and its detectors see the ROSAT User's Handbook (Briel et al. 1996).

2.1. HRI

We proposed HRI pointed observations of NGC 4303 (ROSAT sequence number 600854, PI: N. Junkes), which were carried out in the time periods July 2–8, 1996, June 9–23, 1997, and January 6–7, 1998 with integration times of 16055 sec, 27538 sec, and 5600 sec, respectively (see Table 2). All three observations are centered on RA(2000) = $12^{\rm h}21^{\rm m}55.^{\rm s}2$; Dec(2000) = $+04^\circ 28' 11.''5$.

The three photon lists were combined to create one single image. The data were analyzed using the commercial interactive data language software package IDL (Interactive Data Language). All presented images contain pixel values with units of counts per pixel and second. The images were corrected for vignetting but not for background. To quantify any source counts three circular source-free fields with radii of 49″, 34″, and 39″, respectively, were selected to determine the background level (Table 2). The averaged background flux amounts to 3.52×10^{-7} cts s^{-1} arcsec^{-2}.

Fig. 1 shows the HRI field of view (FOV) of the three combined data sets, convolved with a Gaussian of 5″ FWHM. For reasons of identification the 5σ sources detected with a maximum likelihood method are numbered in Fig. 1 and listed in Table 3. Several single source detections (no. 9–13) coincide with optical peaks in the galaxy. Source no. 18 can be identified as the QSO 1219+044, which served as the central source of the PSPC pointed observation used for spectral analysis in Sect. 2.2. Source no. 7 coincides spatially with the QSO 1219+047 (Bowen et al. 1996). It turned out that the source is variable the X-rays. Its flux increased by a factor of 3 between the second and third HRI observation (June 1997 and January 1998).

2.2. PSPC

Since there exist no particular PSPC observations pointed on NGC 4303, we use ROSAT observations from the archive (ROSAT sequence number 701095, PI: R. Staubert). NGC 4303

Table 2. Date, integration time, and source and background count rates of the HRI and PSPC observations.

	Date	Integration time [s]	Count rate [cts s^{-1}]	Background [cts s^{-1} arcsec^{-2}]
HRI	July 2–8, 1996	16055	8.8×10^{-3} [a]	3.52×10^{-7} [a]
	June 9–23, 1997	27538		
	January 6–7, 1998	5600		
PSPC	December 24–26, 1992	8135	0.062	5.14×10^{-7}

[a] Combined HRI observations

Table 3. EXSAS source detection of X-ray sources in the HRI coinciding with the optical image of NGC 4303.

Source no.	RA (2000)	Dec (2000)	Count rate [10^{-4} cts s^{-1}]	Identification
1	$12^h21^m39\overset{s}{.}8$	$+04^\circ39'17''$	12.5±2.4	
2	$12^h22^m35\overset{s}{.}7$	$+04^\circ38'44''$	16.5±2.9	
3	$12^h21^m14\overset{s}{.}1$	$+04^\circ36'54''$	26.1±3.0	GSC 00285-00416
4	$12^h21^m32\overset{s}{.}3$	$+04^\circ36'01''$	13.5±2.1	unidentified optical point source
5	$12^h22^m03\overset{s}{.}9$	$+04^\circ34'06''$	6.4±1.4	
6	$12^h22^m30\overset{s}{.}7$	$+04^\circ32'19''$	7.9±1.7	
7	$12^h21^m38\overset{s}{.}0$	$+04^\circ30'28''$	47.2±3.2	QSO 1219+047; variable
8	$12^h22^m01\overset{s}{.}2$	$+04^\circ29'40''$	5.3±1.3	
9	$12^h21^m56\overset{s}{.}1$	$+04^\circ29'29''$	10.8±2.0	NGC 4303
10	$12^h21^m54\overset{s}{.}9$	$+04^\circ28'27''$	36.1±3.0	NGC 4303
11	$12^h21^m58\overset{s}{.}3$	$+04^\circ28'15''$	8.5±1.6	NGC 4303
12	$12^h21^m51\overset{s}{.}8$	$+04^\circ28'08''$	6.9±1.5	NGC 4303
13	$12^h21^m54\overset{s}{.}0$	$+04^\circ27'40''$	11.9±2.0	NGC 4303
14	$12^h23^m04\overset{s}{.}4$	$+04^\circ26'03''$	29.4±5.1	
15	$12^h22^m52\overset{s}{.}6$	$+04^\circ23'26''$	28.8±3.5	
16	$12^h21^m34\overset{s}{.}8$	$+04^\circ23'17''$	21.8±2.3	
17	$12^h22^m22\overset{s}{.}5$	$+04^\circ16'23''$	18.8±2.8	
18	$12^h22^m22\overset{s}{.}5$	$+04^\circ13'16''$	351.6±9.2	QSO 1219+044

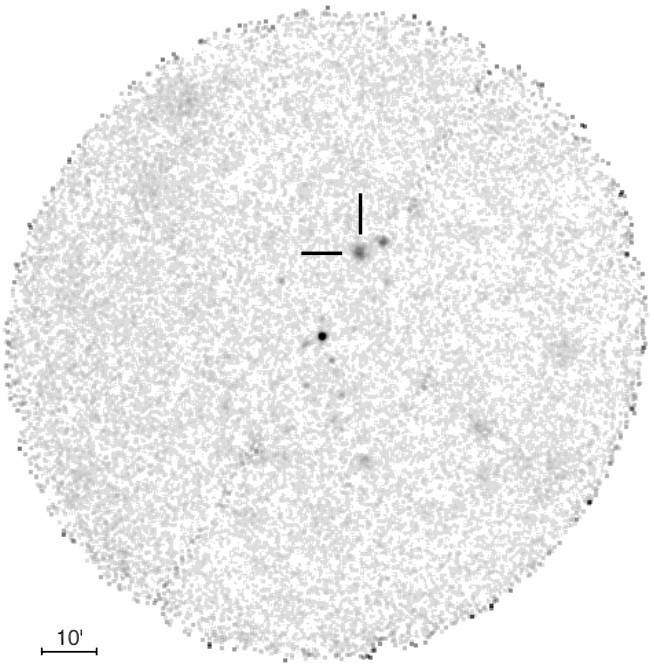

Fig. 2. Total field of view of the ROSAT PSPC observation around the QSO 1219+044. The position of NGC 4303 at an off-axis distance of 17′ is marked.

lies in the FOV at an off-axis distance of 17′ which is still within the inner part of the supporting ring structure of the telescope. The position of the X-ray counterpart of NGC 4303 is given in Fig. 2. The central source is the QSO 1219+044 (no. 18 in Fig. 1). The image has been convolved with a Gaussian of 25″ FWHM. Due to strong asymmetry and broadening of the point spread function (PSF) with radial distance from the optical axis (∼25″ FWHM for an on-axis point source at 1 keV; ∼67″ FWHM for a 17′ off-axis point source at 1 keV; Hasinger et al. 1994) we cannot get any useful spatial information from the PSPC data.

This PSPC exposure was carried out between December 24 and 26, 1992, with an integration time of 8135 sec. The background flux was determined from three circular source-free areas in the field with radii of 83″, 88″, and 75″ and amounts to 5.14×10^{-7} cts s^{-1} arcsec^{-2}. To analyze the PSPC data we used IDL and the software package XSPEC (Arnaud 1996) for interactively fitting X-ray spectra.

For NGC 4303, we adopt the same distance as of M100, the brightest spiral in the Virgo Cluster (16.1 Mpc; Ferrarese et al. 1996). Then the resolution of the ROSAT detectors of ∼5″ full width at half maximum (FWHM) for the HRI and ∼67″ FWHM for the PSPC at an off-axis distance of 17′ scale to 390 pc and 5.3 kpc, respectively.

Table 4. X-ray sources spatially coinciding with the optical galaxy NGC 4303. The source designations refer to Fig. 3.

Source	RA (2000)	Dec (2000)	Count rate [10^{-4} cts s^{-1}]	Source area [arcsec^2]	Flux[a] (0.1–2.4 keV) [10^{-14} erg s^{-1} cm^2]	Luminosity (0.1–2.4 keV) [10^{38} erg s-1]
A	$12^h21^m54\overset{s}{.}5$	$+04°29'38''$	3.4±1.1	200	1.4±0.5	4.3±1.5
B	$12^h21^m56\overset{s}{.}3$	$+04°29'28''$	9.9±1.8	531	4.1±0.8	12.7±2.5
C	$12^h21^m55\overset{s}{.}3$	$+04°29'03''$	5.9±1.4	290	2.5±0.6	7.8±1.9
D	$12^h21^m58\overset{s}{.}3$	$+04°28'14''$	8.9±1.7	380	3.7±0.7	11.5±2.2
E	$12^h21^m51\overset{s}{.}7$	$+04°28'08''$	7.5±1.5	315	3.1±0.6	9.6±1.9
F	$12^h21^m53\overset{s}{.}9$	$+04°27'43''$	8.7±1.7	383	3.6±0.7	11.2±2.2
nucleus	$12^h21^m55\overset{s}{.}5$	$+04°28'28''$	43.9±3.5	1321	87.8±7.0	272±21

[a] Energy conversion factor ECF: disk sources A–F, ECF=2.4×10^{10} cts cm^2 erg^{-1}; nucleus, ECF=5×10^{13} cts cm^2 erg^{-1}

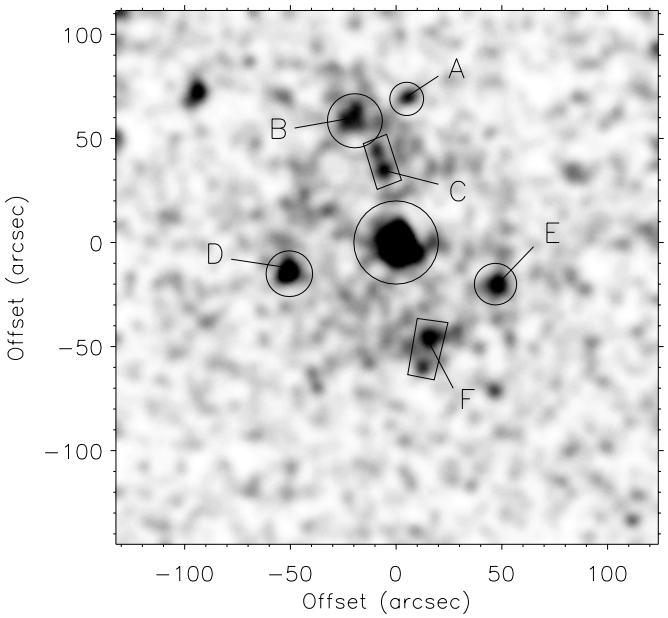

Fig. 3. The inner $4'$ of the pointed HRI observation. The labeled sources (A–F) are the ones spatially coinciding with the optical disk of NGC 4303 (see text and Table 4 for details). The image is centered on the coordinates of the pointed observation. The distances on the axes are relative to the central X-ray source with the coordinates $\alpha(2000) = 12^h21^m55\overset{s}{.}5$; $\delta(2000) = +04°28'28\overset{''}{.}5$. North is up, east is to the left.

3. Results

3.1. Spatial analysis

As already mentioned, no useful spatial information on the X-ray structure of NGC 4303 can be obtained from the PSPC data due to the spatial resolution of the detector, and moreover to the $17'$ off-axis position of the source in the FOV.

In contrast, the more detailed HRI image reveals a number of X-ray sources distributed over the galactic disk (Fig. 4). In comparison to the numbered sources in Fig. 1 the closer view allows to distinguish more details. For example, source no. 9 in Fig. 1 splits into three X-ray spots (labeled A–C in Fig. 3). The most luminous source coincides with the center of NGC 4303 and dominates in the soft X-rays. The count rates and fluxes derived for sources from the HRI are listed in Table 4. The corresponding areas are plotted in Fig. 3. To determine the fluxes we used the energy conversion factor (ECF) from the ROSAT *Call For Proposals* documentation. The ECF determines the ratio between count rates and unabsorbed source flux in the ROSAT band for given spectral parameters. For the disk sources A–F we assume a 0.3 keV Raymond-Smith model (Raymond & Smith 1977) with an absorption column density of 3×10^{20} cm^{-2}. For the nucleus a power law with Γ=2.6 and a column density of 3×10^{20} cm^{-2} (see Sect. 3.2 and Table 5) is applied as spectral model.

The contours of sources B, C, D, and F in Fig. 3 are all located within the optical arm structure and coincide with bright Hα emission regions within the spiral arms (Fig. 4). In addition, source E is embedded in the faint outer part of the southwestern spiral arm. MR92 distinguished 79 H II regions in NGC 4303, mainly in the spiral arms. The X-ray contour overlay over the Hα image in Fig. 4 reveals that the X-ray sources B, C, D, and F coincide with H II regions, while sources A and E are located near such regions.

Gas dynamical models of barred galaxies (Englmaier & Gerhard 1997) show strong gas accumulation at the tips of the bars due to corotation of the bar structure with the disk what should lead to enhanced star formation. H I observations as well as the existence of prominent Hα features strikingly support the outcome of these models. The X-ray contours B and F seem to arise from these regions. The X-ray maximum D is connected with another interesting feature of NGC 4303: in the eastern part the galactic arm seems to be deformed to a boomerang-like bow where source D lies at the bend but without any significant brightening in Hα.

The lower X-ray contours of the nucleus indicate a possible extended source. Recent high-resolution UV observations of the central region with the Hubble Space Telescope reveal a spiral-shaped structure of massive young (2–3 Myr) star-forming regions with an outer radius of 225 pc (CA99). This structure cannot be resolved by HRI. Due to the low age of the star clusters almost no thermal X-ray emission is expected at the galactic nucleus (see Sect. 4). The extended X-ray contours may originate from additional sources at distances of about 1 kpc around the nucleus.

No X-ray emission has been detected from the possible interaction companions NGC 4303 A and NGC 4292.

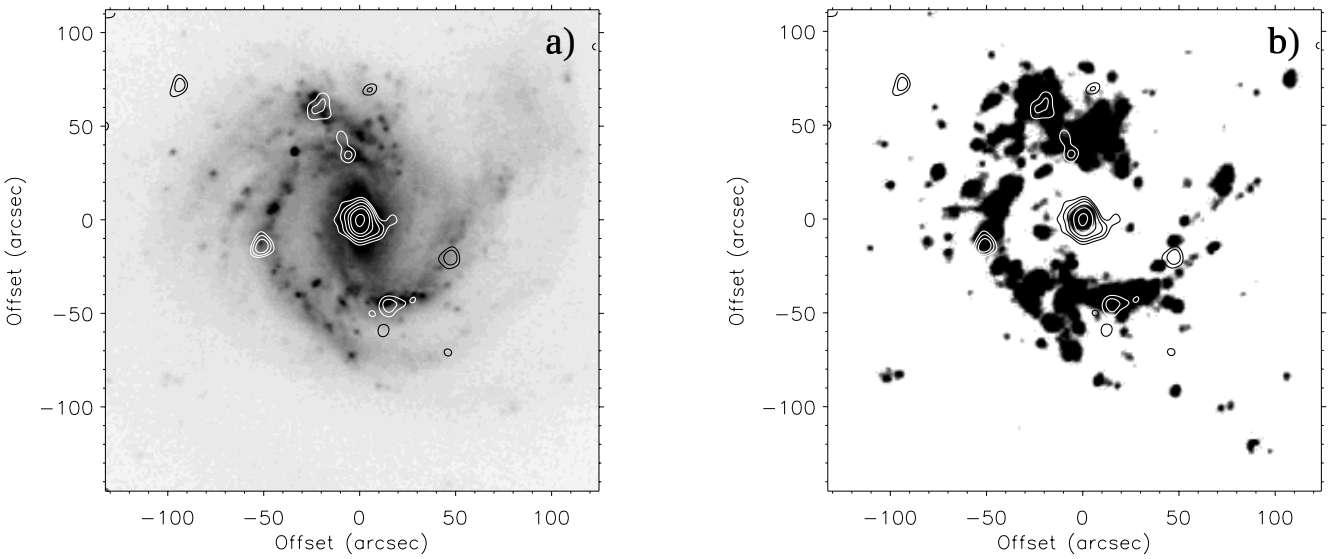

Fig. 4a and b. Overlay of the HRI X-ray contours onto the optical image of NGC 4303 **a** taken from Frei et al. (1996) and the Hα image **b** taken from MR92. The contour levels are at 5, 7, 10, 15, 20, and 30σ above the mean background with σ = 1.5×10^{-7} cts s^{-1} arcsec^{-2}. The images are centered on the coordinates of the pointed observation. The axis scales are relative to the central X-ray maximum at coordinates α = 12$^{\rm h}$21$^{\rm m}$55$^{\rm s}$.5; δ = +04°28′28″.5. North is up, east is to the left.

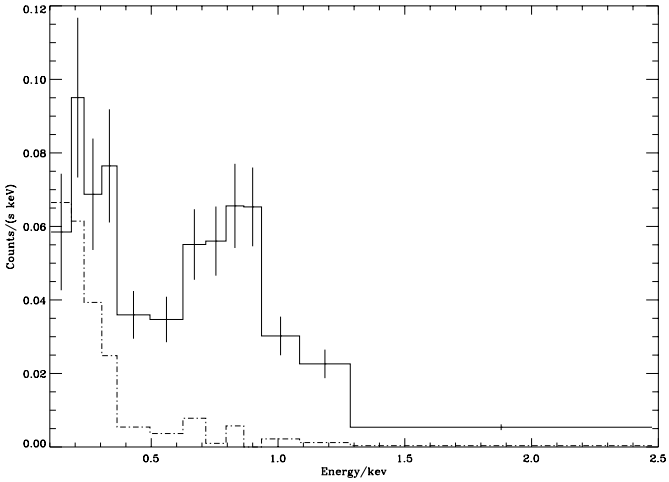

Fig. 5. Background-subtracted ROSAT PSPC spectrum of NGC 4303 in the energy range of 0.1–2.4 keV. The 505 photons were binned to get a signal-to-noise ratio of 6. The dashed-dotted line represents the contribution of the background (see text).

3.2. Properties of the X-ray spectrum

Since the HRI maxima are separated by only 50″, and because of the reasons mentioned in Sect. 2.2, the PSPC observations do not allow to study the spectra of the X-ray components of NGC 4303 individually. ROSAT PSPC detected 505±24 backgroung-subtracted source counts from NGC 4303 in a total integration time of 8135 sec. The spectra of the source and the background are shown in Fig. 5.

We fitted the spectrum with several single-component models, as Bremsstrahlung (BS), Raymond-Smith model (RS), and a power law (PO), and a combined RS-PO model. The results are listed in Table 5.

A single power-law model implies the assumption, that the active nucleus of NGC 4303 dominates the X-ray emission. Furthermore, the sources detected by the HRI in the galactic disk would also have to be described with the same power law. The photon index in this model is Γ=3.2±0.2. The emission of an AGN in the ROSAT energy band is best described by a power law with a photon index of $\Gamma \sim$2.4; nevertheless some cases have been observed with $\Gamma >$3 (MCG –5-23-16: Mulchaey et al. 1993; Mkn 335: Turner et al. 1993). High-mass X-ray binaries (HMXB) found in young star-forming regions in the spiral arms have a similar spectral shape in the 0.1–2.4 keV energy range with a photon index of $\Gamma \sim$2.7 (Mavromatakis 1993). The column density of the absorbing component amounts to 5.7×10^{20} cm^{-2}, which is by a factor of 3 higher than the Galactic foreground H I column density (Dickey & Lockman 1990, DL90). Nevertheless, self-absorption within NGC 4303 must be expected, and small-scale deviations from the observed Galactic value by DL90 cannot be ruled out and may result in a higher absorption from the Milky Way. The resulting 0.1–2.4 keV X-ray luminosity amounts to 1.3×10^{41} erg s^{-1}. The flux portion from the sources outside the nuclear region as observed with the HRI amounts to $\sim$1.4×10^{40} erg s^{-1} in the case of a single power-law emission model with Γ=3.2 using the corresponding ECF of 1×10^{10} cts cm^2 erg^{-1}. Assuming a mean X-ray luminosity of 10^{37} erg s^{-1} for an HMXB, as observed in the Milky Way (Fabbiano et al. 1982; Watson 1990) would require an unlikely high number of 1400 of these systems to produce the observed X-ray flux. The ratio of OB stars to HMXBs is assumed to be $\sim$500 (Fabbiano et al. 1982). This means that a total number of 7×10^5 OB stars would be required to account for the HMXB

Table 5. Best spectral fits to the PSPC data of NGC 4303 and the derived model parameters. For the determination of the X-ray luminosity a distance of 16.1 Mpc is assumed.

Model (1)	$N_{\rm H}$ (2)	kT (3)	Γ (4)	Z (5)	Norm (6)	Red. χ^2 (7)	d.o.f. (8)	$F_{\rm X}$ (9)	$L_{\rm X}$ (10)
RS + PO	$3.34^{+1.95}_{-0.39}$	$0.32^{+0.14}_{-0.07}$	$2.6^{+0.2}_{-0.6}$	1	6.2 (RS) 1.5 (PO)	1.3	8	$1.50^{+0.48}_{-0.44}$ $(0.19^{+0.04}_{-0.01})$	$4.7^{+1.5}_{-1.4}$ $(0.59^{+0.12}_{-0.03})$
PO	$5.72^{+0.68}_{-0.50}$		3.2 ± 0.2		2.1	1.4	10	$4.18^{+1.93}_{-0.88}$	$12.9^{+6.0}_{-2.7}$
RS	$2.87^{+0.67}_{-0.53}$	$0.57^{+0.08}_{-0.09}$		0.006	1.4	1.4	9	$1.13^{+0.08}_{-0.10}$	$3.47^{+0.25}_{-0.31}$
BS	$3.19^{+0.53}_{-0.49}$	$0.56^{+0.09}_{-0.07}$			2.5	1.4	10	$1.26^{+0.12}_{-0.10}$	$3.91^{+0.37}_{-0.31}$

Col. (1) – Spectral models: BS = thermal Bremsstrahlung, RS = Raymond-Smith, PO = power law.
Col. (2) – Column density in units of 10^{20} cm^{-2}.
Col. (3) – Plasma temperature in units of keV.
Col. (4) – Photon index.
Col. (5) – Metallicity in units of $Z_\odot$.
Col. (6) – Scaling factor: for BS in units of $(10^{-18}/(4\pi D^2))\int n_{\rm e} n_{\rm I} {\rm d}V$, $n_{\rm e}, n_{\rm I}$ = electron and ion densities (cm^{-3}); for RS in units of $(10^{-19}/(4\pi D^2))\int n_{\rm e} n_{\rm H} {\rm d}V$, $n_{\rm e}, n_{\rm H}$ = electron and H densities (cm^{-3}); for PO in units of 10^{-4} photons keV^{-1} cm^{-2} s^{-1} at 1 keV.
Col. (7) – Reduced χ^2.
Col. (8) – Degrees of freedom.
Col. (9) – Unabsorbed X-ray flux in units of 10^{-12} erg cm^{-2} s^{-1}. Values in brackets give the contribution of the thermal component.
Col. (10) – X-ray luminosity in units of 10^{40} erg s^{-1}. Values in brackets give the contribution of the thermal component.

X-ray flux in NGC 4303. Even if we consider to have 10^5 OB stars in NGC 4303, as observed e.g. in Mkn 297 (Benvenuti et al. 1979), it is still a factor of 7 higher than expected. Moreover, this is the required number only for the disk sources and would involve almost 1.5×10^7 $M_\odot$ in massive stars with a Salpeter IMF and, by this, would require a moderately high SFR of about 15 $M_\odot$ yr^{-1} in the disk. On the other hand, the corresponding supernova type II (SN II) rate (0.1 yr^{-1}) should contribute to the X-ray emission via hot gas.

The single component models BS and RS show similar results. Consequently, we only achieve an adequate fit of RS with very low metallicity, e.g. the portion of emission lines to the spectrum is very small. In contrast, it is expected that emission lines of highly ionized elements, like Fe and Mg, should play an important role in the X-ray spectrum of SNe II in starburst regions because of the nucleosynthesis of massive SN II progenitor stars (Woosley & Weaver 1985). In both models the column density is about 3×10^{20} cm^{-2} and the plasma temperature is 0.6 keV. For the BS model we get a total X-ray luminosity of 4×10^{40} erg s^{-1}, for the RS model it is 3.5×10^{40} erg s^{-1}. RS models with different higher metallicities yield unacceptable fits.

The fit of the X-ray spectrum with a two-component model (RS+PO) is only slightly better than the one-component fits. Nevertheless, from the points mentioned above and the physical picture discussed in Sect. 4 this model serves as the best explanation for the observed soft X-ray emission. Hydrogen column density ($N_{\rm H}$=3.3×10^{20} cm^{-2}) and power-law spectral index (Γ=2.6) lie within the expected range (as discussed for the single power law above). The plasma temperature of 0.3 keV fits with the observed values of other galaxies (e.g. NGC 253: Forbes et al. 1999; NGC 1808: Junkes et al. 1995). The total 0.1–2.4 keV luminosity for this model amounts to 4.7×10^{40} erg s^{-1} with 13% contribution from the RS component. The spectral fit together with the residuals is plotted in Fig. 6.

4. Discussion

From the quality of the spectral fits alone there is no significance for favoring a single-component model or a combination of two components. Due to the lack of any spatial information in the PSPC image there is no possibility to distinguish between different spatial and spectral components simultaneously. So only the combined information from the PSPC and HRI data allows a more detailed interpretation of the X-ray results.

Several points speak against the single PO component model, as discussed in Sect. 3.2. A more likely scenario is a composition of several different emission sources, like an active nucleus, HMXBs, and supernova remnants (SNRs). In the following we will therefore discuss a composite emission model and the comparison with the UV and optical observations of the galactic core.

4.1. The nucleus of NGC 4303

As can be discerned from the HRI image (Fig. 3 and Table 4), most of the X-ray emission of NGC 4303 (83%) comes from the central region of the galaxy. Three different pictures are imaginable for the nucleus: a central active nucleus, a central or circumnuclear region with enhanced star formation, or a combination of both phenomena. Any of these cases requires a sufficient gas density at the galactic center. This can be achieved by a barred potential which triggers radial gas flow from the outer regions toward the nucleus. On the other hand, from numerical simulations including gas dynamics bar formation has proved to be only a transient phenomenon (Combes 2000). In this pic-

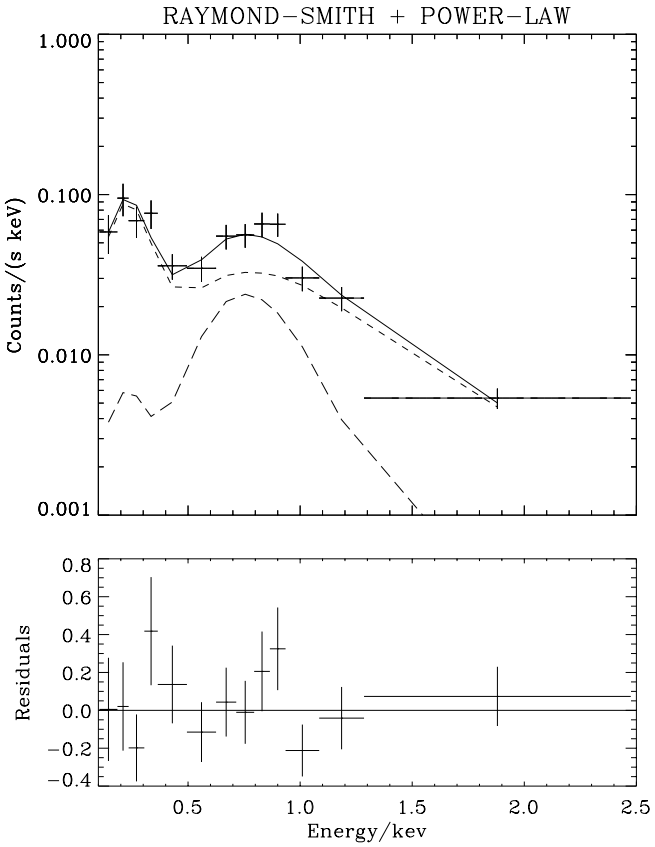

Fig. 6. Fit of the observed ROSAT PSPC spectrum of NGC 4303 with the two-component model RS+PO (solid line). The parameter values for this model are listed in Table 5. The long-dashed line shows the spectrum of the thermal model component, the short-dashed line represents the power-law component. The residuals of the fit are plotted in the lower box.

ture, the galactic bar will be destroyed by the gas inflow after only a few cycles. A new bar-phase can follow this gas infall due to a subsequent gravitational instability from the accreted central mass. The problem with this picture is the contradiction of a necessary gas inflow to form and feed any nuclear activity (starburst and/or AGN) and the fact that this gas inflow destroys the bar. It seems that a sufficiently massive black hole can provide for its fuelling (Fukuda et al. 1998). Another efficient way for gas to flow further into the center is a second smaller bar embedded into the first one due to a second inner Lindblad resonance (Friedli & Martinet 1993). In some cases, a gaseous circumnuclear ring is formed at the end of the second bar.

The concentrated X-ray emission from the galactic core in NGC 4303 may originate from an AGN and/or a nuclear or circumnuclear starburst. A starburst can contribute in two different ways to the X-ray flux. First, the produced star population contains HMXBs, emitting an X-ray radiation in spectral shape similar to an AGN. HMXBs cannot be distinguished from AGN in the ROSAT data. Additionally, high-mass stars (above $\sim$8–10 $M_\odot$) evolve to SNe II at an age of $\sim 10^7$ yr, depending on their initial mass. The SNe II from one star cluster form a cumulative expanding superbubble filled with hot gas which can be described by a thermal Bremsstrahlung spectrum and additional emission lines and recombination edges of highly ionized heavy elements produced in high-mass stars and released by their SN II explosions, e.g. O, Ne, Mg, Si, and Fe. Theoretical models for the spectral emission of such a hot diffuse gas are MEKA (Mewe et al. 1985) and the model by Raymond & Smith (1977), which we used in our spectral fit.

If we apply a two-component model to describe the X-ray spectrum of NGC 4303, the comparison of the flux ratio from the nucleus (83% in the HRI) and the disk sources (17% in the HRI) suggests that the central source can be described by the power-law component (87% in the spectral fit). The thermal RS emission exclusively originates from the disk sources, indicating ongoing star formation. To consider the possible extension of $\sim$25″ of the central source, as represented by the lowest contours, it is imaginable that a small fraction of the X-ray flux is emitted by a circumnuclear starburst at a distance of $\sim$1 kpc around the core. This would add a thermal component to the non-thermal X-ray nucleus. On the other hand, a fraction of the X-ray flux from the disk sources may come from HMXBs within these star forming regions.

Fuelling an AGN on scales of a few parsec at the center of the galaxy leads to the problem of reducing the angular momentum of the central gas by several orders of magnitude, as dynamical simulations show (Barnes & Hernquist 1991). Concentration of gas in a ring-like feature around the nucleus with a radius of $\sim$1 kpc is dynamically much easier to achieve. The HRI image agrees with the picture of an extended X-ray source with a diameter of the order of $\sim$2 kpc at the galactic center of NGC 4303, explained by a circumnuclear starburst region with an additional possible compact nuclear source.The decovered massive rotating circumnuclear disk in NGC 4303 can provide by its spiral-like structure of massive star forming regions an effective mechanism to channel gas from the circumnuclear regions further down to the nucleus to feed the AGN. But one has to consider that the spiral structure in the UV has a diamater of only 225 pc, while the extension of the central X-ray source is about 2 kpc in diameter. The spiral feature detected in the UV cannot be resolved with the HRI.

From the analysis of UV and optical magnitudes and colors of the central 250 pc Colina & Wada (2000) estimated ages of 5–25 Myr for the star-forming regions. Consequently a contribution to the central X-ray flux from SNRs and cumulatively expanding hot gas has to be expected. The question remains whether we observe a pure nucleus of massive star-forming clusters or a composition of these star clusters and a low luminous AGN. If NGC 4303 contains a non-thermal active nucleus, the X-ray luminosity of 4×10^{40} erg s^{-1} points to only a low luminous AGN (LINER). Koratkar et al. (1995) found a correlation between $L_{\rm X}$ and $L_{\rm H\alpha}$ for low luminous AGNs of $L_{\rm X}/L_{\rm H\alpha} \approx 14$. Pérez-Olea & Colina (1996) investigated the correlation between optical and X-ray luminosities of several AGNs with circumnuclear star-forming rings, pure AGNs, and pure starburst galaxies. The pure starbursts in their galaxy sample show $L_{\rm X}/L_{\rm H\alpha}$ values of 0.03–0.3, 100 times smaller than for pure AGNs. If we take the Hα luminosity of NGC 4303

derived by Keel (1983) and assume that 10% originate from the nucleus, we get log $L_{\mathrm{H}\alpha}$(nucleus) = 39.2 (adopted for a distance of 16.1 Mpc). Therefore the X-ray-to-Hα ratio amounts to log($L_{\mathrm{X}}/L_{\mathrm{H}\alpha}$) = 1.4, which agrees with the value found by Koratkar et al. (1995). Even the lower L_{X} value from a single RS model ($\sim 2.5\times10^{40}$ erg s^{-1} for the nucleus) results in log($L_{\mathrm{X}}/L_{\mathrm{H}\alpha}$) = 1.2. Typical pure starburst galaxies show Hα luminosities of the order of their X-ray luminosities or higher.

4.2. The galactic disk

At first glance the optical disk of NGC 4303 seems to have the quite symmetrical morphology of a late-type spiral. A closer look reveals that the eastern spiral arm of the galaxy has a much more prominent form with a boomerang-like shape and a lot more bright emission regions than the western counterpart. The northern disk shows a complex structure with many separate features. This asymmetry is more discernible in the Hα image. The H II regions are mainly located in the northern part of the disk at the junction of the bar with the eastern spiral arm and along that arm. A close encounter of one or both of the nearby galaxies NGC 4303 A and NGC 4292 may have caused these features. The interaction within the Virgo Cluster is another possible source. Infall into the intracluster medium could cause ram pressure effects. Nevertheless, NGC 4303 is located at the outer edge of the cluster, which may produce only a moderate disturbance. This agrees with the H I distribution over the whole optical disk. Galaxies lying nearer to the cluster center show H I deficiencies and concentration of the neutral hydrogen in the central regions, indicating past interactions with the H I gas been stripped off from the outer disk regions.

As a striking indication for accumulation of gas in these regions, the X-ray sources A–C and F within the galactic disk of NGC 4303 are located at the ends of the bar. Gas dynamical simulations of barred galaxies have shown this accumulation due to mass flows along the bar to the center and to the ends of the bar, respectively (Noguchi 1988; Englmaier & Gerhard 1997). The increased densities lead to enhanced star formation.

From the low inclination of NGC 4303 no direct information can be obtained whether the disk is warped or not. But it is striking that source D lies exactly at the bend of the eastern boomerang-shaped arm. This may indicate that this X-ray source is caused by the tidal force leading to a local gas concentration. Another indirect hint for a past interaction comes from the spectra of the QSO 1219+047 (source no. 7 in Fig. 1), a QSO whose line-of-sight penetrates the outer H I disk of NGC 4303. Bowen et al. (1996) detected complex Mg II absorption, spanning a velocity range of $\sim$300 km s^{-1}, despite the low inclined galactic disk. This high velocity is not fully understood. One possible explanation could be the result of interactions between NGC 4303 and the nearby companions.

4.3. Star formation in the disk

Table 4 lists the observed count rates and derived 0.1–2.4 keV luminosities for the single X-ray sources in the disk of NGC 4303. These include the assumptions of a Raymond-Smith plasma with solar abundances at a temperature of 0.3 keV. A power-law model would increase the values by a factor of 2.5. A rough estimation of the SFR in the disk from the X-ray luminosities is done by calculating the SN II rate ν_{SN} using a SNR model by Cioffi (1990), and assuming a Salpeter IMF within a mass interval from 0.1 M$_\odot$ to 100 M$_\odot$ and with all stars with masses above8M $_\odot$ evolving to SNe II. According to Cioffi, a SNR expanding into an ISM with a density of 1 cm^{-3} radiates a total energy of 4.7×10^{49} erg in the soft X-ray regime above 0.1 keV for a time of $\sim10^4$ yr. Norman & Ikeuchi (1989) investigated the cumulative effect of a number of SNRs. The total SFR in the disk of NGC 4303 from the X-ray luminosity amounts to 0.5 M$_\odot$ yr^{-1}. This however is just a very simple estimation, containing several simplifications, as e.g. the sum of the single SN model from Cioffi (1990) for several cumulatively expanding SNRs in an evolving OB assoziation, or the derivation of the total disk SFR from single X-ray sources. A more detailed determiation of the SFR, for example using an analytic suberbubble model by Suchkov et a. (1994), would need information about the extensions and expansion time of the superbubbles, in order to determine the mechanical energy release by the SNe and, by this, the SN rate. This can be compared with the observed X-ray luminosity.

Besides the mentioned restrictions the difference between the SFR estimated from the X-ray flux and the SFR derived by the Hα flux by Kennicutt (1983) (14 M$_\odot$ yr^{-1}) may be due to several reasons. Kennicutt used a Miller-Scalo IMF which increases the SFR by a factor of about 1.5. The total Hα luminosity underlies a distance determination with a Hubble constant of 50 km s^{-1} Mpc^{-1}. Taking a radial velocity of 1569 km s^{-1} (de Vaucouleurs et al. 1991) leads to a 3.8 times higher luminosity than taking the distance of 16.1 Mpc which we used. Additionally, the fact that not all H II regions may emit an adequate X-ray flux or are not strong enough to be detected lowers the estimated SFR from the X-ray luminosity which implies the existence of high-mass stars having been evolved to SNe II. Possible X-ray emission from diffuse hot gas within the disk may lie below the detection limit of 1.1×10^{-6} cts s^{-1} arcsec^{-2} (5σ above background level). A very faint component located at the spiral arms can be seen in outlines in Fig. 3, but is not detected at a 3σ level. This limit corresponds to an X-ray flux of 4.6×10^{-17} erg s^{-1} cm^{-2} arcsec^{-2} (ECF for a RS model as in Table 4). Kennicutt (1983)also admitted to treat the derived Hα flux and resulting SFR with extreme caution because of only moderate accuracy due to possibly strong extinction effects. The Hα flux derived by Keel (1983) is by a factor of 30 lower than the one derived by Kennicutt, after adopting the same distance.

Strikingly, the sources B and F both coincide with some of the most Hα luminous H II regions (Sources no.s 27 and 69 with log $F_{\mathrm{H}\alpha}$=$-$12.12 and log $F_{\mathrm{H}\alpha}$=$-$11.99, respectively, in MR92). Depending on the fraction of the central X-ray flux steming from SNRs and superbubbles or from an AGN component, the SFR for the core is of the order of 1 M$_\odot$ yr^{-1}.

5. Conclusions

We have analyzed spatial and spectral data from the barred late-type spiral galaxy NGC 4303 in the soft X-ray regime. Several separate X-ray sources can be observed in the core and disk of the galaxy. The locations of the sources correspond to several H II regions and indicate a concentration of gas at the center and at the ends of the galactic bar, in agreement with numerical simulations of gas dynamics in a barred potential.

The low spatial resolution of the PSPC observation of NGC 4303 does not allow a distinction of several individual X-ray sources within the object. The best fit of the soft X-ray spectrum taking into account the information from the high resolution HRI observation is a combination of a RS component with a temperature of 0.3 keV and a power-law component with a spectral index of 2.6. The total 0.1–2.4 keV X-ray luminosity amounts to 4.7×10^{40} erg s^{-1}, in agreement with other comparable barred galaxies with a nuclear starburst, like e.g. NGC 4569 (Tschöke et al. in preparation). A pure starburst model for the nucleus of NGC 4303 would require a special explanation for the unusually high $L_{\rm X}/L_{\rm H\alpha}$ ratio.

The combination of the flux fraction of the separate sources, the spectral information, and the comparison with the Hα luminosity from the core leads to the following picture: the soft X-ray emission originates from a composition of several distinct emission regions. The central source consists of a low luminous AGN and a circumnuclear starburst. The disk sources are dominated by SNRs and superbubbles in star forming regions preferably at the ends of the bar and along the eastern spiral arm. Several HMXBs may contribute to the X-ray flux.

The disk X-ray sources are coincident with some of the most luminous H II regions in the galaxy. The estimated total SFR from the X-ray flux is 1–2 M$_\odot$ yr^{-1}. Most H II regions are not detectable in the X-ray, like most Hα sources in the eastern boomerang-shaped arm. The enhanced star formation in NGC 4303 may have been caused by some kind of interaction although the H I morphology of the galaxy does not support very strong perturbation. If a dwarf galaxy has fallen in and merged with NGC 4303 in the past, the bar may have been produced with the subsequent triggering of the star formation at the center and in the spiral arms. The accreted dwarf galaxy would be resolved and not directly detectable.

Acknowledgements. The authors are grateful to Dominik Bomans for stimulating discussions, and to Dr. Olga Sil'chenko for her substantial and constructive report. The ROSAT project is supported by the German Bundesministerium für Bildung, Wissenschaft, Forschung und Technologie (BMBF) and the Max-Planck-Society. This research has made use of the NASA/IPAC Extragalactic Database (NED) which is operated by the Jet Propulsion Laboratory, Caltech, under contract with the NASA. Observations made with the NASA/ESA Hubble Space Telescope were used, obtained from data archive at STScI. STScI is operated by the Association of Universities for Research in Astronomy, Inc. (AURA) under the NASA contract NAS 5-26555.

References

Arnaud K.A., 1996, Astronomical Data Analysis Software and Systems V, ASP Conf. Ser. vol. 101, eds. Jacoby G., Barnes J., p. 17
Arsenault R., 1989, A&A 217, 66
Balick B., Heckman T.M., 1982, ARA&A 20, 431
Barnes J.E., Hernquist L.E., 1991, ApJ 370, L65
Beck R., Ehle M., Shoutenkov V., Shukurov A., Sokoloff D., 1999, Nat 397, 324
Benvenuti P., Casini C., Heidmann J., 1979, Nat 282, 272
Bowen D.V., Blades J.C., Pettini M., 1996, ApJ 472, L77
Briel U., Aschenbach B., Hasinger G., et al., 1996, ROSAT User's Handbook (MPE, Garching)
Cayatte V., van Gorkom J.H., Balkowski C., Kotanyi C., 1990, AJ 100, 604
Cioffi D., 1990, in "Physical Processes in Hot Plasmas", NATO ASI Series C, Vol. 305, eds. Brinkmann W., Fabian A.C., Giovanelli F., Kluwer, Dordrecht, p. 1
Colina L., Arribas S., 1999, ApJ 514, 637 (CA99)
Colina L., García-Vargas M.L., Mas-Hesse J.M., Alberdi A., Krabbe A., 1997, ApJ 484, L41
Colina L., Wada K., 2000, ApJ 529, 845
Combes F., 2000, in "Galaxy Dynamics: from the Early Universe to the Present", ASP Conference Series, Vol. 197, eds. Combes F., Mamon G.A., Charmandaris V., p. 15
Condon J.J., 1983, ApJS 53, 459
de Vaucouleurs G., de Vaucouleurs A., Corwin Jr. H.G., et al., 1991, Third Reference Catalogue of Bright Galaxies, Springer Verlag, New York
Dickey J.M., Lockman F.J., 1990, ARA&A 28, 215 (DL90)
Elmegreen D.M., Elmegreen B.G., Bellin A.D., 1990, ApJ 364, 415
Englmaier P., Gerhard O., 1997, MNRAS 287, 57
Fabbiano G., Feigelson E., Zamorani G., 1982, ApJ 256, 397
Ferrarese L., Freedman W.L., Hill R.J., et al., 1996, ApJ 464, 568
Filippenko A.V., Sargent W.L., 1986, in "Structure and Evolution of Active Galactic Nuclei", eds. Giuricin G., Mardirossian F., Mezetti M., Ramella M., Dordrecht: Reidel, p. 21
Forbes D.A., Polehampton E., Stevens I.R., Brodie J.P., Ward M.J., 1999, submitted to MNRAS, *astro-ph/9908048*
Frei Z., Guhathakurta P., Gunn J.E., Tyson J.A., 1996, AJ 111, 174
Friedli D., Martinet L., 1993, A&A 277, 27
Friedli D., Benz W., Kennicutt R., 1994, ApJ 430, L105
Fukuda H., Wada K., Habe A., 1998, MNRAS 295, 463
Guhathakurta P., van Gorkom J.H., Kotanyi C.G., Balkowski C., 1988, AJ 96, 851
Hasinger G., Boese G., Predehl P., et al., 1994, Legacy 4, 40, MPE/OGIP Calibration Memo CAL/ROS/93-015, Version: 1995, May 8
Ho L.C., Filippenko A.V., Sargent W.L.W., 1997, ApJ 487, 591
Hodge P.W., Kennicutt R.C., 1983, AJ 88, 296
Hummel E., van der Hulst J.M., Keel W.C., 1990, A&A 236, 333
Junkes N., Zinnecker H., Hensler G., Dahlem M., Pietsch W., 1995, A&A 294, 8
Keel W.C., 1983, ApJS 52, 229
Kennicutt R.C. 1983, ApJ 272, 54
Kennicutt R.C., Keel W.C., Blaha C.A., 1989, AJ 97, 1022
Koratkar A., Deustua S.E., Heckman T., et al., 1995, ApJ 440, 132
Martin P., Roy J.-R., 1992, ApJ 397, 463 (MR92)
Martin P., Roy J.-R., 1994, ApJ 424, 599
Martinet L., Friedli D., 1997, A&A 323, 363
Mavromatakis F., 1993, A&A 273, 147
Mewe R., Gronenschild E.H.B.M., van den Oord G.H.J., 1985, A&AS 62, 197
Mulchaey J.S., Colbert E., Wilson A.S., et al., 1993, ApJ 414, 144
Noguchi M., 1988, A&A 203, 259

Norman C.A., Ikeuchi S., 1989, ApJ 345, 372
Pérez-Olea D.E., Colina L. 1996, ApJ 468, 191
Raymond J.C., Smith B.W., 1977, ApJS 35, 419
Sellwood J.A., Wilkinson A., 1993, Rep. Prog. Phys. 56, 173
Simkin S.M., Su H.J., Schwarz M.P., 1980, ApJ 237, 404
Suchkov A.A., Balsara D.S., Heckman T.M., Leitherer C., 1994, ApJ 430, 511
Tully R.B., 1988, Nearby Galaxies Catalog, Cambridge University Press, Cambridge
Turner T.J., George I.M., Mushotzky R.F., 1993, ApJ 412, 72
van Dyk S.D., 1992, AJ 103, 1788
Warmels R.H., 1988, A&AS, 72, 427
Watson M.G., 1990, in "Windows on Galaxies", eds. Fabbiano G., Gallagher J.S., Renzini A., Kluwer, Dordrecht, p. 177
Woosley S.E., Weaver T.A., 1985, in "Radiation Hydrodynamics in Stars and Compact Objects", Proc. of the IAU Colloquium No. 89, eds. Mihalas D., Winkler K.-H., p. 91

Chapter 6

A giant outflow of the Virgo cluster galaxy NGC 4569

Submitted to
Astronomy and Astrophysics

A giant outflow of the Virgo cluster galaxy NGC 4569

D. J. Bomans[1], D. Tschöke[2], G. Hensler[2], and A. Boselli[3]

[1] Astronomisches Institut, Ruhr-Universität Bochum, Universitätsstr. 150, D-44780 Bochum, Germany, email: bomans@astro.ruhr-uni-bochum.de
[2] Institut für Theoretische Physik und Astrophysik, Universität Kiel, D-24098 Kiel, Germany, email: hensler,tschoeke@astrophysik.uni-kiel.de
[3] Laboratoire d'Astrophysique de Marseille, BP-8, Traverse du Siphon, F-13376 Marseille Cedex 12, France, email: Alessandro.boselli@astrsp-mrs.fr

Abstract. In this paper we report the detection of a giant region of diffuse Hα emission extending to at least 8.8 kpc above the plane of the nuclear starburst/LINER galaxy NGC 4569. The structure of the emission region strongly resembles that of galactic scale outflows observed in several other nuclear starburst galaxies, but the spatial size of the Hα structure places it at the top of all outflows of local starburst galaxies known today. While the interpretation as outflow is most appealing, we discuss several other aspects which may play a role in forming this giant Hα spur. Most being linked to the nature of NGC 4569 as HI deficient spiral galaxy moving very fast through the hot gas of the Virgo Cluster.

Key words: Galaxies: active – Galaxies: starburst – Galaxies: individual: NGC 4569 – Galaxies: halos

1. Introduction

NGC 4569 (M90) is a bright early-type spiral galaxy of type Sab (Tully 1988) or SAB(rs)ab (Ho et al. 1997) within 2° from the center of the Virgo Cluster at $\alpha(2000)=12^h36^m49^s.8$, $\delta(2000)=+13°09'46''$. It is one of the very few galaxies outside the local group with a negative radial velocity of almost -250 km s^{-1} (Stauffer et al. 1986). Due to its HI properties (see below) NGC 4569 is a certain cluster member and we therefore use a distance of 16.8 Mpc (Tully 1988; H_o=75 km s^{-1} Mpc^{-1}), consistent with the Cepheid distance to the Virgo cluster of 15.9±2 Mpc (Graham et al. 1999), corresponding to an absolute scale of 81 pc arcsec^{-1}.

The galaxy exhibits a bright, extremely compact nucleus in optical and UV bands which has not been resolved by HST observations in the UV (Maoz et al. 1995). This results in an upper limit of 0.05″ or 4 pc for the diameter of the nucleus in the HST F220W filter (Pogge et al. 2000, hereafter: P00). From the optical spectrum it is classified as LINER2 AGN with some doubt because of weak [OI] and [SII] lines (Stauffer 1983, Keel 1983). Of all LINER (low ionization nuclear emission region) galaxies observed with HST, NGC 4569 has the brightest UV nucleus (P00). The UV spectrum is dominated by emission of massive stars (Maoz et al. 1998); an optical investigation by Keel (1996) that compared starburst and AGN features of the nucleus of NGC 4569 explains it as a very compact starburst.

Most interestingly, the HI 21cm emission of NGC 4569 is clearly confined to the central part (Cayatte et al. 1990, hereafter: C90). The HI distribution has a ring-like structure and is located within the high surface brightness part of the optical disk. Since galaxy clusters as the Virgo Cluster are known to be permeated by large amounts of hot intracluster medium (ICM), the observed neutral gas deficiency of spiral galaxies can be attributed to the interaction of the hot ICM with the interstellar medium (ISM) of the galaxies. There are other Virgo Cluster members having similar morphological type as NGC 4569 which also show LINER activity, like NGC 4388 and NGC 4579. NGC 4569's individual line-of-sight velocity with respect to the Virgo Cluster velocity amounts to almost 1250 km s^{-1}, which is very similar to that of NGC 4388. In NGC 4388 two effects were recently detected (Veilleux et al. 1999), namely, a large-scale outflow caused by the nuclear activity, as well as an extended gas halo created from ram-pressure stripping by the ICM.

In this letter we present Hα observations of NGC 4569 that reveal filaments on galactic scales proceeding from the galactic disk of NGC 4569. We discuss the formation and evolution of this prospective giant outflow briefly in the context of the cluster membership of its parent galaxy.

2. Observations and Data Reduction

We observed NGC 4569 with the 1m telescope at Mt. Laguna Observatory (California) in June 1995. Images were taken through a Hα+[NII] narrow band filter (6567/62 Å) and Johnson B and R band filters. The detector was a thinned 2048^2 pixel CCD giving a pixel scale 0.4″ per pixel. All images were reduced and registered using the IRAF data reduction package. The continuum subtracted Hα+[NII] image was produced by subtracting the scaled

R image from the Hα image. Care was taken to match the point spread functions and the optimal scaling factor was determined by minimizing the residuals of the stars in the field of view. The data were flux calibrated by linking our CCD R band image to R band photometry of the background galaxy VPC 1071 (Young & Currie 1998), which is also present in the field. No Johnson R band photometry of NGC 4569 and the neighboring dwarf galaxy IC 3583 is yet available. Using the calibration of the R image we can transfer the calibration to the Hα image due to our knowledge of the scaling factor, as demonstrated by e.g. Golla et al. (1996).

We corrected the observed Hα flux and surface brightness for 30% [NII] contamination, as estimated from the spectral library of Kennicutt (1992). This may be a slight underestimate when dealing with diffuse ionized gas. Since we concentrate on halo emission, corrections for underlying stellar Hα absorption will be negligible. The Galactic foreground extinction to NGC 4569 is $E_{B-V} = 0.046$ (Schlegel et al. 1998), which we applied to correct the Hα fluxes and surface brightnesses used in the analysis.

A second (somewhat less deep) data set of NGC 4569 was take with the OHP 1.2m telescope. The technical details are described in Boselli & Gavazzi (2000).

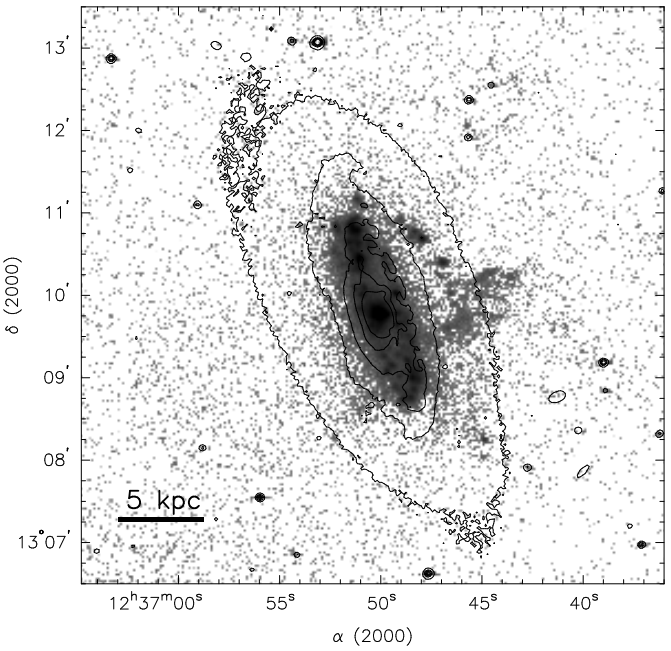

Fig. 1. A 9′ cutout of our Hα image centered on NGC 4569. The broad-band R image is overlayed as contours. Note the large diffuse Hα to the west and the faint broad spur to the south-east of the disk.

3. Morphology and Structural Features

3.1. Disk and nuclear region

The broad band B and R images of NGC 4569 clearly show the low surface brightness outer disk that surrounds the well known high-surface brightness inner disk. The northern part shows a distinct spiral arm, which connects into the higher surface brightness region. In addition to this arm, a faint structureless 'disk' is visible.

The HST Hα image (P00) shows details of the extreme surface brightness peak in the center of the high surface brightness disk. The dominant Hα source in NGC 4569 is its nucleus which appears as a compact, giant HII region. P00 show in their image an arm-like structure or closed loops extending 2″ from the nucleus in nearly north-south direction. Enhancing the contrast compared to Fig.1c in P00 reveals additional spike-like filaments pointing from the edges of the ellipsoidal nucleus to the east and less pronounced to the west. Although this may indicate that the whole central star-forming region experiences an outflow that is confined by chimney-like or conical Hα walls, no further prolongation of Hα structures in the same direction is visible on the HST image.

Fig. 1 shows that the Hα emission is furthermore concentrated to the inner 2.′0 of NGC 4569. A number of emission peaks with their brightest spot at the galactic center are distributed throughout the inner disk, surrounded by a diffuse component. Some fainter diffuse HII gas is present between the HII regions in the high-surface brightness disk. But no large Hα shells and loops are detected within the disk, which may be due to the relatively low spatial resolution of our ground based images.

3.2. The north-western Hα arm

From the northern end of the main Hα body an arm extends to the west consisting of several Hα knots. Comparing the shape of this Hα chain with the broad-band R isophotes in Fig. 1, we conclude that this does not fit to the global spiral-arm structure. A closer look also to the winding of this arm shows that its direction deviates from the elliptical shape of the inclined disk and opens southwards. This leads us to suggest that this outer arm does not belong to the global spiral pattern, but represents an own entity, that is individually bended as the whole. K band data (taken by one of us (AB)) do not unambiguously support the interpretation. Because of the lack of local kinematical and spatial information the direction of this arm relatively to the main galactic body cannot be proven (or disproven) with the current data. We still favor the interpretation as a tidally/ram pressure disturbed feature reaching out of the galactic plane.

3.3. Extended Hα filaments

Diffuse Hα emission is present west of the Hα disk, forming a broad spur. The most prominent feature in the Hα image is the diffuse western filament. It reaches out to a distance of 1.′8 from the major axis and appears to form a coherent structure. With the assumed distance of 16.8

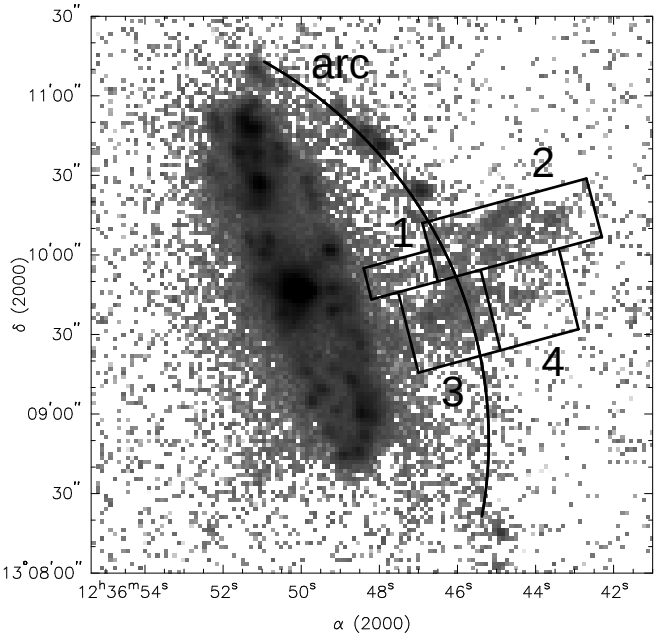

Fig. 2. Continuum subtracted Hα image of NGC 4569: enlarged image of Fig. 1. The different prominent Hα features of the filament are marked by rectangular zones. The north-western Hα arm is marked with curved line.

Mpc this implies a linear size of 8.8 kpc. This feature has been independently confirmed by our other data set. If we take the inclination of the disk ($i = 64°$) into account and assume its direction perpendicular to the disk, this filament may extend up to 9.8 kpc above the galaxy disk. This is the largest known Hα outflow observed in a spiral galaxy so far. The only comparable object is a small isolated Hα filament 11.6 kpc above the starburst galaxy M 82 reported by Devine & Bally (1999) and the Hα outflow of the merger galaxy Arp 220 (Heckman et al. 1990). The north-western arm crosses the Hα filament and is visible as pronounced knots, but can be only vaguely extrapolated through the filament further to the south. In Fig. 2 we subdivide the filament into four regions: Boxes no. 1 and 2 contain parts of the Hα emission which lie on one axis with the nucleus in east-west direction. In the left box (no. 1) a 25″ (2 kpc) long faint spur seems to originate in the galactic center and points toward the large western extension. In box no. 4 a faint Hα loop appears, suggestive for a bubble wall. The brightest part of the whole filament is enclosed in box no. 3. Its morphology looks very complex and seems to be connected with the Hα disk and the crossing Hα arc. The emission also seems to form the basis of the Hα loop in box no. 4.

It is important to note here, that the whole region south of the large Hα filaments shows faint diffuse Hα emission more extended than the high surface brightness disk. There are also several individual spurs discernible extending away from the east side and south side of the Ha disk. All this spurs and filaments can be best understood as signs of large scale disk-halo interaction in NGC 4569.

4. Discussion

Because we are currently lacking detailed spectroscopic data from the Hα filament and especially the large spur, kinematics and ionization structure and, by this, the process that is responsible for this feature is yet uncertain. Therefore, our intention here is to present this extreme case of an extended Hα structure reaching from the main Hα disk of NGC 4569 to a distance of almost 10 kpc and to emphasize its uniqueness. By a simple approach one can start to derive some physical parameters from the observed quantities.

At first, from the measured Hα flux $F_{H\alpha}$ of the filament and its projected size the electron volume density n_e can be determined. If we consider the filament at 3.4 kpc above the messy area near the nucleus, $F_{H\alpha}$ of the whole western filament amounts to 7.1×10^{-13} erg s^{-1} cm^{-2}. For an approximate collective area of $50''\times70''$ and an assumed electron filling factor of unity, the emission measure for the ionized gas amounts to 100 cm^{-6} pc (see e.g. Dettmar 1992). If we adopt a simplified geometry for the 3d filamentary structure, i.e. a cylinder with 50″ (4.1 kpc) in diameter and 70″ in height, i.e. 6.3 kpc long for the given inclination, we derive a volume of 83.7 kpc^3 homogeneously filled with ionized plasma of solar abundances and for an (impact-parameter weighted) averaged thickness a mean n_e of 0.167 cm^{-3}. The total mass of this inclined cylinder then amounts to around 6.25×10^8 M$_\odot$.

Although NGC 4569 is characterized by a central starburst, it is hard for the stellar radiation from the starburst to photoionize this massive filament up to such a distance above the galactic disk.

Seyfert 2 nuclei are featuring gaseous outflows with ionization cones, like e.g. NGC 3281 (Storchi-Bergmann et al. 1992) and Mrk 348 (Simpson et al. 1996). The general interpretation of this high-excitation gas is that partially collimated ionizing radiation escapes from the active nucleus and hits the presumably bipolar outflow. Nevertheless, the conically shaped ionized gas does not exceed an extension of only a few kpc (at most 2 kpc in NGC 3281; Storchi-Bergmann et al. 1992).

Another possible ionization mechanism stems from the cooling radiation of the outflowing superbubble itself. Freyer & Hensler (2000) have recently examined the ionization structure of gas enveloping a hot superbubble and could explain the observed line ratios of the diffuse ionized gas in edge-on spirals under particular conditions. This would mean that the Hα is emitted from an HII shell. In addition, if the outflow is expanding into a gaseous environment, it will produce shock fronts that also emit Hα. Again, spectra are highly needed to test this hypothesis.

Although such large-range expansion of a single superbubble is unheard despite of the extreme starburst in the core of NGC 4569, X-ray observations have recently detected hot halo gas in NGC 4569 (Tschöke et al. 2000) that must be replenished by continuous outflows of hot gas. The X-ray emitting gas is visible to one side of the disk only, to the north-west as the filament, and is directly bordered to the south by the Hα filament suggesting a causal link. The problems for this scenario however are two-fold: First, one has to explain the nuclear Hα spikes to the east in the HST Hα image that are suggestive for a one-sided outflow from the central starburst, while no further extension of this outflow direction exists on galactic scales., which may be due to limited sensitivity of the HST data. Still, large filament appears at the opposite side of the nucleus. Secondly, superbubble models from centrally accumulated supernova explosions have revealed collimated outflows (Suchkov et al. 1994) so that in NGC 4569 the broad and complex Hα morphology requires the action of multiple superbubbles.

One can derive the gravitational energy of the filament from the HI rotation velocity (C90) that is only measured out to 1′ from the center where it reaches almost 180 km s^{-1}. Under the assumption of a static Hα emitting homogeneous cylinder of the derived mass in virial equilibrium one obtains 4×10^{56}ergs. This is nearly equivalent to 4×10^{5} SNII explosions, but gives only a lower energy input that must be exceeded if the filament is still expanding or if work has been executed against an external pressure like the hot gas inside the Virgo Cluster.

For a better understanding of the physical cause one can also study the overall distortions of NGC 4569. As mentioned in sect. 3.1 a slight twist of the Hα disk is discernible. Because of the truncated HI disk, the HI rotation curve (C90) only reflects the innermost disk dynamics that should look regularly since the galaxy's gravitation dominates external influences like tidal effects. Yet minor deviations from regularity can be seen in the northern part (C90) by a steeper and inclined velocity gradient, but needs clarification by higher spatial and velocity resolutions.

Assuming a 3d structure of the Hα chain lying above the disk and of the diffuse Hα filament, also a physical connection between these two features might be possible. But what is the physical mechanism that produces both features? The filament's morphology resembles that of NGC 4388 but is mirrored in east-west direction. Veilleux et al. (1999) have constructed a dynamical model in which ram-pressure stripping by the ICM is responsible for the structures. Compared with NGC 4569, NGC 4388 is located on the opposite direction from the Virgo Cluster core and moves with the same velocity in opposite direction with respect to the cluster velocity. In addition, a possible interaction of NGC 4569 with IC 3583 should not be excluded. This aspect is discussed in detail in the accompanying paper (Tschöke et al. 2000). NGC 4569 also shows a huge radio continuum halo, which may be linked to the outflow described here (Knapik et al. 2000).

Concluding, one has to emphasize the importance of further spectroscopic and desirably multi-wavelength studies of NGC 4569 in order to solve the above raised questions and to provide an insight into the structural and kinematical properties of this most exciting galaxy. NGC 4569 can serve as an ideal laboratory to manifest the mechanisms in detail for the central starburst, its extraordinary outflow and the exceptional features.

Acknowledgements. We are grateful to K. Weis, J. Rossa, and M. Urbanik for helpful comments. This work was partly supported by the *Deutsche Forschungsgemeinschaft* (DFG) under grant no. He 1487/23-1 (D.T.). This paper is partly based on observations taken at the OHP. The OHP is operated by the French CNRS.

References

Binggeli B., Sandage A., Tammann G.A., 1985, AJ 90, 1681
Boselli A., Gavazzi G., 2000, in prep.
Cayatte V., van Gorkom J.H., Balkowski C., Kotanyi C., 1990, AJ 100, 604 (C90)
Dettmar R.-J., 1992, Fund.Cosm.Phys. 15, 143
Devine D., Bally J., 1999, ApJ 510, 197
Freyer T., Hensler G., 2000, in *Stars, Gas, Dust: Exploring the Links*, eds. D.Alloin et al., ASP Conf. Ser., in press
Golla G., Dettmar R.-J., Domgörgen H., 1996, A&A 313, 439
Graham J.A., Ferrarese L., Freedman W.L., et al., 1999, ApJ 516, 626
Heckman T.M., Armus L., Miley G.K., 1990, ApJS 74, 833
Ho L.C., Fillippenko A.V., Sargent W.L, 1997, ApJS 112, 315
Keel W.C., 1983, ApJ 269, 466
Keel W.C., 1996, PASP 108, 917
Kennicutt R.C., 1992, ApJS 79, 255
Knapik J., et al., 2000, in prep.
Maoz D., Filippenko A.V., Ho L.C., et al., 1995, ApJ 440, 91
Maoz D., Koratkar A.P., Shields J.C., et al., 1998, AJ 116, 55
Pogge R.W., Maoz D., Ho L.C., Eracleous M, 2000, ApJ 532, 323 (P00)
Schlegel D.J., Finkbeiner J., Douglas P., Davies M., 1998, ApJ 500, 525
Simpson C., Mulchaey J.S., Wilson A.J., et al., 1996, ApJ 457, L19
Stauffer J.R., 1983, ApJ 264, 14
Stauffer J.R., Kenney J.D., Young J.S., 1986, AJ 91, 1286
Storchi-Bergmann T., Wilson A.S., Baldwin J.A., 1992, ApJ 396, 45
Suchkov A.A., Balsara D.S., Heckman T.M., Leitherer C. 1994, ApJ 430, 511
Tschöke D., Bomans D.J., Hensler G., Junkes N., 2000, A&A, submitted
Tully R.B., 1988, Nearby Galaxies Catalog, Cambridge University Press, Cambridge
Veilleux S., Bland-Hawthorn J., Cecil G., et al., 1999, ApJ 520, 111
Young C.K., Currie M.J., 1998, A&AS 127, 367

Chapter 7

Hot halo gas in the Virgo cluster galaxy NGC 4569

Submitted to
Astronomy and Astrophysics

Hot halo gas in the Virgo cluster galaxy NGC 4569

D. Tschöke[1], D. J. Bomans[2], G. Hensler[1], and N. Junkes[3]

[1] Institut für Theoretische Physik und Astrophysik, Universität Kiel, D-24098 Kiel, Germany
email: tschoeke@astrophysik.uni-kiel.de
[2] Astronomisches Institut, Ruhr-Universität Bochum, Universitätsstr. 150, D-44780 Bochum, Germany

[3] Max-Planck-Institut für Radioastronomie, Auf dem Hügel 69, D-53121 Bonn, Germany

Abstract. We have observed the Virgo cluster spiral NGC 4569 in X-rays with ROSAT (0.1–2.4 keV) and in the optical. From the PSPC image one can distinguish different components, like the dominant source in the nuclear region, the galactic disk, and a diffuse soft component extended to the west. This latter one coincides with a giant Hα structure. In both spectral ranges the structure reaches up to 9 kpc out of the disk. This coincidence, the soft X-ray energy distribution, and the existence of a central starburst in NGC 4569 let us conclude that the X-ray gas traces a large scale outflow from accumulating supernova explosions and stellar winds in the galactic center. The resulting physical properties of this X-ray halo are comparable to those derived from X-ray halos in edge-on galaxies, like e.g. NGC 253. We also discuss the influence of the intracluster medium on the observed X-ray and Hα morphology.

The nature of the very compact core of NGC 4569 is not yet fully understood. Nevertheless, the spectral 0.1–2.4 keV distribution of the central source and the X-ray–to–Hα luminosity ratio favours a supermassive star cluster at the very compact core rather than an accretion-powered active nucleus.

The nearby Magellanic dwarf galaxy IC 3583 at a projected distance of only 30 kpc reveals an unresolved X-ray point source, several blue knots in the optical, and a narrow Hα spur, pointing toward NGC 4569, detected also in the B band image. This is an indication for ongoing star formation also in IC 3583. Some interaction with NGC 4569 will be discussed although the relative radial velocity between both objects of about 1300 km s^{-1} makes it rather unlikely.

Key words: Galaxies: active – Galaxies: starburst – Galaxies: halos – Galaxies: ISM – Galaxies: individual: NGC 4569, IC 3583 – X-rays: galaxies

1. Introduction

Since starburst activities, i.e. short epochs in the life of galaxies with exceedingly high star formation rate (SFR) comared to the averaged one, must have played an important role in the evolutionary course of most galaxies, increasing attention is drawn to understand the different mechanisms that produce such starbursts. In the recent past we have e.g. investigated a number of galaxies with clear attributes of nuclear starbursts: NGC 1808 (Junkes et al. 1995), NGC 2903 (Junkes & Hensler 1996; Tschöke et al. 2001), NGC 4410 (Tschöke et al. 1999), and NGC 4303 (Tschöke et al. 2000). The first two of these objects have so-called hot-spot regions within 1 kpc in the center, which can be identified with tracers of star formation like H II regions in the optical and supernova remnants (SNRs) or superbubbles in the radio regime. The situation for the first two above-mentioned objects in our sample differs from galaxies like NGC 4410, NGC 4303, and NGC 4569 since one cannot simply distinguish between starburst activity in the nuclear region and an active galactic nucleus (AGN) for these three. The close galaxy pair NGC 4410a/b is strongly influenced by their interaction, causing central activity. A major difficulty for this system is the large distance of about 100 Mpc, resulting in resolution problems. But even for the more nearby galaxies NGC 4303 and NGC 4569 the nature of their nuclei leaves open questions. Central starbursts can e.g. be fueled by dissipative gas accumulation in a barred potential (see e.g. NGC 2903, NGC 4303). In addition to the external influence by close encounters, interaction with the cluster gas can obviously enhance the star formation activity.

Hydrodynamical simulations predict large extraplanar X-ray emitting outflows of hot gas from central ands circumnuclear starbursts in giant gas-rich spirals (Suchkov et al. 1994; Strickland et al. 2000). Also AGNs can produce central outflows, but these differ from the former ones in the sense that they are produced by the central accretion mechanism and collimated to jets by magnetic fields. Starburst induced gaseous outflows, also called galactic superwinds, receive their energy from stel-

lar winds of massive young stars and accumulating supernova explosions, driving hot gas into the interstellar medium (ISM). Because of the density stratification in galactic disks the resulting superbubble expands mainly towards the steepest gradient, i.e. perpendicular to the disk. In its "snowplow" phase the bubble sweeps up and shock-heats the ambient ISM. Depending on the strength of the starburst and the fraction of kinetic energy in the outflow, the hot gas breaks out of the dense ISM and propagates into the galactic halo (Norman & Ikeuchi 1989; Heckman et al. 1993). If the cooling timescale takes longer than the dynamical one, the hot gas disperses in the halo and can be observed by X-rays in edge-on galaxies (Dahlem 1997). The low densities and the problem to distinguish between X-rays from above the disk and within it make a detection of X-ray halos around galaxies with intermediate or low inclination very difficult.

As one candidate for an observed X-ray halo at intermediate inclination here we present NGC 4569, a bright early-type spiral galaxy (type Sab; Tully 1988) located within the inner 2° of the Virgo cluster. It is one of the very few galaxies outside the local group with a negative radial velocity (~ -250 km s^{-1}; Stauffer et al. 1986). Its low content of H I gas makes it difficult to determine correctly the distance by using the Tully-Fisher relation. According to Binggeli et al. (1985) and Stauffer et al. (1986) it is classified as cluster member. Hence, in the whole paper we use a distance of 16.8 Mpc (Tully 1988; $H_0 = 75$ km s^{-1}), which is also confirmed by Cepheid distance measurements to the Virgo cluster (Freedman 1996). Thus $1''$ corresponds to 81 pc. NGC 4569 reveals a deficiency of H I gas (Warmels 1988). Neutral hydrogen is only confined to the central few kpc of the disk, which is typical for spirals near the cluster center. The influence of the intracluster medium (ICM) on the H I distribution in cluster spirals has been observed in several galaxy clusters (Virgo: Cayatte et al. 1990,1994; Hercules: Dickey 1997; Coma: Bravo-Alfaro et al. 2000). The high velocity of $\sim$1250 km s^{-1} relative to the Virgo ICM leads to the presumption that NGC 4569 is close to its pericenter in the cluster potential, just passing the center of the Virgo cluster. Consequently, the interaction with the ICM causes the ISM to be removed from the galactic edge by ram pressure stripping (e.g. Balsara et al. 1994). Furthermore, NGC 4569 is located within the observable central X-ray cooling flow of the Virgo cluster (Böhringer et al. 1994). We will discuss the effect of the interaction between the Virgo ICM and NGC 4569 and its consequences on the observed structure in Sect. 5.5.

NGC 4569 exhibits an extremely compact nucleus which has not even been resolved by HST FOC observations in the UV (Maoz et al. 1995), resulting in an upper limit of $0.05''$ or 4 pc for its diameter in the HST F220W filter (Pogge et al. 2000). Optical observations of this unique compact nucleus led to its interpretation as a LINER 2, however, with some doubt because of weak [O I] and [S II] lines (Stauffer 1983; Keel 1983). An optical investigation by Keel (1996) compares starburst and AGN features of the nucleus of NGC 4569 and explains the target as a very compact starburst dominated by supergiant stars. This stellar cluster is as large as the core of 30 Dor, but more than 6 magnitudes brighter. In a LINER sample of HST observations (Pogge et al. 2000) NGC 4569 has the brightest UV nucleus. According to Keel (1996), the interpretation as an AGN is equivocal because of constraints provided by small line widths and dominance of a single photospheric temperature in the optical spectra. In a previous paper we reported the detection of a giant extraplanar Hα feature up to 9 kpc above the disk of NGC 4569 (Bomans et al. 2000). The origin of this structure is not yet fully understood. Ionization of halo gas from a central starburst region has been discussed. Further analysis, regarding the nuclear activity of NGC 4569 and including the X-ray observations, is one of the subjects of this paper. The extension of the Hα disk is much smaller than the stellar component and coincides with the H I distribution, indicating the effect of the ICM on the ISM of NGC 4569. Moreover, several Hα emission knots are located outside the main Hα disk.

Additionally, we discuss optical broad-band and X-ray data from the nearby Magellanic irregular galaxy IC 3583, which is located $\sim 6'$ or in a projected distance of 30 kpc northwest of NGC 4569. Its radial velocity of $+1022$ km s^{-1} (Garcia 1993) places it into the regime of the Virgo cluster, too. The large difference of $\sim$1300 km s^{-1} in radial velocity to NGC 4569 makes a direct connection between both galaxies rather unlikely but cannot be excluded without any doubt. Garcia (1993) classified different galaxy groups in the Virgo cluster according to spherical position and radial velocity, and associates IC 3583 with the NGC 4472 group of galaxies. A lower limit of 14 Mpc for the distance to IC 3583 is derived by Tanvir et al. (1991) from a search for supergiant stars in a high-resolution CCD image of that galaxy. Sandage & Bedke (1985) have included this object as an excellent target in their candidate list for resolving supergiant stars in distant galaxies with the Hubble Space Telescope. Nevertheless, for IC 3583 we also adopt a distance of $d = 16.8$ Mpc according to the Virgo cluster distance (Tully 1988). Some basic parameters of our target galaxies are compiled in Table 1.

The outline of this paper is as follows. In Sect. 2 we present the optical and X-ray data and the reduction process. The results on the optical and X-ray observations are given separately in Sects. 3 and 4. Sect. 5 contains the discussion of the results for nucleus, disk, and halo emission. The paper closes with the conclusions in Sect. 6.

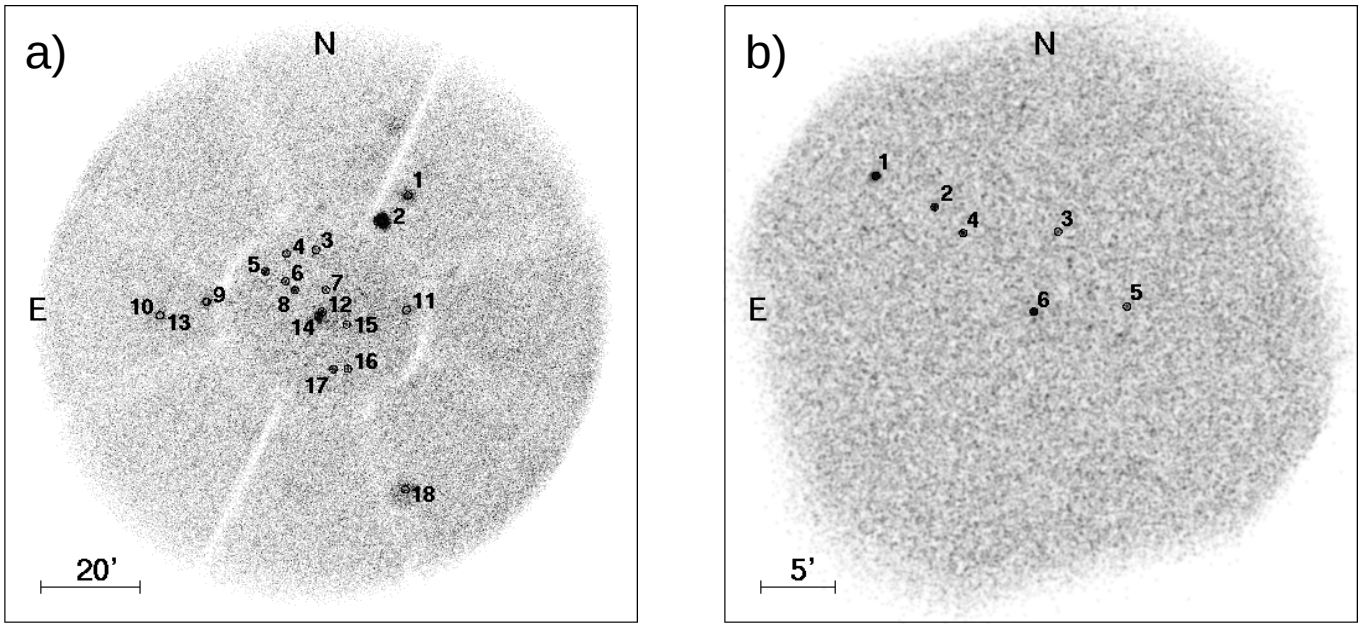

Fig. 1. Field of view from the ROSAT (a) PSPC and (b) HRI pointed observations of NGC 4569. All sources detected with a maximum likelihood threshold of 5σ are plotted. The corresponding labels refer to the source numbers in Tables 3 and 4.

Table 1. NGC 4569 and IC 3583: Some basic parameters.

	NGC 4569	IC 3583	Ref.[a]
alternate name	M 90	UGC 7784	
type	Sab	Irr	1
RA (2000)	$12^h36^m49\overset{s}{.}8$	$12^h36^m43\overset{s}{.}8$	2
Dec (2000)	$+13°09'46''$	$+13°15'30''$	2
radial velocity	-250km s^{-1}	$+1022$ km s^{-1}	3,4
distance	16.8 Mpc	16.8 Mpc	1
D_{25} diameter	$8\overset{'}{.}8$	$2\overset{'}{.}5$	1
axial ratio	0.51	0.64	3
inclination	64°	55°	1
log L_B	10.70	9.20	1
log M_{HI}	9.28	8.73	1

[a] References:
1) Tully (1988)
2) NED database
3) Stauffer et al. (1986)
4) Garcia (1993)

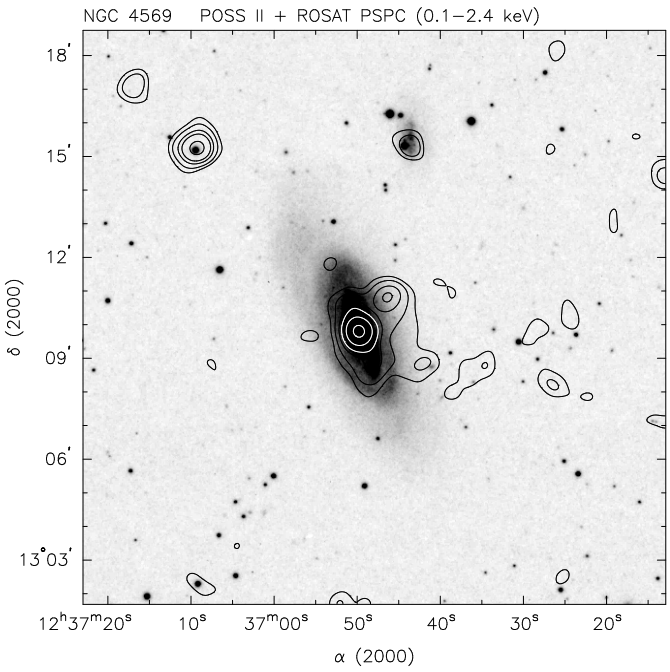

Fig. 2. PSPC observation of NGC 4569 and IC 3583 over an optical $17'\times17'$ POSS II image centered on NGC 4569.

2. Observations and data reduction

2.1. X-ray observations

The field around NGC 4569 was observed with the ROSAT PSPC (central coordinates: RA(2000) = $12^h36^m48\overset{s}{.}0$, Dec(2000) = $+13°10'12''$) with total exposure of 18 ksec and with the HRI (central coordinates: RA(2000) = $12^h36^m48\overset{s}{.}0$, Dec(2000) = $+13°9'36''$) for a total of 24 ksec. For the observation log for both data sets see Table 2.

The observations were analyzed using the EXSAS (Zimmermann et al. 1993), XSPEC (Arnaud 1996) and IDL software packages. All images presented in the following are normalized to values of counts per seconds and pixel. Fig. 2 shows a $17'\times 17'$ POSS II image centered on NGC 4569 overlaid by contours of the central $17'$ of the PSPC field (pixel size of $5''$ and convolved with a Gaussian of $25''$ FWHM). The X-ray images have been corrected for vignetting but not for contributions of the background.

Table 2. ROSAT observations of NGC 4569.

Detector	RA (2000)	Dec (2000)	Time of Obs.	Exposure [s]	No. of OBIs
PSPC	$12^h36^m48^s.0$	$+13°10'12''$	Dec 19 – 21, 1992	17976	14
HRI	$12^h36^m48^s.0$	$+13°09'36''$	Jul 10–11, 1994	2109	1
	$12^h36^m48^s.0$	$+13°09'36''$	Jun 18–21, 1995	21858	10

Table 3. Source detections in the ROSAT PSPC observation of NGC 4569 with a maximum likelihood threshold of 14 (5σ).

No.	RA (2000)	Dec (2000)	Existence likelihood	Count rate (PSPC)[a] [10^{-3} cts s^{-1}]	No. (HRI)	Identification
1	$12^h\ 35^m\ 35^s.7$	$+13°34'43''$	173	29.8±2.1		
2	$12^h\ 35^m\ 57^s.3$	$+13°29'29''$	7237	317±4		BD +14 2519
3	$12^h\ 36^m\ 51^s.8$	$+13°23'34''$	16	3.4±0.7		QSO 1234+136
4	$12^h\ 37^m\ 16^s.2$	$+13°22'43''$	23	4.0±0.8		
5	$12^h\ 37^m\ 33^s.4$	$+13°19'07''$	109	9.0±0.9	1	LBQS 1235+1335
6	$12^h\ 37^m\ 17^s.0$	$+13°17'02''$	35	3.6±0.6	2	
7	$12^h\ 36^m\ 43^s.7$	$+13°15'16''$	40	3.3±0.6	3	IC 3583
8	$12^h\ 37^m\ 09^s.4$	$+13°15'13''$	230	11.2±0.9	4	
9	$12^h\ 38^m\ 22^s.4$	$+13°12'46''$	153	23.1±1.7		QSO 1235+1329
10	$12^h\ 39^m\ 00^s.9$	$+13°10'00''$	53	18.4±2.1		
11	$12^h\ 35^m\ 36^s.9$	$+13°11'05''$	20	9.1±1.4		
12	$12^h\ 36^m\ 46^s.6$	$+13°10'48''$	78	6.0±0.7		NGC 4569[b]
13	$12^h\ 39^m\ 01^s.0$	$+13°09'59''$	58	21.2±2.3		
14	$12^h\ 36^m\ 49^s.9$	$+13°09'46''$	490	20.4±1.2	6	NGC 4569
15	$12^h\ 36^m\ 26^s.5$	$+13°08'10''$	20	2.4±0.5		
16	$12^h\ 36^m\ 25^s.4$	$+12°58'58''$	20	2.9±0.6		
17	$12^h\ 36^m\ 37^s.3$	$+12°58'53''$	40	4.7±0.7		
18	$12^h\ 35^m\ 38^s.0$	$+12°34'00''$	36	26.7±2.5		NGC 4552

[a] background subtracted
[b] probably stellar foreground source, see text

They contain the total X-ray emission in the energy interval of 0.1–2.4 keV. The 5σ sources detected in the PSPC and HRI field of view with a maximum likelihood method are numbered in Fig. 1, and listed in the Tables 3 and 4 together with optical identifications. Source no. 14 in the PSPC image coincides with NGC 4569 while source no. 7 is located at the optical IC 3583. These two sources correspond to no. 6 and no. 3 in the HRI image. Source no. 12 in Fig. 1a near NGC 4569 is probably a stellar foreground source (see Sect. 4.1.1).

The background value in the PSPC image was determined by three circular source-free fields near NGC 4569 with diameter of $164''$, $158''$, and $150''$, respectively. The average background flux amounts to 6.3×10^{-7} cts s^{-1} $arcsec^{-2}$. This value is twice the one given by Böhringer et al. (1994) for the underlying X-ray halo around M87, which however has been fitted to the 0.4–2.4 keV emission, while the background specified here is based on the total ROSAT energy range of 0.1–2.4 keV. The background determination corresponding to the energy band used by Böhringer et al. (1994) results in 2.6×10^{-7} cts s^{-1} $arcsec^{-2}$ for our data, in agreement with the value from the literature. The gradient of the hot ICM is too flat to show significant changes of the background in the direct vicinity of NGC 4569 and IC 3583. Nevertheless, a very slight increase is perceptible at the western edge of the FOV (Fig. 1a) toward M87. The same procedure as for the PSPC data was carried out in the HRI image with the same background fields. The background for the HRI exposure was determined to be 3.5×10^{-7} cts s^{-1} $arcsec^{-2}$.

2.2. Optical imaging

We observed NGC 4569 and IC 3583 with the 1m telescope at Mt. Laguna Observatory (California) in June 1995. Images were taken through a Hα+[N II] narrow band filter and Johnson B and R band filters. The detector was a thinned Tektronics 2048^2 pixel CCD. The resulting field of view of the setup is $13'\times13'$, therefore large enough to contain both NGC 4569 and IC 3583 on one image. The seeing was about $2''$ during the observations. The atmospheric transmission was slightly variable during the observations,

Table 4. Source detections in the ROSAT HRI observation of NGC 4569 with a maximum likelihood threshold of 14 (5σ).

No.	RA (2000)	Dec (2000)	Existence likelihood	Count rate (HRI)[a] [10^{-3} cts s^{-1}]	No. (PSPC)	Identification
1	$12^h\ 37^m\ 33\overset{s}{.}46$	$+13°19'09''$	155	7.8±0.7	5	LBQS 1235+1335
2	$12^h\ 37^m\ 17\overset{s}{.}18$	$+13°17'01''$	55	2.5±0.4	6	
3	$12^h\ 36^m\ 43\overset{s}{.}19$	$+13°15'18''$	14	0.7±0.2	7	IC 3583
4	$12^h\ 37^m\ 09\overset{s}{.}37$	$+13°15'13''$	84	2.4±0.4	8	
5	$12^h\ 36^m\ 24\overset{s}{.}12$	$+13°10'09''$	18	0.7±0.2		
6	$12^h\ 36^m\ 49\overset{s}{.}78$	$+13°09'48''$	162	4.6±0.5	14	NGC 4569

[a] background subtracted

therefore we did not attempt to perform an absolute flux calibration of these data. All images were reduced and registered using the IRAF data reduction package. Particular results from the Hα+[N II] exposure of NGC 4569 are discussed in a separate paper (Bomans et al. 2000).

3. Optical results

In addition to the well known high-surface brightness inner disk, NGC 4569 clearly exhibits a low surface brightness outer disk in the B and R broad band images. The northern part reveals a distinct spiral arm, which connects with the higher surface brightness region. In addition to this arm a faint, structureless 'disk' is visible which seem to be distorted roughly in the direction to IC 3583. We also produced a B-R color image (not displayed) indicating a bluer outer disk compared to the inner region. This may reflect the large dust content or higher metallicity of the inner high-surface brightness disk. In our continuum subtracted Hα+[N II] image (Fig. 1 from Bomans et al. 2000) the extreme confinement of recent star formation to the inner part of the disk and its correspondence with the X-ray emission (Sect. 4.1.1) in extension is striking. In Fig. 3 the Hα+[N II] contours are plotted onto the B and R broad band images of NGC 4569 and IC 3583. A specific attribute of NGC 4569 is the H I 21cm deficiency and that its emission is also confined to the central part (Cayatte et al. 1990). The H I distribution has a ring-like structure and is located within the high surface brightness part of the optical disk. Our optical images clearly reflect a high level of star formation activity concentrated to a relatively small area of the disk of NGC 4569 (about 12 kpc in diameter). A dominant Hα source in the central region of NGC 4569 appears as unresolved giant H II region in our images. Faint diffuse emission is present between the large H II regions in the high-surface brightness disk. The most remarkable structure in the Hα+[N II] image (Fig. 5) is the giant diffuse emission west of the disk, forming a broad spur roughly pointing to the LINER nucleus of NGC 4569. This diffuse emission coincides with an extended X-ray component and may be due to ionized gas above the disk of NGC 4569, tracing a large scale outflow or gaseous halo (see below). It is subject of a more comprehensive discussion in Bomans et al. (2000).

The optical images of IC 3583 reveal that it is a Magellanic irregular galaxy experiencing a phase of high star formation activity. The B and R band images exhibit a number of blue knots coinciding with large H II regions in our Hα+[N II] image. In addition to the bright clumps a faint, more extended light component is present. The centroid of this faint emission is displaced with respect to the star formation regions. The overall color is very blue compared to NGC 4569, not unexpected for a dwarf irregular galaxy. A detailed structural analysis of IC 3583 is hampered by 3 bright stars near and on top of the galaxy body. Some diffuse H II appears to be present between the H II regions, but no large H II shells as present in some other actively star-forming irregular galaxies (e.g. NGC 4449: Hunter & Gallagher 1990; Bomans et al. 1997) could be detected. The most remarkable feature in IC 3583 is a narrow Hα spur at its southern rim pointing toward NGC 4569. Since it is also traceable in the B image but not in the R image, it represents probably a spur of star formation regions and not genuine diffuse H II.

4. X-ray results

4.1. NGC 4569

4.1.1. Spatial analysis

The X-ray emission in the direction of NGC 4569 is clearly extended. From the superposition of the PSPC contours onto the optical B band image of NGC 4569 (Fig. 4a) one can distinguish different components in X-rays. In the following the numbers refer to the division of the X-ray area into different zones and the compilation of the X-ray parameters (Table 5, see also Fig. 6). The maximum of the X-ray emission originates from the nuclear region of the galaxy (area 2), but disk emission is also clearly visible (area 3a and 3b). Additionally, the X-ray

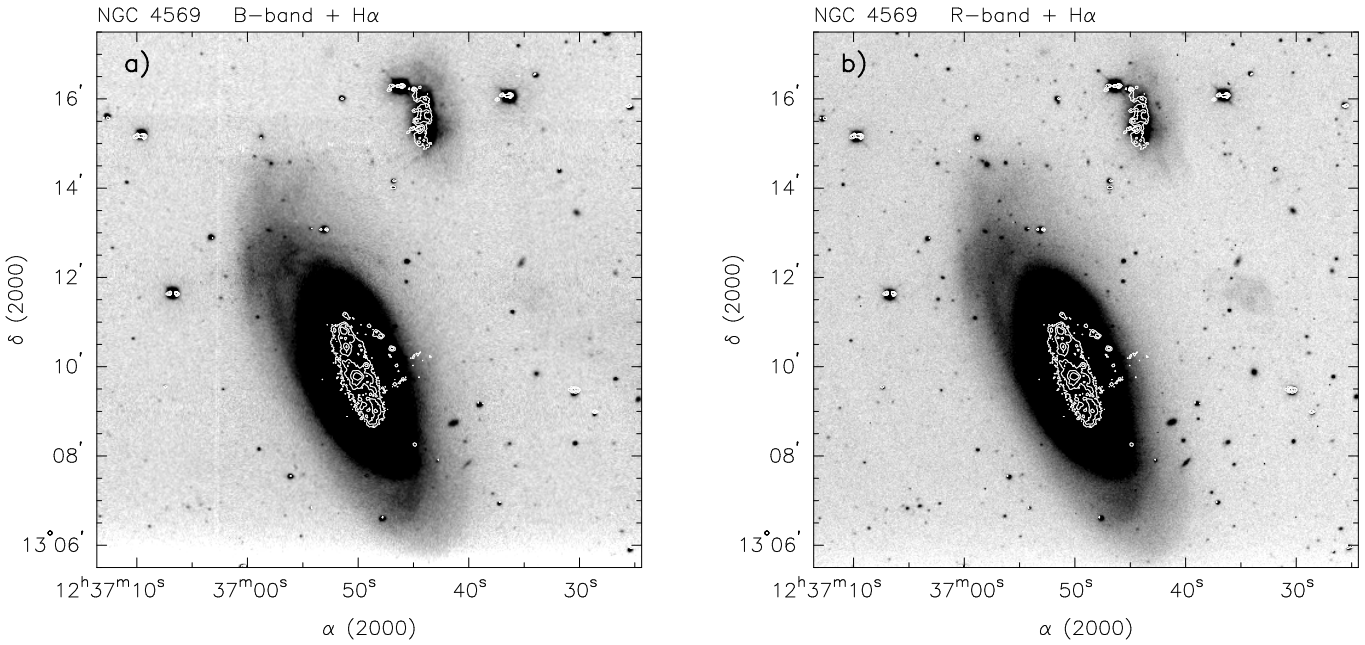

Fig. 3. Hα+[N II] contours over B (a) and R (b) broad band images of NGC 4569 and IC 3583. Contours are (1.2, 3.4, 9.1, 24.8)$\times 10^{-16}$ erg s^{-1} cm^{-2} arcsec^{-2} in logarythmic steps. Hα emission is confined within the inner 6 kpc radius, similar to the H I disk (compare Fig. 17b from Cayatte et al. 1990). Note the faint southern spur in IC 3583 in the B band image pointing toward NGC 4569, not visible in the R band (see also Fig. 8).

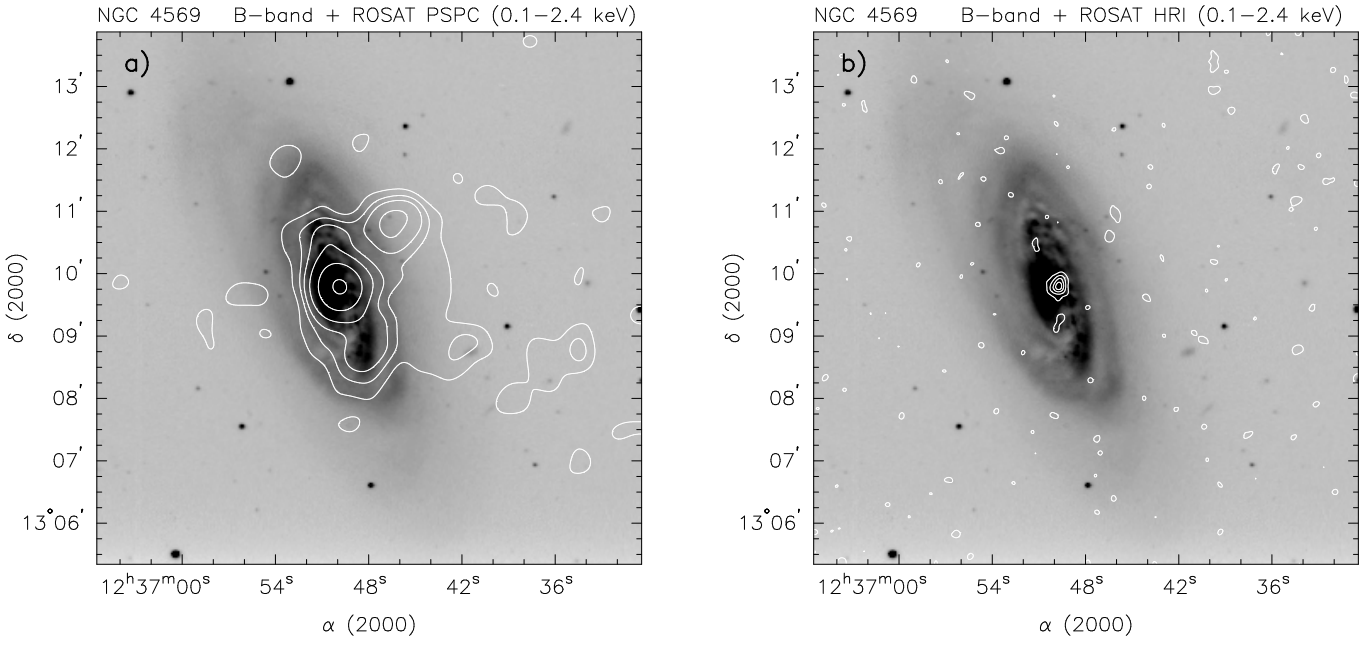

Fig. 4. The central 9′ of the ROSAT observation of NGC 4569 overlaid onto the B band image. (a) The PSPC contours represent 2, 4, 6, 10 , 20 and 40σ above the mean background of 6.5×10^{-7} cts s^{-1} arcsec^{-1}, with $\sigma = 2.0\times10^{-7}$ cts s^{-1} arcsec^{-1}. (b) The HRI contours represent 3, 10 , 20 and 30σ above the mean background of 3.7×10^{-7} cts s^{-1} arcsec^{-1}, with $\sigma = 2.3\times10^{-7}$ cts s^{-1} arcsec^{-1}.

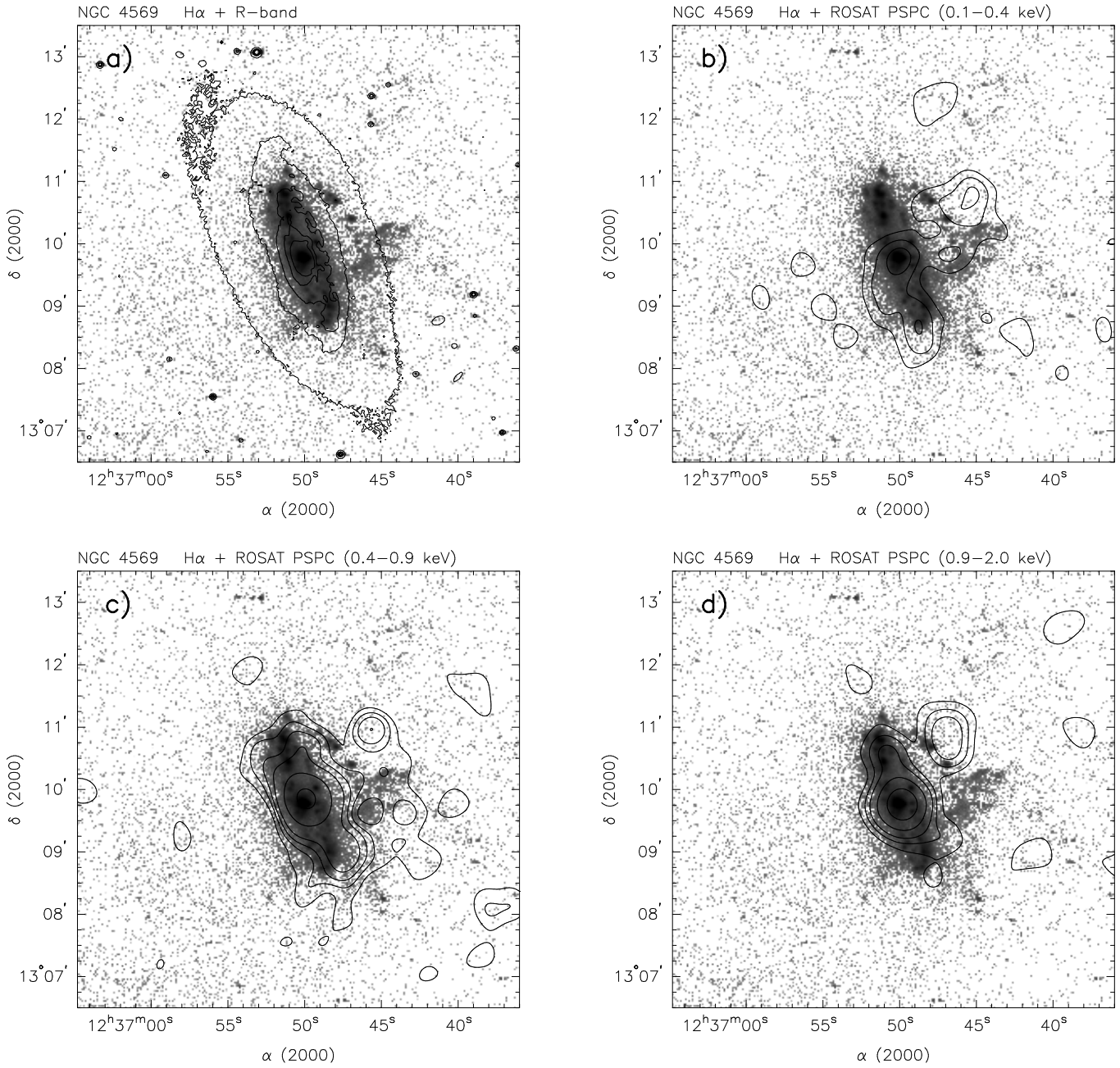

Fig. 5. (a) R band, (b) 0.1–0.4 keV X-ray, (c) 0.5–0.9 keV X-ray, and (d) 0.9–2.0 keV X-ray contours overlaid on an Hα+[N II] image of NGC 4569. The contour levels in the X-ray overlays (b–d) all start at 3σ above the mean background.

disk component fits well with the extension of the H I contours (Cayatte et al. 1990) and the Hα+[N II] emission, whereas the optical disk is much wider extended (Fig. 3). Two nearby X-ray components are probably not directly connected to NGC 4569: The source 2′ northwest of the center (area 4) may be associated with an X-ray source in the stellar disk of NGC 4569, but it is more likely connected to an independent foreground/background source not related to the galaxy. A further source southwest of the center of NGC 4569 (area 5) can be identified as the background galaxy VPC 1071 visible in our B and R band images (Fig. 3). Diffuse X-ray emission most likely in connection with NGC 4569 is found west of the center (area 6) , its soft spectral distribution lets us suggest a hot gas bubble as the source of diffuse emission and indicates its origin from above the disk (see below).

Table 5 compiles count rates and hardness ratios of the different X-ray emission components in the direction of NGC 4569 in comparison to the total area 1. We define the hardness ratio by $HR = \frac{B-A}{B+A}$ with A and B being the counts summed over the 11–41 and 52–201 energy channels, respectively (with a conversion factor E [keV] =

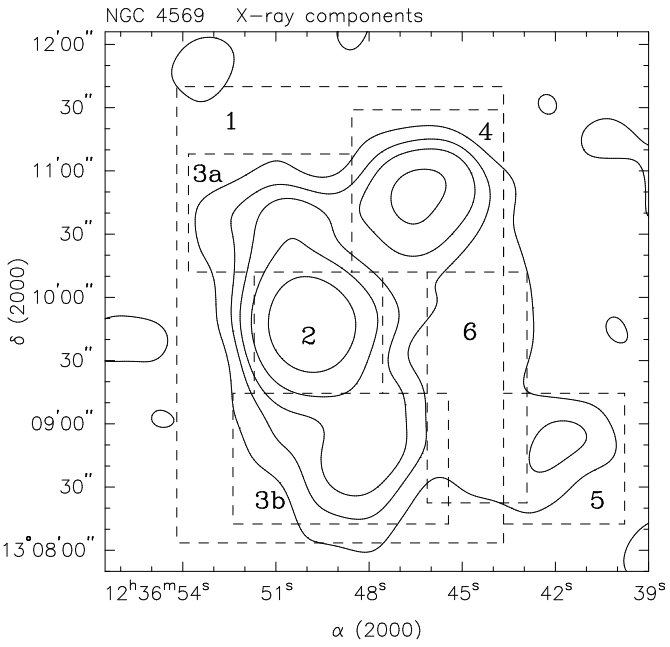

Fig. 6. Definition of disk, bulge, halo, and external source areas in the ROSAT PSPC image. Corresponding count rates and hardness ratios are listed in Table 5.

Table 5. PSPC count rates and hardness ratios of the X-ray components of NGC 4569, as labeled in Fig. 6.

Component	Count rates[a] [cts s^{-1}]	Hardness ratio
1	33.8±1.9	0.51±0.04
1[b]	27.9±1.4	0.56±0.04
2	14.4±0.9	0.77±0.05
3a	3.4±0.6	0.99±0.12
3b	5.3±0.7	0.06±0.10
4	5.8±0.7	0.26±0.09
5	1.9±0.3	0.19±0.15
6	2.7±0.4	0.13±0.13

[a] background subtracted
[b] excluding area 4 (see text)

channel number/100).[1] It is quite obvious that the nuclear emission of NGC 4569 is strongly absorbed (hardness ratio $HR = 0.8$), whereas the contribution from area 6 is much softer. This diffuse emission is of particular interest for the possible existence of an extraplanar X-ray component in NGC 4569 and will be discussed in detail in Sect. 5.3. Another interesting point is the appearance of the northern and southern part of the disk emission of the galaxy. The hardness ratios of both differ significantly. This is corroborated by the comparison of the X-ray emission in different PSPC spectral ranges (Fig. 5): There is no emission in the soft PSPC band (0.1–0.4 keV) visible from the northern disk, whereas it is pronounced in the southern disk.

Although the exposure time of the HRI observation was larger by a factor 1.3 than the one of the PSPC observation, only the nuclear source can be clearly identified, but is unresolved at length scales of 5″ or 400 pc (Fig. 4b). The HRI detector is about 3 times less sensitive than the PSPC detector.

4.1.2. The X-ray spectrum

In Fig. 7 the PSPC spectra of the different components of NGC 4569 as labeled in Fig. 6 and from IC 3583 are given. Whereas the distribution from the entire galaxy contains a significant portion in the lower energy channels below 0.5 keV, which is assumed to be mainly attributed to emission from the southern disk and halo of NGC 4569, the soft spectral part of the nuclear region is significantly absorbed. The corresponding hardness ratios also support this picture ($HR = 0.77\pm0.05$ for area 2) and an overall softer disk and halo component ($HR = 0.56\pm0.04$ for area 1, excluding area 4). The much softer spectrum of the peak emission in area 4 ($HR = 0.26\pm0.09$) points to a foreground location of this source.

As already mentioned area 3a has a much harder spectral distribution compared to area 3b (Table 5). Additionally, the 0.1–2.4 keV X-ray emission from the disk seems to be slightly asymmetric toward the south. We will discuss possible explanations for the difference in the disk components in Sects. 5.2 and 5.5. The very soft component westward of the disk (area 6) is of particular interest and will be considered in Sect. 5.3.

The raw background-subtracted X-ray spectra from the entire galaxy excluding area 4 and from the nucleus are composed by 501±25 and 259±16 counts, respectively. They are fitted with several single component models, like a Raymond-Smith model of a hot thermal plasma (Raymond & Smith 1977: RS), a power-law model (PO), and a thermal Bremsstrahlung model (BS). Additionally, we fit the spectrum of the galaxy by a two-component (RS+PO) model and by a single RS component but with two different fixed abundances (i.e. 0.1 $Z_\odot$ and 1 $Z_\odot$). The resulting parameter combinations are listed in Tables 6 and 7.

The best spectrum fit of the whole NGC 4569 is achieved with a combined RS+PO model for the X-ray emission in the ROSAT band, accounting for contributions from the hot gas in the disk and the halo and from possible central sources, like an AGN, high-mass X-ray binaries (HMXBs), and SNRs in the starburst region and the disk. Since resolution and intensity of the PSPC spectrum are not sufficient to determine the element abundances in the Raymond-Smith plasma directly by fitting, only fixed values are applied to find an appropriate fit. We test models with solar and 0.1 times solar abundances. The best fit for

[1] The definition of HR here is slightly different to the one used by Junkes et al. (1995).

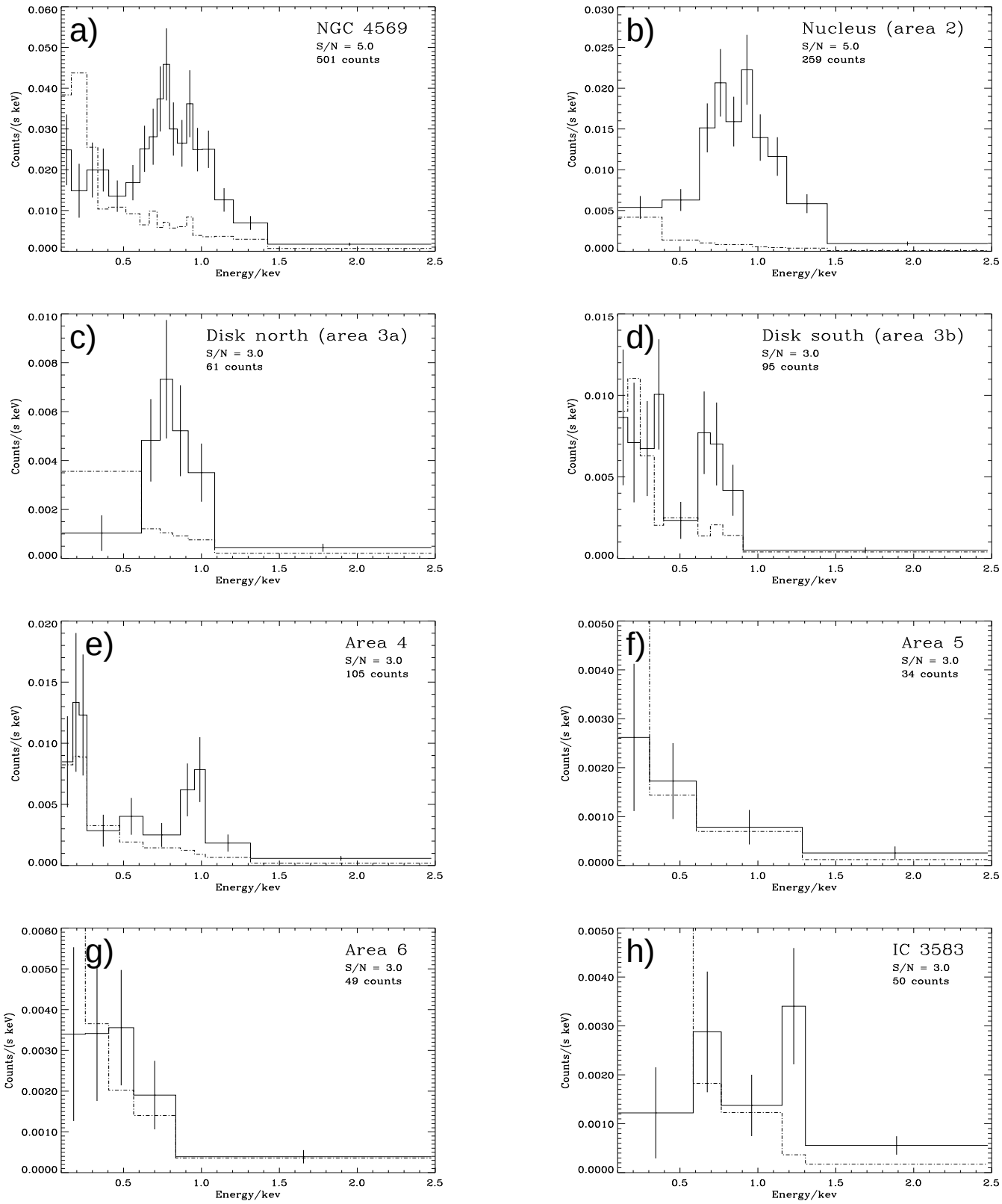

Fig. 7. Background-subtracted ROSAT PSPC spectra of (a) NGC 4569 (area 1 excluding area 4), (b) the nucleus (area 2), (c) the northern disk (area 3a), (d) the southern disk (area 3b), (e) the northwestern point source (area 4), (f) the southwestern source (area 5), (g) the western diffuse component (area 6), and (h) IC 3583 in the energy range of 0.1–2.4 keV. The photons of each spectrum were binned to get a signal-to-noise ratio of 5 for the entire galaxy and the nucleus and 3 for the other sources. In each case the dashed-dotted line represents the contribution of the background.

the nuclear component results in a pure RS model with low metallicity of 0.1 $Z_\odot$. This spectral fit does not support the assumption that the central X-ray emission is dominated by an active non-thermal nuclear source, also indicated by the relatively bad fit with a single PO model.

For all fits to the spectra of nucleus and total galaxy, except the RS model with solar metallicity for the nucleus, the corresponding absorption value lies at least at the Galactic H I column density of 2.47×10^{20} cm^{-2} in the direction of NGC 4569 (Dickey & Lockman 1990) or several times above. From the matching spatial distributions in X-rays and H I an additional inherent absorption in NGC 4569 is expected. H I maps of NGC 4569 (Cayatte et al. 1990) give column densities above 5×10^{20} cm^{-2} (up to 2×10^{21} cm^{-2} in the northern part of the disk component). This, however, would support the single PO model for the nucleus, since this is the only one with an absorption component higher than 10^{21} cm^{-2}.

For the single RS model the resulting X-ray luminosity in the ROSAT band (0.1–2.4 keV) for the total galaxy amounts to 1.3×10^{40} erg s^{-1}. Fits with the two-component RS+PO models yield a 2–3 times higher luminosity of 2.8×10^{40} erg s^{-1} and 4.4×10^{40} erg s^{-1} for subsolar and solar abundances, respectively. The nuclear X-ray luminosity amounts to 8×10^{39} erg s^{-1} for a RS model with low metallicity 0.1 $Z_\odot$ and 1.6×10^{40} erg s^{-1} for a BS model. A single PO model for an AGN in NGC 4569 provides a much higher nuclear luminosity of 6×10^{40} erg s^{-1}, which would at least be expected for a LINER or Seyfert core. However, the worst fit quality seems to rule out this model.

4.2. The nearby irregular dwarf galaxy IC 3583

IC 3583 has been tentatively identified in the *Einstein* observation of NGC 4569 (Fabbiano et al. 1992), however, with a significant position offset. In our ROSAT image of the field, IC 3583 appears as a compact source. In Fig. 8 the contours of the X-ray emission in the energy range 0.1–2.4 keV are overlaid onto the B band and Hα+[N II] image. The compact X-ray source at the position of IC 3583 has been detected by the PSPC with a count rate of $(2.8\pm0.4)\times10^{-3}$ cts s^{-1} and by the HRI with $(5.9\pm1.9)\times10^{-4}$ cts s^{-1}, respectively. It is not possible, however, to spatially distinguish emission from IC 3583 from a foreground star lying exactly on the line of sight to the galaxy. For this reason we also investigate its spectrum. After correction for the background we have a total of 50 ± 8 counts in the 18 ksec exposure. The resulting hardness ratio is 0.95 ± 0.12 which indicates a significant foreground absorption and/or a rather hard X-ray spectrum. This supports the identity of the X-ray source with the irregular galaxy IC 3583 and not to be a foreground star. A 3σ spectrum (i.e. a signal-to-noise ratio of 3 in each bin) results in only 5 bins (Fig. 7h). Fits of standard models (e.g. power law and Raymond-Smith thermal plasma fit) to this spectrum do not result in a good conformity to get any suitable quantitative information.

5. Discussion

5.1. Nuclear activity in NGC 4569

The X-ray emission from the nucleus of NGC 4569 is not spatially resolved by ROSAT, so that an upper limit of ~400 pc can be derived for its total extent from the HRI. From high-resolution optical and UV data the nature of the core of NGC 4569 is equivocal: It consists of a normal bulge population, a supergiant dominated A-type population within a radius of 20 pc, and a very compact, UV-luminous core of less than 2 pc, undetected in the V band. Keel (1996) studied two possibilities for the core: (a) an active accretion-powered nucleus and (b) a compact and very luminous central star cluster, as large as but more than 6 magnitudes brighter than the core of 30 Dor. A possible young starburst would be required as an explanation for the existence of this unusually high number of A supergiants, while the spectral shape, flat in the UV with a steep drop in the optical, is not expected for an AGN.

From the X-ray data two interpretations for the nuclear emission seem possible: X-ray emission from an unresolved compact nuclear source is associated either with the LINER-type nucleus of NGC 4569 in the optical, or with a slightly extended nuclear starburst region, similar to the ones found in NGC 1808 (Junkes et al. 1995), NGC 2903 (Tschöke et al. 2001), and NGC 4303 (Colina & Arribas 1999; Tschöke et al. 2000) at a scale of ~1 kpc. From the optical and radio appearance, however, NGC 1808 and NGC 2903 are rather different: These galaxies are clearly extended in the optical as well as in the radio with several single emission peaks, leading to the classification as hot spot galaxies (Saikia et al. 1990; Sérsic 1973). In contrast, NGC 4303 resembles more NGC 4569 in the sense that both exhibit a compact central source with a diameter clearly below 1″ (Maoz et al. 1995; Colina & Arribas 1999). But contrary to NGC 4569, an additional circumnuclear starburst of several hundred pc in diameter can be resolved in the optical image of NGC 4303. Finally, NGC 2903 and NGC 4303 belong to the class of barred spirals.

The spectrum of the nuclear source in NGC 4569 can well be fitted with a RS spectrum, either contributed by cumulative stellar winds in a central super star cluster (SSC), expanding supernovae of type II (SNe II) bubbles from extinguished massive stars in these SSCs, or a combination of both. With the spectral resolution of the ROSAT PSPC it is not possible to clearly determine the nature of the core emission, whether of thermal or non-thermal origin. The low photon statistics of the central source (10 bins for a 5σ spectrum) does not fully exclude the possibility of

Table 6. Fit results on the X-ray spectrum from NGC 4569 (area 1 excluding area 4).

Model (1)	$N_{\rm H}$ (2)	kT (3)	Γ (4)	Z (5)	Norm (6)	Red. χ^2 (7)	d.o.f. (8)	$F_{\rm X}$ (9)	$L_{\rm X}$ (10)
RS	$2.39^{+0.83}_{-0.57}$	$0.63^{+0.12}_{-0.14}$		0.1	42	1.2	15	$0.37^{+0.01}_{-0.03}$	$1.25^{+0.03}_{-0.10}$
RS	$0.20^{+0.39}_{-0.01}$	$0.63^{+0.16}_{-0.18}$		1	5.8	2.4	15	$0.22^{+0.01}_{-0.03}$	$0.74^{+0.03}_{-0.10}$
BS	$5.79^{+1.06}_{-0.75}$	$0.45^{+0.05}_{-0.06}$			2.1	1.2	15	$0.91^{+0.06}_{-0.10}$	$3.06^{+0.21}_{-0.33}$
PO	$9.39^{+1.33}_{-0.86}$		3.6±0.2		13.1	1.5	15	$5.21^{+2.17}_{-1.47}$	$17.6^{+7.4}_{-5.0}$
RS + PO	$4.91^{+3.21}_{-1.13}$	$0.44^{+0.19}_{-0.12}$	$2.7^{+1.3}_{-2.0}$	0.1	5.3 (PO) 34 (RS)	0.9	13	$0.84^{+3.72}_{-0.42}$ (0.26±0.04)	$2.84^{+12.6}_{-1.42}$ (0.88±0.13)
RS + PO	$5.85^{+0.79}_{-0.71}$	$0.46^{+0.18}_{-0.11}$	3.0±0.4	1	7.4 (PO) 3.3 (RS)	0.9	13	$1.31^{+0.92}_{-0.54}$ $(0.12^{+0.01}_{-0.02})$	$4.42^{+3.10}_{-1.82}$ $(0.41^{+0.03}_{-0.06})$

Col.(1) Spectral models: BS = thermal Bremsstrahlung, RS = Raymond-Smith, PO = power law.
Col. (2) Column density in units of 10^{20} cm^{-2}.
Col. (3) Plasma temperature in units of keV.
Col. (4) Photon index.
Col. (5) Metallicity in units of $Z_\odot$ (fixed).
Col. (6) Scaling factor: for BS in units of $(10^{-18}/(4\pi D^2))\int n_{\rm e} n_{\rm I} {\rm d}V$, $n_{\rm e}, n_{\rm I}$ = electron and ion densities (cm^{-3}); for RS in units of $(10^{-19}/(4\pi D^2))\int n_{\rm e}^2 {\rm d}V$, $n_{\rm e}, n_{\rm H}$ = electron density (cm^{-3}); for PO in units of 10^{-5} photons keV^{-1} cm^{-2} s^{-1} at 1 keV.
Col. (7) Reduced χ^2.
Col. (8) Degrees of freedom.
Col. (9) Unabsorbed X-ray flux in units of 10^{-12} erg cm^{-2} s^{-1}. Values in brackets give the contribution of the thermal component.
Col. (10) X-ray luminosity in units of 10^{40} erg s^{-1}. Values in brackets give the contribution of the thermal component.

Table 7. Fit results on the X-ray spectrum from the nucleus of NGC 4569 (area 2).

Model (1)	$N_{\rm H}$ (2)	kT (3)	Γ (4)	Z (5)	Norm (6)	Red. χ^2 (7)	d.o.f. (8)	$F_{\rm X}$ (9)	$L_{\rm X}$ (10)
RS	$4.10^{+1.54}_{-0.91}$	$0.77^{+0.11}_{-0.13}$		0.1	27	0.5	7	0.24±0.01	0.81±0.03
RS	$1.21^{+0.53}_{-0.37}$	$0.84^{+0.04}_{-0.05}$		1	4.9	1.7	7	$0.15^{+0.02}_{-0.01}$	$0.52^{+0.05}_{-0.04}$
BS	$7.41^{+2.09}_{-1.29}$	$0.56^{+0.10}_{-0.08}$			9.4	1.5	7	$0.46^{+0.05}_{-0.04}$	$1.56^{+0.17}_{-0.15}$
PO	10.5±2.0		$3.2^{+0.3}_{-0.4}$		8.6	2.4	7	$1.8^{+1.1}_{-0.8}$	$6.0^{+3.8}_{-2.6}$

Col.(1) Spectral models: BS = thermal Bremsstrahlung, RS = Raymond-Smith, PO = power law.
Col. (2) Column density in units of 10^{20} cm^{-2}.
Col. (3) Plasma temperature in units of keV.
Col. (4) Photon index.
Col. (5) Metallicity in units of $Z_\odot$.
Col. (6) Scaling factor: for BS in units of $(10^{-19}/(4\pi D^2))\int n_{\rm e} n_{\rm I} {\rm d}V$, $n_{\rm e}, n_{\rm I}$ = electron and ion densities (cm^{-3}); for RS in units of $(10^{-19}/(4\pi D^2))\int n_{\rm e}^2 {\rm d}V$, $n_{\rm e}, n_{\rm H}$ = electron density (cm^{-3}); for PO in units of 10^{-5} photons keV^{-1} cm^{-2} s^{-1} at 1 keV.
Col. (7) Reduced χ^2.
Col. (8) Degrees of freedom.
Col. (9) Unabsorbed X-ray flux in units of 10^{-12} erg cm^{-2} s^{-1}.
Col. (10) X-ray luminosity in units of 10^{40} erg s^{-1}.

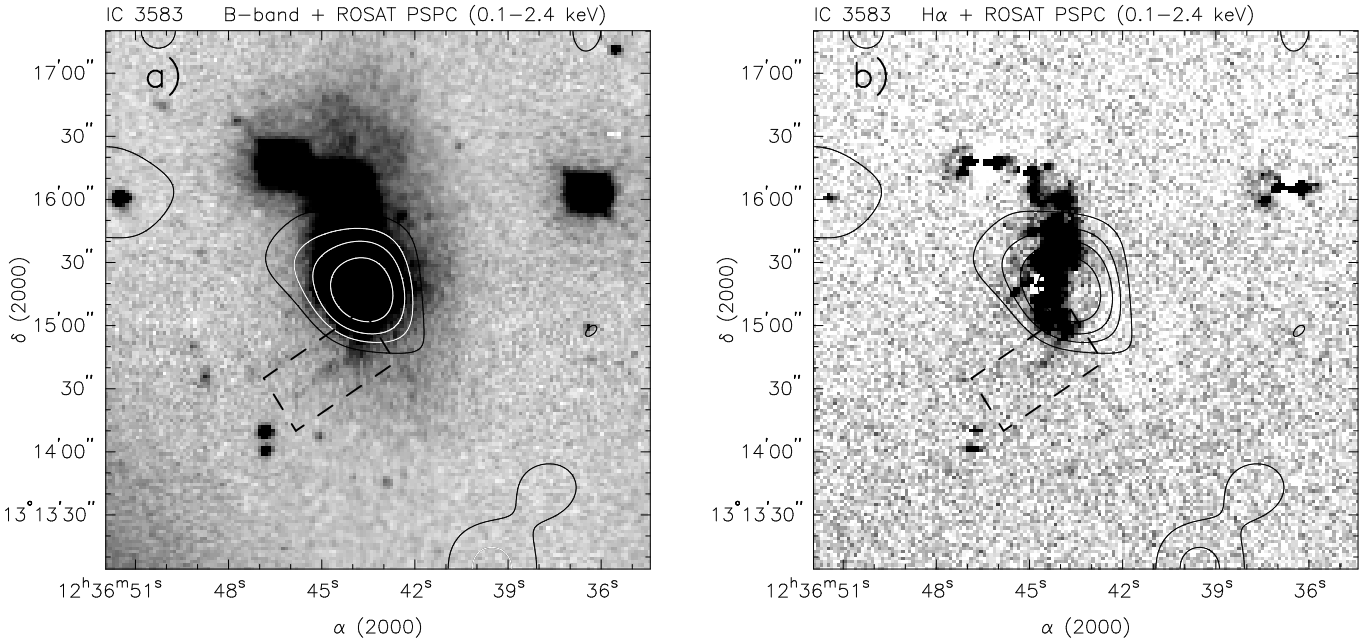

Fig. 8. ROSAT PSPC contours in a $4' \times 4'$ around IC 3583 overlaid onto the (a) B band and (b) Hα+[N II] image. The X-ray contours are 3, 5, 7, and 10 σ above the mean background of 5.3×10^{-7} cts s^{-1} arcsec^{-1} ($\sigma = 1 \times 10^{-7}$ cts s^{-1} arcsec^{-1}). A narrow Hα spur is visible at the southern end of IC 3583, also weakly traceable in the B band, pointing toward NGC 4569. The spur is marked by the dashed box in each image.

an AGN component with a spectral distribution described by a PO fit.

The total X-ray luminosity of 1–4$\times 10^{40}$ erg s^{-1} (depending on the applied model) is not too high to be explained solely by strong star-forming activity in NGC 4569. From our analysis, we can interpret the spectrum of the total X-ray emission from NGC 4569 in two possible ways: At first, the soft X-ray emission contains contributions from two components - a hot thermal plasma (RS) from the starburst as well as a PO component which can either be attributed to an unresolved AGN component or to HMXBs and SNRs in a compact nuclear starburst. Secondly, the central X-ray source is dominated by a very compact luminous central SSC, described by a RS plasma model in the ROSAT energy band.

Further evidence against an AGN-dominated nucleus in NGC 4569 arises from the X-ray to Hα luminosity ratio. For AGNs this ratio is up to 100 times higher than for pure nuclear starbursts. With an Hα flux of 9.4×10^{40} erg s^{-1} for NGC 4569 (Kennicutt et al. 1994) we derive $\log(L_X/L_{H\alpha}) = -1.1$ to -0.3, consistent with other starburst galaxies, like NGC 1069 or NGC 1097 (Pérez-Olea & Colina 1996). Typical AGNs have values of more than -0.2.

5.2. Disk emission

The total disk emission in X-rays from either side (NE vs. SW) is comparable, their distributions throughout the ROSAT band, however, differ significantly. The contribution from the northern part is clearly harder (Table 5). This may be caused by a higher fraction of hard point sources, like HMXBs and SNRs, and less contribution from soft diffuse X-ray emission compared to the southern region. A higher intrinsic absorption of the southern disk is also likely to cause the observed properties. However, in the northern part the H I column density reaches 2×10^{21} cm^{-2} (Cayatte et al. 1990), while its southern maximum is at 1.5×10^{21} cm^{-2}. A third possibility takes into account the interaction with the Virgo ICM; this would mean that the southern soft component is a result from the central starburst, as supposed for the western soft X-rays (Sect. 5.3), and experiences a strong impact from the surrounding hot ICM. This interpretation will be discussed in a more complete framework for the entire galaxy in Sect. 5.5.

5.3. Contribution from the halo

NGC 4569 has an inclination of $i \approx 64°$. The galaxy shows extended soft X-ray emission with contributions from outside the nucleus and outside the disk. In contrast to edge-on galaxies, where emission components from disk and halo can be quite easily distinguished (e.g. Vogler et al. 1996), it is more difficult to disentangle these components in the case of NGC 4569. Additional difficulties arise from the nearby two foreground/background sources, northwest and southwest of the nucleus.

The overall distribution of the soft X-ray emission appears to be very asymmetric with a spur of soft emission extending from the galaxy center and some additional diffuse patches both west of the galaxy. We mark a rectangle area of $50''\times100''$ (Fig. 6, area 6) taking care to avoid any contamination by area 4. The expected halo emission in area 6 becomes mainly polluted by the closer and brighter northwestern source. To check its effect on the X-ray flux in area 6 we subtract a point source from the original image. Therefore we fit a Gaussian to the nucleus of NGC 4569 (resulting FWHM $22''$) and normalize it with the peak emission of the source in area 4. From the residual image we get a reduction of the count rate in area 6 by 14%. We derive a hardness ratio of 0.13 ± 0.13 for this area which strongly depends on the choice of the area coverage. Contamination from the much harder nuclear emission increases the hardness ratio, if we shift the eastern edge of area 6 closer toward area 2. The total number of counts in the area 6 with boundaries as defined in Fig. 6 is 49 ± 7 after background subtraction. If we apply a RS model with strongly constraint parameters, i.e. assuming a reasonable column density value of $N_{\rm H}=3\times10^{20}$ cm^{-2} (Galactic foreground value; H I observations from Cayatte et al. (1990) give $N_{\rm H}$ values below 5×10^{20} cm^{-2} in the relevant halo region) and solar abundances, we obtain a plasma temperature of about 0.2 keV, resulting in a flux of 2.4×10^{-14} erg s^{-1} cm^{-2} in the ROSAT band and an X-ray luminosity of 8×10^{38} erg s^{-1}. Even abundances of 0.1 $Z_\odot$ do not alter the result significantly. If we take $HR = 0.39$ as an upper limit for the hardness ratio, a corresponding RS spectrum with a column density of 3×10^{20} cm^{-2} would have a temperature of 0.24 keV. A column density of 5×10^{20} cm^{-2} would drop the temperature to 0.19 keV. With a lower hardness ratio of 0.13 and a column density of 3×10^{20} cm^{-2} we again get a plasma temperature of 0.2 keV. Again, an increase of the absorption component will decrease the corresponding temperature for the observed spectral distribution. Hence, for the X-ray emission from area 6 we deduce a low plasma temperature of approximately 0.2 keV, similar to NGC 4449 (Bomans et al. 1997) or NGC 1705 (Hensler et al. 1998).

An additional strong argument in favour of diffuse X-ray emission in the halo of NGC 4569 arises from the good spatial connection of the soft (0.1–0.4 keV) X-ray emission with a large diffuse Hα spur (Fig. 5; Bomans et al. 2000). Similar correlations were observed in a number of nearby starburst galaxies (e.g. M82: Strickland et al. 1997; NGC 253: Shopbell & Bland-Hawthorn 1998; Lehnert et al. 1999; Strickland et al. 2000; NGC 3628: Dahlem et al. 1996; NGC 4666: Dahlem et al. 1997) and are interpreted as a signature for hot gas outflow from the starburst center. Our optical and X-ray data are fully consistent with such an interpretation in the case of NGC 4569.

5.4. Physical properties of the hot halo

In general, three different morphologies for a hot gaseous halo are possible, depending on the types of outflow mechanisms from the galactic disk: (a) If the star formation takes place in a compact central starburst, a conical outflow of gas occurs, driven by stellar winds of massive stars and SN II explosions. A similar morphology arises from an AGN producing a jet, which heats up the halo gas. (b) If the star formation is distributed over large parts of the galactic disk, several distinct star-forming regions blow out hot gas into a more extended region around the disk. (c) Another possibility is a mixture of these two morphological cases.

If we assume a simplified geometry of an outflow from a central starburst for the diffuse X-ray gas in area 6 (a cylindric shape with a height of 6 kpc and a diameter of 4 kpc, and therefore a volume V of 8×10^{10} pc^3), we can estimate the mean electron density of the gas. Applying solar abundances, the derived plasma temperature of 0.2 keV is consistent with an emissivity $\Lambda_{\rm R}(T)$ of 2.5×10^{-23} erg cm^3 s^{-1} in the energy range of 0.1–2.4 keV. This value is most sensitive to the chosen metallicity; for 0.3 times solar abundances it is about 1×10^{-23} erg cm^3 s^{-1}. With $L_{\rm X} = n_{\rm e}^2\,\Lambda_{\rm R}(T)\,V$ we derive a mean electron density of $n_e \approx 4\times10^{-3}\,f^{-1/2}$ cm^{-3}, with f being the volume filling factor of the halo gas. The total mass of the hot gas is then $M \approx 7\times10^6\,f^{1/2}$ M$_\odot$, and the total thermal energy is $E_{\rm th} \approx 4\times10^{54}\,f^{1/2}$ erg. Pressure $P = 2nkT$ and cooling time $\tau_{\rm cool} = 3kT/n\Lambda$ amount to $3\times10^{-12}\,f^{-1/2}$ dyn cm^{-2} and $3\times10^8\,f^{1/2}$ yr, respectively. A compilation of the physical properties of the halo of NGC 4569 and a few other observed X-ray halos for comparison are given in Table 8. The X-ray halo of NGC 4569 is in extension, luminosity, mass, and density quite similar to the one of NGC 253. Both galaxies reveal a few times lower X-ray luminosity, at most 10^{39} erg s^{-1}, while other X-ray halos have luminosities of several times 10^{39} erg s^{-1}. The electron densities of NGC 4569 and NGC 253 are also somewhat lower compared to the other galaxies. The two irregular galaxies M82 and NGC 4449 may not directly be comparable to the rest of the sample because of their different morphology, metallicity, and mass.

Applying the model for a single SNR by Cioffi (1990) and taking into account the cumulative radiation of a number of SNRs in a star-forming region (Norman & Ikeuchi 1989), we can estimate the SFR from the observed X-ray emission of disk and bulge in NGC 4569 (Junkes et al. 1995). A SNR expanding into an ISM with a mean density of 1 cm^{-3} radiates a total energy of 4.7×10^{49} erg in the ROSAT energy band for about 10^4 yr.

With a total X-ray luminosity of 1.8×10^{40} erg s^{-1} from disk and bulge we derive a number of 120 SNRs and a SN II rate of 0.012 yr^{-1}. With a Salpeter IMF, between 1 M$_\odot$ and 100 M$_\odot$ and all stars with masses above 8 M$_\odot$ evolving to SNe II, we derive a SFR of 1.6 M$_\odot$ yr^{-1} for

Table 8. Properties of a number of observed X-ray halos.

	kT (1)	L_X (2)	n_e (3)	M (4)	τ_{cool} (5)	h (6)	Ref. (7)
M82	0.4–0.6	1.9×10^{40}	0.02	1.3×10^{8}	1×10^{8}	6	1
NGC 4449	0.2	7×10^{38}	0.03	2×10^{6}	2×10^{7}	1.8	2
NGC 253	0.2	1.6×10^{39}	2×10^{-3}	5×10^{6}	2×10^{8}	10	3, 4
NGC 3079	0.3	5.8×10^{39}	7×10^{-4}	2×10^{8}	1.5×10^{9}	13.5	5
NGC 3628	0.16	6.7×10^{39}	6×10^{-4}	4×10^{8}	3.8×10^{8}	15/25	6
NGC 4565	0.17	2.6×10^{39}	6×10^{-4}	2.2×10^{7}	4.2×10^{8}	13	7
NGC 4569	0.2	8×10^{38}	4×10^{-3}	7×10^{6}	3×10^{8}	9	8

Col. (1) — Plasma temperature in units of keV.
Col. (2) — X-ray luminosity (0.1–2.4 keV) in units of erg s^{-1}.
Col. (3) — Mean electron density in units of cm^{-3}.
Col. (4) — Mass in units of $M_\odot$.
Col. (5) — Cooling time scale in units of yr.
Col. (6) — Maximal extension in z-direction above galactic disk in units of kpc. The two values for NGC 3628 are for the northern and southern halo.
Col. (7) — References: 1) Strickland et al. (1997); 2) Bomans et al. (1997); 3) Pietsch (1993); 4) Dahlem et al. (1998); 5) Pietsch et al. (1998); 6) Dahlem et al. (1996); 7) Vogler et al. (1996); 8) this work.

NGC 4569. According to Thronson & Telesco (1986) we can estimate the SFR from the far-infrared luminosity[2] $L_{FIR} = 5.64\times10^{9}$ $L_\odot$ (Rice et al. 1988), which results in 3.7 $M_\odot$ yr^{-1}, about 2 times higher than the result from the X-ray luminosity.

A more extended spherical X-ray halo cannot be excluded with absolute certainty. As can be seen in Figs. 4 and 5 the soft diffuse X-ray emission outside the galactic disk of NGC 4569 is only visible in the western part. This might imply that the outflow from the starburst core takes place asymmetrically to only one side of the disk. This can happen if the starburst cluster is not located exactly in the equatorial plane so that the direction of lower density is preferred (Suchkov et al. 1994). Another possibility is that emission from an existing eastern X-ray halo component in NGC 4569 is fully absorbed because the eastern side of the disk is lying in front of the halo. The coincidence of the Hα disk sources and the X-ray disk emission indicates ongoing star formation throughout the galactic disk up to radii of about 6 kpc. The extension of the western X-ray halo component to the north and south can be hardly determined because of the two X-ray sources in the areas 4 and 5. Assuming a spherical X-ray halo around NGC 4569 with a radius of 6 kpc and an X-ray luminosity of $L_X \approx 10^{39}$ erg s^{-1} cm^{-2} would decrease the electron density to $1\times10^{-3}\,f^{-1/2}$ cm^{-3}, and enlarge the thermal energy to 5×10^{55} erg, so that the cooling timescale increases to 1.3×10^{9} yr. The total halo mass then amounts to $2.7\times10^{7}\,f^{1/2}$ $M_\odot$ due to the much higher halo gas volume of 900 kpc^3.

[2] Value adapted for the distance of 16.8 Mpc.

5.5. Interaction with the ICM in the Virgo cluster and with IC 3583

The morphology of the X-rays in NGC 4569 still leaves several questions open. For example, the distribution in the 0.5–0.9 keV range (Fig. 5c) is quite symmetrical in the disk, whereas the 0.1–0.4 keV image leads to a contrary picture: The northern part of the disk does not appear in X-rays, while in the south extended emission is present. This asymmetry has been mentioned above with explanations to be caused by differences in absorption strength or different unresolved X-ray sources. Now, we want to discuss an alternative interpretation.

The high radial velocity of NGC 4569 relative to the Virgo cluster and the close projected distance of 1°.7 toward M87 suggest that the influence from the ICM on the morphology of the gas content in the galaxy is of importance. Taking 1000 km s^{-1} for the mean radial velocity of the Virgo cluster (Yasuda et al. 1997), NGC 4569 has a relative radial velocity component of about 1250 km s^{-1} to the cluster. Numerical models of the interaction between galactic ISM and the ICM lead to the result that significant removal of ISM gas from a galaxy penetrating through a cluster medium happens not before the galaxy has already passed its pericenter (Vollmer etal. 2000). On the other hand, the high relative velocity of NGC 4569 to Virgo might indicate a location close to this pericenter. From this fact in combination with the low amount of H I gas in the outer parts of the galaxy it seems conclusive that NGC 4569 is not on its first passage through the cluster. Furthermore it penetrates the ICM supersonically. A sound speed of $c_s \approx 500$ km s^{-1} (Veilleux et al. 1999) for the ICM leads to a Mach number of $M = v/c_s \approx 2.5$. The galaxy and any large-scale outflow from the disk are

exposed to the strong ram pressure from the ICM. Hence, the spatial orientation of the disk becomes important.

Let us assume that the disk of NGC 4569 is orientated with its western edge in front. Looking from east onto the disk is also consistent with the HST Hα observations of the core by Pogge et al. (2000): With enhanced contrast spike-like features are discernible in their Fig. 1c, mainly pointing from the center toward the east. Let us furthermore assume that a bipolar outflow of hot gas from the central starburst occurs in NGC 4569. How can we interpret the 0.1–0.4 keV image in that context? Firstly, the western soft component represents the outflow at the far side of the disk away from the observer. Since the H I is concentrated mainly at the center of the galaxy (confirm Fig. 17b from Cayatte et al. 1990) the radial extension of the X-ray feature is large enough not to be reduced by the H I disk. But where is the component expanding toward the observer? Such a feature would have to be present on the eastern side of the disk. This part of the galaxy faces the ICM stream, while NGC 4569 drifts through the cluster. So the outflow to that side experiences most of the ram pressure. Looking again at Fig. 5b and comparing it with Fig. 5c, one can recognize that the southern soft part does not coincide with the disk. The contours have a bow shape from the galactic center toward the southeast and then bend to the south. At least the emission has a larger extension from the major axis toward the east than in the 0.5–0.9 keV range. From this one can draw the picture that we are actually seeing the eastern part of the bipolar outflow, expanding toward the observer, but hit by the ICM and deformed toward the south. This implies that the eastern outflow is directly compressed and stripped what means, on the other hand, that the motion of NGC 4569 has a small tangential component roughly in northeastern direction. On the other hand, the western component is shielded by the bow shock from the supersonic motion of the galaxy. Such a protecting phenomenon has been discussed by Veilleux et al. (1999) for another Virgo cluster galaxy, NGC 4388, which shows a large-scale ionization cone in Hα from the central Seyfert nucleus. This object has roughly the same high relative velocity to the cluster gas as NGC 4569. Veilleux et al. (1999) argue by the formation of a bow shock, separating the high velocity ICM gas from the slowed-down post-shock gas, with the outflow feature lying in the lee site of the galaxy. The opening angle of the bow shock is determined by the Mach number.

The interaction of NGC 4569 with the ICM could also provide an explanation for the chain of Hα knots west of the main Hα disk emission with its shape diverging from the disk ellipticity. In this context it is interpreted as been stripped off by ram pressure from the northern edge and possibly falling back onto the disk after crossing the bow shock. Hydrodynamical simulations lean support of this scenario. Also diffuse emission is visible at the eastern edge of the main Hα disk. A broad feature lies at the south of the disk, coinciding partly with the southern extended soft X-ray feature. The complex structure of the overall Hα+[N II] in NGC 4569 has been discussed in Bomans et al. (2000).

The low number of X-ray counts from IC 3583 does not allow a reliable prediction for the nature of the X-ray source in this object. However, the faint southern Hα spur, also traceable in the B band but not in the R band, which therefore may not stem from diffuse H II, indicates ongoing star formation activity. The projected distance of 6′ from NGC 4569 leads to the question as to what extent any interaction between the two objects occurs . One important argument against any perturbation effect is their high relative radial velocity of 1300 km s^{-1}. This also makes any detection of connecting features in H I very difficult, since the velocity range is too large to be covered by the dynamical range of H I images. In addition, a H I bridge with a continuous brightness and velocity distribution from NGC 4569 to IC 3583 is very unlikely. A fast passage and the resulting temporary perturbation of the gravitational potential from NGC 4569 may have some influence on the gas component in IC 3583 and may trigger shock-induced star formation. Any such feature would be expected to show a structure perpendicular to the relative motion of both galaxies. As argued above the main motion of NGC 4569 is expected to be toward the observer. With 1022 km s^{-1} IC 3583 has a radial velocity close to the mean Virgo cluster radial velocity. Thus a major tangential component in its motion can not be excluded. Although no strong tidal feature has been detected in IC 3583 and NGC 4569, some minor distortion like the faint Hα spur may be caused by some weak interaction.

6. Conclusions

We have observed the Virgo cluster spiral NGC 4569 and the nearby Magellanic-type irregular galaxy IC 3583 in the optical R and B broad band, in Hα+[N II], and in the 0.1–2.4 keV energy band. From the X-ray results the nature of the very compact core of NGC 4569 still remains unsolved, whether it is a very compact nuclear SSC or an accretion-powered AGN. Yet several facts support a central starburst: The spectral distribution of the nuclear X-ray source favours a thermal plasma emission rather than an AGN-typical power law. The resulting X-ray to Hα luminosity ratio of $\log(L_{\rm X}/L_{\rm H\alpha}) = -1.1$ to -0.3 is typical for galaxies with a central starburst and much too low for LINER or Seyfert galaxies. On the other hand, the much higher X-ray luminosity of 1.8×10^{41} erg s^{-1} for a single power-law model results in an X-ray–to–Hα ratio consistent with other LINERS or Seyferts. Nevertheless, this model is not reasonable for the whole extended X-ray emission in NGC 4569. Also, the extension of the observed diffuse western soft X-ray component reveals a shape more typical for a galactic wind from a central and/or circumnuclear starburst rather than a more collimated ionization cone from an AGN.

This soft western X-ray emission is remarkably connected with a very extended Hα filament (Bomans et al. 2000). This structure reaches from the disk up to at least9 kpc into the halo of NGC 4569 which in combination with its soft X-ray flux allows to be interpreted as an X-ray halo fed by the central starburst driven outflow. Such an X-ray halo has by now only been detected in edge-on galaxies, where an easier distinction between sources within and above the galactic disk is possible. NGC 4569 is the first spiral galaxy, where a direct connection of extraplanar Hα and X-ray emitting gas at scales of 10 kpc has been observed. A comparable phenomenon has only been reported by Devine & Bally (1999) for M82. In this object a filament at a distance of 11 kpc from the galactic center has been detected in Hα and X-rays. Nevertheless, this structure is isolated with no detectable connection to M82, and its association with the galaxy is questionable.

The X-ray halo in NGC 4569 has a plasma temperature of 0.2 keV and a mean electron density of 0.004 cm^{-3} so that its total mass amounts to 7×10^6 M$_\odot$. The cooling time of 3×10^8 yr is long enough to be traceable in X-rays at a galactic height of 9 kpc for an outflow velocity as small as 30 km s^{-1}. One crucial aspect in obtaining a global picture of NGC 4569 is the spatial orientation of the disk and extraplanar components. Several facts speak for the western extraplanar features being located behind the galactic disk. The extension of the H I disk is small enough not to hide the western X-ray component. Additional features in the X-rays, like the southern soft emission, and in Hα, like several emission knots outside the disk, fit in the hydrodynamical interpretation of a strong interaction with the Virgo ICM at a high relative velocity of about 1250 km s^{-1}.

The Magellanic irregular galaxy IC 3583 contains an unresolved X-ray source which is suggested not to originate from a foreground star present in the optical because of a very hard spectrum. A narrow Hα spur pointing from the southern end toward NGC 4569, also visible in the B band, indicates ongoing star formation in IC 3583. The question of an interaction between the two galaxies at very high relative radial velocity of about 1300 km s^{-1} has to be addressed to and must be explored by more detailed observational and model analyses.

Acknowledgements. The authors are grateful for helpful discussions with Ch. Theis. The ROSAT project is supported by the German Bundesministerium für Bildung, Wissenschaft, Forschung und Technologie (BMBF) and the Max-Planck-Society. This research has made use of the NASA/IPAC Extragalactic Database (NED) which is operated by the Jet Propulsion Laboratory, Caltech, under contract with the NASA. This work was partly supported by the Deutsche Forschungsgemeinschaft under grant no. He 1487/23-1 (D.T.).

References

Arnaud K.A., 1996, Astronomical Data Analysis Software and Systems V, ASP Conf. Ser. Vol. 101, eds. Jacoby G., Barnes J., p. 17
Balsara D.S., Livio M., O'Dea C.P., 1994, ApJ 437, 83
Binggeli B., Sandage A., Tammann G.A., 1985, AJ 90, 1681
Böhringer H., Briel U.G., Schwarz R.A., et al., 1994, Nature 368, 828
Bomans D.J., Chu Y.-H., Hopp U., 1997, AJ 113, 1678
Bomans D.J., Tschöke D., Hensler G., Boselli A., 2000, A&A, submitted
Bravo-Alfaro H., Cayatte V., van Gorkom J.H., Balkowski C., 2000, AJ 119, 580
Cayatte V., Kotanyi C., Balkowski C., van Gorkom J.H., 1994, AJ 107, 1003
Cayatte V., van Gorkom J.H., Balkowski C., Kotanyi C., 1990, AJ 100, 604
Cioffi D., 1990, in *Physical Processes in Hot Plasmas*, NATO ASI Series C, Vol. 305, eds. Brinkmann W., Fabian A.C., Giovanelli F., Kluwer, Dordrecht, p. 1
Colina L., Arribas S., 1999, ApJ 514, 637
Dahlem M., 1997, PASP 109, 1298
Dahlem M., Heckman T.M., Fabbiano G., Lehnert M.D., Gilmore D., 1996, ApJ 461, 724
Dahlem M., Petr M.G., Lehnert M.D., Heckman T.M., Ehle M., 1997, A&A 320, 731
Dahlem M., Weaver K.A., Heckman T.M., 1998, ApJS 118, 401
Devine D., Bally J., 1999, ApJ 510, 197
Dickey J.M., 1997, AJ 113, 1939
Dickey J.M., Lockman F.J., 1990, ARA&A 28, 215
Fabbiano G., Kim D.-W., Trinchieri G., 1992, ApJS 80, 531
Freedman W.L., 1996, in *Critical Dialogs in Cosmology*, ed. Turok N., World Scientific Publishing, p. 92
Garcia A.M., 1993, A&AS 100, 47
Heckman T.M., Lehnert M.D., Armus L., 1993, in *The Environment and Evolution of Galaxies*, eds. Shull J.M., Thronson H.R., Jr., Kluwer Academic Publishers, Dordrecht, p. 455
Hensler G., Dickow R., Junkes N., Gallagher J.S., 1998, ApJ 502, L17
Hunter D.A., Gallagher J.S., 1990, ApJ 362, 480
Junkes N., Zinnecker H., Hensler G., Dahlem M., Pietsch W., 1995, A&A 294, 8
Junkes N., Hensler G., 1996, in *The Interplay between Massive Star Formation, the ISM and Galaxy Evolution*, 11th IAP Meeting, eds. Kunth D., et al., p. 533
Keel W.C., 1983, ApJ 269, 466
Keel W.C., 1996, PASP 108, 917
Kennicutt R.C., Jr., Tamblyn P., Congdon C.E., 1994, ApJ 435, 22
Lehnert M.D., Heckman T.M., Weaver K.A., 1999, ApJ 523, 575
Maoz D., Filippenko A.V., Ho L.C., et al., 1995, ApJ 440, 91
Norman C.A., Ikeuchi S., 1989, ApJ 345, 372
Pérez-Olea D.E., Colina L., 1996, ApJ 468, 191
Pietsch W., 1993, in *Panchromatic View of Galaxies – their Evolutionary Puzzle*, eds. Hensler G., Theis Ch., Gallagher J.S., p. 137
Pietsch W., Trinchieri G., Vogler A., 1998, A&A 340, 351
Pogge R.W., Maoz D., Ho L.C., Eracleous M., 2000, ApJ 532, 323

Raymond J.C., Smith B.W., 1977, ApJS 35, 419
Rice W., Lonsdale J.C., Soifer B.T., et al., 1988, ApJS 68, 91
Saikia D.J., Unger S.W., Pedlar A., et al., 1990, MNRAS 245, 397
Sandage A., Bedke J., 1985, AJ 90, 2006
Sérsic J.L., 1973, PASP 85, 103
Shopbell P.L., Bland-Hawthorn J., 1998, ApJ 493, 129
Stauffer J.R., 1983, ApJ 264, 14
Stauffer J.R., Kenney J.D., Young J.S., 1986, AJ 91, 1286
Strickland D.K., Heckman T.M., Weaver K.A., Dahlem M., 2000, AJ, in press, *astro-ph/0008182*
Strickland D.K., Ponman T.J., Stevens I.R., 1997, A&A 320, 378
Suchkov A.A., Balsara D.S., Heckman T.M., Leitherer C., 1994, ApJ 430, 511
Tanvir N.R., Shank T., Major J.V., 1991, MNRAS 253, 21p
Thronson H.A., Telesco C.M., 1986, ApJ 311, 98
Tschöke D., Hensler G., Junkes N., 1999, A&A 343, 373
Tschöke D., Hensler G., Junkes N., 2000, A&A 360, 447
Tschöke D., Hensler G., Junkes N., 2001, A&A, submitted
Tully R.B., 1988, Nearby Galaxies Catalog, Cambridge University Press, Cambridge
Veilleux S., Bland-Hawthorn J., Cecil G., Tully R.B., Miller S.T., 1999, ApJ 520, 111
Vogler A., Pietsch W., Kahabka P., 1996, A&A 305, 74
Vollmer B., Marcelin M., Amram P., et al., 2000, A&A, submitted
Warmels R.H., 1988, A&AS 72, 19
Yasuda N., Fukugita M., Okamura S., 1997, ApJS, 108, 417
Zimmermann H.U., Belloni T., Izzo C., Kahabka P., Schwentker O., 1993, EXSAS User's Guide, Edition 3, ROSAT Scientific Data Center, Garching

Chapter 8

An X-ray halo in the 'hot-spot' galaxy NGC 2903

Submitted to
Astronomy and Astrophysics

An X-ray halo in the 'hot-spot' galaxy NGC 2903

D. Tschöke[1], G. Hensler[1], and N. Junkes[2]

[1] Institut für Theoretische Physik und Astrophysik, Universität Kiel, D-24098 Kiel, Germany
email: tschoeke@astrophysik.uni-kiel.de
[2] Max-Planck-Institut für Radioastronomie, Auf dem Hügel 69, D-53121 Bonn, Germany

Abstract. The existence of galactic superwinds, giant kpc-scale outflows from the center of starburst galaxies, has been studied in several hydrodynamical simulations, and observed in a number of edge-on galaxies, especially in the X-ray regime. The detection of such hot gas above the disk of spirals also with intermediate inclination encounters the difficulty of separating that contribution from disk and active nuclear region.

In this paper we present ROSAT PSPC and HRI observations of the 'hot-spot' galaxy NGC 2903. This isolated system strikingly reveals a soft X-ray feature extending in north-west direction up to a projected distance of 5.2 kpc from the center into the halo. The luminosity of the extraplanar X-ray gas is several 10^{38} erg s^{-1}, comparable to X-ray halos in other starburst galaxies. The counterpart from an expected bipolar outflow has not been detected, indicating that the observed X-ray emitting gas lies in front of the galactic disk moving toward the observer. The extension of the X-ray emission from the disk coincides with numerous H II regions visible in Hα. The estimated star formation rates derived from both wavelength ranges result in 1–2 M$_\odot$ yr^{-1}.

Key words: Galaxies: active – Galaxies: starburst – Galaxies: individual: NGC 2903 – X-rays: galaxies

1. Introduction

Starbursts are important mechanisms for the chemical and dynamical evolution of galaxies; the mass exchange processes between different components (stars — interstellar medium, ISM — cloudy medium) and also between disk and halo strongly influence the nature of these systems and occur on rather short timescales. Typical durations of starbursts are a few 10^7 yr. Numerous observations in different spectral ranges trace different evolutionary phases and components of connected processes: Supernova remnants (SNRs) in starburst regions are detectable by non-thermal radio continuum emission; strong infrared sources point to a huge amount of dust heated up by young massive stars; giant extragalactic star-forming H II regions in the optical and OB associations in the UV are strong tracers for the actual star formation (Shields 1990).

Our interest is directed on hot components observable in the X-ray regime. Stellar winds from young massive O- and B-type stars heat up the ambient ISM by shocks (Leitherer 1994; Freyer & Hensler 2000). These stars end in supernova explosions of type II (SN II), which then expand into the ISM. Due to the strong spatial concentration of OB associations and because of the short evolution timescale of massive stars, the subsequent SNe II accumulate to build so-called superbubbles, filled with several million Kelvin hot plasma. These superbubbles expand mainly perpendicular to a galactic disk, due to the radial density gradient, and heat up the swept-up ambient medium thru shocks. If enough energy from the starburst is converted into kinetic energy of the propagating hot gas, it breaks out of the disk into the galactic halo (Norman & Ikeuchi 1989; Heckman et al. 1990; Suchkov et al. 1994; Strickland & Stevens 2000). These hot gaseous outflows or superwinds have been detected in the soft X-rays in several edge-on disk galaxies (Dahlem et al. 1998, hereafter DWH98).

We investigate a small sample of spiral galaxies with nuclear starburst activity in order to probe their evolution (NGC 1808: Junkes et al. 1995; NGC 4410: Tschöke et al. 1999; NGC 4303: Tschöke et al. 2000b; NGC 4569: Bomans et al. 2000; Tschöke et al. 2000a). From the theoretical point of view, hot gaseous outflows from OB associations in the disk into the halo must be a common phenomenon. Direct observations of these outflows, however, are rather difficult to achieve. The best candidates are edge-on spiral galaxies with significant star formation where any X-ray component outside the disk can be well distinguished, and where a sufficient amount of hot gas can be detected. Most prominent examples are the two closest starburst galaxies, M82 and NGC 253 (Weaver et al. 2000; Pietsch et al. 2000). In contrast, for the X-ray emission of galaxies observed at low or intermediate inclination angles the location of the diffuse component, whether within or above the disk, is indistinguishable. Furthermore, parts of the soft (typically 0.2 keV) X-rays from such gaseous outflows can be easily absorbed via obscuration by the disk of the galaxy.

One candidate of a galaxy at intermediate inclination with an observed X-ray halo is NGC 4569 (Tschöke et al. 2000a). Another one is NGC 2903, a nearby barred galaxy where most of the investigations so far have been concerned with its nucleus containing a central starburst. NGC 2903 has been classified as 'hot-spot' galaxy (Sérsic 1973) because of its complex optical nuclear structure (Oka et al. 1974; Laques et al. 1980; Simons et al. 1988; Planesas et al. 1997). It shows six separate emission peaks over an area of about 20″ in diameter. Radio maps of the nuclear region do not exactly correspond to the optical hot spots. As an explanation, Wynn-Williams & Becklin (1985) suggested the possibility of patchy extinction. Recent near-infrared observations of the galactic core indeed reveal a ring-like morphology with a diameter of 625 pc (Alonso-Herrero et al. 2000), coinciding with the radio rather than with the Hα structure. The nucleus contains a strong non-thermal radio source (van der Kruit 1973), reflecting SNRs in the nuclear starburst, and a moderately high FIR luminosity of $\leq 7\times10^9$ $L_\odot$ mainly produced by central OB stars (Telesco & Harper 1980). Hα images of the full galaxy clearly trace the bar and spiral structure with a dominant central source (Jackson et al. 1991). A few basic properties of NGC 2903 are listed in Table 1.

In this paper we present spectral and imaging data of NGC 2903 obtained by the X-ray satellite ROSAT in the 0.1–2.4 keV band. We discuss the contributions from different components of NGC 2903 (nucleus, disk, and halo) in order to get a more complete picture from the processes in this nuclear starburst galaxy. Sect. 2 presents the observation protocol and reduction techniques of the used ROSAT data, Sect. 3 the results from imaging and spectral analysis. In Sect. 4 we discuss the derived X-ray properties of NGC 2903, compare the derived star formation rate (SFR) with results from other wavelengths, and confirm the existence of an extraplanar X-ray gas component above the galactic disk. The results are summarized in Sect. 5. Throughout the paper we adopt the recent photometric distance estimation of 8.9 Mpc for NGC 2903 (Drozdovsky et al. 2000). Hence 1″ corresponds to 43 pc.

Table 1. NGC 2903: Some basic parameters.

	NGC 2903	Reference[a]
alternate name	IRAS 09293+2143	
type	SAB(rs)bc	1
RA (2000)	$09^h32^m10\overset{s}{.}1$	2
Dec (2000)	$+21°30'04''$	2
distance	8.9 Mpc	3
radial velocity	556	3
D_{25} diameter	$11\overset{'}{.}6$	1
axis ratio	0.49	1
inclination	66°	1
log L_B	10.13	1
log M_{HI}	9.25	1

[a] References:
1) Tully (1988)
2) NED database
3) Drozdovsky et al. (2000);

2. Observations and data reduction

The presented data were taken by the High Resolution Imager (HRI) and the Position Sensitive Proportional Counter (PSPC) onboard the X-ray satellite ROSAT. For details concerning ROSAT and its detectors see the ROSAT User's Handbook (Briel et al. 1996). Some basic information on the observations are given in Table 2. Source detection (Tables 3 and 4) was performed with the EXSAS software package (Zimmermann et al. 1997). Images and spectra were created by using the Imaging Data Language (IDL) software package. To fit the spectral distribution of the X-ray source we used XSPEC (Arnaud 1996).

2.1. HRI

Two separate observation runs were taken with the HRI detector on April 27–29, 1994 (exposure time 13.6 ksec) and November 7, 1994 (8.3 ksec) according to the proposal by one of us (N.J.; ROR no. 600602h). Both exposures are centered on the coordinates RA(2000) = $09^h32^m09\overset{s}{.}6$; Dec(2000) = $+21°30'00''$. The data were combined, creating one exposure of 21.9 ksec, corrected for vignetting, but not for background contamination. The resulting image was convolved with a Gaussian of 5″ FWHM. To determine the background level, three source-free circular fields around NGC 2903 were chosen, with radii of 93″, 79″, and 60″, respectively. The derived background amounts to 3.6×10^{-7} counts s^{-1} arcsec^{-2}.

The source detection in the HRI field of view (FOV) was carried out with a maximum likelihood method and a lower detection limit of 5σ. The detected sources, corresponding sources in the PSPC FOV, and identifications are given in Table 3.

2.2. PSPC

The PSPC exposure (ROR no. 600093p; PI: H. Zinnecker; CoI: N. Junkes) was carried out between May 6 and 7, 1991, with an integration time of 9184 sec. The observation is centered on the same coordinates as the HRI observations. The created image was corrected for vignetting and convolved with a Gaussian of 25″. The background flux was determined from three circular source-free areas in the field with radii of 95″, 71″, and 59″. It amounts to 3.2×10^{-7} cts s^{-1} arcsec^{-2}. The source detection in the FOV was carried out the same way as in the case of the HRI observations. Results are given in Table 4.

Table 2. ROSAT observations of NGC 2903.

	Central coordinates		Date	Exposure	Count rate[a]	Background	PI
	RA(2000)	Dec(2000)		time [s]	[cts s^{-1}]	[cts s^{-1} $arcsec^{-2}$]	
HRI	$9^h\,32^m\,9\overset{s}{.}6$	$+21°30'00''$	April 27–29, 1994	13619	0.020 [b]	3.6×10^{-7} [b]	N. Junkes
	$9^h\,32^m\,9\overset{s}{.}6$	$+21°30'00''$	November 7, 1994	8284			N. Junkes
PSPC	$9^h\,32^m\,9\overset{s}{.}6$	$+21°30'00''$	May 6–7, 1991	9184	0.091	3.2×10^{-7}	H. Zinnecker

[a] background subtracted
[b] combined HRI observations

Table 3. Source detections in the ROSAT HRI observation of NGC 2903 with a maximum likelihood threshold of 14 (5σ).

No.	RA (2000)	Dec (2000)	Existence likelihood	Count rate (HRI)[a] [10^{-3} cts s^{-1}]	No. (PSPC)	Identification
1	$9^h\,32^m\,05\overset{s}{.}4$	$+21°32'36''$	23	0.8±0.2	9	H II region in NGC 2903
2	$9^h\,33^m\,22\overset{s}{.}2$	$+21°32'07''$	18	3.3±0.7	10	2E 0930.5+2145
3	$9^h\,32^m\,10\overset{s}{.}1$	$+21°30'07''$	180	7.8±0.6	11	NGC 2903
4	$9^h\,31^m\,48\overset{s}{.}7$	$+21°24'43''$	20	1.0±0.3	14	

[a] background subtracted

Table 4. Source detections in the ROSAT PSPC observation of NGC 2903 with a maximum likelihood threshold of 14 (5σ).

No.	RA (2000)	Dec (2000)	Existence likelihood	Count rate (PSPC)[a] [10^{-3} cts s^{-1}]	No. (HRI)	Identification
1	$9^h\,32^m\,13\overset{s}{.}2$	$+21°51'35''$	31	7.6±1.4		HD 82394 / BD +22 2102B
2	$9^h\,32^m\,12\overset{s}{.}9$	$+21°48'12''$	20	4.4±1.0		
3	$9^h\,33^m\,14\overset{s}{.}3$	$+21°46'00''$	31	9.9±1.6		
4	$9^h\,31^m\,55\overset{s}{.}2$	$+21°43'58''$	19	4.4±1.0		QSO 0929+2157
5	$9^h\,32^m\,33\overset{s}{.}3$	$+21°41'54''$	36	5.1±1.0		
6	$9^h\,30^m\,56\overset{s}{.}5$	$+21°34'34''$	37	6.7±1.2		
7	$9^h\,32^m\,56\overset{s}{.}3$	$+21°33'57''$	23	3.5±0.8		
8	$9^h\,31^m\,25\overset{s}{.}6$	$+21°33'46''$	46	5.1±0.9		
9	$9^h\,32^m\,05\overset{s}{.}5$	$+21°32'33''$	33	3.6±0.8	1	H II region in NGC 2903
10	$9^h\,33^m\,21\overset{s}{.}9$	$+21°32'12''$	214	21.6±1.8	2	2E 0930.5+2145
11	$9^h\,32^m\,09\overset{s}{.}9$	$+21°30'14''$	1157	73.8±3.0	3	NGC 2903
12	$9^h\,31^m\,20\overset{s}{.}7$	$+21°29'44''$	19	3.0±0.8		
13	$9^h\,30^m\,59\overset{s}{.}9$	$+21°29'09''$	18	3.7±0.9		
14	$9^h\,31^m\,48\overset{s}{.}7$	$+21°24'48''$	19	2.6±0.7	4	
15	$9^h\,31^m\,44\overset{s}{.}4$	$+21°17'04''$	33	5.0±1.0		
16	$9^h\,32^m\,06\overset{s}{.}3$	$+21°15'03''$	17	4.7±1.1		QSO 0929+2128
17	$9^h\,33^m\,47\overset{s}{.}9$	$+21°14'33''$	376	55.2±3.3		QSO 0930+2128
18	$9^h\,30^m\,45\overset{s}{.}5$	$+21°02'17''$	50	18.7±2.5		HD 82157

[a] background subtracted

3. Results

3.1. X-ray imaging

The X-ray emission in the ROSAT PSPC image of NGC 2903 (Fig. 2) is clearly extended. It covers the whole inner region with the galactic bar and the inner spiral structure up to a radius of 5 kpc, showing a strong emission peak near the optical center and significant contribution from the northern and southern disk component. The northern elongation of the disk component at intermediate contours indicate a second X-ray peak coincident with a luminous H II region about 1′ north from the center, prominent in the Hα image. This is more clearly traceable at a better spatial resolution in the HRI image (Fig. 4).

The point source about 2′.7 northwest from the center (Table 4, source no. 9) spatially coincides with an H II region in the norther spiral arm, supported by the coincidence in the HRI image (Fig. 4; see also Table 3, source no. 1). Furthermore, the spectral distribution is compara-

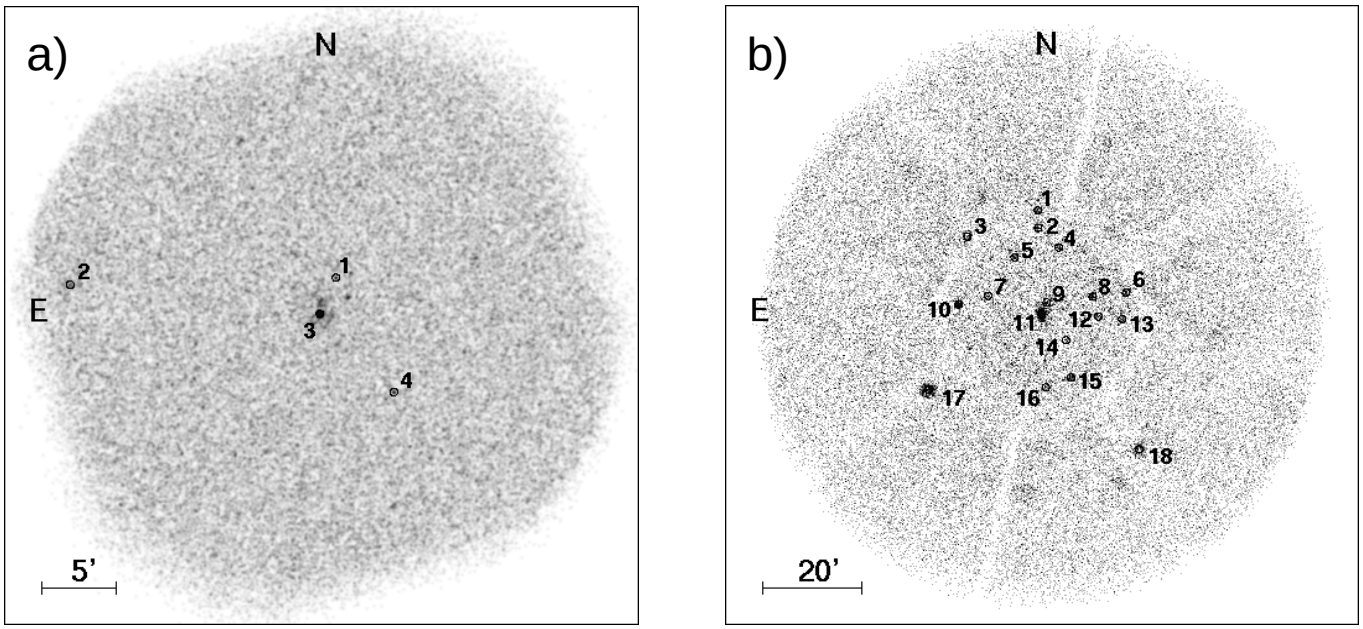

Fig. 1. Source detections in the ROSAT HRI (a) and PSPC (b) observation of NGC 2903 with a maximum likelihood threshold of 14 (5σ). The source numbers are listed in Table 3 (HRI) and Table 4 (PSPC), respectively.

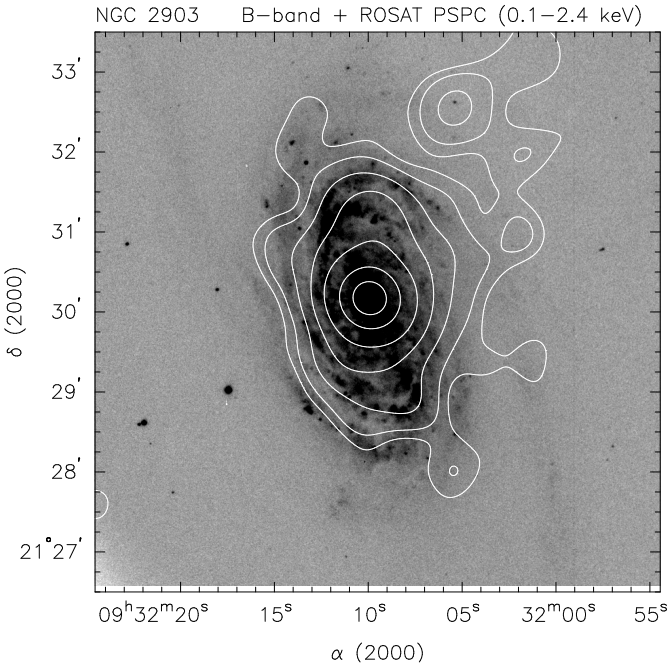

Fig. 2. ROSAT PSPC contours over B-band image of NGC 2903. Contour levels are (0.7, 1.0, 1.6, 2.9, 5.4, 10.4, 15.4)$\times 10^{-6}$ cts s^{-1} arcsec^{-2}, corresponding to 3, 5, 10, 20, 40, 80, and 120σ.

ble with the one of the main disk emission (Component no. 5 in Table 5; Fig. 3).

In Fig. 3 we directly compare the X-ray emission of NGC 2903 from four energy bands, the total spectral range of the PSPC (0.1–2.4 keV), the soft range (0.1–0.4 keV), the intermediate regime (0.5–0.9 keV), and the hard X-ray band (0.9–2.0 keV). The 0.9–2.0 keV band is clearly dominated by the nuclear source. The lower contours do not coincide with the bar's S-shape and are rather caused by two unresolved point sources in the spiral arms. Its northern part coincides with a luminous H II region in the disk of NGC 2903, indicating possible contribution from unresolved hard point sources, i.e. SNRs and/or high-mass X-ray binaries. In the intermediate band the X-ray emission covers the entire inner $4'$ of the disk and traces quite good the most prominent H II emission regions. The northern point source visible in the HRI image located at the H II region in the northern spiral arm is also present in the PSPC exposure.

The structure in the soft image is of particular interest, because of the distinct extension in western direction perpendicular to the major axis. It significantly exceeds the inner spiral structure in Hα and the 0.5–0.9 keV emission from the disk. At the given distance of 8.9 Mpc for NGC 2903 the projected radius of this soft feature is 5.2 kpc from the center. We will discuss this feature in detail in Sects. 4.2 to 4.4. In the soft energy band the luminous H II region $1'$ north of the central source, as detected in Hα and the hard ROSAT band, also appears.

In the HRI image (Fig. 4) no diffuse X-ray component in the disk of NGC 2903 is discernible. The most prominent source is again the nuclear region, covering the area of the optical hot spots. The resolution of about $5''$ is not sufficient to clearly separate any single source. Nevertheless, the X-ray emission covers an area of about $40''\times 30''$ from the 3σ level contours. The northern luminous H II region at a distance of $1'$ is again clearly detectable by the HRI, as already indicated in the PSPC image. The sec-

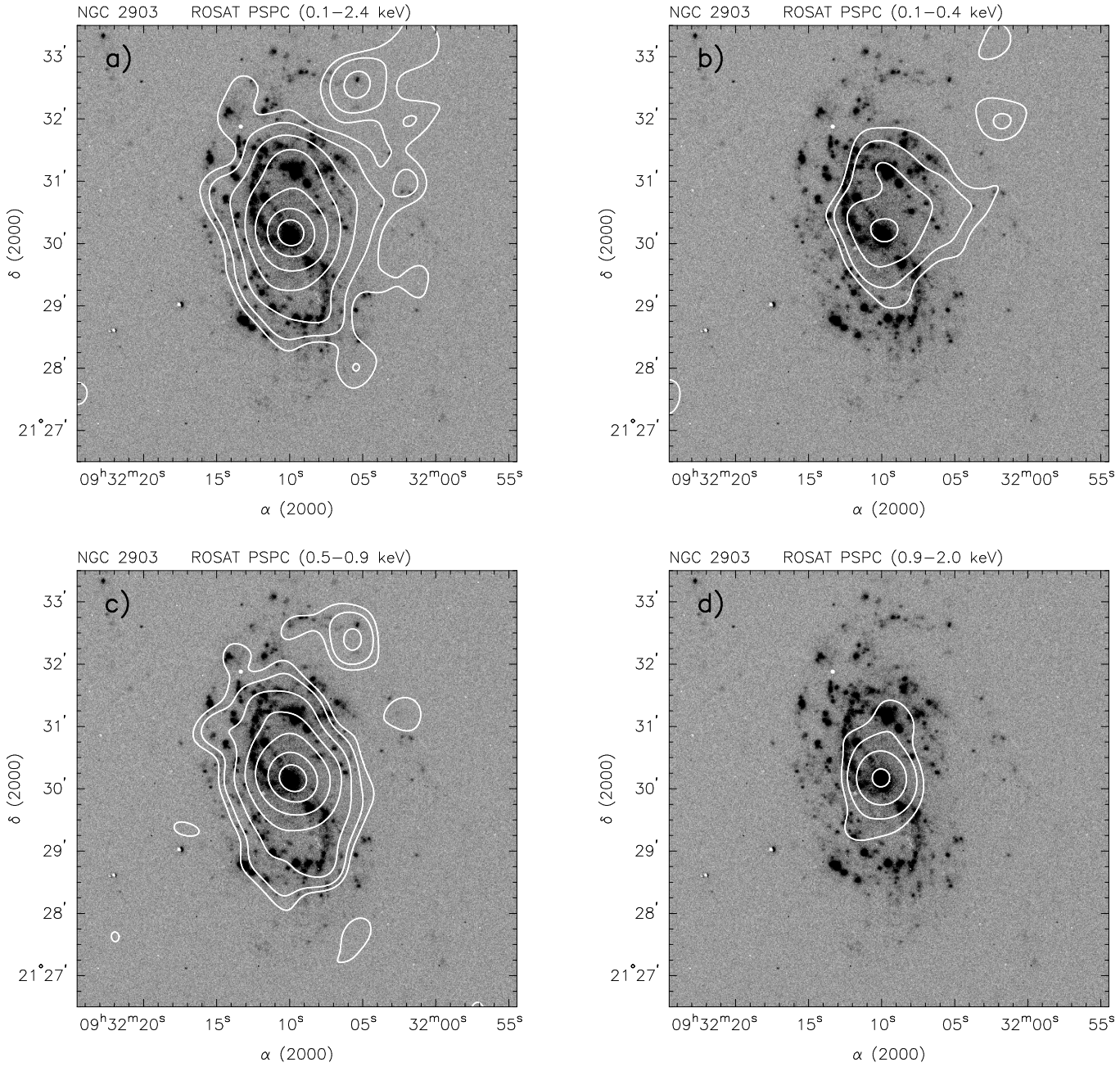

Fig. 3. ROSAT PSPC contours on top of the Hα image (Boselli, private communication) of NGC 2903 in four different energy ranges: **(a)** 0.1–2.4 keV, **(b)** 0.1–0.4 keV, **(c)** 0.5–0.9 keV, **(d)** 0.9–2.0 keV. The contour levels in each image start at 3σ and increase by the same steps as in Fig.2

.

ond most luminous X-ray source in the HRI image is the point source at the position of northern outlying bright H II region at a distance of 2′.7 from the center.

3.2. Spectral distribution

As can be seen from Fig. 3, different contributions in the energy range emerge from different components of the galaxy. Therefore we subdivide the PSPC image in several regions (see Fig. 5), namely the entire galaxy (area 1), nucleus (area 2), disk (areas 3a and 3b), eastern soft component (area 4), and northern prominent point source (area 5). A quantitative conclusion of the spectral distribution for the different areas can be drawn from the hardness ratio HR, defined by $(B-A)/(B+A)$, where A and B are the numbers of counts in the energy channels 11–41 (0.1–0.4 keV) and 52–201 (0.5–2.0 keV), respectively. The

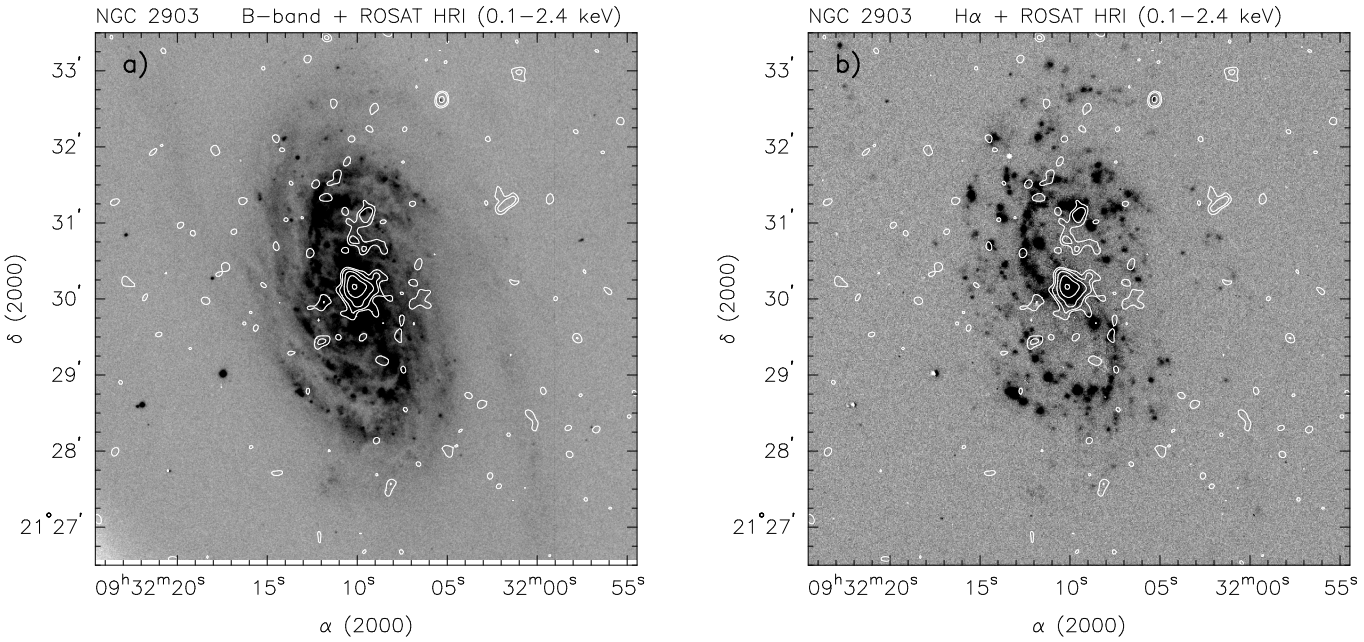

Fig. 4. ROSAT HRI contours over (a) B-band and (b) Hα image of NGC 2903. Contour levels are (1.0, 1.4, 2.5, 4.7, 9.0)$\times 10^{-6}$ cts s^{-1} arcsec^{-2}, corresponding to 3, 5, 10, 20, and 40σ.

hardness ratio of the different components from Fig. 5 together with their count rates are listed in Table 5. It is striking that $HR = -0.16$ of component no. 4 is the only negative value and differs strongly from the other regions which have values between +0.6 and +0.7, i.e. reveal much harder X-ray spectra. Region no. 3a (northern disk) is with $HR = +0.39$ slightly softer than region no. 3b. This can already be perceived in Fig. 3. The bright H II region 1″ north from the center emits a significant fraction in the soft range. Nevertheless, the flux from this region is still quite hard compared to area 4.

In Fig. 6, the 0.1–2.4 keV spectra of the components as labeled in Fig. 5 are plotted. We fit several emission models to the spectra of the entire galaxy (area 1) and of the nucleus (area 2), like a power-law model (PO), a Raymond-Smith model (Raymond & Smith 1977) for a hot plasma (RS), and a thermal Bremsstrahlung model (BS). For area 1 we also compare a combined PO+RS model and a two-temperature RS+RS model considering a high temperature central starburst component and a low temperature halo component. The results are listed in Tables 6 and 7.

From the quality of the fits alone none of the chosen models for the spectral distribution of the entire galaxy is most preferable. A pure single-temperature RS model with solar abundances is obviously not a good fit to the spectrum. The models with a non-thermal component differ from the pure thermal ones in the following points: For the models including a PO component the resulting total 0.1–2.4 keV flux lies in the range of 2.8–4.5$\times 10^{40}$ erg s^{-1}, whereas the pure thermal emission models yield 1–2$\times 10^{40}$ erg s^{-1}. The H I column density is for the latter in the range of the Galactic foreground value of 2.8$\times 10^{20}$ cm^{-2} (Dickey & Lockman 1990), while it is about two times higher for the fits with a PO component. In the RS+PO model the non-thermal component dominates the total flux by 90–95%. So these cases require an explanation

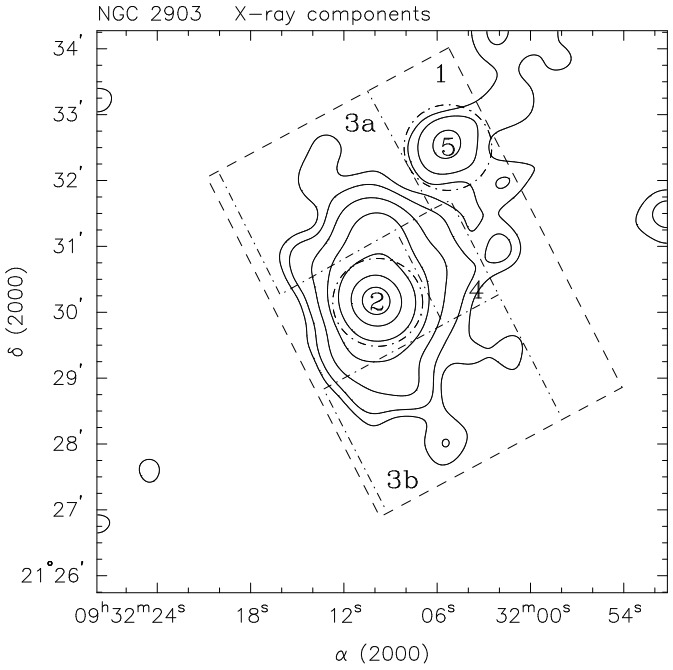

Fig. 5. Definition of areas for the different galaxy components in the PSPC exposure as used in the text: total galaxy (1), nuclear region (2), northern disk (3a), southern disk (3b), halo (4), northern point source (5).

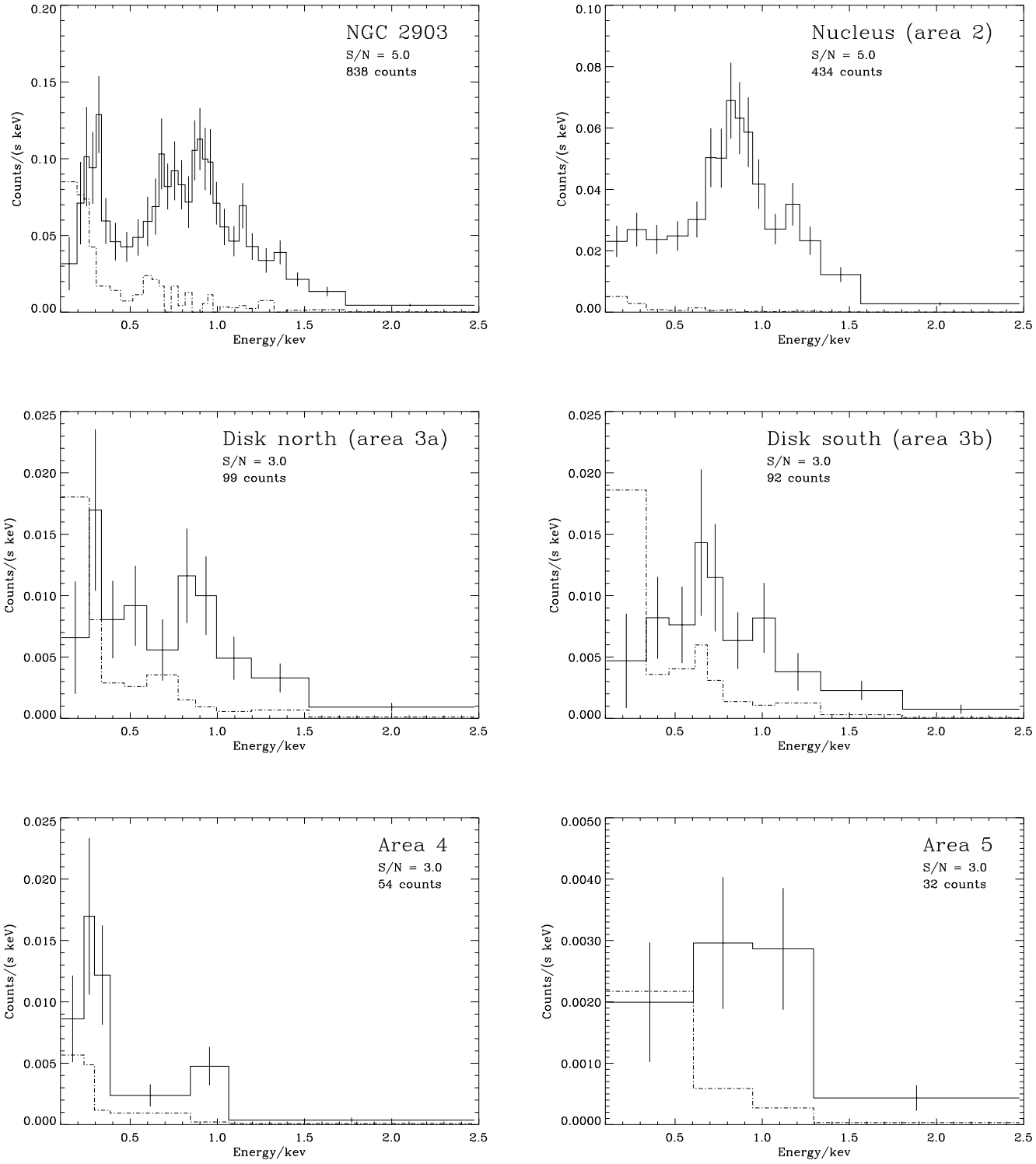

Fig. 6. Spectral distribution of the different components (Fig. 5) in the 0.1–2.4 keV energy range: a) total galaxy, area 1; b) nuclear region, area 2; c) northern disk, area 3a; d) southern disk, area 3b; e) halo, area 4; f) northern point source, area 5. For the total galaxy and the nucleus the spectra were binned to a signal-to-noise ratio of 5, all other spectra have a ratio of 3.

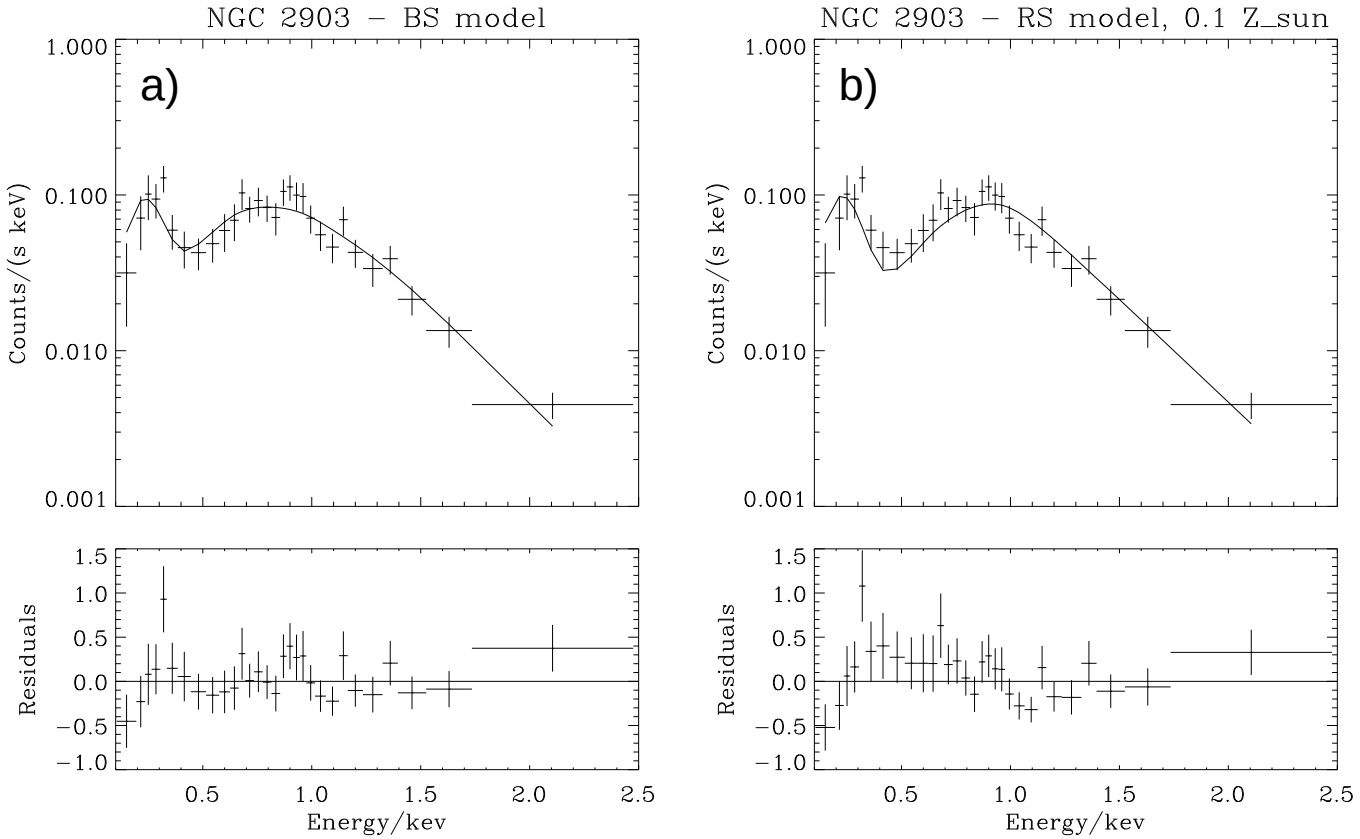

Fig. 7. Fits of a Bremsstrahlung model (a) and a low-metallicity Raymond-Smith model (b) to the 0.1–2.4 keV spectrum of NGC 2903. Fit parameters are listed in Table 6.

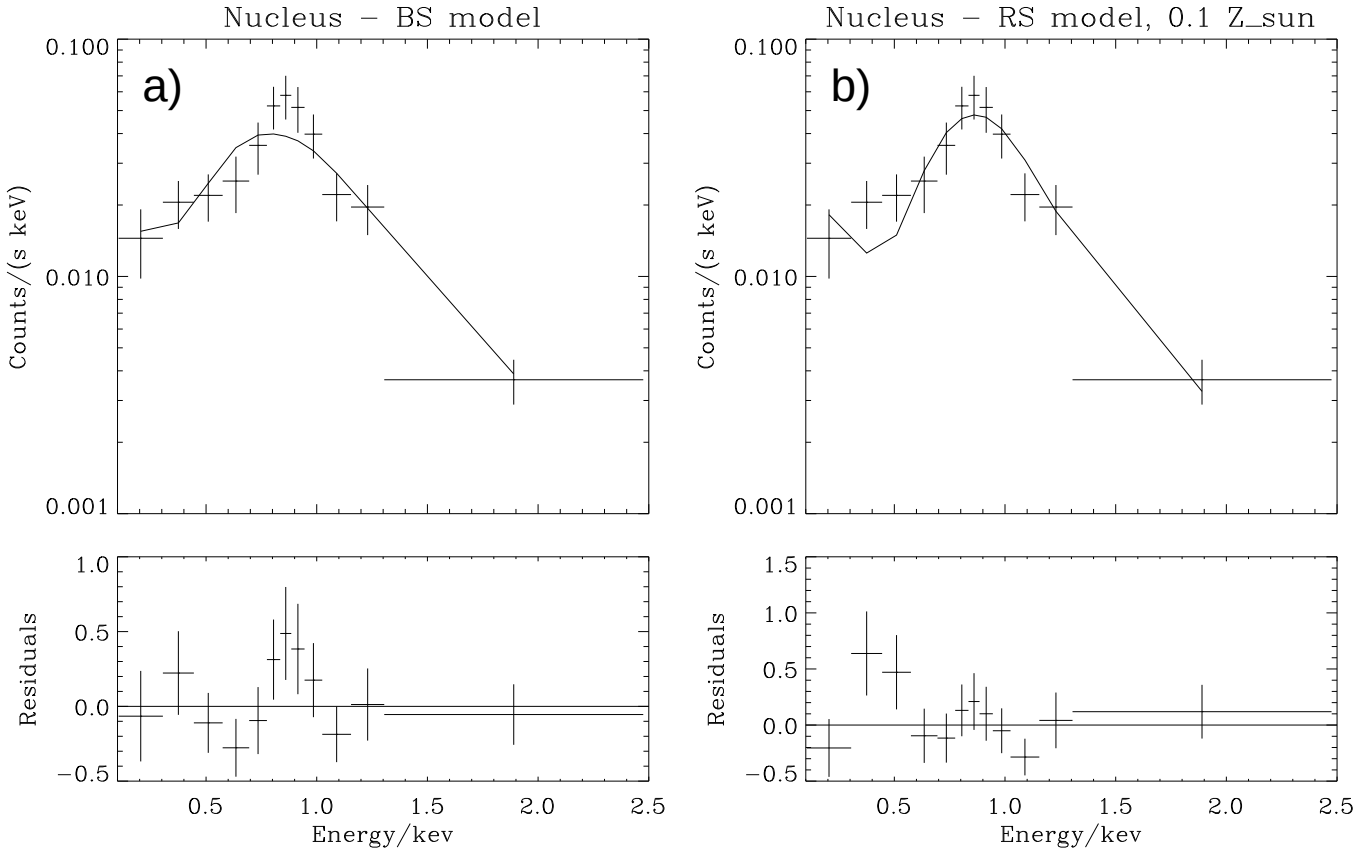

Fig. 8. Model fit of the 0.1–2.4 keV spectrum of the nucleus (area 2) with a Bremsstrahlung model (a) and a low-metallicity Raymond-Smith model (b). Fit parameters are listed in Table 7.

Table 5. Count rates and hardness ratios of the X-ray components of NGC 2903 as labeled in Fig. 5.

Component	Count rate[a] [10^{-3} cts s^{-1}]	Hardness ratio
1	84.0±3.4	+0.56±0.04
2 (nucleus)	36.9±2.2	+0.69±0.04
3a (northern disk)	11.7±1.2	+0.39±0.10
3b (southern disk)	10.0±1.2	+0.63±0.10
4 (halo)	5.9±0.8	−0.16±0.13
5 (point source)	3.5±0.6	+0.60±0.18

[a] background subtracted

for such a high contribution by non-thermal sources, i.e. X-ray binaries, SNRs, and/or a central accretion-powered nucleus. An AGN does not fulfill the general view of the galactic center from other observations. Also the fit results from the nuclear component do not match the assumption of an AGN (see text below).

From the fits of thermal emission the suggestion arises that the X-ray emitting plasma has low metallicity. We achieve a much better fit with a RS model of 0.1 $Z_\odot$ than with solar metallicity and an even better fit with a BS model. The temperature lies in the range of 0.7–1 keV, which also has been observed in other central starbursts (e.g. NGC 1365: Stevens et al. 1999; NGC 2146: della Ceca et al. 1999). To take a low-temperature halo component into account (area 4, see Sect. 4.2) we also fitted the spectrum of NGC 2903 with a two-component RS+RS model, as observed in edge-on starburst galaxies with hot extraplanar gas (DWH98). The abundances were fixed to 1 $Z_\odot$ representing the central starburst with its freshly synthesized material not yet mixed with the ambient ISM, and to 0.1 $Z_\odot$ for the outflowing mixed plasma and the shock-heated swept-up ambient medium. The column density of the best fit lies in the range of the Galactic foreground value, and the plasma temperature for the low-metallicity component is with 0.3 keV compatible with other observed X-ray halos (DWH98). Nevertheless, the luminosity fraction of 50% from such a soft halo component is unexpectedly high. In addition, an acceptable fit is only achieved for the 1 $Z_\odot$ component with a very high plasma temperature of 4 keV. This is not in agreement with ASCA observations analyzed by DWH98. Furthermore, the soft energy range of ROSAT is not suited to verify such a hard component.

The nuclear X-ray spectrum can better be explained by a thermal emission model at low-metallicity. Because of a decreasing contribution from emission lines in the model sequence RS (1 $Z_\odot$), RS (0.1 $Z_\odot$), BS consequently the fraction of absorbed flux increases. This, however, rules out the 1 $Z_\odot$ RS model because the corresponding column density reaches only 9.5×10^{19} cm^{-2} and therefore lies far below the Galactic foreground value of 2.8×10^{20} cm^{-2} and the intrinsic H I measurement by Wevers et al. (1986). For a 0.1 $Z_\odot$ RS model the column density is somewhat higher (3.5×10^{20} cm^{-2}), while the BS model requires a 2.3 times higher value. The influence of emission lines in the spectrum is perceptible also in the nuclear luminosity because of the higher continuum flux for models with lower metallicities. The 0.1 $Z_\odot$ RS and BS fits result in $L_X = 5.9\times10^{39}$ erg s^{-1} and $L_X = 1.2\times10^{40}$ erg s^{-1}, respectively. To achieve a good fit of the nuclear spectrum with a PO model a column density of about 10^{21} cm^{-2} is required. As a consequence the X-ray luminosity amounts to 4.5×10^{40} erg s^{-1}. This is much too high compared to the derived total X-ray luminosity of the entire galaxy in any of the applied models. In the case of a single PO model the nuclear luminosity would be as high as the total luminosity of NGC 2903 without explaining the contributions from the disk. For the other models the nuclear luminosity would even exceed the total luminosity (see Table 6).

4. Discussion

4.1. Nuclear and disk X-ray emission – star formation rate

Comparing the X-ray images from both ROSAT detectors we find that the diffuse disk emission in the low-resolution PSPC image has not been detected with the HRI. Only the strongest disk sources (north and southeast from the center) have counterparts in both HRI and PSPC images (most easily visible in the hard band, Fig.3d). On the other hand, if we notice that the HRI detector is about three times less sensitive compared to the PSPC detector, sources at count rates lower than the strongest disk sources cannot be distinguished from the background in the HRI exposure. Depending on the emission model, the fraction of the luminosity from the disk to the total luminosity amounts to 40–50%. In the thermal emission models the total luminosity yields 6.8×10^{39} erg s^{-1}. This implies the assumption that the X-ray flux originates from star-forming H II regions as indicated by the Hα image and the coinciding point sources in the HRI image.

According to Leitherer (1994), the X-rays from star-forming regions are dominated by supernovae after 10^7 years. To determine the mean SFR in the disk of NGC 2903 one can use the simplistic approach from Junkes et al. (1995) based on the work by Cioffi (1990) for single cooling supernova shells:

$$\mathrm{SFR}\ [M_\odot\ yr^{-1}] = 1.1\times10^{-40}\ L_X\ [\mathrm{erg\ s^{-1}}].$$

However, this approach does not take into account any effect by the accumulating and overlapping single supernova remnants. The SFR for the total galaxy is thus derived to 1.4–2.0 $M_\odot$ yr^{-1}. Corresponding to the results from the spectral distribution of nucleus and total galaxy about 50% of the total SFR takes place in the nuclear region.

The SFR can also be derived from the Hα emission of H II regions under the assumption of a specific IMF

Table 6. Fit results on the X-ray spectrum from NGC 2903 (area 1).

Model (1)	$N_{\rm H}$ (2)	kT (3)	Γ (4)	Z (5)	Norm (6)	Red. χ^2 (7)	d.o.f. (8)	$F_{\rm X}$ (9)	$L_{\rm X}$ (10)
RS	$0.50^{+0.16}_{-0.13}$	$0.88^{+\infty}_{-0.04}$		1	2.7	3.8	27	$0.78^{+0.07}_{-0.78}$	$0.74^{+0.07}_{-0.74}$
RS	$2.26^{+0.26}_{-0.23}$	$1.01^{+0.07}_{-0.08}$		0.1	16	1.4	27	1.31±0.01	1.24±0.01
BS	$3.74^{+0.50}_{-0.45}$	$0.74^{+0.11}_{-0.10}$			3.3	1.0	27	$1.90^{+0.16}_{-0.14}$	$1.80^{+0.15}_{-0.13}$
PO	$6.01^{+0.78}_{-0.64}$		2.81±0.17		4.0	1.0	27	$4.79^{+1.25}_{-0.94}$	$4.54^{+1.18}_{-0.89}$
RS + PO	$4.91^{+1.08}_{-0.92}$	$0.57^{+0.25}_{-0.21}$	$2.61^{+0.26}_{-0.16}$	1	3.3 (PO) 0.38 (RS)	0.9	25	$3.16^{+1.21}_{-0.52}$ (0.15±0.03)	$3.00^{+1.15}_{-0.49}$ (0.14±0.03)
RS + PO	$4.77^{+0.96}_{-0.77}$	$0.55^{+0.29}_{-0.21}$	2.56±0.37	0.1	3.1 (PO) 3.5 (RS)	0.9	25	$2.95^{+1.62}_{-0.91}$ $(0.30^{+0.01}_{-0.07})$	$2.80^{+1.54}_{-0.86}$ $(0.28^{+0.01}_{-0.07})$
RS + RS	$2.68^{+0.82}_{-0.72}$	$4.34^{+\infty}_{-2.65}$ $0.31^{+0.17}_{-0.08}$		1 0.1	6.8 12	1.1	25	$1.50^{+0.42}_{-0.82}$ $(0.76^{+0.21}_{-0.08})$	$1.42^{+0.40}_{-0.78}$ $(0.72^{+0.20}_{-0.08})$

Col.(1) Spectral models: BS = thermal Bremsstrahlung, RS = Raymond-Smith, PO = power law.
Col. (2) Column density in units of 10^{20} cm^{-2}.
Col. (3) Plasma temperature in units of keV.
Col. (4) Photon index.
Col. (5) Metallicity in units of $Z_\odot$; fixed values.
Col. (6) Scaling factor: for BS in units of $(10^{-18}/(4\pi D^2))\int n_{\rm e} n_{\rm I} {\rm d}V$, $n_{\rm e}, n_{\rm I}$ = electron and ion densities (cm^{-3}); for RS in units of $(10^{-18}/(4\pi D^2))\int n_{\rm e}^2 {\rm d}V$, $n_{\rm e}, n_{\rm H}$ = electron density (cm^{-3}); for PO in units of 10^{-4} photons keV^{-1} cm^{-2} s^{-1} at 1 keV.
Col. (7) Reduced χ^2.
Col. (8) Degrees of freedom.
Col. (9) Unabsorbed X-ray flux in units of 10^{-12} erg cm^{-2} s^{-1}. Values in brackets give the contribution of the thermal component.
Col. (10) X-ray luminosity in units of 10^{40} erg s^{-1}. Values in brackets give the contribution of the thermal component. For the RS+RS model the values in brackets are for the low-temperature component.

Table 7. Fit results on the X-ray spectrum from the nucleus of NGC 2903 (area 2).

Model (1)	$N_{\rm H}$ (2)	kT (3)	Γ (4)	Z (5)	Norm (6)	Red. χ^2 (7)	d.o.f. (8)	$F_{\rm X}$ (9)	$L_{\rm X}$ (10)
RS	$0.95^{+0.42}_{-0.31}$	$0.82^{+0.05}_{-0.07}$		1	1.1	2.7	9	$3.58^{+0.42}_{-0.33}$	$3.39^{+0.40}_{-0.31}$
RS	$3.51^{+0.62}_{-0.49}$	$0.78^{+0.07}_{-0.10}$		0.1	6.6	1.2	9	$5.88^{+0.08}_{-0.14}$	$5.57^{+0.08}_{-0.13}$
BS	$6.56^{+1.31}_{-0.92}$	$0.54^{+0.11}_{-0.10}$			2.4	1.1	9	$11.8^{+1.4}_{-1.6}$	$11.2^{+1.3}_{-1.5}$
PO	$9.71^{+1.88}_{-1.00}$		$3.27^{+0.30}_{-0.25}$		2.0	1.4	9	47^{+30}_{-15}	45^{+29}_{-14}

Col.(1) Spectral models: BS = thermal Bremsstrahlung, RS = Raymond-Smith, PO = power law.
Col. (2) Column density in units of 10^{20} cm^{-2}.
Col. (3) Plasma temperature in units of keV.
Col. (4) Photon index.
Col. (5) Metallicity in units of $Z_\odot$; fixed values.
Col. (6) Scaling factor: for BS in units of $(10^{-18}/(4\pi D^2))\int n_{\rm e} n_{\rm I} {\rm d}V$, $n_{\rm e}, n_{\rm H}$ = electron and ion densities (cm^{-3}); for RS in units of $(10^{-18}/(4\pi D^2))\int n_{\rm e} n_{\rm H} {\rm d}V$, $n_{\rm e}, n_{\rm H}$ = electron and H densities (cm^{-3}); for PO in units of 10^{-4} photons keV^{-1} cm^{-2} s^{-1} at 1 keV.
Col. (7) Reduced χ^2.
Col. (8) Degrees of freedom.
Col. (9) Unabsorbed X-ray flux in units of 10^{-13} erg cm^{-2} s^{-1}.
Col. (10) X-ray luminosity in units of 10^{39} erg s^{-1}.

(Kennicutt 1983; Pogge & Eskridge 1987). Jackson et al. (1991) measured the Hα flux resulting in a total luminosity of 2.5×10^{41} erg s^{-1} (for a distance of 8.9 Mpc). Depending on the conversion law the derived SFR amounts to 2.2 M$_\odot$ yr^{-1} (Kennicutt 1983) or 1.4 M$_\odot$ yr^{-1} (Pogge & Eskridge 1987), respectively. About 13% of the total Hα flux originates from the hot-spot region of the galactic center, as denoted by Jackson et al. (1991) and confirmed by the Hα data, provided by A. Boselli. Because of the low spatial resolution of the PSPC the definition of the chosen boundaries for the nuclear region (area 2) is somewhat larger than the hot spots resolved in Hα and, thus, contains also some flux from H II regions of the inner disk component (compare Figs. 3a and 5). This may cause the higher SFR value for the nucleus of about 0.5 M$_\odot$ yr^{-1} derived from the X-ray data.

In the FIR regime the total luminosity (for a distance of 8.9 Mpc) amounts to 8.8×10^9 L$_\odot$ (Rice et al. 1988). By applying the $L_{\rm FIR}$–SFR relationship by Thronson & Telesco (1986) the resulting SFR differs significantly from the latter values. For the total galaxy we get 5.7 M$_\odot$ yr^{-1}, while the nuclear region contributes 2.6 M$_\odot$ yr^{-1}, if we use the estimation of 4×10^9 L$_\odot$ for the central FIR luminosity from Telesco & Harper (1980). This discrepancy may reflect the uncertainty by the simplified model to determine the SFR from the X-ray flux. Since most of the soft X-ray emission originates from the thin bubble shell, the swept-up ambient material, and internal shocks (Heckman et al. 1990) the effect of accumulating bubbles may be essential. Thronson & Telesco (1986) compared SFRs derived from $L_{\rm FIR}$ with those from Hα luminosities pointing to uncertainties due to extinction. The discrepancy for NGC 2903 is well within the range of their result.

4.2. The soft western halo component

As already mentioned in Sect. 3.1 the main interesting feature in the PSPC data is the very soft ($HR = -0.16$) X-ray emission in area 4 (Fig. 3b). It extends 2′ (5.2 kpc) from the nucleus to the west in the 0.1–0.4 keV regime. Comparison with Fig. 3c reveals that it exceeds the extension of the 0.5–0.9 keV disk component. Also the asymmetrical shape relative to the center is only discernible in the soft regime. Whereas the spatial distribution in the intermediate energy range follows the optical disk, the soft emission is primarily directed from the center to the west along the minor axis with no eastern counterpart. Since the H I map of NGC 2903 (Wevers et al. 1986) gives a column density of at least 8×10^{20} cm^{-2} in the inner disk (in particular the region covered by X-ray emission) with a maximum of about 1.7×10^{21} cm^{-1}, this soft extended component cannot originate from behind the galactic disk. Reasonably, the emission may stem from one or several giant H II regions in the disk as is the case for the northern HRI disk source. Whereas, however, the corresponding northern H II region is clearly detectable in the Hα image, no strong Hα emission is visible in the western part of the disk. Even if the soft component would originate from unresolved strong point sources they would also have to appear in the HRI image. A probable foreground star can be excluded because there is no corresponding object in the optical broad band image. We therefore prefer an X-ray outflow as the most plausible explanation of the western diffuse emission.

4.3. A galactic wind

Since NGC 2903 houses a central starburst, an X-ray halo as observed in several edge-on galaxies (M82: e.g. Lehnert et al. 1999; Weaver et al. 2000; NGC 253: e.g. Pietsch et al. 2000; NGC 2146: della Ceca et al. 1999; DWH98; NGC 3628: Dahlem et al. 1996; NGC 4565: Vogler et al. 1996; NGC 4569: Tschöke et al. 2000a) can cause this observational feature. X-ray halos in active galaxies are believed to be produced by giant kpc-scale outflows of hot gas from stellar winds and cumulative SN II explosions in the central starbursts (Tomisaka & Ikeuchi 1988). The outflow material forms a superbubble expanding into the ambient ISM, preferably along the steepest density gradient, i.e. perpendicular to the galactic disk. The hot gas expands with velocities up to several 1000 km s^{-1}, heated up by internal shocks of subsequent explosions to some 10^7 to 10^8 K (Michaelis 1995). Thereby, it sweeps up the ambient material in a shocked thin shell around the superbubble.

Once the diameter of the bubble reaches several times the scaleheight of the disk the thin shell fragments via Rayleigh-Taylor instabilities and the hot gas blows out into the halo. Internal shocks within the bubble are the origin of hard (about 10 keV) X-ray emission, while evaporation of density inhomogeneities (clouds) in the halo and the adiabatic cooling due to expansion lead to soft X-ray emission and optical/UV line emission. Also the thin swept-up shell can cause strong optical line emission and soft X-rays (Heckman et al. 1993; Strickland & Stevens 2000).

We already reported the existence of a similar X-ray feature in the Virgo Cluster galaxy NGC 4569 (Tschöke et al. 2000a). In this object the soft western X-ray emission coincides with a huge Hα filament. This remarkable feature is unique in the sense that a coincidence of Hα and X-ray emission of this extension has not been observed in comparable starburst galaxies so far (Bomans et al. 2000; Tschöke et al. 2000a). In the case of NGC 2903 there is no diffuse Hα emission connected to the soft X-ray feature. Noticeably, NGC 2903 is not a cluster member and has no strongly disturbed morphology or nearby companion. Also the observed X-ray halos in other edge-on galaxies are not linked with Hα filaments as large as the X-ray emission.

The absence of a corresponding eastern counterpart supports the galactic disk orientation in space with the eastern part closer to the observer. Assuming a symmetrical bipolar outflow (i.e. the same extension of the eastern counterpart) any X-ray emission from that region would have to penetrate through the galactic disk with a column density of at least $8{\times}10^{20}$ cm^{-2}. Hence the soft X-ray flux is blocked so that no detection is expected from a possibly existing counterpart.

4.4. Physical halo properties

If we assume the western soft component to originate from a superwind propagating from the galactic center of NGC 2903 perpendicularly into the halo, we can estimate some physical parameters of the hot halo gas, like temperature T, mean electron density $n_{\rm e}$, mass M, and cooling time scale $\tau_{\rm cool}$ from the observed X-ray emission. Given the X-ray luminosity and the volume of the halo gas V we can estimate the electron density from the emissivity of a thin hot plasma Λ for a RS model by the equation $L_{\rm X} = n_{\rm e}^2\,\Lambda(T)\,V$ (see e.g. Bomans et al. 1997). The X-ray flux from the halo region is quite faint. With a signal-to-noise ratio of 3 we get a spectrum of only 6 bins (54 counts, see Fig. 6e). So we have to presume some physical boundaries for the extraplanar gas. For the geometry we assume a conical shape, as sketched in Fig. 9, perpendicular to the disk with an inclination of 66°; the characterizing dimensions are $R_{\rm max} = 4.5$ kpc, $R_{\rm min} = 3.8$ kpc, and $D_{\rm max} = 4.1$ kpc. These boundaries are adapted from region no. 4 in Fig. 5. Contamination from nucleus and disk increases with smaller distance from the center. We furthermore assume a H I column density for this region equal to the Galactic foreground value of $2.8{\times}10^{20}$ cm^{-2}. The hardness ratio of -0.16 corresponds to a plasma temperature of about 0.2 keV for a RS spectrum observed with the ROSAT PSPC. Under these conditions we deduce the 0.1–2.4 keV luminosity for the X-ray halo amounts to $L_{\rm X} \approx 4{\times}10^{38}$ erg s^{-1}. Applying a single RS model with 0.1 Z$_\odot$ leads to an emissivity of $\Lambda = 4.8{\times}10^{-24}$ erg s^{-1} cm^3 and results in a mean electron density for the extraplanar gas of $0.020\,f^{-0.5}$ cm^{-3}, depending on the volume filling factor f of the X-ray emitting gas. The total mass amounts to $3.5{\times}10^6\,f^{0.5}$ M$_\odot$. The cooling time scale $\tau_{\rm cool}$ of the gas is $3\,kT/n\Lambda = 1.6{\times}10^8\,f^{0.5}$ yr. Thermal energy and thermal pressure of the X-ray halo are $E_{\rm th} = \frac{3}{2}\,nVkT = 2.0{\times}10^{54}\,f^{0.5}$ erg, and $P = 2\,nkT = 1.3{\times}10^{-11} f^{-0.5}$ dyn cm^{-2}.

The estimation of these properties is based on several improper assumptions. To determine the reliability of the values for the halo gas we try to confine the most important error sources. The plasma temperature determined from the hardness ratio mostly depends on the chosen absorbing column density. It is much less sensitive with respect to metallicity. If we take an upper limit of $8{\times}10^{20}$ cm^{-2} (the value for the H I disk of NGC 2903) the uncertainty of the temperature is about 40%. Therefore the corresponding emissivity of the RS plasma varies by about 20%. Λ is much more sensitive to the chosen metallicity. Taking solar metallicities the emissivity of the plasma increases by a factor of 5, resulting in a mean electron density about 0.4 times smaller. From the error estimation of plasma temperature and absorbing component the resulting error for the X-ray luminosity reaches up to 50%. Therefore we estimate the uncertainty for the mean electron density to be $7{\times}10^{-3}$ cm^{-3}, not including the error from the metallicity in the determination of Λ and the simplified geometry of the halo volume. The resulting physical parameters for the X-ray halo of NGC 2903 are listed in Table 8.

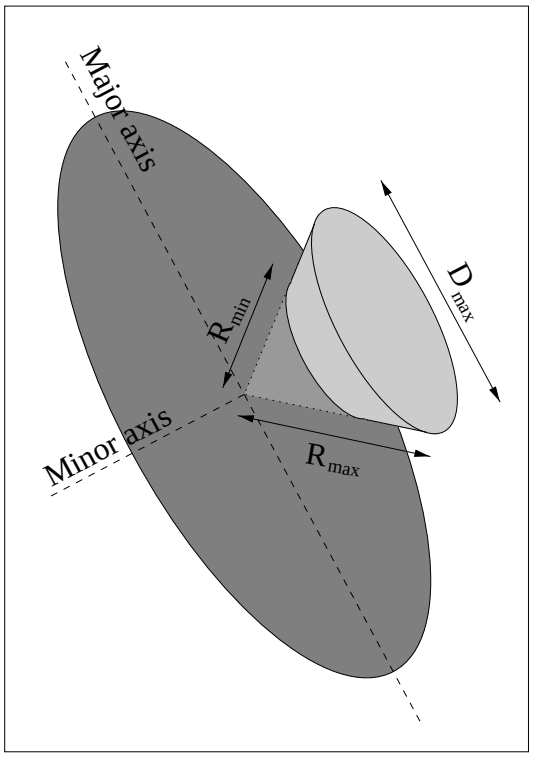

Fig. 9. Sketch of the applied geometry for the central outflow. The lightgray area margins the X-ray emitting volume corresponding region 4 in Fig. 5. To determine $R_{\rm min}$, $R_{\rm min}$, and $D_{\rm max}$, an outflow orientation perpendicular to the disk with the inclination of 66° has been used.

Comparing the halo properties of NGC 2903 with edge-on galaxies we find that the low X-ray temperature fits well in the former observations. The outflows in other starburst galaxies show plasma temperatures in the range of 0.16–0.3 keV. The 0.1–2.4 keV halo luminosity is somewhat lower than the ones in other galaxies. On the other hand one has to note that the given luminosity is only derived from the outer part of the outflow in NGC 2903 because of the inclined disk. Taking this into account the flux probably lies in the lower limit range of the sample.

Table 8. Physical properties of the X-ray halo of NGC 2903 with different volume filling factors and metallicities of the X-ray emitting plasma.

Plasma metallicity $Z/Z_\odot$	0.1	0.1	1	1
Volume filling factor f	1	0.2	1	0.2
Temperature kT/keV	$0.19^{+0.07}_{-0.08}$	$0.19^{+0.07}_{-0.08}$	$0.18^{+0.07}_{-0.08}$	$0.18^{+0.07}_{-0.08}$
Luminosity $L_X/(10^{38}$ erg s$^{-1})$	4±2	4±2	4±2	4±2
Electron density $n/(10^{-2}$cm$^{-3})$	2.0±0.7	4.5±1.6	0.9±0.3	2.0±0.7
X-ray halo mass $M/(10^6$ M$_\odot)$	3.5±1.2	1.6±0.5	1.5±0.5	0.7±0.2
Cooling time $\tau/(10^8$ yr)	$1.6^{+2.5}_{-0.9}$	$0.7^{+1.1}_{-0.4}$	$0.7^{+1.1}_{-0.4}$	$0.3^{+0.5}_{-0.2}$
Thermal energy $E_{th}/(10^{54}$ erg)	$2.0^{+2.0}_{-1.5}$	$0.9^{+0.9}_{-0.7}$	$0.9^{+0.9}_{-0.7}$	$0.4^{+0.4}_{-0.3}$
Pressure $P/(10^{11}$ dyn cm$^{-2})$	1.3±0.9	2.9±2.0	0.6±0.4	1.3±0.9

[a] Taking the inclination $i = 66°$ of the galactic disk into account.
[b] Boundaries are chosen regarding region 4 in Fig. 5.

The cooling time scale of about 10^8 yr is high enough that the expanding plasma still emits in the X-rays at kpc-scale distances from the starburst.

5. Conclusions

The spatial and spectral distribution of the 0.1–2.4 keV X-ray emission of the late-type 'hot-spot' galaxy NGC 2903 observed by ROSAT strongly suggests the existence of an extended X-ray gas component about 5 kpc above the disk of NGC 2903. This galaxy and NGC 4569 are the only reported objects at intermediate inclination with an observed X-ray halo so far. In contrast to NGC 4569 where additionally an Hα filament as extended as the X-ray component has been detected and the interaction with the ICM of the Virgo cluster plays an important role for the observed X-ray and Hα morphology, NGC 2903 is no cluster member, but instead an isolated system with no disturbing companion. So no process induced by external forces like ram-pressure stripping of the internal ISM, as happens in galaxy clusters or by some close encounter, is assumed to produce the extraplanar X-ray component.

The derived properties for the extraplanar feature match the ones determined for the observed X-ray halos in edge-on galaxies. From the spectral distribution we obtain a plasma temperature of 0.2 keV and a luminosity of 4×10^{38} erg s^{-1}. This should be treated as a lower limit because contamination from disk and nuclear region does not allow to quantify the total area of the central outflow down to the galactic center. So the X-ray luminosity may be higher by a factor of 2. Mass and electron density of the X-ray emitting material in the considered region lie in the range of several 10^6 M$_\odot$ and 10^{-3} cm^{-3}, respectively. A more accurate determination of the physical properties of the halo component requires deeper exposures for a stronger spectrum, a higher spectral resolution for a reliable determination of the metallicity of the soft X-ray emitting gas, and a better spatial resolution of the outflow structure

The spatial distribution of the 0.5–0.9 keV emission coincides with the Hα image of NGC 2903, indicating ongoing star formation throughout the disk with a SFR of 1–2 M$_\odot$ yr^{-1}, consistent with the value derived from Hα. The fraction of the SFR from the nuclear region estimated by the X-ray flux is about 50%. This is somewhat higher than the value given by Jackson et al. (1991) who estimated about 13% of the Hα flux contributed by the nuclear region. However, the low spatial resolution of the PSPC has to be taken into account. Because of the simplified model the resulting values are possibly by a factor of 2–5 too low as the FIR emission in NGC 2903 suggests.

Acknowledgements. The authors are grateful to Alessandro Boselli for stimulating discussions, and kindly providing the Hα data, and to Polichronis Papaderos for providing the optical broadband image. The ROSAT project is supported by the German Bundesministerium für Bildung, Wissenschaft, Forschung und Technologie (BMBF) and the Max-Planck-Society. This research has made use of the NASA/IPAC Extragalactic Database (NED) which is operated by the Jet Propulsion Laboratory, Caltech, under contract with the NASA. D.T. was partly supported by the Deutsche Forschungsgemeinschaft under project no. He 1487/23

References

Alonso-Herrero A., Ryder S.D., Knapen J.H., 2000, MNRAS, in press
Arnaud K.A., 1996, Astronomical Data Analysis Software and Systems V, ASP Conf. Ser. vol. 101, eds. Jacoby G., Barnes J., p. 17
Bomans D.J., Chu Y.-H., Hopp U., 1997, AJ 113, 1678
Bomans D.J., Tschöke D., Hensler G., Boselli A., 2000, submitted to A&A
Briel U., Aschenbach B., Hasinger G., et al., 1996, ROSAT User's Handbook, MPE, Garching
Cioffi D., 1990, in "Physical Processes in Hot Plasmas", NATO ASI Series C, Vol. 305, eds. Brinkmann W., Fabian A.C., Giovanelli F., Kluwer, Dordrecht, p. 1
Dahlem M., Heckman T.M., Fabbiano G., Lehnert M.D., Gilmore D., 1996, ApJ 461, 724
Dahlem M., Weaver K.A., Heckman T.M., 1998, ApJS 118, 401 (DWH98)
della Ceca R., Griffiths R.E., Heckman T.M., Lehnert M.D., Weaver K.A., 1999, ApJ 514, 772

Dickey J.M., Lockman F.J., 1990, ARA&A 28, 215
Drozdovsky I.O., Karachentsev I.D., 2000, A&AS 142, 425
Freyer T., Hensler G., 2000, *Astrophysical Plasmas: Codes, Models, and Observations*, eds. J. Arthur, N. Brickhouse, J. Franco, Rev. Mex. Astron. Astrofis. Conf. Ser. Vol. 9, p. 187
Heckman T.M., Armus L., Miley G.K., 1990, ApJS 74, 833
Heckman T.M., Lehnert M.D., Armus L., 1993, in "The Environment and Evolution of Galaxies", eds. Shull J.M., Thronson H.A., Kluwer, Dordrecht, p. 455
Jackson J.M., Eckart A., Cameron M., et al., 1991, ApJ 375, 105
Junkes N., Zinnecker H., Hensler G., Dahlem M., Pietsch W., 1995, A&A 294, 8
Kennicutt R.C., Jr., 1983, ApJ 272, 54
Laques P., Nieto J.-L., Vidal J.-L., Augé A., Despiau R., 1980, Nat 288, 145
Lehnert M.D., Heckman T.M., Weaver K.A., 1999, ApJ 523, 575
Leitherer C., 1994, Rev. Mod. Astr. 7, 73
Michaelis O., 1995, Diploma thesis, University of Kiel
Norman C.A., Ikeuchi S., 1989, ApJ 345, 372
Oka S., Wakamatsu K., Sakka K., 1974, PASJ 26, 289
Pietsch W., Vogler A., Klein U., Zinnecker H., 2000, A&A 360, 24
Planesas P., Colina L., Pérez-Olea D., 1997, A&A 325, 81
Pogge R.W., Eskridge P.B., 1987, AJ 93, 291
Raymond J.C., Smith B.W., 1977, ApJS 35, 419
Rice W., Lonsdale C.J., Soifer B.T., et al., 1988, ApJS 68, 91
Shields G.A., 1990, ARA&A 28, 525
Sérsic J.L., 1973, PASP 85, 103
Simons D.A., DePoy D.L., Becklin E.E., et al., 1988, ApJ 335, 126
Stevens I.R., Forbes D.A., Norris R.P., 1999, MNRAS 306, 479
Strickland D.K., Stevens I.R., 2000, MNRAS 314, 511
Suchkov A.A., Balsara D.S., Heckman T.M., Leitherer C., 1994, ApJ 430, 511
Telesco C.M., Harper D.A., 1980, ApJ 235, 392
Thronson H.A., Jr., Telesco C.M., 1986, ApJ 311, 98
Tomisaka K., Ikeuchi S., 1988, ApJ 330, 695
Tschöke D., Bomans D.J., Hensler G., Junkes N., 2000a, submitted to A&A
Tschöke D., Hensler G., Junkes N., 1999, A&A 343, 373
Tschöke D., Hensler G., Junkes N., 2000b, A&A 360, 447
Tully R.B., 1988, Nearby Galaxies Catalog, Cambridge University Press, Cambridge
van der Kruit P.C., 1973, A&A 29, 231
Vogler A., Pietsch W., Kahabka P., 1996, A&A 305, 74
Weaver K.A., Heckman T.M., Dahlem M., 2000, ApJ 534, 684
Wevers B.M.H.R., van der Kruit P.C., Allen R.J., 1986, A&AS 66, 505
Wynn-Williams C.G., Becklin E.E., 1985, ApJ 290, 108
Zimmermann H.U., Becker W., Belloni T., et al., 1997, EXSAS User's Guide, Edition 5, MPE Report, Garching

Chapter 9

Summary and future work

9.1 Conclusions from the X-ray analysis

The X-ray study of a small sample of four starburst galaxies have been presented, varying in morphology, in influences from their surroundings, and in distance, obtained by the ROSAT satellite telescope. The analysis intends to study the impact of a number of different factors on the star formation activity and on the observable X-ray properties. Besides statistical evaluations of large samples of galaxies, the study of single objects, considering their individual characteristics, is necessary to obtain a better and more global understanding of galaxy evolution.

In each of the objects, the nature of the central activity has been discussed, whether being dominated by a central or circumnuclear starburst or by an accretion-powered AGN. The most distant object in the presented sample, NGC 4410, consists of a close pair of interacting systems. While the eastern elliptical component reveals at most a very faint X-ray source, the nuclear region of the western spiral NGC 4410 a emits 4×10^{41} erg s^{-1} in the ROSAT energy range of 0.1–2.4 keV. It is the most luminous object in the sample. This is remarkable since NGC 4410 is the only strongly interacting object in the galaxy sample. NGC 4410 a is dominated by a non-thermal component, while about 33% are contributed by thermal emission. The origin of a small one-sided extension of this central source has been discussed in this context. Provided NGC 4410 a contains a nuclear starburst, expanding hot gas from a superbubble may cause this emission, being additionally exposed to the complex potential of the disturbed system. As another possibility the existence of a decentral source has been discussed. This is supported by the coincidence with a luminous HII region, visible in a V-band HST exposure.

A better spatial subdivision into several distinct X-ray sources can be performed in the barred galaxy NGC 4303. The face-on orientation of the galactic disk provides a good distinction between nuclear and disk X-ray emission. The distribution of X-ray sources throughout the disk, i.e. a strong central source and additional sources at the ends of the bar and within the spiral arms, is consistent with gas dynamical simulations in systems with barred potential. Comparison of extension, spectral distribution, and X-ray flux of the central source with UV and Hα observations lead to the interpretation of a compact central source (preferably a low luminous AGN) surrounded by a circumnuclear starburst. X-ray disk sources coincide with the most luminous HII regions, originating from stellar winds of massive hot stars, supernova explosions, and/or HMXBs in several star-forming regions.

NGC 4569 attracts attention in its structure, observable in Hα and X-rays. Unlike any other comparable galaxy, this object contains a very extended extraplanar component

of 9 kpc, detectable in both spectral ranges. The soft nature of the X-ray feature and the comparison with several edge-on galaxies with X-ray halos supports the existence of a galactic superwind, originating from the central starburst in NGC 4569. As predicted from hydrodynamical simulations, the coincidence of extended Hα and soft X-ray emission is expected for such a superbubble, expanding from the disk into the halo. The alternative possibility of a photoionization cone from a central AGN does not correspond with observations in other Seyfert galaxies in terms of morphology and extension. Furthermore, it does not explain the soft extraplanar X-ray source. Strong impact from the interaction with the Virgo ICM is discernible in the disturbed Hα morphology, revealing several emission knots beside the disk. The influence from the ambient Virgo ICM on the central gaseous outflow has been discussed. The HI disk of NGC 4569 possibly serves as protection shield for the extraplanar gas at the lee side, as discussed e.g for NGC 4388 (Veilleux et al. 1999).

Similar to NGC 4569, an extraplanar soft X-ray feature is detectable in NGC 2903. Observations of X-ray halos are strongly biased, due to their low luminosity relative to X-rays from nucleus and disk in starburst galaxies. X-ray halos have only been detected in edge-on galaxies so far. NGC 4569 and NGC 2903 are the first reported systems with intermediate inclination and an extraplanar soft X-ray component expanding 9 kpc and 5 kpc, respectively, into the galactic halo. In contrast to the former galaxy, NGC 2903 is an isolated system with no nearby companion or disturbed morphology. Also no coinciding Hα emission, comparable to the one in NGC 4569, is present in NGC 2903. The central X-ray source is slightly extended, covering the area of the optical hot spots. The X-ray spectrum favours the interpretation of a central starburst. Whether the nuclear activity originates from several distinct regions, as observable in the optical, or from a patchy structure of central dust and gas while the central source is more homogeneous, as concluded from radio observations, is not possible to determine from the spatial resolution of the HRI data. Since X-rays in the ROSAT energy range are strongly affected by absorption, any hot-spot structure in the X-rays could be caused by such inhomogeneously distributed central IGM, as well as by several distinct emission regions.

9.2 Open questions

One main difficulty in analyzing the presented ROSAT data turned out to be the relatively low spatial and spectral resolution to meet the complex structure of starburst regions. How important it is to distinguish spatially different components in starburst galaxies and to discriminate their individual spectral distributions, has been indicated for the presented objects, e.g. in terms of composition of the nuclear source or hot halo gas. Partly, the available data allow only to examine blends of distinct components, like in the case of NGC 4410 due to the large distance, or for NGC 4303 where simultaneous spectral and spatial information is only given for the entire system.

The necessity to improve the data quality is obvious, if we note observations of nearby galaxies with comparable properties. As mentioned in Sect. 2.3.2, there is a controversial discussion on the determination of temperature and metallicity of the hot halo gas in NGC 253 from available X-ray observations (Persic et al. 1998; Ptak et al. 1999; Dahlem et al. 2000; Weaver et al. 2000; Pietsch et al. 2000). Comparable differing interpretations have been published for M82. Especially, strong deviations turned out in the resulting metallicity of the halo gas. While the works by Dickow (1995) and Dahlem et al. (1998) yield a significant enhancement of metals compared to solar values, sub-solar abundances down to 0.05 $Z_\odot$ have been stated by Strickland et al. (1999). This contradic-

tion in metallicity determination emphasizes the necessity of improving spectral resolution of X-ray detectors. The ROSAT PSPC provided the opportunity to carry out position sensitive X-ray spectroscopy with moderate resolution. Nevertheless, with this detector only broad blends of emission lines are detectable. The level of underlying continuum and the strength of lines can only be folded into an applied emission model, including the detector properties.

Better spectral resolution not only provides more accurate constraints to theoretical models, but also helps to improve the knowledge on the plasma state in hot gas from SBs. From theoretical considerations, the assumption of ionization equilibrium (IEQ) in hot plasmas is not necessarily correct. The plasma temperature decreases due to expansion work. The low-density halo gas ($n_e \approx 10^{-3}$ cm^{-3}) will be increasingly rarefied in the expansion process. This leads to frozen-in high ionization states. The impact on these conditions on the emissivity of hot gas has been investigated in our working group (Kühnholz 1998). It turns out that deviation from IEQ grows significantly for superbubbles in the blow-out phase. Such a hot plasma in non-IEQ cooling down while expanding conserves higher ionization states than a plasma in IEQ. Therefore its line radiation is much more effective in X-rays at a given temperature. Consequently, the interpretation of its spectral distribution on the assumption of IEQ may lead to a temperature determination which is too high. For solar abundances the effect increases significantly for X-ray halo gas at heights of about 23 kpc or more above the galactic disk, while for a plasma with enhanced metallicity with values according to Woosley & Weaver (1986) the temperature rapidly drops and the deviation from IEQ becomes significant at heights of already 3 kpc.

9.3 Follow-up X-ray missions

The structural complexity of X-rays in starburst galaxies, as observable in M82 and NGC 253, and the consideration of non-IEQ effects, depending on metallicity, make clear the requirements for follow-up X-ray satellites. Spectral resolution has to be improved to put constraints on emission models. Simultaneously, high spatial resolution has to provide the possibility to discriminate structural components. The latest generation of X-ray missions are the American X-ray telescope *Chandra*, developed by NASA, and the European satellite XMM-*Newton*, developed by the European Space Agency (ESA).

Chandra has been launched in July, 1999. It carries two focal plane detectors, the High Resolution Camera (HRC) for imaging with a high spatial resolution of $\sim 0\farcs5$, and the Advanced CCD Imaging Spectrometer (ACIS). The ACIS provides simultaneous imaging with a resolution of $\sim 1''$ and spectroscopy with a moderate spectral resolution of $\Delta E/E = 9$ at 1 keV. In comparison, ROSAT PSPC has $\Delta E/E = 0.43$ at 1 keV. High resolution spectroscopy ($\Delta E/E = 0.01$–0.001) can be performed by two additional gratings. *Chandra* operates in the energy range of 0.08–10 keV.

XMM-*Newton* has been launched in December, 1999. It provides the ability to carry out simultaneous high spectral and spatial resolution observations ($\Delta E/E = 0.06$ at 1 keV; FWHM $\sim 6''$) in the energy range of 0.1–15 keV. This is performed by the two European Photon Imaging Cameras (EPIC). Additionally, with the Reflection Grating Spectrometer (RGS) high resolution spectroscopy ($\Delta E/E = 0.02$) can be done. The advantage of the EPIC detectors lies in the fact that with a spatial resolution, comparable to the one of the ROSAT HRI, the SED of X-ray sources with excellent spectral resolution can be investigated. Another important point is the very large effective area of XMM-*Newton*, providing the observation of very faint sources. This new generation of instruments not only improves the study of nearby objects, but also increases the ability to observe and

analyze X-rays from SBs in more detail.

The next generation of X-ray observatories has already been planned. Currently, ESA is developing the X-ray Evolving Universe Spectroscopy Mission (XEUS), which will be about 250 times more sensitive than XMM-*Newton*. It will provide spectroscopic observation of between 1 and 10 eV resolution over the energy range 0.05 to 30 keV with a spatial resolution of $2''$.

Bibliography

Journal abbrevations:

AJ	The Astronomical Journal
ApJ	The Astronphysical Journal
ApJS	The Astronphysical Journal Supplement Series
Ap&SS	Astrophysics and Space Science
ARA&A	Annual Review of Astronomy and Astrophysics
Astron. Rep.	Astronomy Reports (former Soviet Astronomy)
A&A	Astronomy and Astrophysics
A&AR	The Astronomy and Astrophysics Review
A&AS	Astronomy and Astrophysics Supplement Series
Bull. Astr. Soc. India	Bulletin of the Astronomical Society of India
MNRAS	Monthly Notices of the Royal Astronomical Society
PASJ	Publications of the Astronomical Society of Japan
PASP	Publications of the Astronomical Society of the Pacific
Phys. Rev. Lett.	Physical Review Letters
Rev. Mex. Astron. Astrofis.	Revista Mexicana de Astronomía y Astrofísica
Rev. Mod. Astr.	Reviews in Modern Astronomy

Allen G.E., Keohane J.W., Gotthelf E.V., et al., 1997, ApJ 487, L97

Arnaud K.A., 1996, in *Astronomical Data Analysis Software and Systems V*, ASP Conf. Ser. Vol. 101, eds. G. Jacoby, J. Barnes, p. 17

Bałucińska-Church M., McCammon D., 1992, ApJ 400, 699

Barber C.R., Roberts T.P., Warwick R.S., 1996, MNRAS 282, 157

Berman V., Suchkov A.A., 1991, Ap&SS 184, 169

Binggeli B., 1994, in *Panchromatic View of Galaxies - Their Evolutionary Puzzle*, eds. G. Hensler, J.S. Gallagher, Ch. Theis, Edition Frontières, Gif-sur-Yvettes, p. 173

Binggeli B., Cameron L.M., 1991, A&A 252, 27

Binggeli B., Sandage A., Tammann G.A., 1985, AJ 90, 1681

Binney J., Tremaine S., 1987, *Galactic Dynamics*, Princeton University Press, Princeton, New Jersey

Bookbinder J., Cowie L.L., Krolik J.H., Ostriker J.P., Rees M., 1980, ApJ 237, 647

Borkowski K.J., Lyerly W.J., Reynolds S.P., 2000a, ApJ, submitted (astro-ph/0008066)

Borkowski K.J., Rho J., Reynolds S.P., Dyer K.K., 2000b, ApJ, accepted (astro-ph/0006149)

Borkowski K.J., Szymkowiak A.E., Blondin J.M., Sarazin C.L., 1996, ApJ 466, 866

Bothun G.D., Impey C., Malin D., 1991, ApJ 376, 404

Bradamante F., Matteucci F., D'Ercole A., 1998, A&A 337, 338

Bradt H.V.D., Ohashi T., Pounds K.A., 1992, ARA&A 30, 391
Breitschwerdt D., Schmutzler T., 1999, A&A 347, 650
Briel U.G., Aschenbach B., Englhauser J., et al., 1997, *ROSAT User's Handbook*, Max-Planck-Institut für extraterrestrische Physik, Garching, Germany
Burrows D.N., Mendenhall J.A., 1991, Nature 351, 629
Bushouse H.A., 1986, AJ 91, 255
Castor J., McCray R., Weaver R., 1975, ApJ 200, L107
Chapelon S., Contini T., Davoust E., 1999, A&A 345, 81
Chu Y.-H., Mac Low M.-M., 1990, ApJ 365, 510
Cid Fernandes R., 1997, in *Starburst Activity in Galaxies*, eds. J. Franco, R. Terlevich, A. Serrano, Rev. Mex. Astron. Astrofis. Conf. Ser. Vol. 6, p. 201
Ciotti L., Pellegrini S., Renzini A., D'Ercole A., 1991, ApJ 376, 380
Coe M.J., 2000, in *The Be Phenomenon in Early-Type Stars*, Proceedings of the IAU Colloquium No. 175, eds. M. Smith, H. Henrichs, J. Fabregat, in press
Colless M., Ellis R.S., Taylor K., Hook R.N., 1990, MNRAS 244, 408
Combes F., Gerin M., 1985, A&A 150, 327
Dahlem M., 1997, PASP 109, 1298
Dahlem M., Heckman T.M., Fabbiano G., Lehnert M.D., Gilmore D., 1996, ApJ 461, 724
Dahlem M., Parmer A., Oosterbroek T., et al., 2000, ApJ 538, 555
Dahlem M., Weaver K.A., Heckman T.M., 1998, ApJS 118, 401
Davies R.I, Sugai H., Ward M.J., 1998, MNRAS 300, 388
Decourchelle A., Ellison D.C., Ballet J., 2000, ApJ, submitted (astro-ph/0008344)
Dekel A., Silk J., 1986, ApJ 303, 39
Dere K.P., Landi E., Mason H.E., Monsignori Fossi B.C., Young P.R., 1997, A&AS 125, 149
de Young D.S., 1978, ApJ 223, 47
de Zeeuw T., Franx M., 1991, ARA&A 29, 239
Dickey J.M., Lockman F.J., 1990, ARA&A 28, 215
Dickow R., 1995, Diploma thesis, University of Kiel, Germany
Driver S.P., Windhorst R.A., Griffith R.E., 1995, ApJ 453, 48
Duc P.-A., Mirabel I.F., 1994, A&A 289, 83
Duc P.-A., Mirabel I.F., 1998, A&A 333, 813
Fabbiano G., 1989, ARA&A 27, 87
Fabian A.C., 1992, ARA&A 30, 429
Ferguson H.C., Binggeli B., 1994, A&AR 6, 67
Forman W., Jones C., Cominsky L., et al., 1978, ApJS 38, 357
Forman W., Schwarz J., Jones C., Liller W., Fabian A., 1979, ApJ 234, L27
Franco J., Ferrara A., Rozyczka M., Tenorio-Tagle G., Cox D.P., 1993, ApJ 407, 100
Garnett D.R., 1990, ApJ 360, 142
Giacconi R., Gursky H., Paolini F., Rossi B., 1962, Phys. Rev. Lett. 9, 439
Guzman R., Jangren A., Koo D.C., et al., 1998, ApJ 495, L13
Haberl F., Sasaki M., 2000, A&A 359, 573
Heckman T.M., 1998, in *Origins*, ASP Conf. Ser. Vol. 148, eds. C.E. Woodward, J.M. Shull, H.A. Thronson, Jr., p. 127
Heckman T.M., Armus L., Miley G., 1990, ApJS 74, 833
Heckman T.M., Lehnert M.D., Armus L., 1993, in *The Environment and Evolution of Galaxies*, eds. J.M. Shull, H.A. Thronson, Jr., Kluwer Academic Publisher, Dordrecht, p. 455
Heller C.H., Shlosman I., 1994, ApJ 424, 84

Henke B.L., Lee P., Tanaka T.J., Shimabukuro R.L., Fujikawa B.K., 1982, Atomic Data and Nucl. Data Tables 27, 1
Huang J.H., Gu Q.S., Su H.J., et al., 1996, A&A 313, 13
Hultman J., Pharasyn A., 1999, A&A 347, 769
Izotov Y.I., Lipovetzky V.A., Guseva N.G., et al., 1990, Nature 343, 238
Jog C.J., 1995, Bull. Astr. Soc. India 23, 13
Joseph R.D., Meikle W.P.S., Robertson N.A., Wright G.S., 1984, MNRAS 209, 111
Junor W., Biretta J.A., Livio M., 1999, Nature 401, 891
Kaastra J.S., Mewe R., Nieuwenhuijzen H., 1996, in *UV and X-ray Spectroscopy of Astrophysical and Laboratory Plasmas*, eds. K. Yamashita, T. Watanabe, Univ. Acad. Press, Tokyo, p. 411
Keel W.C., 1985, in *Astrophysics of Active Galaxies and Quasi-Stellar Objects*, ed. J.S. Miller, University Science Books, Mill Valley, p. 1
Kennicutt R.C., 1998, ARA&A 36, 189
Köppen J., Theis Ch., Hensler G., 1995, A&A 296, 99
Köppen J., Theis Ch., Hensler G., 1998, A&A 331, 524
Koo D.C., Guzman R., Faber S.M., et al., 1995, ApJ 440, L49
Kormendy J., Richstone D., 1995, ARA&A 33, 581
Kühnholz S., 1998, Diploma thesis, University of Kiel, Germany
Kunth D., Matteucci F., Marconi G., 1995, A&A 297, 634
Lehnert M.D., Heckman T.M., Weaver K.A., 1999, ApJ 523, 575
Leitherer C., 1994, Rev. Mod. Astr. 7, 73
Lilly S.J., Cowie L.L., Gardener J.P., 1991, ApJ 369, 79
Lonsdale C.J., Persson S.E., Matthews K., 1984, ApJ 287, 95
Lutz D., Genzel R., Sternberg A., et al., 1996, A&A 315, L137
Mac Low M.-M., 2000, in *Astrophysical Plasmas: Codes, Models, and Observations*, eds. J. Arthur, N. Brickhouse, J. Franco, Rev. Mex. Astron. Astrofis. Conf. Ser. Vol. 9, p. 273
Mac Low M.-M., McCray R., 1988, ApJ 324, 776
Marconi G., Matteucci F., Tosi M., 1994, MNRAS 270, 35
Martin C.L., Kennicutt R.C., 1995, ApJ 447, 171
Martinet L., Friedli D., 1997, A&A 323, 363
Mathews W.G., 1989, AJ 97, 42
Matteucci F., Tosi M., 1985, MNRAS 217, 391
McCammon D., Sanders W.T., 1990, ARA&A 28, 657
Mewe R., Lemen J.R., van den Oord G.H.J., 1986, A&AS 65, 511
Mihos J.C., Hernquist L., 1994a, ApJ 425, L13
Mihos J.C., Hernquist L., 1994b, ApJ 431, L9
Mihos J.C., Hernquist L., 1996, ApJ 464, 641
Miller B.W., Whitmore B.C., Schweizer F., Fall S.M., 1997, AJ 114, 2381
Mirabel I.F., Dottori H., Lutz D., 1992, A&A 256, L19
Moran E.C., Lehnert M.D., Helfand D.J., 1999, ApJ 526, 649
Morrison R., McCammon D., 1983, ApJ 270, 119
Mulchaey J.S., Colbert E., Wilson A.S., Mushotzky R.F., Weaver K.A., 1993, ApJ 414, 144
Nagase F., 1989, PASJ 41, 1
Netzer H., 1990, in *Active Galactic Nuclei*, eds. T.J.-L. Courvoisier, M. Mayor, Springer-Verlag, Berlin, p. 57
Netzer H., 1993, ApJ 411, 594

Noguchi M., 1988, A&A 203, 259
Norman C., Ikeuchi S., 1989, ApJ 345, 372
Norman C., Scoville N., 1988, ApJ, 332, 124
Ostriker J.P., Cowie L.L., 1981, ApJ 243, L127
Papaderos P., Loose H.-H., Thuan T.X., Fricke K.J., 1996, A&AS 120, 207
Pérez-Olea D.E., Colina L., 1996, ApJ 468, 191
Perry J.J., 1992, in *Relationships between active galactic nuclei and starburst galaxies*, ASP Conf. Ser. Vol. 31, ed. A.V. Filippenko, p. 169
Persic M., Mariani S., Cappi M., et al., 1998, A&A 277, 42
Phillips M.M., Jenkins C.R., Dopita M.A., et al., 1986, AJ 91, 1062
Pietsch W., Vogler A., Klein U., Zinnecker H., 2000, A&A 360, 24
Pietz J., Kerp J., Kalberla P.M.W., et al., 1998, A&A 332, 55
Pilyugin L.S., 1992, A&A 260, 58
Piner B.G., Stone J.M., Teuben P.J., 1995, ApJ 449, 508
Popov S.B., Lipunov V.M., Prokhorov M.E., Postnov K.A., 1998, Astron. Rep. 42, 29
Ptak A., Serlemitsos P., Yaqoob T., Mushotzky R., Tsuru T., 1997, AJ 113, 1286
Ptak A., Serlemitsos P., Yaqoob T., Mushotzky R., 1999, ApJS 120, 179
Raymond J.C., Smith B.W., 1977, ApJS 35, 419
Reeves J.N., Turner M.J.L., 2000, MNRAS 316, 234
Reynolds S.P., 1998, ApJ 493, 375
Roberts W.W., Jr., Stewart G.R., 1987, ApJ 314, 10
ROSAT AO-2, 1991, *ROSAT - Call for Proposals*, Technical Appendix with the Rosat Mission Description AO-2, Max-Planck-Institut für Physik und Astrophysik, Max-Planck-Institut für extraterrestrische Physik, Garching, Germany
Sanders D.B., Mirabel I.F., 1996, ARA&A 34, 749
Sanders D.B., Soifer B.T., Elias J.H., et al., 1988, ApJ 325, 74
Schiano A., 1985, ApJ 299, 24
Shapiro S., Teukolsky S.A., 1985, ApJ 292, L41
Skillman E.D., Kennicutt R.C., Hodge P.W., 1989, ApJ 347, 875
Slane P., Gaensler B.M., Dame T.M., et al., 1999, ApJ 525, 357
Smith B.J., 2000, ApJ 541, 624
Smith R.K., Brickhouse N.S., 2000, in *Astrophysical Plasmas: Codes, Models, and Observations*, eds. J. Arthur, N. Brickhouse, J. Franco, Rev. Mex. Astron. Astrofis. Conf. Ser. Vol. 9, p. 134
Snowden S.L., 1998, in *The Local Bubble and Beyond*, Proceedings of the IAU Colloquium No. 166, eds. D. Breitschwerdt, M.J. Freyberg, J. Trümper, Lecture Notes in Physics 506, p. 103
Soifer B.T., Houck J.R., Neugebauer G., 1987, ARA&A 25, 187
Steidel C., Giavalisco M., Pettini M., Dickinson M., Adelberger K., 1996, ApJ 462, L17
Strickland D.K., Ponman T.J., Stevens I.R., 1999, A&A 320, 378
Sturm E., Lutz D., Genzel R., et al., 1996, A&A 315, L133
Suchkov A.A., Balsara D.S., Heckman T.M., Leitherer C., 1994, ApJ 430, 511
Telesco C.M., 1988, ARA&A 92, 749
Terlevich R., 1990, in *Windows on Galaxies*, eds. G. Fabbiano, J.S. Gallagher, A. Renzini, Kluwer Academic Publisher, Dordrecht, p. 87
Terlevich R., Melnick J., 1985, MNRAS 213, 841
Terlevich R., Tenorio-Tagle G., Franco J., Boyle B., 1994, in *The Nature of Compact Objects in AGNs*, eds. A. Robinson, R. Terlevich, Cambridge University Press, p. 209
Thompson L.A., Gregory S.A., 1993, AJ 106, 2197

Tomisaka K., Ikeuchi S., 1988, ApJ 330, 695
Tsuru T., Hayashi I., Awaki H., Koyama K., Ptak A., 1997, PASJ 49, 619
Turner T.J., George I.M., Mushotzky R.F., 1993, ApJ 412, 72
Veilleux S., Bland-Hawthorn J., Cecil G., Tully R.B., Miller S.T., 1999, ApJ 520, 111
Vila-Costas M.B., Edmunds M.G., 1992, MNRAS 259, 121
Vogler A., Pietsch W., Kahabka P., 1996, A&A 305, 74
Watson M.G., 1990, in *Windows on Galaxies*, eds. G. Fabbiano, J.S. Gallagher, A. Renzini, Kluwer Academic Publisher, Dordrecht, p. 177
Weaver K.A., Heckman T.M., Dahlem M., 2000, ApJ 534, 684
Weaver R., McCray R., Castor J., Shapiro P., Moore R., 1977, ApJ 218, 377; erratum ApJ 220, 742
Weedman D.W., 1983, ApJ 266, 479
Weedman D.W., Feldman F.R., Balzano V.A., et al., 1981, ApJ 248, 105
White R.E., III, 1990, ApJ 367, 69
Wiklind T., Combes F., Henkel C., 1995, A&A 297, 643
Williams R.J.R., Baker A.C., Perry J.J., 1999, MNRAS 310, 913
Woltjer L., 1990, in *Active Galactic Nuclei*, eds. T.J.-L. Courvoisier, M. Mayor, Springer-Verlag, Berlin, p. 1
Woosley S.E., Weaver T.A. 1986, in *Radiation Hydrodynamics in Stars and Compact Objects*, Proceedings of the IAU Colloquium No. 89, eds. D. Mihalas, K.H. Winkler, p.91
York D.G., Dopita M., Green R., Bechtold J., 1986, ApJ 311, 610
Zimmermann H.U., Becker W., Belloni T., et al., 1997, *EXSAS User's Guide*, Edition 5, MPE Report, Garching

Danksagung

Zu guter Letzt möchte ich all denjenigen Personen danken, die einen Beitrag dazu geleistet haben, diese Arbeit zu erstellen.

Ich danke meinem Doktorvater Prof. Dr. Gerhard Hensler für die sehr motivierende und angenehme Betreuung und die Möglichkeit, Wissenschaft auf dem faszinierendsten aller Forschungsgebiete, der Astronomie, betreiben zu können.

Weiterhin gilt mein Dank Norbert Junkes, Dominik Bomans und Alessandro Boselli für die fruchtbare Zusammenarbeit und produktive Aufenthalte in Bonn, bzw. Bochum, deren Resultate einen wesentlichen Teil der vorliegenden Dissertation ausmachen.

Wichtigen Anteil am Gelingen der Arbeit hatten ebenso die Mitarbeiterinnen und Mitarbeiter des Instituts für Theoretische Physik und Astrophysik, die selbst einen Badener sehr herzlich aufgenommen und für eine tolle Arbeitsatmosphäre gesorgt haben. Hierbei möchte ich mich besonders bei Frau Ingrid Schmidt bedanken, deren offene und freundliche Art und stete Hilfsbereitschaft sehr wohltuend war. Ebenso seien unsere Systemmanager Günter Jonas und Holger Boll erwähnt, deren unermüdlicher Einsatz die Maschinerie immer am Laufen hielt.

Matthias Hünsch, Marc Hempel und Norbert Junkes haben durch ihre Korrekturen freundlicherweise die Arbeit vom gröbsten sprachlichen, grammatikalischen und inhaltlichen Dreck gesäubert.

Für eine sehr interessante Tagungsteilnahme in Mexico City gilt mein Dank Pepe Franco. Gracias. Ich danke Polichronis Papaderos für die Bereitstellung seiner Daten und hilfreiche Diskussionen.

Mens sana in corpore sano. Vielen Dank an die gesamte Fußballmannschaft, insbesondere an Trainer Tim und Assistenten Stefan, auch für das (fast immer) gute Wetter. Die Kaffeeklatschrunde von Zimmer 142 (Lars, Koslowski, Herr V., Derek) hat von Zeit zu Zeit für Auflockerung der komplizierten Gedanken gesorgt.

Zum Schluss möchte ich meiner Familie für ihre Unterstützung danken, besonders meinen Eltern, durch deren Beitrag und Förderung meiner Interessen es mir erst ermöglicht wurde, die Welt der Astrophysik erleben zu dürfen.